

Forschungsberichte aus dem
wbk Institut für Produktionstechnik
Karlsruher Institut für Technologie (KIT)

Lucas Bretz

**Function-oriented in-line quality assurance
of hybrid sheet molding compound**

Band 255

Forschungsberichte aus dem
wbk Institut für Produktionstechnik
Karlsruher Institut für Technologie (KIT)

Hrsg.: Prof. Dr.-Ing. Jürgen Fleischer
Prof. Dr.-Ing. Gisela Lanza
Prof. Dr.-Ing. habil. Volker Schulze

Lucas Bretz

Function-oriented in-line quality assurance of hybrid sheet molding compound

Band 255

Function-oriented in-line quality assurance of hybrid sheet molding compound

Zur Erlangung des akademischen Grades eines
Doktors der Ingenieurwissenschaften (Dr.-Ing.)

von der KIT-Fakultät für Maschinenbau des
Karlsruher Instituts für Technologie (KIT)

angenommene

Dissertation

von

M.Sc. Lucas Bretz

Tag der mündlichen Prüfung: 11.04.2022

Hauptreferentin: Prof. Dr.-Ing. Gisela Lanza

Korreferent: Prof. Dr. Michael Thompson

Bibliographic information published by the Deutsche Nationalbibliothek

The Deutsche Nationalbibliothek lists this publication in the Deutsche Nationalbibliografie; detailed bibliographic data are available in the internet at <http://dnb.d-nb.de>.

Zugl.: Karlsruhe, Karlsruher Institut für Technologie, Diss., 2022

Copyright Shaker Verlag 2022

All rights reserved. No part of this publication may be reproduced, stored in a retrieval system, or transmitted, in any form or by any means, electronic, mechanical, photocopying, recording or otherwise, without the prior permission of the publishers.

Printed in Germany.

ISBN 978-3-8440-8678-2

ISSN 0724-4967

Shaker Verlag GmbH • Am Langen Graben 15a • 52353 Düren

Phone: 0049/2421/99011-0 • Telefax: 0049/2421/99011-9

Internet: www.shaker.de • e-mail: info@shaker.de

Vorwort der Herausgeber

Die schnelle und effiziente Umsetzung innovativer Technologien wird vor dem Hintergrund der Globalisierung der Wirtschaft der entscheidende Wirtschaftsfaktor für produzierende Unternehmen. Universitäten können als “Wertschöpfungspartner” einen wesentlichen Beitrag zur Wettbewerbsfähigkeit der Industrie leisten, in dem sie wissenschaftliche Grundlagen sowie neue Methoden und Technologien erarbeiten und aktiv den Umsetzungsprozess in die praktische Anwendung unterstützen.

Vor diesem Hintergrund soll im Rahmen dieser Schriftenreihe über aktuelle Forschungsergebnisse des Instituts für Produktionstechnik (wbk) des Karlsruher Instituts für Technologie (KIT) berichtet werden. Unsere Forschungsarbeiten beschäftigen sich sowohl mit der Leistungssteigerung von Fertigungsverfahren und zugehörigen Werkzeugmaschinen- und Handhabungstechnologien als auch mit der ganzheitlichen Betrachtung und Optimierung des gesamten Produktionssystems. Hierbei werden jeweils technologische wie auch organisatorische Aspekte betrachtet.

Prof. Dr.-Ing. Jürgen Fleischer

Prof. Dr.-Ing. Gisela Lanza

Prof. Dr.-Ing. habil. Volker Schulze

Vorwort des Verfassers

Die vorliegende Dissertation entstand während meiner Beschäftigung als akademischer Mitarbeiter des Karlsruher Instituts für Technologie (KIT) am wbk Institut für Produktionstechnik.

Frau Prof. Dr.-Ing. Gisela Lanza gilt mein besonderer Dank für die Betreuung meiner wissenschaftlichen Arbeit als Hauptreferentin. Darüberhinaus möchte ich mich für die persönliche Unterstützung, die kontinuierliche Förderung und das entgegengebrachte Vertrauen bedanken. Die Möglichkeit, im Anschluss meiner Tätigkeit in Deutschland das Global Advanced Manufacturing Institute (GAMI) in Suzhou (China) zu leiten, weiß ich sehr zu schätzen. Weiterhin danke ich Prof. Dr. Michael Thompson für das Interesse an meiner Arbeit, die Möglichkeit des Forschungsaufenthalts an der McMaster University in Hamilton (Kanada) und die Übernahme des Korreferates, sowie Prof. Dr.-Ing. Thomas Böhlke für die Übernahme des Prüfungsvorsitzes.

Allen Kolleginnen und Kollegen des wbk, insbesondere im Bereich Produktionssysteme, gilt mein besonderer Dank. Gerne blicke ich auf die gemeinsamen sportlichen Aktivitäten, wie das morgentliche Schwimmen und das Radfahren oder Trainieren in der Mittagspause, zurück. Namentlich erwähnt seien Leonard Schild und Katja Höger für die gemeinsamen, wertvollen Diskussionen und ihre Sorgfalt sowie der hervorragenden Hinweise bei der Korrektur dieser Arbeit. Den Studenten Krzysztof Debowski, Julius Frontzek, Adrian Gärtner, Dominik Koch und Philipp Müller-Welt möchte ich für ihren Beitrag zu dieser Arbeit ebenfalls danken.

Weiterhin danke ich den Kollegen des IRTG, insbesondere Sergej Ilinzeer für die Materialbereitstellung und Miriam Bartkowiak für ihre Beratung zur Experimentdurchführung. In Kanada möchte ich mich bei Austin Bedrosian für seine Unterstützung bedanken. Am KIT/IBPT haben Prof. Dr. Anke-Susanne Müller und ihre Mitarbeiter Dr. Gudrun Niehues und Dr. Stefan Funkner sehr zum Erfolg der Terahertz-Messungen beigetragen.

Meinen Eltern, Petra und Uwe, sowie meinen Geschwistern, Ciara und Tobias, möchte ich für die bedingungslose Unterstützung in allen erdenklichen Lebenslagen danken. Außerdem möchte ich Ann-Kathrin für ihr außergewöhnliches Verständnis an den vielen Wochenenden im vergangenen Jahr und die willkommenen Momente der Ablenkung danken.

Suzhou, im April 2022

Lucas Bretz

Kurzfassung

Die Verwendung von faserverstärkten Kunststoffen (FVK) nimmt weltweit stetig zu. Die Kombination von diskontinuierlichem Sheet Molding Compound (DiCo-SMC) und kontinuierlichem SMC (Co-SMC) in einer neuen, hybriden Materialklasse (CoDiCo-SMC) verspricht günstige Herstellungskosten bei gleichzeitig hoher lokaler Steifigkeit und Festigkeit zu erreichen. Allerdings gefährden auftretende Fertigungsabweichungen die Funktionserfüllung der gefertigten Bauteile. Die resultierende Forderung nach fehlerfreien FVK-Bauteilen gilt neben den hohen Preisen für Rohmaterialien als ein weiterer Kostentreiber.

Mithilfe des Ansatzes einer bauteilindividuellen, funktionsorientierten In-line-Qualitätssicherung soll im Rahmen dieser Arbeit Abhilfe geschaffen werden. Für diese Art der Qualitätssicherung werden In-line-Messergebnisse in Funktionsmodelle integriert. Metamodelle der Funktionsmodelle beschleunigen die Funktionsbewertung und ermöglichen eine Funktionsaussage innerhalb der Zykluszeit in der Produktion.

In der vorliegenden Arbeit wurde die bauteilindividuelle, funktionsorientierte In-line-Qualitätssicherung exemplarisch für die neue Werkstoffklasse CoDiCo-SMC umgesetzt. Zur Quantifizierung von drei relevanten Fertigungsabweichungen (lokale Glasfaseranteile, Pose des Co-SMC Patches, Delamination) wurden drei verschiedene Messtechniken eingesetzt. Die Terahertz-Spektroskopie wurde zum ersten Mal zur In-line-Messung lokaler Glasfaseranteile in DiCo-SMC eingesetzt. Die Puls-Phasen-Thermografie wurde zur Quantifizierung der Delamination und eine Industriekamera zur Messung der Pose des Co-SMC Patches genutzt. Für jede Messtechnik wurde die Messunsicherheit gemäß des „Guide to the expression of uncertainty in measurement“ (GUM) quantifiziert. Die Messergebnisse wurden in einem parametrisierten Finite-Elemente-Modell (FE) weiterverarbeitet und zu einer Funktionssprädiktion aggregiert. Mit Hilfe der Messergebnisse und der modellierten Funktion konnten über diese Input-Output-Beziehungen Metamodelle trainiert werden. In dieser Arbeit wird die prädizierte Bauteilfunktion ebenfalls als Messergebnis verstanden. Daher wurden die Messunsicherheiten sowohl der FE-Modelle als auch der Metamodelle bestimmt.

Der vorgeschlagene Ansatz wurde anhand von zwei exemplarischen Prüfkörpern validiert. Die Ergebnisse zeigen, dass insbesondere die Messung der lokalen Glasfaseranteile und der Pose des Co-SMC Patches Rückschlüsse auf die bauteilspezifische Steifigkeit zulassen. Allerdings muss aufgrund der ermittelten Messunsicherheiten derzeit noch auf eine industrielle Anwendung verzichtet werden. Die Nutzung bauteilspezifischer Funktionsinformationen nach der Fertigung ermöglicht es, gängige Sicherheitsfaktoren in der Dimensionierung von FVK-Bauteilen zu reduzieren.

Contents

Contents	I
Abbreviations	IV
1 Introduction	1
1.1 Motivation	1
1.2 Problem statement	3
1.3 Research goal	4
1.4 Structure of this work	5
2 Fundamentals	7
2.1 Measurement and quality assurance	7
2.1.1 Measurement	7
2.1.2 Function-oriented measurement	7
2.1.3 Production-integrated metrology	8
2.1.4 Measurement uncertainty	9
2.1.5 Summary: Function-oriented quality assurance	12
2.2 Fiber-reinforced polymers (FRPs)	13
2.2.1 Definition of FRPs	13
2.2.2 Sheet molding compound (SMC)	14
2.2.3 Hybrid sheet molding compound	17
2.2.4 Measurement technologies for FRPs	20
2.2.5 Mechanics and failure behavior	21
2.2.6 Summary: Properties of hybrid sheet molding compound	27
2.3 Finite element (FE) method	27
2.3.1 Necessity and concept	28
2.3.2 Element types	29
2.3.3 Extended finite element analysis (XFEM)	30
2.3.4 Summary: FE model for hybrid SMC	30
3 State of the art	31
3.1 Requirements	31
3.2 Literature review of research focus areas	32
3.2.1 Measurement technologies for FRPs	32
3.2.2 Assessment of manufacturing deviations in FRPs	41
3.2.3 Applications of function-oriented measurements not related to FRPs	43

3.2.4	Surrogate modeling of FE simulations	44
3.3	Research deficit	47
4	Approach	50
5	Qualification and assessment of measurement technologies	52
5.1	Initial assessment and selection of measurement technologies for CoDiCo-SMC	52
5.2	Terahertz spectroscopy for the measurement of glass fiber fraction	55
5.2.1	Apparatus and methods	56
5.2.2	Regression model	59
5.2.3	THz measurement uncertainty	62
5.2.4	Added value of Terahertz measurements	64
5.2.5	Measures for improved measurement time	65
5.3	Industrial image processing (IIP) for the measurement of Co-SMC positioning	73
5.3.1	Apparatus and methods	73
5.3.2	IIP measurement uncertainty	75
5.4	Active thermography for the measurement of delaminations	76
5.4.1	Apparatus and methods	76
5.4.2	Measurement uncertainty of pulsed phase thermography	79
6	Methodology for in-line measurement propagation	82
6.1	Functional assessment of interacting manufacturing deviations	82
6.1.1	FE model structure	82
6.1.2	Key metrics for assessment	85
6.1.3	Uncertainty of the FE model	86
6.2	In-line qualification of the functional assessment	88
6.2.1	Selection of data-driven surrogate models	88
6.2.2	Model training	89
6.2.3	Model assessment	91
6.2.4	Uncertainty of the surrogate models	92
7	Application of function-oriented measurements for CoDiCo-SMC	95
7.1	Pre-study on tensile specimens	95
7.1.1	Experimental design	95
7.1.2	General observations	98
7.1.3	FE model	101
7.1.4	Assessment of the FE model	102
7.1.5	Surrogate model	107

7.1.6	Assessment of surrogate models	108
7.2	Multi-axial stress state in flexural specimens	111
7.2.1	Experimental design	111
7.2.2	Measurement procedure	117
7.2.3	General observations	118
7.2.4	FE Model	121
7.2.5	Assessment of the FE model	122
7.2.6	Surrogate model	127
7.2.7	Assessment of surrogate models	127
8	Discussion and outlook	130
8.1	Discussion	130
8.2	Outlook	135
9	Conclusion	137
	List of own publications	138
	References	141
	List of figures	162
	List of tables	165
	Appendix	167
A1	Further equations for DiCo-SMC homogenization	167
A2	THz measurements results of DiCo-SMC reference specimens	169
A3	Assessment of THz regression model (M2)	172
A4	Further uncertainty budgets for PPT of delaminations	173
A5	List of simulation parameters	174
A6	Critical energy release rate for DiCo-SMC	177
A7	Convergence study of finite element simulations	179
A8	Input quantities for surrogate model training	181
A9	Requirements according to VDA 5.1	182
A10	Required safety factors using function-oriented measurements	183

Abbreviations

Abbreviation	Description
2D	Two-dimensional
3D	Three-dimensional
ALLSE	Elastic strain energy in Abaqus
ANN	Artificial neural network
API	Application programming interface
a.u.	Arbitrary unit
BK	Benzeggagh-Kenane
C3D20	Twenty node solid element
C3D8	Eight node solid element
CA	Clamping area
CAE	Computer-aided engineering
CFRP	Carbon fiber-reinforced polymer
CMM	Coordinate measuring machine
CNC	Computerized numerical control
CO ₂	Carbon dioxide
CoDiCoFRP	Continuous-discontinuous fiber-reinforced polymer
CoDiCo-SMC	Continuous-discontinuous sheet molding compound
CoP	Cloud of points
Co-SMC	Continuous sheet molding compound
Cov	Covariance
CSE	Continuum shell elements
CSYS	Coordinate system
CT	Computed tomography
DCB	Double cantilever beam
DFG	Deutsche Forschungsgemeinschaft e.V.
DFT	Discrete Fourier transform
DiCo-SMC	Discontinuous sheet molding compound
ECT	Eddy current testing
FE	Finite element
FEM	Finite element analysis
FF	Fiber fracture
FFT	Fast fourier transform
FMF	Fiber mass fraction
FRP	Fiber-reinforced polymer

Abbreviation	Description
FVF	Fiber volume fraction
GFRP	Glass fiber-reinforced polymer
GUM	Guide to the expression of uncertainty in measurement
HPC	High performance computing
ICT	Fraunhofer Institute for Chemical Technology
IFF	Inter-fiber fracture
IIP	Industrial image processing
IRT	Infrared thermography
IRTG	International Research Training Group
LHS	Latin hypercube sampling
LT	Lock-in thermography
MCM	Monte Carlo method
MPE	Mean permissible error
MR	Measurement region
MSE	Mean squared error
MT	Mori-Tanaka
MU	Measurement uncertainty
NDT	Non-destructive testing
PDF	Probability density function
PoD	Probability of detection
POD	Proper orthogonal decomposition
PPT	Pulsed phase thermography
Prepreg	Pre-impregnated fibers
PT	Pulsed thermography
ReLU	Rectified linear unit
RMSE	Root mean squared error
ROI	Region of interest
RP	Reference point
RTW	Recording time window
SC8R	Eight node continuum shell element
SD	Standard deviation
SMC	Sheet molding compound
SNR	Signal-to-noise ratio
TGA	Thermogravimetric analysis
THz	Terahertz
UDL	Unidirectional lamina

Abbreviation	Description
UPPH	Unsaturated polyester polyurethane hybrid resin
US	Ultrasonic
UT	Ultrasonic testing
vol.-%	Volume fraction in %
w.r.t.	with respect to
wt.-%	Weight fraction in %
XFEM	Extended finite element method

Symbol	Description	Unit
a	Aspect ratio	-
A	Area	m ²
b	Systematic deviation (bias)	a.u.
b_{ξ}	Systematic deviation of FMF in prepreg production	wt.-%
c	Speed of light	m/s
C	Number of test sets	-
\mathbb{C}	Stiffness tensor (4 th order)	MPa
CV_{RMSE}	Coefficient of variation (Normalized RMSE)	-
d	Material thickness	mm
d_j^e	Nodal displacement (FEM)	mm
e	Essential specimen composition	-
E	Youngs' modulus	GPa
E_f	Flexural modulus	GPa
$E_{f,\text{rel}}$	Relative change in flexural modulus	-
\hat{E}_l	Estimate of the component stiffness for a set l of combined manufacturing deviations	GPa
\mathbf{f}	3D force	N
f	Frequency	Hz
F	Force	N
F_{max}	Force at failure	N
f_E	Stress exposure	-
$\hat{f}_{E,l}$	Estimate of the component stress exposure for a set l of combined manufacturing deviations	-
$f_{E,\text{Puck,FF}}$	Puck criterion for fiber fracture	-
$f_{E,\text{Puck,IFF,A}}$	Puck criterion for inter-fiber fracture, mode A	-
$f_{E,\text{Puck,IFF,B}}$	Puck criterion for inter-fiber fracture, mode B	-
$f_{E,\text{Puck,IFF,C}}$	Puck criterion for inter-fiber fracture, mode C	-
f_s	Sampling frequency	Hz
f_S	Stretch factor	-
f_{Safe}	Safety factor	-
G	Shear modulus	GPa
G_{IC}	Critical energy release rate in fracture mode I	N/mm
I_F	Fracture condition	-
k	Coverage factor	-
K	Bulk modulus	GPa
\mathbf{K}	Stiffness matrix	N/m

Symbol	Description	Unit
l	Length	m
L	Support span	m
m	Mass	kg
m_{avg}	Number of averaged THz time domain signals	-
$m_{\sigma F}$	Puck magnification factor	-
n	Refractive index	-
\mathbf{N}	Fiber orientation tensor (2 nd order)	-
\mathbb{N}	Fiber orientation tensor (4 th order)	-
$N_j^e(\mathbf{x})$	Shape function	-
p	Puck inclination parameter	-
P_1	Test set generated using LHS	a.u.
\mathbf{p}	Unit vector of fiber direction	m
P_2	Test set of virtual experiments	a.u.
P_3	Test set of physical experiments	a.u.
Q	Number of realized input variables for determination of model uncertainty	-
Q_{MS}	Capability ratio	-
r	Counting variable	-
r_{D}	Radius of a delamination	mm
R	Strength	MPa
R^-	Compression strength	MPa
R^+	Tensile strength	MPa
R	Realized numbers of ANNs for determination of model uncertainty	-
R_{adj}^2	Adjusted coefficient of determination	-
\mathbb{S}	Compliance tensor (4 th order)	1/Pa
S	Shear strength	MPa
s	Standard deviation	a.u.
sf	Scale factor	-
T	Training set for surrogate model training	a.u.
\mathbf{u}	3D displacement (FEM)	mm
U	Expanded measurement uncertainty	a.u.
U_{Sim}	Expanded measurement uncertainty for FE simulation	a.u.
U_{SM}	Expanded measurement uncertainty for surrogate model	a.u.

Symbol	Description	Unit
u	Standard uncertainty	a.u.
$u(x)$	Local displacement function (FEM)	mm
u_b	Standard uncertainty from systematic deviations	a.u.
u_c	Combined standard uncertainty	a.u.
u_{cal}	Standard uncertainty of calibration	a.u.
$u_{c,d}$	Combined thickness uncertainty	mm
$u_{c,Sim}$	Combined uncertainty of FE simulation	GPa
$u_{c,SM}$	Combined uncertainty of surrogate model	GPa
$u_{\hat{E}}$	Uncertainty in planar isotropic Young's modulus of THz measurement model	GPa
$u_{\bar{n}}$	Uncertainty of mean refractive index	-
u_p	Standard uncertainty of measurement procedure	a.u.
$u_{Sim,D}$	Uncertainty of FE simulation based on discretization	GPa
$u_{Sim,S}$	Uncertainty of FE simulation based on solution error	GPa
$u_{Sim,I}$	Uncertainty of FE simulation based on input uncertainties	GPa
$u_{Sim,M}$	Uncertainty of FE simulation based on modeling error	GPa
$u_{SM,I}$	Uncertainty of surrogate model based on input uncertainties	GPa
$u_{SM,T}$	Uncertainty of FE simulation based on training data	GPa
u_w	Standard uncertainty from variations in material and production	a.u.
u_{ξ}	Uncertainty in FMF of THz measurement model	wt.-%
$u_{\xi,prod}$	Uncertainty in FMF originating from production process	wt.-%
u_z	Displacement in z-direction	mm
ν_{eff}	Effective degrees of freedom	-
w	Width	m
W	Strain energy	Nm
x_{cal}	Calibrated value of a measurand	a.u.
x_D	x-coordinate of a delamination	mm
x_{spec}	x-axis of specimen	mm
x_T	x-coordinate of Co-SMC patch	mm
x_w	x-axis of world coordinate system	mm
Y	Measurand	a.u.

Symbol	Description	Unit
\hat{y}	Estimate of the measurand	a.u.
\hat{y}_l	Estimate of the component function for a set l of combined manufacturing deviations	a.u.
\hat{y}_{ANN}	Predicted function by ANN	a.u.
y_{CMM}	Measurand for a feature using a CMM	a.u.
y_{CT}	Measurand for a feature using CT	a.u.
y_D	y-coordinate of a delamination	mm
y_{IIP}	Measurand for a feature using IIP	a.u.
\hat{y}_{Kr}	Predicted function by Kriging model	a.u.
y_{PPT}	Measurand for a feature using PPT	a.u.
\hat{y}_{Sim}	Predicted function by simulation	a.u.
\hat{y}_{SM}	Predicted function by surrogate model	a.u.
y_{spec}	y-axis of specimen	mm
y_T	y-coordinate of Co-SMC patch	mm
y_w	y-axis of world coordinate system	mm
α	Absorption coefficient	-
β_i	Regression parameters	a.u.
γ_{ij}	Shear strain component	-
γ_T	Rotation of Co-SMC patch	°
δ_{ij}	Kronecker delta	-
Δ	Difference	a.u.
ε_i	Strain component	-
ζ	Phase shift of electromagnetic wave	°
ν	Poisson's ratio	-
ρ	Density	kg/m ³
σ_i	Stress component	MPa
τ_{ij}	Shear stress component	MPa
ϕ	Fiber volume fraction	vol.-%
ϕ_{Void}	Void fraction	vol.-%
ξ	Fiber mass fraction	wt.-%
ξ_{nom}	Nominal fiber mass fraction	wt.-%
$\psi(\mathbf{p})$	Fiber orientation distribution	-
ϵ	Strain tensor (2 nd order)	-
σ	Stress tensor (2 nd order)	MPa
ω	Set of manufacturing deviations	a.u.

Symbol	Description	Unit
$(\cdot)^e$	Element-related (FEM)	-
$(\hat{\cdot})$	Estimate of a quantity	-
$(\bar{\cdot})$	Mean	-
$(\tilde{\cdot})$	Median	-
$(\cdot)_{\parallel}$	Parallel to fiber direction	-
$(\cdot)_{\perp}$	Perpendicular to fiber direction	-
$(\cdot)_{Co}$	Reference to Co-SMC	-
$(\cdot)_{DiCo}$	Reference to DiCo-SMC	-
$(\cdot)_F$	Reference to fiber	-
$(\cdot)_{\xi}$	Reference to fiber mass fraction	-
$(\cdot)_M$	Reference to matrix	-
$(\cdot)_{TGA}$	TGA-measured	-
$(\cdot)_{UPPH}$	Reference to UPPH	-
$(\cdot)^*$	Void fraction included in material property	-
$\langle \cdot \rangle$	Volume average	-

1 Introduction

This work deals with in-line metrology for fiber-reinforced polymers. A 100% component assessment based on in-line measurements combined with a functional model is proposed for component-specific quality assurance, considering the individually realized component function.

1.1 Motivation

Lightweight design increases resource efficiency. Material and energy are saved both during manufacturing and the life cycle of a product. The same or improved product performance is achieved with fewer resources. (May 2020) The advantages of lightweight design are particularly evident for moving masses. Examples from the transportation sector, reinforced by the existing legal framework conditions (European Commission 2019), are widely discussed. For example, a weight reduction of 10% in an internal combustion engine vehicle reduces fuel consumption by up to 8% (Chu & Majumdar 2012). The trend towards battery-electric drives also requires the exploitation of existing lightweight design potential to compensate for the weight disadvantages of battery-electric vehicles (Schuh et al. 2014). Significant advantages can also be achieved in machinery and plant engineering, especially for highly dynamic applications (Bauernhansel 2016). Lightweight design is therefore still of utmost importance. However, high material and development costs are existing disadvantages (May 2020).

Lightweight material design, as one possibility, involves replacing conventional with innovative materials, which simultaneously provide a lower density and higher mechanical properties. Fiber-reinforced polymers (FRP) have a high lightweight potential due to their low weight, excellent mechanical properties and a high freedom in design. Using carbon fiber-reinforced polymers (CFRP) in an application-specific design can save up to 70% of the required component weight compared to steel or 30% compared to aluminum, while fulfilling the same function. In recent years, however, potentials for weight reduction have been exploited mainly for prestige objects and non-structural parts. (Cherif 2016) Thus, the consequent next step to further reduce vehicle weight is to substitute structural steel components for cost-efficient lightweight FRP.

Continuous CFRP are characterized by their high stiffness and strength in fiber direction, which make them very attractive for structural components. The excellent material properties are opposed by higher material and manufacturing costs. Therefore, full-scale deployment is often economically not viable (May 2020). Glass fiber reinforced polymers (GFRP) achieve a significantly higher market penetration, with a market share of over 90% in the area of FRP. The sheet molding compound (SMC) process is the most widespread manufacturing

process with a production volume of 205kt in 2019 in Europe alone. (Witten & Mathes 2019) Discontinuous fiber-reinforced SMC stands out with significant lower material costs. Its advantages include a high freedom in design due to its high formability during the compression moulding step and low manufacturing costs. In contrast, the chopped, discontinuous glass fibers used in conventional SMC composites provide lower stiffness and strength. As result, SMC is used in non-structural components, such as lightweight body panels for vehicles or interior parts of trains (European Alliance for SMC/BMC 2016; Cherif 2016).

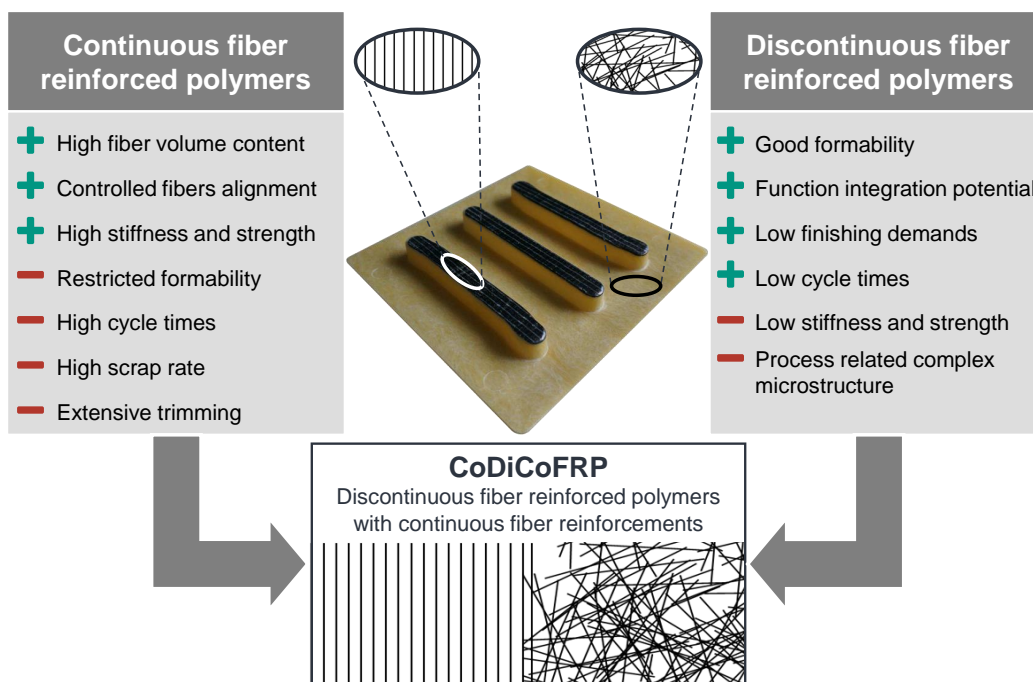


Figure 1.1: Advantages and disadvantages of continuous and discontinuous sheet molding compound; own illustration according to Böhlke & Kärger et al. (2016)

The use of fiber-reinforced components must be increased globally to fully exploit the economical, ecological and technological advantages of lightweight construction. Only a cost-efficient, large-scale production with a high degree of automation can achieve this goal. Hybrid composites could theoretically combine the benefits of different composite materials. The International Research Training Group (IRTG, DFG GRK 2078) "Integrated engineering of continuous-discontinuous long fiber reinforced polymer structures (CoDiCoFRP)¹" follows an innovative approach to accomplish exactly this goal (Böhlke & Henning et al. 2019). Continuous and discontinuous SMCs are united in a co-molding process to tailor a material class with the freedom in design of discontinuous SMC and the superior mechanical properties of continuous CFRP. Ultimately, complex geometries are produced from discontinuous SMC,

¹Karlsruhe Institute of Technology (KIT). *International Research Training Group CoDiCoFRP*. <https://www.grk2078.kit.edu> (accessed on Jan. 5, 2022).

while load paths are locally reinforced by unidirectional carbon fiber patches. An overview of this new material class is given in Figure 1.1.

1.2 Problem statement

FRPs originated in applications with high performance requirements, such as the aerospace industry. Here, harsh rejection criteria, such as a limit of 2% void fraction, exist. This traditional demand for a “defect-free” component is considered as a cost driver and needs to be reconsidered, especially for less performance-driven components. In today’s mass applications, low manufacturing costs are of decisive importance to ensure further dissemination of the technology. (Talreja 2015) The comparatively high costs of FRP components, often caused by relatively high material costs and manufacturing processes that are not yet fully developed for larger series, are seen as one of the main obstacles to the widespread industrial use of FRP (May 2020). Current costs of about 80 Euro/kg for CFRP components are far above the acceptance threshold of less than 20 Euro/kg for an economic large-scale production in automotive engineering (Reden & Schüppel 2019).

Manufacturing deviations are inevitable for composite structures due to process variations and varying quality of input materials (Donaldson & Miracle 2001; Talreja 2015). They can be reduced, but not completely avoided. It follows that even “defect-free” components contain defects below the metrological detection limit. The significance of those defects is directly linked to the local performance requirements of a component. A component-specific assessment of the effects of defects could reduce manufacturing costs, because individual components would no longer be rejected based on generalized criteria. An individual assessment requires a characterization of existing defects by means of in-line non-destructive testing (NDT) and a subsequent measurement-based mechanical evaluation of the influence on the functionality of the component. This functional assessment needs to adhere to the cycle time. Hence, computationally intensive models (finite element models) that describe the component behavior in detail must be replaced by models that are faster to evaluate (surrogate models). However, these data-driven surrogate models are to be trained on the computationally intensive models. Therefore, both the suitability of computational expensive and surrogate models needs to be guaranteed.

Overall, defects could be regarded as an inherent characteristics of the component state. This engineering approach tolerates defects as long as they do not jeopardize the safe use of a component. In return, manufacturing costs could be reduced. Figure 1.2 depicts a vision of the overall methodology for a cost-effective FRP design approach, allowing a balanced relationship between manufacturing costs and level of performance. Process models and component simulations are already created during the design phase, before manufacturing. This

knowledge shall be used to characterize the relevant material properties and manufacturing deviations. Making use of the existing models, the component performance can be evaluated based on characterization results. The more precise knowledge about component-specific properties allows to prevent overperformance and thus, to reduce costs. By knowing the individual component performance, a design closer to the actual functional requirements can be chosen. The characterization and performance evaluation need to adhere to the cycle time to ensure a 100% component assessment.

This work focuses on the characterization by means of in-line measurements and a subsequent performance evaluation making use of in-line functional models.

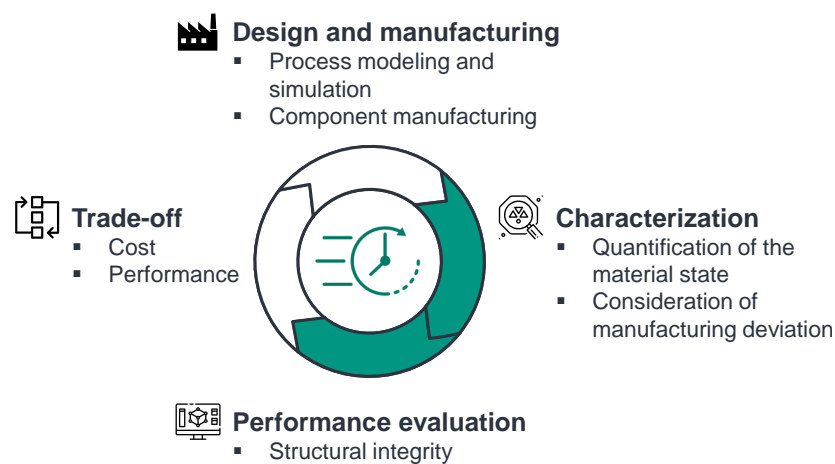


Figure 1.2: Cost-efficient design and manufacturing process for fiber-reinforced polymers; own illustration based on Talreja (2015)

1.3 Research goal

The problem statement is addressed by the following overall research goal:

Function-oriented quality assurance of hybrid sheet molding compound based on in-line measurements and in-line surrogate models of finite element simulations

Four research questions are derived from the research goal:

1. **In-line measurements:** Is it possible to quantify common manufacturing deviations of hybrid sheet molding compound within the cycle time?
2. **Parametrized simulations:** Do simulations with imported measurement results of manufacturing deviations represent the material behavior of hybrid sheet molding compound accurately?

3. **In-line surrogate model:** Can virtual training data, generated from simulations, be used to achieve "real-time capability" of the functional assessment?
4. **Measurement uncertainty:** Do the measurement uncertainties of the in-line measurement technologies, the simulation, and the surrogate model allow for an industrial application?

Additionally, the research aims for the underlying idea that any produced composite material can be characterized based on its manufactured component state. In-line measurement technologies allow for generating component-specific, function-relevant data. This measurement data serves as input for creating digital representations of the real component (digital twin) via parametrized finite element models. A surrogate model is trained using an extensive collection and combination of potential manufacturing deviations (database of component states) as well as the input-output relation from the computationally more expensive model for each of the components states in the data base. Afterwards, the trained surrogate model is able to perform quality assurance tasks of functional requirements within the cycle time, because the mapping between input (measured component state) and output (function) is stored in a model easier to evaluate. This property refers to the term "real-time capability" in the third research question. Thereby, the human effort focuses on identifying suitable measurement technologies, creating appropriate functional models and the respective surrogate models. Furthermore, the approach shall not be bound to the exemplary material system (CoDiCo-SMC) used in this work, but should make a first step towards a function-oriented measurements for all kind of composites and hybrid composites, such as CFRP laminae and intrinsic CFRP-metal hybrids.

1.4 Structure of this work

After the problem statement and the research goal have been motivated in Chapter 1, a general overview on the further course of this thesis shall be given (cf. Figure 1.3). In Chapter 2, an introduction to required fundamentals follows, which enable the understanding of the contextual relationships and their integration into the subsequent research approach. Then, in Chapter 3, the existing research approaches are presented based on formulated requirements from the state of the art in research and technology. Taking the existing approaches into account, Chapter 3 closes with the derivation of the research deficit. Chapter 4 presents the solution approach and the general framework of the research approach to address the research deficit. In Chapter 5, suitable measurement technologies are selected, qualified, and evaluated for the hybrid SMC at hand. This measurement data forms the general prerequisite for the methodological procedure of data propagation for enabling a function-oriented quality assurance presented in Chapter 6. In Chapter 7, the solution approach will be tested on

two different specimen geometries. Chapter 8 contains a discussion, followed by an outlook, before the summary in Chapter 9 concludes the thesis.

1 Introduction	
1.1 Motivation	1.2 Problem statement
1.3 Research goal	1.4 Structure of this work
2 Fundamentals	
2.1 Measurement and quality assurance	2.2 Fiber-reinforced polymers
2.3 Finite element method (FEM)	
3 State of the Art	
3.1 Requirements	3.2 Literature review of research focus areas
3.3 Research deficit	
4 Approach	
5 Qualification and assessment of measurement technologies	
5.1 Initial assessment and selection	5.2 Terahertz spectroscopy
5.3 Industrial image processing	5.4 Active thermography
6 Methodology for in-line measurement propagation	
6.1 Functional assessment of interacting manufacturing deviations	6.2 In-line qualification of the functional assessment
7 Application of function-oriented measurements for CoDiCo-SMC	
7.1 Pre-study on tensile specimens	7.2 Multi-axial stress state
8 Discussion and outlook	
9 Conclusion	

Figure 1.3: Structure of this thesis

2 Fundamentals

This chapter focuses on the fundamentals for a function-oriented quality assurance of fiber-reinforced polymers. A common understanding of measurement and quality assurance is established, the characteristics of sheet molding compounds (SMCs) as a class of fiber-reinforced polymers are described and the finite element analysis as a common tool in the design and dimensioning process is introduced. Each section closes with the most important takeaways for the remainder of this work.

2.1 Measurement and quality assurance

The central terms of measurement, measurement uncertainty and different degrees of integration for production-integrated metrology are defined.

2.1.1 Measurement

The term *measurement* is defined as “*the process of experimentally obtaining one or more quantity values that can reasonably be attributed to a [...]*” measurand (JCGM200 2012). A measurand is a property of an object expressed as a number and a reference unit (JCGM100 2008). Generally, the result of a measurement is only an estimate of the measurand. Thus, it needs to be accompanied by a statement of the uncertainty of that estimate. (JCGM100 2008)

In this work, the term measurand is understood in a broader sense. In particular, the predicted product function of a fiber-reinforced component is considered similar to an indirectly determined measurand. This allows the quantification of the measurement uncertainty for the component-related function prediction. (JCGM100 2008; Häfner 2017)

2.1.2 Function-oriented measurement

A function-oriented measurement of the quality relates measured product characteristics to its individual function. Thus, a comparison to the required function is enabled. A mathematical-physical model of the function, fed with measurement results, must be created to establish a function-oriented evaluation.

Functional models and simulations are often already created during the design process. In this case, these models only need to be adapted for the measurement process and the evaluation of the measured quantities. Instead of standardized parameters, the functional model is used for an individual analysis of multiple measurement results and serves as “virtual functional gauge”. A high model quality in combination with measurements under low measurement uncertainty is a decisive factor for the reduction of functional uncertainty. Functional capability

becomes quantitatively predictable, whilst insufficiently described component characteristics, tolerances and measurement evaluations can be omitted. This implies a paradigm shift to the language of function rather than the language of tolerance and implies a rethinking of the entire process chain. Designers and metrologists, as a cooperating team, have to understand the functional relationships in order to derive function-oriented measurands from the mathematical-physical model. (Weckenmann & Hartmann 2013; Hartmann & Weckenmann 2014; Weckenmann & Hartmann 2015)

Advantages arise along the entire process chain (Weckenmann & Hartmann 2013):

- 1) Causal relationships are better understood and an approach for design optimization exists.
- 2) Scrap rates are reduced because excessively strict component requirements are avoided.
- 3) Multiple measurement results are combined in the functional model (data fusion).

Therefore, quality assurance has the significant task to generate information from measurements that permits a functional assessment of the specified requirements. If selected properties and characteristics of a unique component are processed as data by means of models, one can refer to a digital twin (Stark & Damerau 2018).

2.1.3 Production-integrated metrology

In-line metrology, as a part of the production system, provides a continuous stream of quality information on the component and the production system. Off-shopfloor measurements are generally conducted in the measurement laboratory. The use of production-integrated metrology enables an early detection of product quality and possible manufacturing deviations close to the value-adding process. Production-integrated metrology (on-shopfloor) can be divided into different integration levels (cf. Figure 2.1). In-line measurements, including the respective information flow, are performed within the cycle time of the manufacturing process, while off-line measurements next to the production line are used for random sample measurements. In-line measurements are further distinguished between a direct integration into the production machine (on-machine) or integrated into the production line, but at separate test stations (off-machine). In the production machine, measurements can be performed during (in-process), before or after the actual processing step (off-process: pre- or post-process). The integration of in-line measurement technology is associated with additional expenditures compared to end-of-line inspections. Additionally, high demands exist on the resilience and the measurement uncertainty (cf. Section 2.1.4) of the in-line measurement system, even in harsh production environments. However, its use provides a 100% (component-specific) inspection

and avoids value creation on defective products. Thus, in-line inspection for quality-critical features is often more economical than the cumulative costs of subsequent value-added processes on defective components. (Lanza et al. 2019; Gao et al. 2019) In-line metrology offers particularly high potential for increased value creation when quality information is directly linked to the product function (Wagner et al. 2020).

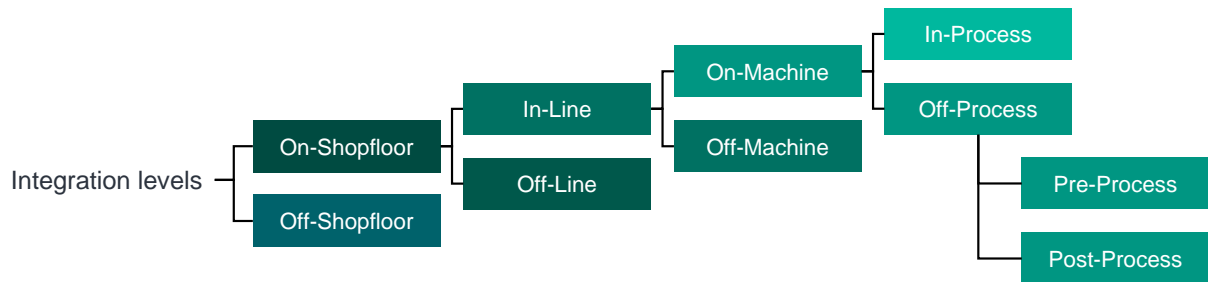


Figure 2.1: Integration levels of production-integrated metrology; own illustration according to Lanza et al. (2019) and Gao et al. (2019)

2.1.4 Measurement uncertainty

The term *measurement uncertainty* is defined as a non-negative parameter associated with the measurand. It characterizes the dispersion of quantity values that can be assigned to the measurand based on known information about the measurement process. (JCGM200 2012)

2.1.4.1 Guide to the expression of uncertainty in measurement (GUM)

A standardized procedure for determining measurement uncertainties is defined in the “International Guide to the Expression of Uncertainty in Measurement (GUM)”. Its goal is to provide a method which is applicable to all kinds of measurements, including all possible input data used in measurements.

It is based on the concept of *the expanded uncertainty* U , which describes an interval $\pm U$ around the estimate of the measurand \hat{y} . This interval contains, based on the available information, the set of quantity values of the measurand with a defined probability. A mathematical function describes the relationship between the estimate of the measurand \hat{y} and the N input estimates x_1, x_2, \dots, x_N . Equation 2.1 is called *measurement function*. (JCGM100 2008)

$$\hat{y} = f(x_1, x_2, \dots, x_N) \quad 2.1$$

Estimated values for the standard uncertainties $u(x_i)$ of all input quantities x_i must be determined. Uncertainty components are either calculated from a series of repeated measurements

leading to a probability distribution (type A), or based on an assumed probability distribution from a subjective degree of belief (type B). In the latter, the information comes from other sources, such as a calibration certificate or an expert estimate. In each case, determining the standard uncertainty of an input variable x_i is based on the assumption of an adequate probability density function. The *combined standard uncertainty* $u_c(\hat{y})$ is calculated according to Equation 2.2, based on the estimated standard uncertainty of each input estimate $u(x_i)$. The covariances $u(x_i, x_j)$ need to be taken into account if correlations between the input estimates prevail. (JCGM100 2008)

$$u_c^2(\hat{y}) = \sum_{i=1}^N \sum_{j=1}^N \frac{\partial f}{\partial x_i} \frac{\partial f}{\partial x_j} u(x_i, x_j) = \sum_{i=1}^N \left(\frac{\partial f}{\partial x_i} \right)^2 u^2(x_i) + 2 \sum_{i=1}^{N-1} \sum_{j=i+1}^N \frac{\partial f}{\partial x_i} \frac{\partial f}{\partial x_j} u(x_i, x_j) \quad 2.2$$

The expanded uncertainty U is calculated by multiplying the combined standard uncertainty $u_c(\hat{y})$ by a *coverage factor* k , as given in Equation 2.3 (JCGM100 2008).

$$U = k \cdot u_c(\hat{y}) \quad 2.3$$

Often, repeated estimates of the measurand \hat{y} are assumed to be normally distributed around the measurand Y . The coverage factor can be calculated based on the effective degrees of freedom ν_{eff} of the uncertainty contributions. Commonly, a confidence level of 95.45% is chosen, leading to a coverage factor $k \approx 2$ for a sufficient number of measurements. (JCGM100 2008)

2.1.4.2 Simulative approach (GUM supplement 1)

Additionally, a procedure for the simulative determination of the measurement uncertainty (MU) using the Monte Carlo method (MCM) is defined by JCGM101 (2008). The measurement uncertainty is calculated based on repeated random simulation experiments. For each experiment, random values are drawn according to the statistical distributions that can be assumed for the input variables x_i . The estimate of the measurand \hat{y} is calculated based on the random input values using a mathematical model of the measurement. Evaluating the model for M repeated random experiments yields to a probability density. The realized model values can be written as

$$\hat{y}_r = f(\mathbf{x}_r), r = \{1, \dots, M\}. \quad 2.4$$

The r^{th} draw \mathbf{x}_r contains the realizations $x_{1,r}, \dots, x_{N,r}$ for the N input variables. The average \bar{y} and the sample standard deviation $s_{\hat{y}}$ are reasonable estimates for Y and $u(Y)$, as given in

Equation 2.5 and 2.6:

$$Y \approx \bar{y} = \frac{1}{M} \sum_{r=1}^M \hat{y}_r \quad 2.5$$

$$u^2(Y) \approx s_{\hat{y}}^2 = \frac{1}{M-1} \sum_{r=1}^M (\hat{y}_r - \bar{y})^2 \quad 2.6$$

An associated probability density function $p(\hat{y})$ can be calculated based on the experimental values and an assumption for the underlying distribution. The determination of measurement uncertainty using the MCM comes with two main advantages (JCGM101 2008):

- 1) No calculation of partial derivatives for complicated or non-linear models is needed, leading to a reduced analysis effort.
- 2) The estimate of the measurand is improved for non-linear models.

2.1.4.3 Other standards

Deutsches Institut für Normung e.V. (2011b) defines an experimental method for the tactile coordinate metrology. At least 20 repeated measurements are performed on a calibrated standard in the same way as on the actual component. A calibrated standard must be similar to the component in size, shape and material. Measurement procedures and environmental conditions should also be comparable. Four uncertainty contributions are considered to determine the expanded uncertainty U of each measured quantity:

- 1) the standard uncertainty of the calibration of the standard u_{cal} ,
- 2) the standard uncertainty of the measurement procedure u_{p} ,
- 3) the standard uncertainty from variations in material and production u_{w} ,
- 4) and the standard uncertainty from systematic deviations of the measurement procedure u_{b} .

Alternatively, u_{b} can be considered as a systematic deviation from the calibration value, named b , leading to (Schwenke & Franke 2007):

$$U = k \sqrt{u_{\text{cal}}^2 + u_{\text{p}}^2 + u_{\text{w}}^2 + b^2} \quad 2.7$$

The procedure described above can equally be applied to all types of optical and tactile sensors (Wendt et al. 2007).

2.1.4.4 Uncertainty evaluation in continuous modeling

Continuous models, such as finite element models, use continuous differential or integral equations to describe reality. Usually, discrete representations of those equations are derived

for numerical solution. An uncertainty estimation of those models is a key requirement for application in metrological problems. (Esward et al. 2003)

Four main sources of uncertainty exist (Esward et al. 2003), whereby modeling and solution errors are comparatively small so that they can be neglected in most cases (Lord & Wright 2003; Häfner 2017):

- 1) Modeling error $u_{\text{Sim},M}$: The chosen continuous equation does not adequately describe reality.
- 2) Discretization error $u_{\text{Sim},D}$: The chosen discrete time step or mesh leads to errors.
- 3) Input quantity error $u_{\text{Sim},I}$: Input quantities are inaccurate.
- 4) Solution error $u_{\text{Sim},S}$: Solving differential equations using linear algebra leads to errors.

The combined modeling uncertainty $u_{c,\text{Sim}}$ is calculated according to GUM:

$$u_{c,\text{Sim}} = \sqrt{u_{\text{Sim},M}^2 + u_{\text{Sim},D}^2 + u_{\text{Sim},I}^2 + u_{\text{Sim},S}^2} \quad 2.8$$

Sampling methods, such as the MCM, are particularly suited for the uncertainty determination of input quantities. The main advantage is that statistical distributions do not need to be explicitly propagated through the model equations for sampling methods. However, repeated model runs are time-consuming (Esward et al. 2003). Latin Hypercube Sampling (LHS) reduces the number of model runs while providing good estimates of output quantity means and standard deviation (Lord & Wright 2003). The proposed number of runs should be around ten times as large as the number of input quantities (Loeppky et al. 2009).

2.1.5 Summary: Function-oriented quality assurance

Based on the concepts described, the following conclusion can be drawn:

1. The goal of a modern quality assurance is not to evaluate measured product characteristics with the help of tolerances, but to evaluate the product function using a mathematical-physical model in the sense of a digital twin. A function-oriented quality assurance is enabled.
2. Higher integration levels of production-integrated metrology enable component-specific measurements.
3. Each measurement needs to be accompanied by a measurement uncertainty in order to quantify the quality of the measurement. A quantified product function can also be understood as a measurement.

4. Measurement uncertainties are determined according to GUM (JCGM100 2008), whereby simulative approaches are equivalent. The measurement uncertainty of optical and tactile sensors can be evaluated according to Deutsches Institut für Normung e.V. (2011b).
5. Numerical solutions of continuous models, such as the finite element analysis (FEM), are also subject to uncertainties. The discretization error and the input quantity error are of particular importance.

2.2 Fiber-reinforced polymers (FRPs)

Sheet molding compounds (SMCs) as a type of fiber-reinforced polymers (FRPs) are introduced. An overview of existing measurement principles for FRPs is given. The described material models for FRPs relate measurement results to material behavior.

2.2.1 Definition of FRPs

Composites are a macroscopic combination of at least two distinct materials. The materials have a recognizable interface and substantially differ in their mechanical properties. A continuous matrix constituent (matrix) binds together and provides form to the stronger and stiffer reinforcement constituent. The combination of the constituents leads to a balanced set of structural properties, superior to its constituent materials alone. Thermosets or thermoplastics usually serve as matrix material and transfer the load to the reinforcement material. Glass and carbon fibers are widely used reinforcements and primarily carry the load, providing strength and stiffness to the component on the macroscopic level. At least 10% volume fraction of reinforcement constituent are required to usefully increase structural properties. (Donaldson & Miracle 2001)

Common forms of the reinforcement constituents are straight continuous fibers, discontinuous fibers, particles or woven fabrics (Donaldson & Miracle 2001). Discontinuous fibers usually have a fiber length of 25 to 50 mm (Schürmann 2007). Continuous fiber composites consist of fibers with a fiber length similar to the overall dimension of the composite part (Donaldson & Miracle 2001).

Generally, higher reinforcement volume fractions provide higher component strength and stiffness, as long as a sufficient impregnation of all reinforcements is given. A fiber alignment along the loading direction increases strength and stiffness in this particular direction. Composites behave quasihomogeneous on the macroscopic level. (Cherif 2016; Dominghaus 2012)

Advantages of composites are an improved corrosion resistance, long fatigue lives and tailorable properties, besides their high stiffness, high strength, and low density. The current major challenges are cost saving measures and proving the presumed advantages of the materials in terms of an improved overall life cycle sustainability. This requires a complex consideration of the economic, ecological and social effects of production along the entire value chain. (Mathes & Witten 2013)

2.2.2 Sheet molding compound (SMC)

Sheet molding compound is a processable, flowable, sheet-like molding material consisting of cross-linkable resins, fibers, and additives. It flows under pressure and fills the mold cavity. Curing is initiated by an increased mold temperature. SMC was developed in the early 1960s and is one of the most processed FRPs. (Mathes & Witten 2013) SMC accounts for 18% (205 kt) of the European production volume of glass-fibre-reinforced polymers (Witten & Mathes 2019).

SMC technology allows designers excessive freedom in design. Low processing pressure, low tooling costs, low cycle times, good surface finish and paintability, low specific weight, good stiffness and high temperature resistance were decisive criteria for the use of this new group of materials in the electrical and automotive industries, e.g. for housings and body panels. Further applications can be found in civil engineering and mass transportation.

The large number of individual components in the matrix formulation (resin, hardener, fillers, additives) complicates the reproducible fabrication with respect to a constant compound quality. This is further complicated by the common batch production. Even minor deviations and production fluctuations in the semi-finished product (agglomeration of filler material or insufficient fiber impregnation) can lead to a scrap rate of up to 7% in the subsequent production steps. (Mathes & Witten 2013; Neitzel et al. 2014)

2.2.2.1 Production process of discontinuous sheet molding compound

SMC prepregs (abbreviation for *pre-impregnated fibers*) are required for the compression molding process, in which the heated cavity of the mold determines the final shape of the component. This general principle separates the fiber impregnation process from the shaping of the component for SMCs. (Cherif 2016)

Within the fiber impregnation process, the mixture of resin, hardener, and filler is continuously knife-coated onto an upper and lower carrier foil with a defined thickness in a special prepreg plant. Glass or carbon fiber rovings are cut by a cutting unit to the desired length of 25 to 50 mm for the production of discontinuous SMC (DiCo-SMC). After cutting, the roving must break up loosely into individual filaments so that it can be finely distributed. The cut

fibers fall without a preferential orientation onto the resin film (planar isotropy). Sandwiched between a second resin film, the components are compacted in a calendar zone, preventing air inclusions and ensuring a complete resin impregnation of the fibers. Figure 2.2 illustrates the principle. The fiber content is adjusted via the web speed and is usually around 30 weight percent (wt.-%). After calendaring, the SMC is matured for several days up to weeks at 30 °C to increase its viscosity. The shelf life of the semi-finished SMC is limited to a few months. (Schürmann 2007)

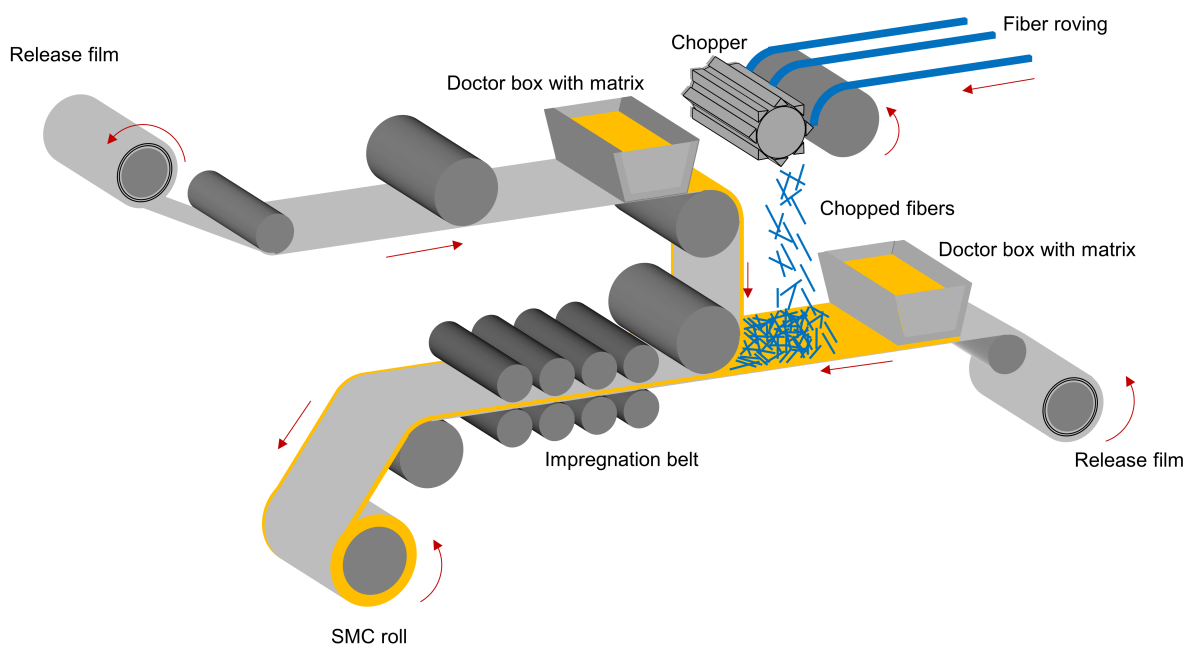


Figure 2.2: Principle of a SMC prepreg plant (Böhlke & Henning et al. 2019)

Afterwards, SMC prepregs are further processed in a compression molding process, using pressures of 25 to 250 bar and temperatures between 140 and 160 °C. Mostly rectangular SMC cuttings are stacked and inserted into the mold (cf. Figure 2.3). Pressure and temperature reduce the viscosity of the matrix system during compression molding. The closing movement of the mold induces a material flow and the mold cavities are filled. A local orientation of the discontinuous fibers in flow direction emerges. A chemical cross-linking of the matrix takes place because of the increased temperature. The pressure is held during the curing process. An automated process achieves cycle times around one to three minutes, dependent on the size of the component. Post processing, such as deburring or drilling, is necessary after molding. (Cherif 2016; Böhlke & Henning et al. 2019)

The moulding cycle time is considered as time constraint for both in-line measurements and real-time applicability of functional evaluations within this work.

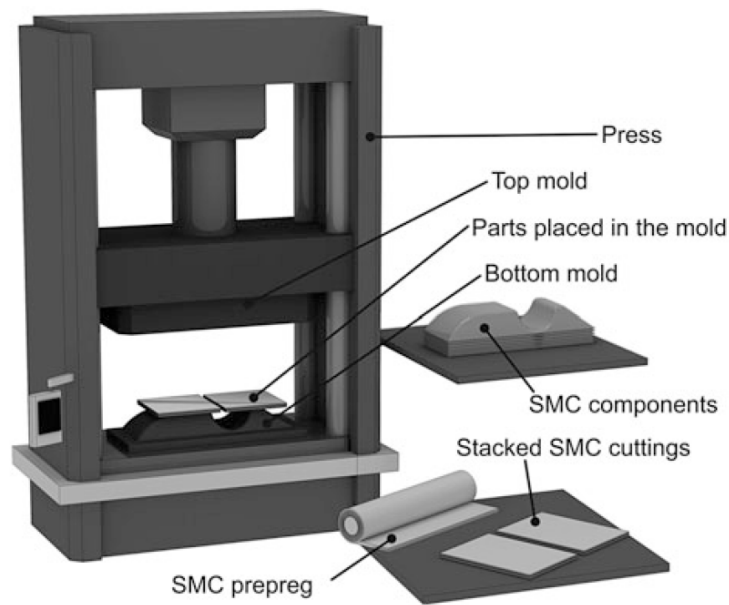


Figure 2.3: Compression molding of SMC components (Cherif 2016)

2.2.2.2 Production process of continuous sheet molding compound

Continuous, unidirectional SMC (Co-SMC) prepregs consist of continuous glass or carbon reinforcement fibers, aligned in the direction of motion of the carrier foil during prepreg production. The melt resin impregnation process is the most common manufacturing process (cf. Figure 2.4).

Initially, the matrix resin is applied to a carrier film in a dedicated process at elevated temperature and stored temporarily. Subsequently, the fibers are impregnated in a separate plant. The resin film is tempered by heated calender rolls and the resin viscosity is thereby adjusted to a range favorable for impregnation. At the same time, the roll pressure supports the impregnation of the fibers, and the defined roll gap allows for a precise adjustment of the fiber volume fraction, commonly up to 60 vol.-%. After passing through a cooling section, edge trimming and winding take place. In contrast to discontinuous SMC, maturing takes place directly on the plant within a few minutes.

The process results in very good reproducibility of the basis weight. Co-SMC meets extreme mechanical requirements due to the parallel fiber orientation and the higher fiber volume fraction compared to discontinuous SMC. However, flowability is drastically reduced. Thus, the whole mold needs to be covered when using continuous prepregs. Carbon fibers, due to their inherent high strength and stiffness, are of special interest for this material class, but come at a higher cost. (Cherif 2016; Neitzel et al. 2014; Böhlke & Henning et al. 2019)

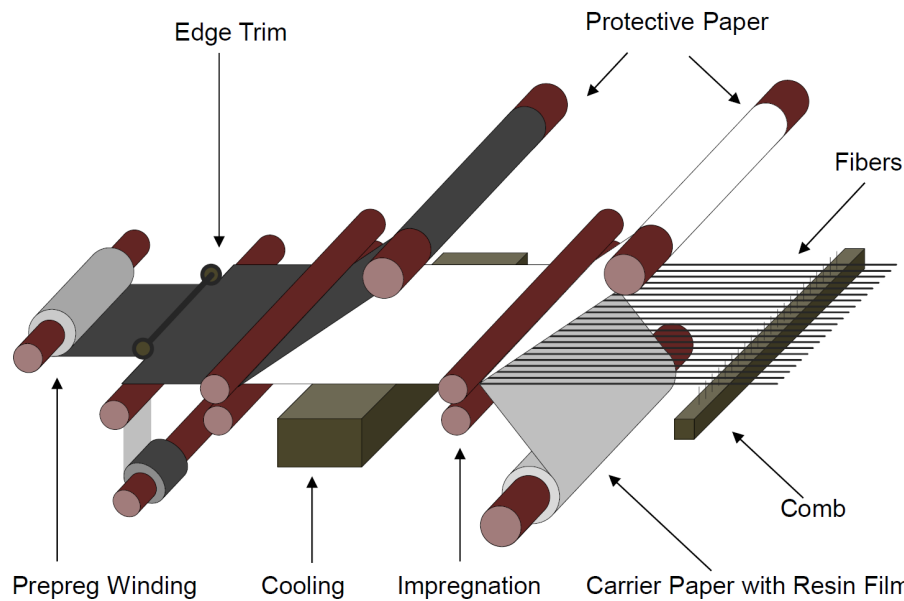


Figure 2.4: Principle of a unidirectional prepreg plant (Schäferling 2019)

2.2.3 Hybrid sheet molding compound

The innovative research approach of a hybrid SMC within the DFG GRK2078, hereinafter also referred to as CoDiCo-SMC, requires some specific characteristics, which are presented in the following subsections. The hybrid manufacturing process, the material formulation required for it and any process-related manufacturing deviations that may occur are presented in more detail.

2.2.3.1 Production process of CoDiCo-SMC

The manufacturing of locally continuous-fiber reinforced components based on discontinuous SMC enables the economic production of stiff structures with a reasonable freedom in design (Bücheler 2018). The flowability of discontinuous SMC allows the molding of complex geometries and the integration of inserts, while the positioning and alignment of the continuous SMC provides the required structural integrity of the component (Böhlke & Henning et al. 2019). A cured CoDiCo-SMC component is produced in a sequence of three steps, shown in Figure 2.5. The illustrated prepregs, stored on coils, originate from the presented production process described in Section 2.2.2.1 and 2.2.2.2. Stacking leads to the desired fiber architecture of the continuous SMC. Complex geometries pose a challenge to the draping of the hybrid preform. *Co-molding* describes the simultaneous hot pressing of both prepreg types. (Böhlke & Henning et al. 2019) It demands special resin properties to permit the material flow of discontinuous fibers, while inhibiting changes in position and orientation of the continuous fibers (cf. Section 2.2.3.2. Special molding tools with magnetic fixations additionally increase the positional stability of Co-SMC CF prepregs. (Bücheler 2018) However, 100% mold coverage

is proposed in literature as well (Pangboonyanon et al. 2016). Optimized post-processing strategies are required for the hybrid material (Böhlke & Henning et al. 2019).

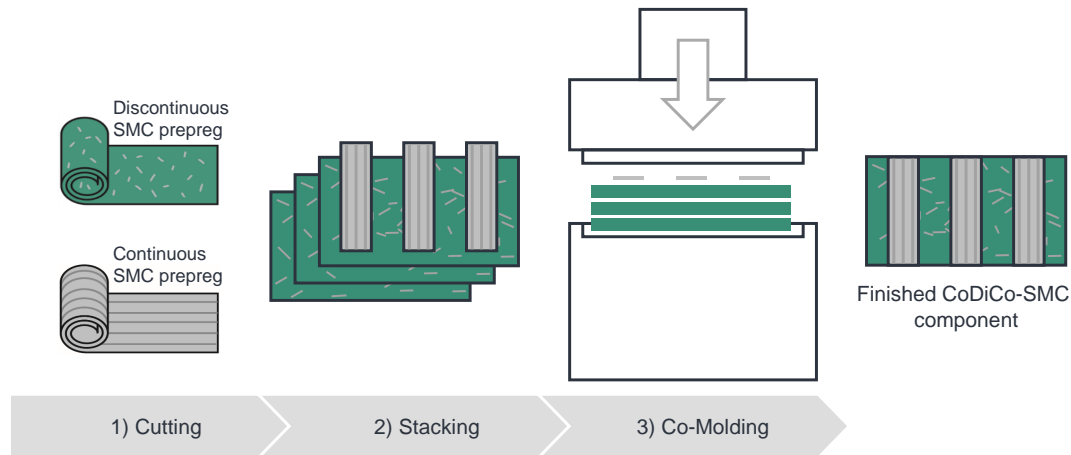


Figure 2.5: Production process of CoDiCo-SMC components; according to Schäferling (2019)

Overall, the manufacturing process of hybrid components is prone to multiple process variations, because manufacturing deviations of the individual components and the compound material occur. A detailed analysis on observed manufacturing deviations follows in Section 2.2.3.3.

2.2.3.2 Material formulation

The used resin systems for both discontinuous glass and continuous carbon fiber SMC semi-finished materials are based on an unsaturated polyester polyurethane hybrid (UPPH). The resin formulation was developed at the Fraunhofer Institute for Chemical Technology (ICT) (Bücheler 2018). The specimen material used in this work was also produced at the ICT. Detailed material compositions are given in Table 2.1 and Table 2.2, respectively. The length of a glass fiber was 25.4 mm with a fiber diameter of 13.5 μm (Görthofer et al. 2019).

Table 2.1: Composition of discontinuous UPPH GF Sheet Molding Compound (Trauth 2018)

Component	Trade name	Supplier	Quantity
UPPH resin	Daron ZW 14141	Aliancys	100 parts
Release agent	BYK 9085	BYK	2.0 parts
Deaeration aid	BYK A-530	BYK	0.5 parts
Inhibitor	pBQ	Fraunhofer ICT	0.3 parts
Peroxide	Trignox 117	Akzonobel	1.0 part
Thickener (Isocyanate)	Lupranat M20R	BASF	19.5 parts
Glass fiber	Multistar 272	Johns Manville	41 wt.-% (nom.)

Table 2.2: Composition of continuous UPPH CF Sheet Molding Compound (Trauth 2018)

Component	Trade name	Supplier	Quantity
UPPH resin	Daron AQR 9001	Aliancys	100 parts
Release agent	BYK 9085	BYK	2.0 parts
Impregnation additive	BYK 9076	BYK	3.0 parts
Inhibitor	pBQ	Fraunhofer ICT	0.3 parts
Styrene	Mono Styrol	BASF	2.9 parts
Peroxide	Trignox 117	Akzonobel	1.0 part
Thickener (Isocyanate)	Lupranat M20R	BASF	25.0 parts
Accelerator	BorchiKat 0243	Borchers	0.17 parts
Carbon fiber	PX3505015W-13	Zoltek	60 wt.-% (nom.)

2.2.3.3 Manufacturing deviations in CoDiCo-SMC

FRPs are manufactured by various methods (Neitzel et al. 2014). All those manufacturing processes are subject to variations in process parameters or input quality (Donaldson & Miracle 2001). These variations lead to deviations of the manufactured component from the designed, ideal component. SMC, as a class of FRPs, is also affected by manufacturing deviations (defects). Generally, defects are grouped into three categories: matrix, fiber and interface defects. Incomplete curing and voids are possible matrix defects; fiber misalignments and irregularities in fiber distribution are attributed to fiber defects; and separation between layers (delamination) are interface defects. (Talreja 2015)

A brief overview of reported manufacturing deviations in CoDiCo-SMC, without claim to completeness, is given in Table 2.3. Further defects might occur during the service life of the product (Donaldson & Miracle 2001; ASTM International E07.10 Committee 2017; Wang & Zhong et al. 2020). The interested reader is referred to Wang & Zhong et al. (2020), who categorized reported manufacturing-induced and in-service defects in FRPs into different scale dimensions (nano-scale, micro-scale, meso-scale, macro-scale).

Defects jeopardize the structural integrity of a component. Voids reduce the stiffness (Gross & Seelig 2018; Talreja 2015), the strength and the fatigue life (Schürmann 2007; Donaldson & Miracle 2001). Voids lead to stress and strain concentrations and are often the starting point of failure (Mehdikhani et al. 2018). Fiber misorientations and decreased fiber volume fractions lower stiffness and strength as well, both for Co-SMC (Schürmann 2007; Schäferling et al. 2019) and DiCo-SMC (Kehrer & Pinter et al. 2017; Trauth 2018). Delaminations cause a loss of interlaminar shear strength (Donaldson & Miracle 2001).

Table 2.3: Overview of manufacturing deviations in CoDiCo-SMC

Manufacturing deviation	Reference
Matrix defects	
Voids	Krämer et al. (2014), Böhlke & Henning et al. (2019)
Fiber defects	
Fiber fraction in DiCo-SMC	Mathes & Witten (2013), Trauth (2018), Schäferling et al. (2019), Bretz & Häfner et al. (2021)
Fiber orientation in DiCo-SMC	Görthofer et al. (2019), Meyer et al. (2020)
Fiber fraction in Co-SMC	Neitzel et al. (2014), Trauth (2018)
Misalignment of Co-SMC	Pangboonyanon et al. (2016), Bücheler & Henning (2016), Fengler & Schäferling et al. (2019), Schäferling et al. (2019)
Interface defects	
Delamination	Böhlke & Henning et al. (2019), Bretz & Hinze et al. (2019)

2.2.4 Measurement technologies for FRPs

Measurement technologies in the field of FRPs are often referred to as *non-destructive testing* (NDT). This term is defined as the development and application of techniques to examine materials or components in ways without impairing their future usefulness. It includes the activities of detecting, locating, measuring, evaluating, and assessing. (Technical Committee ISO/TC 135 2005) The integration of NDT technologies into production processes enables process monitoring and control, so that manufacturing costs are reduced (Imkamp & Berthold 2009).

Research and industry have been developing and improving NDT for FRPs for more than 30 years. Numerous NDT technologies, based on different physical principles, exist (Wang & Zhong et al. 2020; Technical Committee ISO/TC 135 2005). The most relevant procedures are illustrated in Figure 2.6. Each technology has its advantages, but none of them is able to fully characterize the component state and possible defects, especially when in-line measurements are required (Schäferling 2019; Wang & Zhong et al. 2020). The selection and combination of suitable NDT technologies poses a challenge, but is indispensable to provide appropriate information to assess the structural integrity of FRPs (Wang & Zhong et al. 2020).

Non-destructive testing and evaluation (NDT)			
Optical techniques	Acoustic techniques	Imaging techniques	Electromagnetic techniques
Visual inspection	Acoustic emission	Computed tomography	Eddy current testing
Shearography	Ultrasonic testing	Infrared thermography	Magnetic flux leakage testing
Digital image correlation		Terahertz spectroscopy	

Figure 2.6: Overview of common NDT technologies; own illustration

2.2.5 Mechanics and failure behavior

Existing models suited for the description of the material behavior of Co- and DiCo-SMC in the linear elastic range are introduced. A brief introduction on basic failure criteria is given as well.

2.2.5.1 Mechanics of discontinuous SMC

In the following, the material class of discontinuous SMC is regarded as a two-phase material, consisting of a matrix and a fiber phase (Brylka 2017). Eshelby initially found an analytical solution for the inhomogeneity problem, consisting of an ellipsoidal inclusion perfectly bonded to an infinite homogeneous elastic matrix (Eshelby 1957). The Mori-Tanaka method expands this idea towards ellipsoidal particle reinforced composites (Mori & Tanaka 1973; Benveniste 1987). This approach is still frequently used due to its simple and explicit formulation. The effective stiffness of the homogenized composite material with discontinuous, non-interacting fibers is given by the Mori-Tanaka approach based on orientation averages (Kehrer & Pinter et al. 2017):

$$\mathbb{C}^{\text{MT}} = \mathbb{C}_M + \phi_F \left(\phi_M \underbrace{\langle ((\mathbb{C}_F - \mathbb{C}_M)^{-1} + \mathbb{P}^{\text{ud}})^{-1} \rangle_F}_{\langle \mathbb{A}^* \rangle_{\text{oa}}}^{-1} + \phi_F (\mathbb{C}_F - \mathbb{C}_M)^{-1} \right)^{-1} \quad 2.9$$

\mathbb{C}_M describes the stiffness tensor of the isotropic matrix material, \mathbb{C}_F the stiffness tensor of the isotropic fiber material, ϕ_F the fiber volume fraction, and $\phi_M = 1 - \phi_F$ accordingly the matrix volume fraction. Hill's polarization tensor \mathbb{P}^{ud} for a prolate spheroidal inclusion in an isotropic medium is given in Equation A1.1 in the Appendix A1. The orientation average $\langle \mathbb{A}^* \rangle_{\text{oa}}$ for the transverse isotropic tensor \mathbb{A}^* is calculated based on the orientation tensors of 2nd and 4th

order N and \mathbb{N} according to Equation 2.10 (Kehrer & Pinter et al. 2017). Again, the calculation of the coefficients is given in the Appendix A1 (cf. Equation A1.3).

$$\begin{aligned} \langle A_{ijkl}^* \rangle_{\text{oa}} = & b_1 N_{ijkl} + b_2 (N_{ij} \delta_{kl} + N_{kl} \delta_{ij}) + b_3 (N_{ik} \delta_{jl} + N_{il} \delta_{jk} + N_{jl} \delta_{ik} + N_{jk} \delta_{il}) \\ & + b_4 (\delta_{ij} \delta_{kl}) + b_5 (\delta_{ik} \delta_{jl} + \delta_{il} \delta_{jk}) \end{aligned} \quad 2.10$$

The symmetric fiber orientation tensors of second and fourth order N and \mathbb{N} , respectively, give the statistical distribution of fibers in a representative volume element (cf. Equation 2.11 (a) and (b)). Here, \mathbf{p} is a unit vector that describes the direction of a fiber. $\psi(\mathbf{p})$ indicates the probability that fibers are aligned in direction \mathbf{p} . (Advani & Tucker 1987)

$$(a) N_{ij} = \oint p_i p_j \psi(\mathbf{p}) d\mathbf{p} \quad (b) N_{ijkl} = \oint p_i p_j p_k p_l \psi(\mathbf{p}) d\mathbf{p} \quad 2.11$$

2.2.5.2 Mechanics of continuous SMC

Co-SMC can be described as a continuous, unidirectional lamina (UDL). A UDL is considered as a transversely isotropic material, because same material properties prevail perpendicular to the longitudinal direction of the fibers. Figure 2.7 shows the normal and shear stresses in a representative volume element of a UDL.

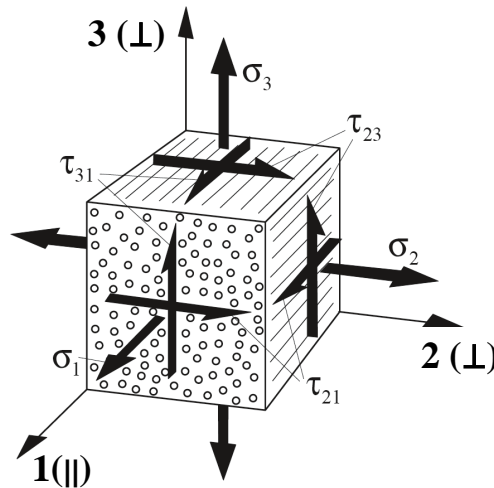


Figure 2.7: Representative volume element of an unidirectional lamina, according to Schürmann (2007)

Usually, Hooke's law of elasticity is described by the engineering constants E (Young's modulus), G (shear modulus), and ν (Poisson's ratio):

$$\begin{bmatrix} \varepsilon_1 \\ \varepsilon_2 \\ \varepsilon_3 \\ \gamma_{23} \\ \gamma_{31} \\ \gamma_{21} \end{bmatrix} = \underbrace{\begin{bmatrix} \frac{1}{E_{\parallel}} & \frac{-\nu_{\parallel\perp}}{E_{\perp}} & \frac{-\nu_{\parallel\perp}}{E_{\perp}} & 0 & 0 & 0 \\ \frac{-\nu_{\perp\parallel}}{E_{\parallel}} & \frac{1}{E_{\perp}} & \frac{-\nu_{\perp\parallel}}{E_{\perp}} & 0 & 0 & 0 \\ \frac{-\nu_{\perp\parallel}}{E_{\parallel}} & \frac{-\nu_{\perp\perp}}{E_{\perp}} & \frac{1}{E_{\perp}} & 0 & 0 & 0 \\ 0 & 0 & 0 & \frac{1}{G_{\perp\perp}} & 0 & 0 \\ 0 & 0 & 0 & 0 & \frac{1}{G_{\perp\parallel}} & 0 \\ 0 & 0 & 0 & 0 & 0 & \frac{1}{G_{\perp\parallel}} \end{bmatrix}}_{\text{matrix representation of compliance tensor } \mathbb{S}} \cdot \begin{bmatrix} \sigma_1 \\ \sigma_2 \\ \sigma_3 \\ \tau_{23} \\ \tau_{31} \\ \tau_{21} \end{bmatrix} \quad 2.12$$

Based on the transverse isotropy, the following notifications and simplifications hold:

$$E_1 = E_{\parallel}; E_2 = E_3 = E_{\perp}; G_{31} = G_{21} = G_{\perp\parallel}; \nu_{31} = \nu_{21} = \nu_{\perp\parallel}; G_{\perp\perp} = \frac{E_{\perp}}{2(1 + \nu_{\perp\perp})} \quad 2.13$$

Thus, only five independent elastic constants are to be determined for the case of transverse isotropy. The basic elastic constants are:

- the two Young's moduli E_{\parallel} and E_{\perp} ,
- the shear modulus $G_{\perp\parallel}$,
- and the two Poisson's ratios $\nu_{\parallel\perp}$ and $\nu_{\perp\perp}$.

Fiber-reinforced structures are predominantly thin-walled. It can usually be assumed that a plane stress condition is present. Thus, $\nu_{\perp\perp}$ is not demanded and the number of required basic elastic constants reduces to four.

The values for the independent elastic constants of a UDL can either be determined experimentally or, in the case of widely used fiber-matrix systems, taken from literature (cf. Table A5.1). Alternatively, data from similar systems can be used or the constants can be approximately calculated analytically from the individual components of the used fibers and matrix material. (Schürmann 2007) The analytical calculation of the engineering constants is recommended, because it avoids additional experimental investigations in the case of changing material parameters (Barbero 2013). The elastic properties of the composite are calculated, based on the rule of mixtures, from the elastic properties of the individual components (fibers and matrix) according to their fraction in the FRP as a series or parallel connection. Corrections factors are needed in some cases to adapt the analytical relationships to the experimental results. The semi-analytical equations for calculating the elastic constants, based on the material properties of the individual components, are as follows (Schürmann 2007):

$$E_{\parallel} = \phi_F \cdot E_{\parallel F} + (1 - \phi_F) \cdot E_M \quad 2.14$$

$$E_{\perp} = \frac{E_M}{(1 - \nu_M^2)} \cdot \frac{1 + 0.85 \cdot \phi_F^2}{(1 - \phi_F)^{1.25} + \frac{\phi_F \cdot E_M}{(1 - \nu_M^2) \cdot E_{\perp F}}} \quad 2.15$$

$$G_{\perp\parallel} = G_M \cdot \frac{1 + 0.4 \cdot \phi_F^{0.5}}{(1 - \phi_F)^{1.45} + \frac{G_M}{G_{\perp\parallel F}}} \quad 2.16$$

$$\nu_{\perp\parallel} = \phi_F \cdot \nu_{\perp\parallel F} + (1 - \phi) \cdot \nu_M \quad 2.17$$

$$\nu_{\parallel\perp} = \frac{\nu_{\perp\parallel}}{E_{\parallel}} \cdot E_{\perp} \quad 2.18$$

$$\nu_{\perp\perp} = \phi_F \cdot \nu_{\perp\perp F} + (1 - \phi_F) \cdot \nu_M \left(\frac{1 + \nu_M - \nu_{\perp\parallel} \frac{E_M}{E_{\parallel}}}{1 - \nu_M^2 + \nu_M \cdot \nu_{\perp\parallel} \frac{E_M}{E_{\parallel}}} \right) \quad 2.19$$

Supplementary, it deserves to be mentioned that further homogenization schemes have been developed within the IRTG. The scheme of Kehrer (2019) holds for transversal isotropic fibers as well.

2.2.5.3 Failure criteria

Failure criteria predict the load conditions under which a material fails. Most of the criteria were developed between the end of the 19th and the beginning of the 20th century. In continuum mechanics, these criteria have been pushed into the background due to advances in the fields of fracture mechanics and micromechanics. However, they are still in use due to their simple formulation and can be applied with sufficient accuracy from an engineer's perspective. In general, materials are categorized into ductile and brittle material behavior. (Gross & Seelig 2018) In contrast to ductile materials, brittle materials, like continuous and discontinuous SMC, show no significant inelastic deformations prior to fracture (Gross & Seelig 2018; Trauth 2018). Failure predictions in finite element softwares often rely on strength-based failure criteria. The general form of a failure criterion is given in Equation 2.20, with stress components σ_j and material strengths R_j . The fracture condition is met, when $I_F \geq 1$. (Barbero 2013; Schürmann 2007)

$$I_F = \sum_{j=1}^n \frac{\sigma_j}{R_j} \begin{matrix} \geq \\ \leq \end{matrix} 1 \quad 2.20$$

The stress exposure f_E was introduced to help the design engineer in predicting the risk of failure. It compares the current stress state to the maximum stress state that can be withstood. A visualization of f_E as a fraction is given in Equation 2.21. Using the stress exposure in Equation 2.22 circumvents the usage of the inequation in Equation 2.20. The reciprocal of the

stress exposure f_E^{-1} is called stretch factor f_S and gives the factor by which the existing stress state must be multiplied until failure is reached. Failure occurs, when $f_E = 1$. (Schürmann 2007; Verein Deutscher Ingenieure e.V. 2006)

$$f_E = \frac{\text{vector length of the existing stresses}}{\text{vector length of stresses causing failure}} \quad 2.21$$

$$\sum_{j=1}^n \frac{\sigma_j}{f_E \cdot R_j} = 1 \quad 2.22$$

Failure criteria are characterized into phenomenological criteria and criteria which distinguish between fracture types. The maximum stress criterion is one of the simplest phenomenological criteria, while the Tsai-Wu criterion describes failure of anisotropic materials based on interactions of the stress tensor components. More material parameters need to be determined to parametrize the Tsai-Wu criteria compared to the maximum stress criterion. Hashin and Puck failure criteria are widely used criteria for FRPs and distinguish between fiber and matrix failure. (Barbero 2013) In the following, the maximum stress criterion and the Puck criterion are presented in more detail.

Maximum stress criterion According to this criterion, the material behavior is characterized by a tensile strength R^+ , a compression strength R^- and a shear strength S . Failure occurs when the maximum principal stress reaches R^+ , the minimum principal stress reaches R^- , or the shear stress reaches S . Different strength values, dependent on the material orientation, can be used to describe an anisotropic material. (Barbero 2013; Gross & Seelig 2018)

$$f_E = \max \left\{ \begin{array}{ll} \frac{\sigma_1}{R_1^+} & \text{if } \sigma_1 > 0 \\ \frac{\sigma_2}{R_2^+} & \text{if } \sigma_2 > 0 \\ \frac{\sigma_3}{R_3^+} & \text{if } \sigma_3 > 0 \\ \frac{|\tau_{12}|}{S_{12}} & \\ \frac{|\tau_{13}|}{S_{13}} & \\ \frac{|\tau_{23}|}{S_{23}} & \end{array} \right. \quad \text{or} \quad \begin{array}{ll} \frac{-\sigma_1}{R_1^-} & \text{if } \sigma_1 < 0 \\ \frac{-\sigma_2}{R_2^-} & \text{if } \sigma_2 < 0 \\ \frac{-\sigma_3}{R_3^-} & \text{if } \sigma_3 < 0 \end{array} \quad 2.23$$

Puck criterion Stress interactions as well as fiber and matrix failure are considered in Puck's criterion. Fiber fracture (FF) is primarily caused by a stress σ_1 in the fiber direction. Nevertheless, uniaxial stresses σ_2 and σ_3 also lead to additional longitudinal strains in the fiber direction. Thus, a fiber fracture criterion for a continuous lamina is proposed, which

includes the stresses σ_2 and σ_3 . (Knops 2008) However, the influences of these Poisson's ratio effects is in the low single-digit percentage range. Therefore, the maximum stress criterion is often used in practice. (Verein Deutscher Ingenieure e.V. 2006)

$$f_{E,\text{Puck,FF}} = \frac{1}{\pm R_{\parallel}^{\pm}} \left[\sigma_1 - \left(\nu_{\perp\parallel} - \nu_{\perp\parallel F} \cdot m_{\sigma F} \frac{E_{\parallel}}{E_{\parallel F}} (\sigma_2 + \sigma_3) \right) \right] \quad 2.24$$

with $\begin{cases} R_{\parallel}^+ & \text{for } [...] \geq 0 \\ -R_{\parallel}^- & \text{for } [...] < 0 \end{cases}$

In the equation above, $\nu_{\perp\parallel}$, $\nu_{\perp\parallel F}$, E_{\parallel} , and $E_{\parallel F}$ stand for the Poisson's ratios and the Young's moduli of the lamina and the fiber, respectively. The magnification factor $m_{\sigma F}$ accounts for biaxial strain close to the interface between matrix and fiber. It is proposed to set $m_{\sigma F} = 1.1$ for CFRP. (Knops 2008)

Puck developed an inter-fiber fracture (IFF) condition related to stresses in the fracture plane. The IFF fracture planes are fiber-parallel planes, oriented in the longitudinal direction of the fibers. Stresses are not given in the lamina coordinate system, but as stresses in fiber direction, normal to the fiber-parallel plane, and tangential to the fiber-parallel plane. The resulting stresses in the fracture plane are calculated from the lamina stresses by a coordinate transformation to the fracture plane. Stresses in the thickness direction can be neglected for thin lamina. Thus, the following three different IFF modes are discerned for thin lamina (Puck et al. 2002).

IFF mode A:

$$f_{E,\text{Puck,IFF,A}} = \sqrt{\left[\left(\frac{1}{R_{\perp}^+} - \frac{p_{\perp\parallel}^+}{R_{\perp\parallel}} \right) \cdot \sigma_2 \right]^2 + \left(\frac{\tau_{21}}{R_{\perp\parallel}} \right)^2} + \frac{p_{\perp\parallel}^+}{R_{\perp\parallel}} \cdot \sigma_2; \text{ for } \sigma_2 \geq 0 \quad 2.25$$

IFF mode B:

$$f_{E,\text{Puck,IFF,B}} = \sqrt{\left(\frac{\tau_{21}}{R_{\perp\parallel}} \right)^2 + \left(\frac{p_{\perp\parallel}^-}{R_{\perp\parallel}} \sigma_2 \right)^2} + \frac{p_{\perp\parallel}^-}{R_{\perp\parallel}} \cdot \sigma_2; \text{ for } \sigma_2 < 0 \text{ and } \left| \frac{\sigma_2}{\tau_{21}} \right| \leq \left| \frac{R_{\perp\perp}^A}{\tau_{21,c}} \right| \quad 2.26$$

IFF mode C:

$$f_{E,\text{Puck,IFF,C}} = \left[\left(\frac{\tau_{21}}{2(1 + p_{\perp\perp}^-) R_{\perp\parallel}} \right)^2 + \left(\frac{\sigma_2}{R_{\perp}^-} \right)^2 \right] \frac{R_{\perp}^-}{-\sigma_2}; \text{ for } \sigma_2 < 0 \text{ and } \left| \frac{\tau_{21}}{\sigma_2} \right| \leq \left| \frac{\tau_{21,c}}{R_{\perp\perp}^A} \right| \quad 2.27$$

Traditional criteria are usually based on basic lamina strengths R_{\perp}^+ , R_{\perp}^- , $R_{\perp\parallel}$, and $R_{\perp\perp}$ (Puck et al. 2002). These strengths can be determined in experiments. Transformations of the basic

strengths, such as $R_{\perp\perp}^A$, are necessary, because Puck's criterion assumes that only stresses acting in the fracture plane are causing failure (Puck et al. 2002). The shear stress $\tau_{21,c}$ is present at the transition point from mode B to C. More information about the strength transformation and the transition point can be found in literature (Puck et al. 2002; Schürmann 2007; Knops 2008). Guidelines on the choice of inclination parameters are given in Verein Deutscher Ingenieure e.V. (2006). The Puck criterion is an essential part of the aforementioned standard as an initiative to standardize the design and dimensioning of FRP components (Verein Deutscher Ingenieure e.V. 2006). Additionally, an Abaqus user subroutine is available based on this standard¹.

2.2.6 Summary: Properties of hybrid sheet molding compound

The summary of this section, relevant to the hybrid SMC under consideration, is given as follows:

1. Manufacturing processes of SMC are prone to process variations and variations of input quality, leading to individual combinations manufacturing deviations for each component.
2. Various technologies exist for non-destructive testing of FRPs. However, no method is suitable to characterize all defects. Additionally, the suitability for an in-line application needs to be considered.
3. The linear-elastic material behavior can be modeled using Mori-Tanaka homogenization based on orientation averages for DiCo-SMC and semi-analytical approaches for the Co-SMC. Classical failure criteria apply for a general assessment.
4. The homogenization approach is capable to consider variations in fiber fraction or void content.

2.3 Finite element (FE) method

The finite element method (FEM) is an established tool for the dimensioning of components during the design phase (Mathes & Witten 2013). In the following, the basic steps for building a FE model are described. Thus, the integration of occurring manufacturing deviations at different levels in the model structure can be understood.

¹Kremer, T., *KLuB-VDI2014 v2.0: Subroutine zur Festigkeitsanalyse von Faser-Kunststoff-Verbunden nach der VDI-Richtlinie 2014, Teil 3 für ABAQUS*. https://www.klub.tu-darmstadt.de/media/fachgebiet_klub/downloads_3/KLuB-VDI2014_v2.zip (accessed on Jan. 5, 2022).

2.3.1 Necessity and concept

The deformation behavior of components is mathematically described by partial differential equations. Analytical solutions of those differential equations do not exist for every problem. Especially for complicated geometries and load conditions, or for complex material laws in case of anisotropy or nonlinearity, an analytical solution might not be given. Many numerical methods have been developed over the years to solve such problems. The FEM is only one of them, but the most widely used in the field of engineering. (Fish & Belytschko 2007)

The basic idea of FEM is to divide the solid geometry into a finite number of small, geometrically simple subdomains, the finite elements. These elements itself consist of multiple nodes. The discretization is typically referred to as meshing and the totality of all elements and nodes as the mesh of the FE model. In practice, the geometries under consideration are often so complex that a finite number of elements is not sufficient to exactly represent the geometry. The resulting inaccuracies are called geometric discretization error. (Fish & Belytschko 2007)

The local displacement function $\mathbf{u}(\mathbf{x})$, dependent on the position vector \mathbf{x} , needs to be found to solve the differential equation for a linear elastic problem. The differential equation itself initially requires a twofold differentiability of $\mathbf{u}(\mathbf{x})$, leading to a strongly restricted set of potential solutions. This problem is circumvented by transforming the differential equation for each element into its weak form. The weak form can be solved by functions which can be only differentiated once. The element-related displacement functions $\mathbf{u}^e(\mathbf{x})$ can be expressed by:

$$\mathbf{u}^e(\mathbf{x}) = \mathbf{u}^e(x, y, z) = \mathbf{N}^e(x, y, z) \mathbf{d}^e = \sum_{j=1}^{n_{\text{en}}} N_j^e(\mathbf{x}) \mathbf{d}_j^e, \quad 2.28$$

with the known polynomial $N_j^e(\mathbf{x})$, called shape function, and the unknown nodal displacement \mathbf{d}_j^e . At least linear shape functions, with nodes at the corner points of each element, are required to prevent displacement jumps at the element boundaries. Thus, the stress is constant within an element. The solution is interpolated between the nodes. Generally, a finer mesh or shape functions of higher order improve the solution accuracy, but the computational cost increases as well. A global system of linear equations is built upon the element-wise formulation. Here, the same displacement of a shared node in each adjacent element is used as a boundary condition. The system of equations, given in Eq. 2.29, is obtained:

$$\mathbf{f} = \mathbf{K} \mathbf{u}, \quad 2.29$$

with the force f , the displacement u and the stiffness matrix K . The vectors f and u contain the 3D forces and displacements at every node of the mesh. (Fish & Belytschko 2007; Barbero 2013)

The following systematic step-by-step approach is given by Fish & Belytschko (2007). In today's CAE environment, the focus lies on the pre- and postprocessing for the end user.

- 1) **Preprocessing:** Subdivision of the problem domain into finite elements
 - (a) Determination of the relevant geometry
 - (b) Definition of material properties
 - (c) Definition of initial and boundary conditions
 - (d) Consideration of potential further constraints (e.g. contact definition)
 - (e) Spatial discretization of the geometry
- 2) **Element-wise consideration:** Development of element-related equations
- 3) **Assembly:** Generation of the global system of equations from the individual elements
- 4) **Solution:** Solving the global system of equations
- 5) **Postprocessing:** Evaluation of the results and visualization

2.3.2 Element types

Solid elements are 3D elements to discretize a volume. Typically, a 3D solid element is a tetrahedron or hexahedron in shape. Every node has three displacement degrees of freedom. In principle, it can be used to model all kind of problems. However, solid elements are only accurate when a reasonable aspect ratio is maintained. Thus, it is demanding on computational resources, especially for thin structures. (Neto 2015)

Shell elements are used for modeling structures that are thin in one dimension compared to their other two dimensions. Thus, the displacement field and the stress take a very simple form. Sheet metals, vehicle frames or fuselages of an aircraft are exemplary objects that are conventionally modeled by shell elements rather than by solid elements. The element thickness is defined as an element property. Nodes typically have three displacement and three rotational degrees of freedom and are in the midsurface of the element. The shell theory assumes that normals to the midsurface remain straight and normal. These simplifications reduce the computational costs compared to solid elements. They are used for an efficient modeling of bending problems and deformations in the plane. However, stresses in thickness direction are neglected and connections to solid elements are challenging. (Fish & Belytschko 2007; Nasdala 2015)

Continuum shell elements (CSE) have only displacement degrees of freedom and depict the element thickness through additional nodes compared to conventional shell elements. They

can easily be stacked and connected to solid elements. The 3D shell geometry is discretized by CSE in the same way as 3D solid elements do. (Barbero 2013; Nasdala 2015)

2.3.3 Extended finite element analysis (XFEM)

The classical FEM requires continuity of displacement of neighboring elements (cf. Equation 2.28). Discontinuities, such as cracks or delaminations, cannot directly be handled by the FEM. Tedious meshing procedures, using fine meshes that conform to the boundaries as well as mesh refinements, are necessary. The Extended Finite Element Method (XFEM) overcomes this problem and uses fixed meshes. The position of discontinuities is not considered during meshing. XFEM uses enrichment functions and additional degrees of freedom as a central approach for the approximation of the local displacement function $\mathbf{u}(\mathbf{x})$ in the region of the discontinuity. The approximation of $\mathbf{u}(\mathbf{x})$ is enriched as:

$$\mathbf{u}(\mathbf{x}) = \underbrace{\sum_{i \in I} \mathbf{N}_i(\mathbf{x}) \mathbf{d}_i}_{\substack{\text{standard FEM,} \\ \text{cf. Eq. 2.28}}} + \underbrace{\sum_{i \in I^*} \mathbf{N}_i^*(\mathbf{x}) \cdot \psi(\mathbf{x}) \cdot \mathbf{d}_i^*}_{\text{enrichment}}, \quad 2.30$$

with the unknown nodal displacement \mathbf{d} and \mathbf{d}^* . I denotes all nodes in the mesh, and the set of enriched nodes is given by I^* . The localized enrichment functions $\mathbf{N}_i^*(\mathbf{x}) \cdot \psi(\mathbf{x})$ capture the discontinuities of $\mathbf{u}(\mathbf{x})$. Typically, the shape functions $\mathbf{N}_i(\mathbf{x})$ and $\mathbf{N}_i^*(\mathbf{x})$ are chosen identically. Jumps are commonly modeled using the Sign or Heaviside function for $\psi(\mathbf{x})$. Singular stress and strain states can be captured using additional enrichment functions. (Fries 2018)

2.3.4 Summary: FE model for hybrid SMC

Summarizing the key concepts of FEM leads to the following conclusion:

1. The FEM allows to model the behavior of anisotropic material systems and hybrid components under different load conditions.
2. Variations in the assembly of hybrid components, such as misalignments of Co-SMC, can be considered during the preprocessing step of the FEM.
3. The XFEM is generally suited to consider manufacturing deviations leading to discontinuities, such as delaminations, in DiCo-SMC.

3 State of the art

In this chapter, the state of the art of the topics required for the solution approach is presented. First, requirements for the implementation of a function-oriented in-line quality assessment of hybrid SMC are defined in Section 3.1. Relevant scientific approaches are then presented in Section 3.2 and compared with the previously defined requirements. Finally, Section 3.3 concludes with the research deficit addressed in this thesis.

3.1 Requirements

On the basis of the previously outlined fundamentals, three overall requirements for a method for the function-oriented in-line quality assurance of hybrid SMC are derived. These requirements are related to the research questions (RQ, cf. Section 1.3), subdivided into further evaluation criteria and explained below. The requirements and evaluation criteria provide the foundation for deriving the research deficit. Table 3.1 summarizes the review and is based on the requirements and evaluation criteria presented in this section.

Measurement technologies for FRPs (RQ 1): Many different measurement technologies exist for FRPs. Therefore, the most promising technologies including respective research approaches are initially presented. Non-destructive testing is a prerequisite for an in-line deployment. However, suitable reference measurement technologies are considered in this section as well. Existing research work in the field of measurement technology is evaluated whether an *SMC-like application* has taken place and whether *multiple defects* could be detected. An already existing *in-line integration* is addressed as well for deriving the research deficit.

In-line functional assessment of manufacturing deviations (RQ 2 and 3): *Experimental investigations* are often used to establish a basic understanding. However, a *simulative assessment* of manufacturing deviations is favorable compared to cumbersome experiments. Ideally, in-line measured data is directly integrated into simulations (*measurement data integration*), according to RQ 2. *Interactions* of multiple manufacturing deviations need to be considered. A *real-time applicability* of the functional assessment, facilitated by suitable surrogate models (RQ 3), needs to be guaranteed to allow for a 100% inspection.

Analysis of measurement uncertainty (RQ 4): The in-line *measurement technologies* themselves, *FE simulations* and *surrogate models* are all subject to uncertainties and build upon each other. Thus, the measurement uncertainty of all of them needs to be considered.

3.2 Literature review of research focus areas

This section mainly describes recent works in the field of FRPs relevant for a function-oriented quality assurance of hybrid SMC. The existing scientific contributions are categorized into four subsections: measurement technologies, assessment of manufacturing deviations, function-oriented measurements, and surrogate modeling of FE simulations. In the last two categories, works not related to FRPs are as well considered.

3.2.1 Measurement technologies for FRPs

Recent works in NDT technologies, according to Figure 2.6, and suitable reference measurement technologies relevant for this thesis are presented in this section. A concise overview and comparison to the reported manufacturing deviations in CoDiCo-SMC (cf. Table 2.3) is given in Table 5.1.

3.2.1.1 Computed tomography

X-ray computed tomography (CT) is used extensively for both qualitative and quantitative assessments in the aerospace and automotive industries. Especially the use of CT for NDT of aerospace composites has increased significantly. The multiscale structure of FRPs can be non-destructively detected by CT with high spatial resolution. CT provides both 2D and 3D information on the outer and inner composite structure. (Kruth et al. 2011; Naresh et al. 2020)

Schipp et al. (1992) measured X-ray absorption coefficients of CFRP samples. The fiber mass fraction was calculated using the measurement results as well as an analytical equation for the effective absorption coefficient of matrix and fibers. The authors estimated the experimental error to be less than 3 wt.-%.

Bertram et al. (2016) developed an in-line measurement approach for fiber volume fraction (FVF) of SMC using CT. The resin material formulation was adjusted to increase the contrast between matrix and fibers. Different nominal FVF between 0 and 20 vol.-% were realized by stacking DiCo-SMC and pure resin specimen. Fast evaluation results of the FVF were generated using a support vector regression approach based on single X-ray projection images. The relative attenuation and the attenuation path length were chosen as feature space. Cross-validated error measures were between 0.60 and 1.68 vol.-%. This approach overcomes the challenging FVF measurements based on volumetric images. Time consuming generation of volumetric images, image blur and the lack of transferability of the parameterization of different image thresholding techniques traditionally limit the use of CT volumetric images for the measurement of FVF (Pinter 2018).

CT was further used to determine fiber orientations of both discontinuous (Pinter 2018; Schöttl & Weidenmann et al. 2021) and continuous FRP (Lightfoot et al. 2017; Schöttl & Dörr et al. 2020). Voids (Little et al. 2012; Tserpes et al. 2016; Naresh et al. 2020), delaminations (Léonard et al. 2017), and cracks (Naresh et al. 2020; Schöttl & Kolb et al. 2020) were detected as well. However, the latter methods are only suitable for reference measurements due to high measurement times. In addition, micro-CT is often used in these applications.

3.2.1.2 Terahertz spectroscopy

Terahertz (THz) technology has emerged as a promising candidate in the field of NDT over the past two decades. THz waves are in the frequency range between 100 GHz and 10 THz and penetrate most non-metallic and non-polar media. The frequency-dependent profile of a material, which among other things consists of the refractive index $n(f)$ and the absorption coefficient $\alpha(f)$, can be calculated from the time domain by means of the Fourier transform. THz waves offer great potential for in-line and in-process measurements due to their non-contact and non-ionizing nature. (Rieh 2021; Nüßler & Jonuscheit 2021)

Wietzke et al. (2007) conducted one of the first investigations on optical properties of composites in the THz range. They identified a mostly linear correlation between the refractive index and the nominal additive content of granulate additives as well as glass fibers in compounded polymers. In contrast to the refractive index, the absorbance did not prove to be a useful measure for the additive content.

Jördens & Scheller & Wichmann et al. (2009) estimated the orientation of short glass fiber-reinforced liquid crystal polymers based on their birefringence properties in a transmission setup. However, this method assumed 100% oriented fibers. Jördens & Scheller & Wietzke et al. (2010) overcame this restriction and determined the average orientation of all short fibers and the percentage of fibers oriented in the preferential direction in a measurement region. The GFRP was considered as a dielectric mixture with possible orientations of the short fibers in all three spatial directions. Analytical calculations of the refractive index, based on the dielectric mixture model, were linear in the fiber volume fraction. Samples were measured three times under varying sample orientations with respect to the polarization axis of the THz pulse, allowing the determination of the ordinary and extraordinary refractive index. Subsequently, the local fiber content was inferred.

Krumbholz et al. (2009) integrated a THz transmission setup into the extrusion die of a polymer compounding process. Temperature and density changes were considered due to their influence on the refractive index. The evaluation of pulse amplitudes at fixed time stamps enabled in-process measurements of the additive content, because higher additive contents

increased the optical path length and led to time delays of the electromagnetic wave. The material thickness was assumed to be constant in the measurement section.

Hauck et al. (2014) used a reflection setup for determining the orientation-dependent refraction indices based on three consecutive measurements under different sample orientations. The sample was an injection molded, 4 mm thick short-fiber reinforced polymer plate. Furthermore, the filler content of CaCO_3 in polypropylene was determined based on time differences and received pulse energies with a resolution of 2 wt.-%. A high linear correlation was observed between the water content in polymers and the absorbance. Since water absorption only marginally affects the refractive index of a polymer, a thickness correction could be made in a combined evaluation of refractive index and absorbance.

Dong et al. (2015) investigated artificial delaminations (Teflon films) between eight GFRP layers using a reflective THz set-up. The sample size was 50 mm x 50 mm x 1.85 mm. It was raster-scanned with a spatial step size of 0.1 mm. THz measurements were compared to ultrasonic (US) C-scans. Both, lateral and axial resolution were significantly better when using the THz system. In contrast to US, THz measurements could provide quantitative information on the individual lamina and delamination thickness.

Ryu et al. (2016) successfully detected three overlapped, differently shaped, multi-delaminations in a unidirectional GFRP using a reflective THz set-up with a 25° incidence angle. Determined thicknesses of the delaminations deviated less than 10% from their nominal value and the depth of the defects in the specimen was measured with less than 5% error. The authors confirmed the higher resolution of THz spectroscopy compared to US.

Im et al. (2020) obtained defect information in a CF-skin honeycomb sandwich composite panel using a reflection setup. The investigations showed a reasonable signal-to-noise ratio (SNR) when the electrical field was perpendicular to the fiber orientation. In contrast, THz radiation does not penetrate through CFRP at 0° . A linear behavior of the normalized resistance, dependent on the angle between fibers and electrical field, was found.

Overall, THz spectroscopy shows promising results for multiple NDT tasks in GFRPs, especially for the measurement of local FVF. So far, multiple measurements of the same specimen region are necessary to estimate the FVF. Up to now, long glass-fiber reinforced SMCs have not been subject to investigations in the THz spectrum. Reference measurements according to international standards have not been performed to quantify the quality of existing results. A measurement uncertainty analysis has also not been performed to date. However, the detection and measurement of delaminations in larger areas is time-consuming because of limited measurements areas of the THz beam. Measurements of CFRPs as polar media are limited.

3.2.1.3 Infrared thermography

Infrared thermography (IRT) allows for fast NDT of large surfaces. Generally, an infrared camera records the response of a specimen in the infrared spectrum. Enclosed anomalies in the component change the heat diffusion rate and become apparent in the thermographic image. IRT is mostly categorized into active and passive methods, based on the origin of heat differences. In passive thermography, heat differences between specimen and environment are inherently present. Contrary, active thermography uses an external heat stimulus to excite the component and investigate its thermal response. Pulsed phase thermography (PPT) is an active technique which combines the time efficiency of pulsed thermography (PT) while providing depth information based on phase images like lock-in thermography (LT). In PPT, the discrete Fourier transform (DFT) is applied to a time series of infrared images recorded after an impulsive excitation. Active thermography proved to be a useful NDT applications for many composites. (Maldague 2001; Yang & He 2016).

Meola & Carlomagno (2010) investigated in-process temperature differences in continuous GFRP specimens under low velocity impact. Local delaminations developed during the impact experiment and were identified through elevated temperatures. In a subsequent LT examination, the induced delaminations were also detected.

Montanini (2010) quantitatively measured artificial subsurface defects in a Plexiglas specimen using LT and PPT. Defects were represented by flat-bottomed holes. A thorough MU analysis according to GUM was carried out for diffusivity measurements and defect depths. Defect size measurements were only assessed by their standard deviation based on three measurements using different geometrical reference circles.

Amenabar et al. (2011) investigated delaminations in 10 mm thick GFRP wind turbine blades with different NDT techniques. Teflon films of 250 μm and 55 μm thickness were integrated into the specimens to artificially represent delaminations. Using thermography, five defects of different shape and in different depths could be detected in both test specimens with a mean areal deviation of 8%. The authors further concluded that both a transmissive and reflective setup can be suited for inspection, dependent on the material under investigation. Image blur and acquisition time limited high-thickness measurements.

Duan et al. (2012) quantified the suitability of IRT as a testing technique using probability of detection (PoD) curves for various heating sources and post processing techniques. The object under investigation was a CFRP specimen with embedded Teflon delaminations of different sizes and depths. Overall detection rates as well as size-to-depth ratios with 90% PoD were determined.

Schäferling (2019) developed a multisensory system, consisting of a laser light section system and PPT, for the simultaneous detection and quantification of multiple defects in CoDiCo-SMC. A data fusion approach for 2D thermographic images and 3D cloud of points (CoP), generated by laser light section, was developed. Fused measurement results were visualized in a 3D layer model of the component. PPT was considered as a measurement technology instead of a testing method. Consequently, measurement uncertainty analyses were conducted according to GUM for the individual systems as well as for the data fusion process. Flat-bottomed holes were used for the investigation of the PPT measurement uncertainty.

Manta et al. (2019) measured differences in thermal diffusivity in a graphene nanoplatelet/epoxy nanocomposite using PT in a transmission setup. A fixed threshold was employed to the normed temperature distribution for void detection. The relative void fraction was fed forward into a FE simulation of a representative volume element for assessing the influence on thermal properties. Numerical simulation results were in accordance with the validation limits, defined by the experimental uncertainty.

Altogether, IRT is an established NDT method. Artificial delaminations and voids were successfully detected in various composites. Several authors have already evaluated the application possibilities as a measurement technology. However, MU analyses were conducted with flat-bottomed holes only, although integrated Teflon films are preferable as artificial representation of delaminations in FRPs. PPT offers the best balance between information and measurement time.

3.2.1.4 Machine vision

Machine vision covers a wide range of tasks. This subsection focuses on the feature extraction (shape, position, and orientation) of CFRPs, especially in hybrid composites. For the foundations and further application examples, the interested reader is referred to Beyerer (2016).

Kosse et al. (2014) implemented a robot-guided camera system and laser light section sensor for automated quality assurance of CFRP preforms. Diffuse dome lighting guaranteed homogeneous illumination and minimized reflections of the preform for 2D surface detection using an industrial camera. The 3D geometry of the preform was recorded by the laser light section system. Data fusion of 2D and 3D information enabled the evaluation of fiber orientation and fiber waviness. A detailed analysis of the measurement uncertainty was presented in a subsequent work (Kosse 2018).

Bücheler & Henning (2016) investigated the influences of different molding conditions and matrix formulations on the accuracy of Co-SMC patch positioning. DiCo- and Co-SMC were

separated using a gray value threshold and a bounding box was drawn around the patch. Deviations were quantified by the displacement of the centroid of the patch as well as the rotation, length and width changes of the bounding rectangle. Information about a camera calibration was not given.

Corbridge et al. (2017) used a grid technique to measure displacements of unidirectional prepregs in a co-molding process. Parallel lines were drawn onto the surface of the unidirectional prepreg in two perpendicular directions with a grid distance of 20 mm. The prepreg as well as the finished material were scanned in a flatbed scanner. Intersections were determined in both scans using the MATLAB[®] image processing toolbox. Thus, a displacement field was calculated based on 4-noded linear elements.

Zaiß & Demmerle et al. (2017) showed that differences in the reflectivity of both material components in CoDiCo-SMC become visible in scans using a laser light section system. The approach was not further pursued, but could enable positional detection of Co-SMC. Conversely, the different materials were clearly visible in thermographic images. In a subsequent work, Schäferling (2019) manually identified the orientation and position of Co-SMC in fused 3D thermographic images using the software Geomagic Control.

Schmidt et al. (2017) and Groß et al. (2018) integrated a laser line scanner into the automated fiber placement process for the production of multi-layer inserts. The contour of the CFRP prepregs was measured to correctly place metal sheets in the hybrid layup (CFRP and metal sheets). The edges of the tapes were identified based on height differences with respect to the previous layer. Subsequently, the metal insert was detected by an infrared camera.

Brabandt (2018) extended the use of laser light section systems for the in-line quantification of defects critical to quality in CFRP preforms. Using data fusion of two laser light section sensors, even complex 3D preform geometries could be scanned. The measurement uncertainty of the system was evaluated according to GUM.

Fengler & Schäferling et al. (2019) detected the centroid and the orientation of a Co-SMC patch in thermographic images. The longitudinal edges of the patch were identified and used for the calculation of the orientation. Image processing was conducted using MATLAB[®]. The same approach was as well performed by the author of this thesis for camera images (Bretz & Häfner et al. 2019).

Existing works show that sophisticated systems are necessary when manufacturing deviations have to be quantified on fiber level. However, simpler systems, such as an industrial or thermographic camera, are sufficient for the detection of local CF patch reinforcements in a hybrid material.

3.2.1.5 Ultrasonic testing

Ultrasonic testing (UT) is one of the most common NDT technologies for composite materials. The measurement of ultrasonic parameters provides extensive quality information. Delaminations, voids, and stiffness parameters can be determined in composite structures. The ultrasonic method itself uses longitudinal, shear, Lamb, Rayleigh or guided waves. Traditionally, UT uses a couplant between the ultrasonic transducer and the media under inspection to bridge the large acoustic impedance difference between air and solid media. Thus, UT are comparably slow and require significant setup time. In contrast, air-coupled UT is challenging because of large acoustic impedance differences between air and solid media. This results in a low acoustic energy input. However, frequencies between 50 kHz and 5 MHz have been successfully applied. Laser UT describes a method for a non-contact ultrasonic excitation in the media using lasers. (Donaldson & Miracle 2001; Fischer et al. 2019)

The work presented below highlights new research findings from recent years in the field of UT of FRP. In particular, non-contact UT is addressed.

Grimberg et al. (2013) determined elastic properties of planar isotropic thermoset based on Lamb waves using a commercial air-coupled UT system. A comparison of the experimentally determined dispersion curves with a theoretical modeling allowed a nonlinear optimization of the material parameters. Mechanical tests showed a good agreement to the non-destructively determined Young's moduli and the shear modulus.

Karabutov & Podymova (2014) linearly correlated the void fraction in CFRP with the maximum resonance attenuation peak of a transmitted ultrasonic signal. The resonance bandwidth further showed a quadratic correlation with the void fraction. The authors proposed critical threshold values as an evaluation criterion, since interply delaminations occurred for porosities higher than 5 vol.%. Although ultrasonic wave were laser-excited, the specimen under investigation was still in contact with a transmitter material and a piezoelectric detector, making this principle inadequate for in-line measurements.

Park et al. (2014) developed a contactless ultrasonic wavefield imaging technique for delamination detection. Ultrasonic waves were excited by a laser and a laser Doppler vibrometer was used for the contactless measurement of the specimen response. The application was demonstrated on exemplary sections of a CFRP aircraft wing segment and GFRP wind turbine blades. Delaminations and debondings were successfully visualized. Nevertheless, a special surface treatment of the sample structures was necessary.

Webersen et al. (2016) induced a broadband, multi-modal ultrasound signal in a continuous FRP plate using a laser. The signal was received by a piezoceramic transducer attached

to the plate. A developed semi-analytical FE solver allowed inverse parameter identification based on two measurements for an orthotropic material model. For planar isotropic materials, a single measurement was sufficient to determine the material parameters.

Zaiß & Jank et al. (2017) evaluated several UT methods regarding their application potential for NDT of CoDiCo-SMC. Resonant frequencies for Co- and DiCo-SMC were determined by ultrasonic spectroscopy using a couplant. Air-coupled UT C-scans showed areas of different transmitted amplitudes. However, attempts to categorize different defects led to ambiguous results. The authors considered thermography to be more promising compared to UT, although not fully satisfactory.

Essig (2018) integrated an air-coupled ultrasonic transmitter and receiver in a demonstrative pultrusion line for continuous in-line inspection of continuous CF tape. The energy transmitted through the CF tape was analyzed with respect to cracks and deviating fiber impregnations. Cracks were successfully detected even with continuous tape feed, whereas varying degrees of impregnation were characterized purely qualitatively without tape movement.

Zhang et al. (2018) compared an air-coupled piezoceramic receiver to an optical microphone in a raster scanning transmission mode with respect to their detection capabilities of delaminations. Another piezoceramic transmitter was used to excite ultrasonic waves in the CFRP and GFRP specimens. Results were further compared to thermographic images. The optical microphone was more sensitive than the traditional air-coupled receiver and acoustic results were comparable to thermographic results. However, thermography has a time advantage over the raster scanning technique.

Fischer et al. (2019) assessed impact damages in composites using laser excitation and a broadband, air-coupled optical microphone for detection. The technique provided a high resolution of damaged regions in transmission mode. Especially low impact damages could be detected in contrast to CT scans.

The author of this thesis used non-contact ultrasonic to investigate DiCo-SMC specimens of different glass fiber fractions. The aim was to characterize the fiber fractions based on the sound velocities of the symmetric and asymmetric modes using laser-excited Lamb waves and an optical microphone as receiver (Bretz & Häfner et al. 2019). Similar approaches successfully correlated ultrasonic speed with fiber fractions in concrete (Benaicha et al. 2015; Ham & Popovics 2015). Due to comparatively long measurement times and time-consuming evaluations, this method was not further pursued.

Even though UT has been firmly established in NDT of FRPs for many years due to its good measurement resolution (Donaldson & Miracle 2001), research activities have only paved

the way for cost-efficient, prototypical in-line applications in recent years (Essig 2018). Since non-contact measurement is desirable due to shorter measurement times, large reflection losses at the air-solid interface and the large attenuation of high-frequency ultrasound in air limit its use due to low SNR at the receiver. The use of an optical microphone as a receiver is shown to be a promising new technology (Zhang et al. 2018; Fischer et al. 2019).

3.2.1.6 Eddy current testing

Eddy current testing (ECT) can be used for FRPs with conductive fibers, such as CF. According to Maxwell's equations, electrical currents are induced in the fibers by a changing magnetic field of the measurement device. Defects influence the local electrical conductivity, leading to changes in the eddy currents. The changes can be measured. (Donaldson & Miracle 2001)

Mizukami & Watanabe (2018) measured the through-thickness conductivity of CFRPs. Conductivity in fiber direction depends on the CF fraction. However, conductivity in transverse and thickness direction are stronger influenced by contacts between carbon fibers. The authors assumed a constant CF fraction.

Berger (2019) developed a tool-integrated eddy current sensor for the preforming process of CF layups. CF misorientations were detected in classes of approximately 6.7° . Missing rovings, gaps, and folds were successfully classified using support vector machines.

Brasington et al. (2021) provided an overview of inspection techniques for a variety of defects in the automated fiber placement process. Gaps and overlaps of CF were detected, but detection capabilities depended on the size of the defects.

Wang & Wu et al. (2021) introduced an 8-shaped eddy current probe to generate a stronger vertical eddy current component. The authors measured a maximum eddy current loss of 19.6% for delamination defects in CFRP. Noise was reduced. Lift-off distance reduced the capability to detect delamination.

Meng et al. (2021) used ECT for investigating self-sensing capacities of cement paste. Steel and carbon fibers were used as fillers in the cement paste. CF fraction was kept constant close to the electrical percolation thresholds of the filler materials. Multiple influencing factors on the electrical resistance, such as voids, cracks, debonded fiber length, and fiber fraction, were reported.

3.2.1.7 Thermogravimetric analysis (TGA)

Destructive matrix removal allows for a precise measurement of fiber mass fraction (FMF) in FRPs. Matrix dissolution in either a hot liquid medium or in a furnace for combustion leaves only fibers behind. The FMF ξ is calculated based on the weight measurement of the

total specimen mass m and the remaining fiber mass m_F after matrix removal using a high precision scale. (ASTM International D30.04 Committee 2015a)

$$\xi = \frac{m_F}{m} \quad 3.1$$

The fiber volume fraction (FVF) ϕ is calculated based on the respective densities of fiber ρ_F and matrix ρ_M according to

$$\phi = \frac{\frac{m_F}{\rho_F}}{\frac{m_F}{\rho_F} + \frac{m_M}{\rho_M}}, \quad 3.2$$

including the relation of fiber mass m_F and matrix mass m_M with $m = m_F + m_M$.

Generally, TGA is recommended for GFRPs in national and international standards (ASTM International E37.01 Committee 2020; Deutsches Institut für Normung e.V. 2020). The standard procedure for determining FMF in CFRP is sulfuric acid digestion. However, Bücheler & Kaiser et al. (2016) expanded the field of application for TGA towards CFRPs. Nonetheless, TGA is not applicable for an in-line measurement due to its destructive character, but is suited for reference measurements.

3.2.2 Assessment of manufacturing deviations in FRPs

The research work that the authors in this subsection have in common are they all assessed manufacturing deviations in FRPs, either in experiments or simulations.

Colombo & Vergani (2014) experimentally investigated the effect of delaminations in non-crimp GF tensile specimen on static and dynamic properties. Static properties were not affected, but fatigue life was reduced by almost 40%. The presence of delaminations changed the failure mode in fatigue testing. Debonding was observed using a thermographic camera.

Talreja (2015) proposed to assess voids in FE simulations on the microstructural level rather than in homogenized volumes. The author further highlighted that voids at a crack tip of a delamination impede the critical energy release rate.

Dong (2016) created representative volume elements of carbon fiber reinforced epoxy composites for a FE analysis. The author analytically and numerically investigated the influence of different void fractions on effective composite properties. Especially matrix-dominated properties were reduced by higher void fractions.

Stamopoulos et al. (2016) produced unidirectional CFRP laminates with four different void fractions in an autoclave process. Reference samples were extracted from the four different plates and the void fraction was analyzed using CT and the commercial software VGStudio Max. Further specimens were extracted for four different mechanical tests. Especially the

matrix-dominated material properties were reduced by higher void contents. Strength values were stronger reduced compared to elastic properties.

Tserpes et al. (2016) measured porosity in unidirectional CFRP laminate samples in CT scans using VGStudio Max and integrated the void fraction into FE simulations. Porosity characteristics extracted from CT were validated by optical microscopy measurements. The detected voids were categorized into different sizes and analytically integrated into representative volume elements of the epoxy resin in a two-step procedure. A series of tests was conducted to mechanically characterize the epoxy resin itself. The rule of mixtures and the Hashin damage criteria were applied to predict the material behavior of porous CFRP on component level. A good agreement between tensile tests and simulations was achieved. A greater influence of void fraction on strength compared to stiffness was confirmed.

Fengler & Kärger et al. (2018) determined optimal Co-SMC patch positions for product design. Optimal positions minimized both the global strain energy of the component and the patch length in CoDiCo-SMC. A linear elastic material behavior was assumed. In a subsequent work, Fengler & Schäferling et al. (2019) identified robust patch positions. Experimentally determined manufacturing deviations were integrated into the evaluation. Robust patch positions were defined by two different robustness measures. Both measures indicated a design space in which acceptable manufacturing deviations did not jeopardize the product function in terms of stiffness.

Schäferling et al. (2019) experimentally determined the individual influence of different defects in CoDiCo-SMC tensile specimens. Resin accumulations (lower FMF), folds, fiber misorientations and delaminations were deliberately integrated into the Co-SMC of different specimens. The tensile strength was stronger impaired than the Young's modulus. CoDiCo-SMC specimens with delaminations showed a slight reduction in tensile strength.

Görthofer et al. (2019) proposed a virtual process chain for DiCo-SMC. Local fiber orientations from compression molding simulations were mapped to structural simulations. Simulated fiber orientation distributions were in good agreement with CT measurements. Structural simulation results were experimentally validated. Influences of varying fiber orientation distribution were investigated, but a constant fiber volume fraction of 25 vol.-% was assumed in the simulations. Integrating simulated and measured fiber orientation distributions increased the simulation accuracy with respect to the experiments.

Franz et al. (2019b) investigated potential production variations in 500 FE simulations with random laminate orientations. The quasi-isotropic CFRP layup was additionally reinforced by two unidirectional CF patches. A tensile load case and two bending load cases were considered. Outer layers and layers with a nominal orientation of 45° were more sensitive

regarding deviating orientations. The authors recommended to individually tolerance ply stack-ups based on the load case. Franz et al. (2019a) simultaneously considered the FVF and the ply thickness besides the patch angle. The statistical variations of the three patch characteristics were investigated for 26 patches on a topology optimized geometry in 2000 FE simulations. Angle variations dominated the behavior when variations in thickness and FVF were coupled. Without coupling, all three variations were almost equally important. Franz et al. (2021) incorporated deviating CFRP ply-orientation angles and angles of CF reinforcement patches into a tolerance optimization approach. Costs, modeled by an exponential penalty function, were minimized while structural integrity was guaranteed using a constraint function.

Trauth et al. (2021) investigated DiCo-SMC tensile specimens, water jet cut from charge and flow regions parallel and perpendicular to the flow of different sheets. Representative FVF were obtained by multiple TGA measurements at different regions of the sheets. The tensile specimens were further CT-scanned to determine fiber orientation tensors. A mean field method, including the results from TGA and CT, approximated the effective elastic behavior well. Varying fiber fractions showed significant influence on mechanical properties in experiments and simulations.

Manufacturing deviations in FRPs are a well-known challenge, which is given attention especially during the design process (Mesogitis et al. 2014). The focus in the investigation of manufacturing deviations has so far been primarily on unidirectional lamina. Although measurement technologies have been used in some papers, no work has yet integrated individual in-line measurement results into a FE simulation. In both experimental and simulative investigations of manufacturing deviations in CoDiCo-SMC, no combinations of manufacturing deviations have been considered so far.

3.2.3 Applications of function-oriented measurements not related to FRPs

The authors covered in this subsection used mathematical-physical models in various fields of application to convert acquired measurement results into functional capabilities.

Weckenmann & Hartmann (2013) coined the term function-oriented measurement (cf. Section 2.1.2). The authors demonstrated this approach by modeling the ink transfer of a microstructured anilox roll as a use case. A physical model equation was set up taking into account the pick-up volume and the transfer ratio of the ink. Anilox rolls with varying surface parameters were manufactured while manufacturing imperfections were quantified using optical measurements. Subsequently, resulting form deviations were considered in time-consuming simulations. Higher measurement data resolution further increased the computing time. The individually simulated function showed a good correlation to conducted experiments.

Häfner & Lanza (2017) presented an approach for individual function prediction for manufactured micro gears. In this approach, high-precision off-line 3D measurements of micro gears were processed by FE simulations to determine actual tooth root stresses and correlated with experimental data from life cycle experiments. The model uncertainty was quantified according to the principles of GUM (cf. Section 2.1.4.1). In a subsequent work, Häfner & Biehler et al. (2018) replaced the computationally expensive FE models with an artificial neural network (ANN). A higher model uncertainty was accepted for a faster function prediction using the ANN.

Wagner et al. (2020) and Wagner (2020) developed function-oriented production control strategies for high precision products. An exemplary application was carried out in the production of injections systems. State-space models were used as a digital twin to predict the realized product function (volume of injected fuel) based on individual in-line measured quality characteristics. The adaptation of the model parameters to experimental results reduced the model uncertainty. Sampled input data from statistical distributions was propagated through the state-space model to gain a large amount of virtual data sets for surrogate model training. The surrogate model (Elastic Net method) with minimal overall uncertainty was determined. In a further step, this surrogate model was integrated into a discrete-event material flow simulation, enabling a virtual end-of-line test to ensure the optimum pairing of components with respect to the function.

The use of functional models to provide more meaningful measurement results is emerging as a trend in different industries. Real-time requirements are considered as a main challenge. Only one work demonstrated in-line measurements and data processing according to the production cycle (Wagner et al. 2020).

3.2.4 Surrogate modeling of FE simulations

In general, surrogate models replace computationally expensive simulations with functions that are cheaper to evaluate, making them significantly faster. Most surrogate models converge to their original simulation with increased training effort. However, an uncertainty is to be expected. A model function can be approximated in different ways. Response surfaces denote mathematical functions, often polynomials, fitted to the response of the model function. Artificial neural networks (ANNs) also belong to this category. Emulators are probability distributed collections of functions, whereas the model function is assumed to be a realization of these functions. The averaged collection of functions also defines a response surface. Additionally a measure for the uncertainty is given by the variance between the individual functions. Gaussian processes (Kriging models) are most frequently used. A visualization of response surfaces and emulators is given in Figure 3.1. Response surfaces and emulators

are data-driven, meaning they are only constructed from input and output values. As a third method, the computational effort can further be reduced by deliberately neglecting physical aspects in order to enhance the computation speed. (Sinsbeck 2017) Such low fidelity models are not further considered within this work.

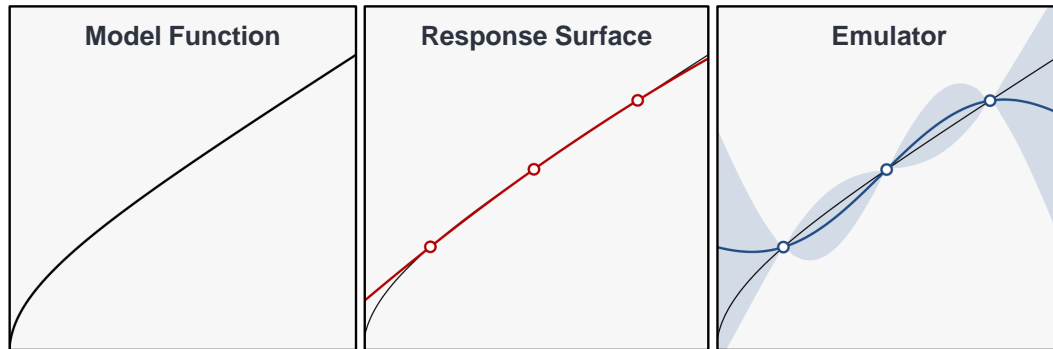


Figure 3.1: Comparison of response surfaces and emulators; according to Sinsbeck (2017)

The authors in this subsection showed successful applications of surrogate models in the context of FE simulations. Most of the presented contributions apply surrogate modeling to the field of lightweight design using FRPs.

Dey et al. (2017) presented an extensive review on existing surrogate model techniques and suitable sampling methods. For performance evaluation, they examined the natural frequencies of a laminate composite cantilever plate. The authors compared the surrogate modeling techniques in terms of the number of training data required and resulting model uncertainties for uncertain input variables (material parameters and ply-orientation angle). A polynomial regression showed high performances for this use case. According to the authors, ANN are especially suited for higher dimensional inputs, but a lot of training data is needed. Nevertheless, the authors emphasized the inherent problem-dependency of surrogate modeling, so that no model can be said to be universally superior.

Häfner & Biehler et al. (2018) developed a surrogate model which related shape deviations of micro gears, obtained via time-consuming off-line measurements at a coordinate measuring machine (CMM), to tooth root stresses. Nine gear properties served as input values into the ANN, while one scalar stress value was returned. The authors further evaluated the measurement uncertainty of the ANN. Different surrogate model realizations were generated by partially shuffling training and validation sets. Furthermore, different combinations of input values, according to their probability distribution, were fed into the various surrogate models. This procedure led to statistically distributed tooth root stresses. The standard uncertainty of the surrogate model was estimated by assuming a normal distribution of the stress values.

Pfrommer et al. (2018) optimized the stiffness of 50 grippers in a composite draping process. A deep ANN, initially trained by 584 FE simulations, predicted the shear angle of all composite elements. Optima in the surrogate model were found using differential evolution. Identified candidates were evaluated using FE simulations and added to the training data to iteratively improve model accuracy. The prediction of all shear angles yielded better results than predicting a scalar maximum. However, training costs were significantly increased. The authors noted that systematic generation of training data should be considered in future models.

Hürkamp et al. (2019) investigated the influence of process parameter variations on component properties using surrogate models. The object of investigation was a multi-material lightweight component, produced in consecutive deep drawing and injection molding processes. The FE simulated effects of varying blank holder forces and different injection times were mapped using proper orthogonal decomposition (POD), similar to a principal component analysis. The aim of the procedure was an in-line prediction of the relevant resulting component properties and providing them for subsequent structural simulations.

Fengler & Schäferling et al. (2019) substituted costly FE simulations by a Kriging model to identify optimal Co-SMC patch positions. Numerous evaluations of the objective function were necessary to calculate the robustness measures. The design parameters of the patch served as input variables. The output value was the objective function composed of component stiffness and patch length. Only design parameters which led to results close to the Pareto front were used as training data of the Kriging models.

Lee et al. (2020) investigated the influence of corroded steel wires on the tensile strength of entire strands. A strand consisted of a core wire and six twisted helical wires. Different types of corrosion were geometrically represented in FE models at the wire level. These results were used to train a Kriging model. The influence on the entire strand was modeled analytically, whereby the stress values of the individual wires were obtained from the surrogate model. The statistical distribution of the input variables was represented by a Monte Carlo simulation (MCS) so that confidence levels for the predicted tensile strength could be provided. The authors identified the tensile strength and strain of steel as the most critical input variables using a sensitivity analysis.

Franz et al. (2021) proposed a design approach for optimized tolerances of CFRP ply-orientation angles and local CF reinforcement patches based on a Kriging model. Training sets of 1000 to 1200 FE simulation results were generated for surrogate model training. The usage of LHS guaranteed an efficient coverage of the entire design space. A genetic algorithm was used to identify optimal tolerances with respect to manufacturing costs. The authors proposed to use the cost-optimal tolerances for quality assurance.

The presented studies show that surrogate models have so far mainly been used in the design phase. Yet, there is a trend towards further use of design phase results during production for quality assurance (Franz et al. 2021). Measurement results in the context of quality assurance were fed into the surrogate model in only two of the presented works (Häfner & Biehler et al. 2018; Lee et al. 2020). However, no in-line measurements were used.

3.3 Research deficit

Using the requirements presented in Section 3.1, Table 3.1 categorizes the research works just presented. From this overview, it is clear that a large number of different measurement technologies as well as assessment approaches of detected manufacturing deviations exist. The research deficit can be summarized as follows:

The production of FRPs, and accordingly also of hybrid SMC, is subject to a wide range of manufacturing deviations. In particular, the use of multi-sensor systems has emerged as the means of choice in recent years to exhaustively evaluate component quality. However, in the presented research, data fusion is only performed on sensor level with a limited number of measurement technologies. A detailed consideration of the measurement uncertainty is conducted in the fewest number of applications. Especially for the still very young THz measurement technology, which offers great potential for in-line measurement of FRPs, detailed uncertainty considerations are missing.

The well-known influence of manufacturing deviations has so far only been taken into account in component design. In a few papers, representatively averaged off-line measurement results were used in simulations for functional predictions. However, component-specific quality assurance cannot be achieved using this methodology if off-line measurements or functional evaluations take longer than the respective cycle time of a product.

The successful integration of modeled relationships between geometrical features and realized function into function-oriented quality control loops of a large-scale injection system production highlights the enormous potential of a function-oriented quality approach (Wagner 2020). However, a large-scale injection system production contrasts with the production of FRPs, which is still perceived as immature and costly. A function-oriented approach to quality assurance based on in-line measured quality characteristics using surrogate models trained on simulation results does not exist in the field of FRP production. Integrated measurement data was so far off-line obtained and only few approaches used surrogate models.

Overall, no approach was so far presented for FRPs that integrates multiple in-line measurements into surrogate models for a function-oriented assessment of the component function, adherent to the cycle time.

Literature	MT			FA					MU		
	Application to FRP (●) / SMC (●)	Multi defect characterization	In-line integration	Experimental investigation	Simulation	Integrated measurement data	Interacting manufacturing deviations	Real-time applicability	Measurement technology	Simulation	Surrogate model
Legend: ● – considered ◐ – partially ○ – not											
Assessment of manufacturing deviations in FRPs											
Colombo '14	○	○	○	●	○	○	○	○	○	○	○
Talreja '15	○	○	○	○	●	○	●	○	○	○	○
Dong '16	○	○	○	○	●	○	○	○	○	○	○
Stamopoulos '16	◐	○	○	●	○	○	○	○	○	○	○
Tserpes '16	◐	○	○	●	●	◐	○	○	○	○	○
Fengler '18, '19	●	○	●	○	●	◐	○	○	○	○	○
Görthofer '19	●	○	○	●	●	◐	○	○	○	○	○
Franz '19, '19, '21'	○	○	○	○	●	○	●	◐	○	○	○
Trauth '21	●	◐	○	●	●	◐	○	○	○	○	○
Applications of function-oriented measurements not related to FRPs											
Weckenmann '13, '15	○	○	○	●	●	●	●	○	◐	○	○
Häfner '17, '17, '18	○	○	○	●	●	●	●	◐	●	●	●
Wagner '20, '20	○	●	●	●	●	●	●	●	●	●	●
Surrogate modeling of FE simulations											
Dey '18	○	○	○	○	●	○	○	●	○	◐	◐
Pfrommer '18	○	○	○	○	●	○	○	●	○	○	○
Hürkamp '18	○	○	○	○	●	○	◐	●	○	○	◐
Lee '20	○	○	○	●	●	●	○	●	○	◐	◐

4 Approach

Based on the identified research deficits (cf. Section 3.3) and the developed research questions (cf. Section 1.3), this work aims at extending the approaches of quality assurance for FRPs by the further processing of obtained measurement data in functional models. CoDiCoSMC, as a hybrid material class, serves as an exemplary material. The use of a functional model shall provide a remedy for tolerance limits determined under incomplete knowledge from the design engineer and resulting harsh rejection criteria. Thus, the production of functionally adequate fiber composite components should be facilitated more cost-effectively, by reducing scrap.

Figure 4.1 illustrates the fundamental concept of an individual, function-oriented component assessment (component-specific quality assurance). The functional requirements determine the component design and its dimensioning in product development. However, ideal production processes cannot be expected, so manufacturing deviations are to be accounted for (cf. Table 2.3). In-line measurements facilitate the characterization of the individual component state, according to the concepts described in Section 1.2. The integration of these individual measurement results into FE simulations, which originate from the product design process, shall enable an individual evaluation based on the realized function. However, FE simulations do not meet the requirements for an assessment within the cycle time in production due to high computational efforts. Data-driven surrogate models, trained on vast results from parameterized FE models, should be used to enable function evaluations based on measurement inputs in real time (production cycle time).

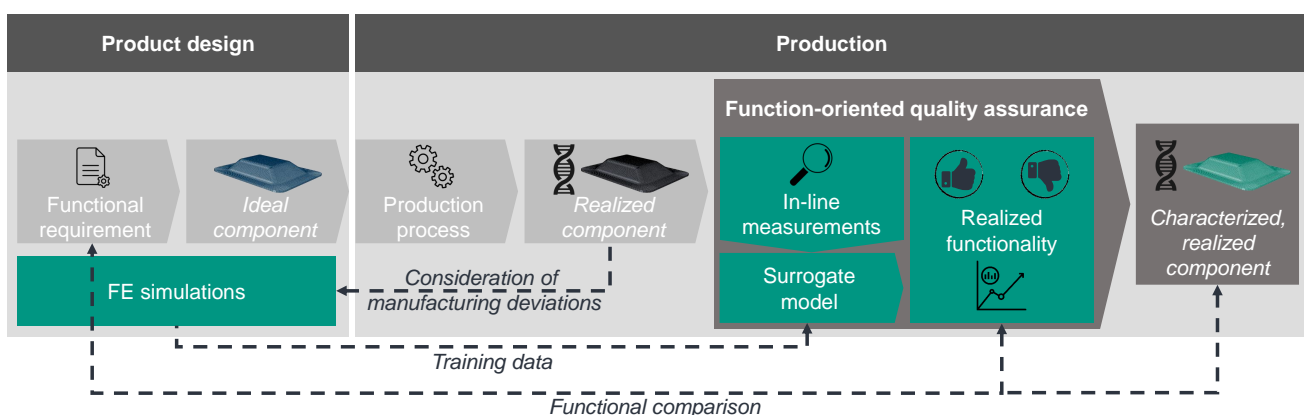


Figure 4.1: Fundamental concept for the function-oriented quality assurance of FRP components

The solution approach is divided into two chapters (cf. Figure 4.2). First, suitable measurement technologies for quantifying relevant manufacturing deviations of the exemplary material class

(CoDiCo-SMC) are selected, qualified (if necessary), and assessed. Previous works indicated that multisensory systems are required to quantify the spectrum of possible manufacturing deviations (cf. Table 3.1). In a second step, the additional information obtained (in-line measurements) are processed in a functional model to obtain information about the functional capability of a component. The in-line measurements serve as an input for the functional model. Thus, partial quality data (in-line measurements) is enriched towards a functional statement. This process is referred to as *in-line propagation of measurements*. Here, the first task is to develop a suitable off-line modeling (FE model) of the combined influences of manufacturing deviations (cf. Section 6.1). Possibilities for the analytical consideration of manufacturing deviations as well as the representation of deviations in the model structure are addressed. An uncertainty evaluation also provides information on the adequacy at this point. Data-driven surrogate models are proposed (cf. Section 6.2) to empower the off-line model for an in-line application. Benefits of different models are considered and the surrogate models are then evaluated for their capability, through the quantification of measurement uncertainty.

The methodology is applied using two validation specimens in Chapter 7. Measurements of multiple specimens are acquired and evaluated in a function-oriented manner to explain differences in stiffness and strength. Tensile specimens represent components under uniaxial loading, whereas a more complex stress state is realized using a modified specimen in analogy to a three-point flexural test.

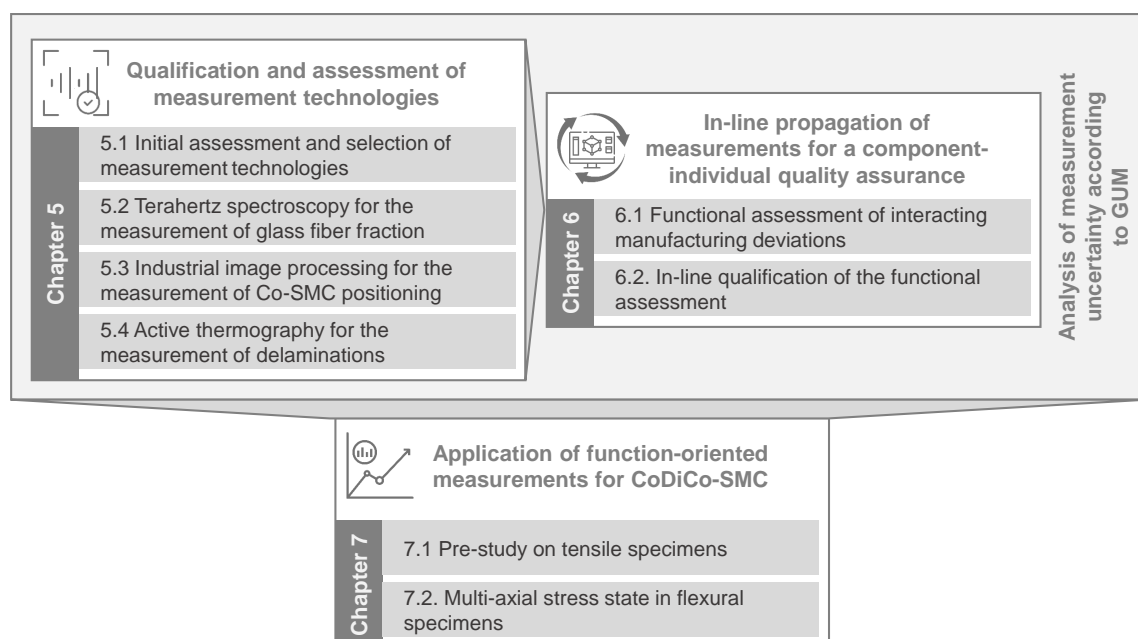


Figure 4.2: Methodological solution approach for a function-oriented quality assurance of hybrid sheet molding compounds

5 Qualification and assessment of measurement technologies

In this chapter, three in-line measurement technologies are identified for CoDiCo-SMC and examined in detail. THz spectroscopy is enabled to measure local differences of fiber mass fractions (FMF) by a developed measurement model. An industrial camera is proposed to quantify Co-SMC position and orientation on a CoDiCo-SMC specimen. Using a thermographic camera, the position and size of a delamination can be measured. An analysis of the measurement uncertainty according to GUM is performed for all three measurement technologies.

5.1 Initial assessment and selection of measurement technologies for CoDiCo-SMC

The previously presented general measurement technologies for FRPs (cf. Section 3.2.1) are evaluated regarding their suitability for the detection and measurement of observed manufacturing deviations in CoDiCo-SMC (cf. Table 2.3). Of several measurement technologies under consideration for a certain manufacturing deviation, the preferred technology further considered within the scope of this thesis is highlighted in gray (cf. Table 5.1). *Non-destructive testing* is a prerequisite. The in-line potential can be estimated from the *measurement time* and *resolution*. A thorough examination follows in the subsequent sections of this chapter.

Voids could not reliably and repeatably be integrated into DiCo-SMC for reference measurements. Although random voids were induced by applying small amounts (< 100 mg) of the propellant ammonium bicarbonate (NH_4HCO_3) between two DiCo-SMC layers before the molding process, substantial surface damages and discolorations of the specimen occurred as well. IRT measurements were strongly impeded by these side effects. Thus, the measurement of void fraction was discarded within the scope of this thesis.

Fiber fraction in DiCo-SMC is traditionally measured using computed tomography (CT). Approaches using ultrasonic testing (UT) exist as well. Both technologies are characterized by high measurement times. **THz spectroscopy** is a promising measurement technology that offers reduced measurement times. Its potential for quality assurance of DiCo-SMC has not yet been exhausted and will therefore be considered more intensively in the course of this work to quantify fiber fraction in DiCo-SMC. High resolution, but destructive thermogravimetric analysis (TGA) serves for reference measurements.

Fiber orientation in DiCo-SMC is usually measured using CT, but high measurement times are required. THz spectroscopy provides an alternative. However, additional material handling is

necessary for performing measurements in different orientations of the object under investigation. Ideally, these handling operations need to be automated. Reliably reproducing different fiber orientation distributions (FODs) poses another challenge. Therefore, the measurement of fiber orientation was excluded of the scope of this work.

Deviations in carbon fiber (CF) fraction of Co-SMC should be physically noticeable in the electrical resistance. However, several potential micro-defects influence the electrical resistance as well. Thus, it is so far not possible to distinguish between the different defects due to a lack of resolution. The development of a suitable measurement methodology by means of eddy current testing (ECT) is not pursued in this work.

Misalignment of Co-SMC have already been measured using imaging technologies in the visible and infrared spectrum. Since the relevant measurement information of the Co-SMC patch position could also be obtained without a dome light, the simpler measurement setup using an **industrial camera** was chosen.

Delaminations were measured in high resolution using UT and THz spectroscopy. Both technologies offer shorter measurement times than CT. However, the measurement times for large areas are considered too high based on the inherent measurement principle (local measurement). **Infrared thermography** (IRT) as an areal measurement technology was chosen to be further considered. Additionally, preliminary works in the field of CoDiCo-SMC exist (Fengler & Schäferling et al. 2019; Schäferling 2019).

Table 5.1: Comparison of measurement technologies for quantifying manufacturing deviations in CoDiCo-SMC

Measurement technology	References	Requirements for in-line integration		
		non-destructive	short measuring time	high resolution
Legend: ● – fulfilled ◐ – partially ○ – not				
Voids				
CT	Tserpes et al. (2016)	●	○	●
IRT	Manta et al. (2019)	●	●	◐
UT	Karabutov & Podymova (2014)	●	○	◐

Measurement technology	References	Requirements for in-line integration		
		non-destructive	short measuring time	high resolution
Legend:				
● – fulfilled				
◐ – partially				
○ – not				
Fiber fraction in DiCo-SMC				
CT	Bertram et al. (2016) Pinter (2018)	●	○	◐
TGA	ASTM International E37.01 Committee (2020) ASTM International D30.04 Committee (2015a)	○	○	●
THz	Jördens & Scheller & Wichmann et al. (2009) Krumbholz et al. (2009)	●	◐	●
UT	Grimberg et al. (2013) Webersen et al. (2016)	●	○	◐
Fiber orientation in DiCo-SMC				
CT	Pinter (2018)	●	○	●
THz	Jördens & Scheller & Wietzke et al. (2010)	●	◐	◐
Fiber fraction in Co-SMC				
CT	Schöttl & Dörr et al. (2020)	●	○	◐
ECT	Berger (2019)	●	●	○
TGA	Bücheler & Kaiser et al. (2016)	○	○	●
Misalignment of Co-SMC (patch position)				
CT	Schäferling (2019)	●	○	●
Industrial camera	Bücheler & Henning (2016) Bretz & Häfner et al. (2019)	●	●	●
Dome light camera	Kosse et al. (2014)	●	●	●
IRT	Fengler & Schäferling et al. (2019)	●	●	◐
IRT (3D)	Schäferling (2019)	●	●	◐
Delamination				
CT	Léonard et al. (2017)	●	○	◐
IRT	Amenabar et al. (2011) Schäferling (2019)	●	●	◐
THz	Dong et al. (2015) Wang & Zhong et al. (2020)	●	◐	●
UT	Park et al. (2014) Zhang et al. (2018)	●	◐	●

Overall, three measurement technologies are used in this work, each for a different task. An overview of the different measurement technologies used in this work and the respective measurands are given in Figure 5.1.



Figure 5.1: Proposed measurement technologies and respective measurands for CoDiCo-SMC

The comparatively young THz technology is enabled to be deployed as an in-line measurement technology for the measurement of fiber fractions in DiCo-SMC by means of a regression model (cf. Section 5.2). In addition, methods for reducing the measurement time are derived and examined with respect to their applicability. The measurement uncertainty is considered in accordance to JCGM100 (2008) both for the measured fiber mass fraction (FMF) and the resulting, homogenized component stiffness in the sense of a component function (cf. Section 2.1.1). The basic requirements for the use of established areal measurement technologies (industrial and thermographic camera) are already fulfilled according to the state of the art. Measurement uncertainty analyses according to JCGM100 (2008) are also carried out to evaluate the deployment potential related to CoDiCo-SMC (cf. Section 5.3 and 5.4).

5.2 Terahertz spectroscopy for the measurement of glass fiber fraction

Since local variations in FMF can occur in a component due to random variations in the production process, these should be quantified non-destructively. Thus, the aim of the THz measurements is the non-destructive measurement of the FMF. Both the presented state of the art (cf. Section 3.2.1.2) and an own preliminary work (Bretz & Häfner et al. 2021) showed promising results for the application of THz spectroscopy as a non-destructive measurement technology for the local FMF in DiCo-SMC. In a preliminary work, the refractive index in the THz spectrum has already been determined as a well-suited independent variable in a regression model to predict local FMF (Bretz & Häfner et al. 2021).

In this section, this approach is further elaborated. This implies first of all an extended number of samples with different nominal thicknesses compared to the 4 mm thick samples used so far. A detailed measurement uncertainty analysis of the established measurement model is used to evaluate the suitability of the measurement technology. This evaluation

is also carried out at the functional level (material stiffness). The suitability for an in-line use is demonstrated by investigating different measurement diameters and approaches for improving the measurement speed.

5.2.1 Apparatus and methods

The following subsections describe the general experimental setup, the properties of the reference specimen, and the data processing.

5.2.1.1 Terahertz system and measurement setup

The basic principle for generating a pulsed THz radiation is to excite a very fast change in electric current in a photoconductive material using a femtosecond laser beam (Rieh 2021). The TERA K15 (Menlo Systems GmbH), a fiber-coupled turn-key THz time-domain spectrometer, was used to characterize the specimen within the THz spectrum. It operates in the far infrared spectral range up to 4.5 THz with a spectral resolution of less than 1.2 GHz. The standard spot size of the THz beam at the specimen surface was 10 mm, approximately 740 times larger than a fiber diameter. Only local measurements can be recorded in the beam path. These local measurement regions have the size of the beam cross section. Initially, 100 time domain signals were recorded for the time period of 400 ps and averaged by the commercial software ScanControl (Menlo Systems GmbH). Thus, multiple Fabry-Pérot echoes were captured. The initial overall measuring time for a measurement region was about 50 s, as recommended in the manual¹. The linear guidance of the designed specimen holder ensured the precise positioning of the measurement region in the optical beam path. The test setup in transmission mode is shown in Figure 5.2. A slightly converging beam was set between the optical lenses L1 and L2. Thus, different measurement diameters could be achieved by different distances of the specimen holder from the lens L2. The optical beam path is highlighted by the white dashed line in Figure 5.2b.

5.2.1.2 Reference specimens

Only a destructive measurement, such as TGA, allows the separation of fibers and matrix for the determination of the FMF with negligible uncertainty compared to other measurement technologies. Therefore, reference specimens are first measured non-destructively using THz spectroscopy and then destructively using TGA. This allows to relate the properties in the THz spectrum to the destructively determined fiber mass fractions. Thus, the non-destructive THz measurement model is established.

¹Menlo Systems GmbH (2016), *TERA K15/TERA SYNC Time-Domain THz Spectrometer - User Manual*.

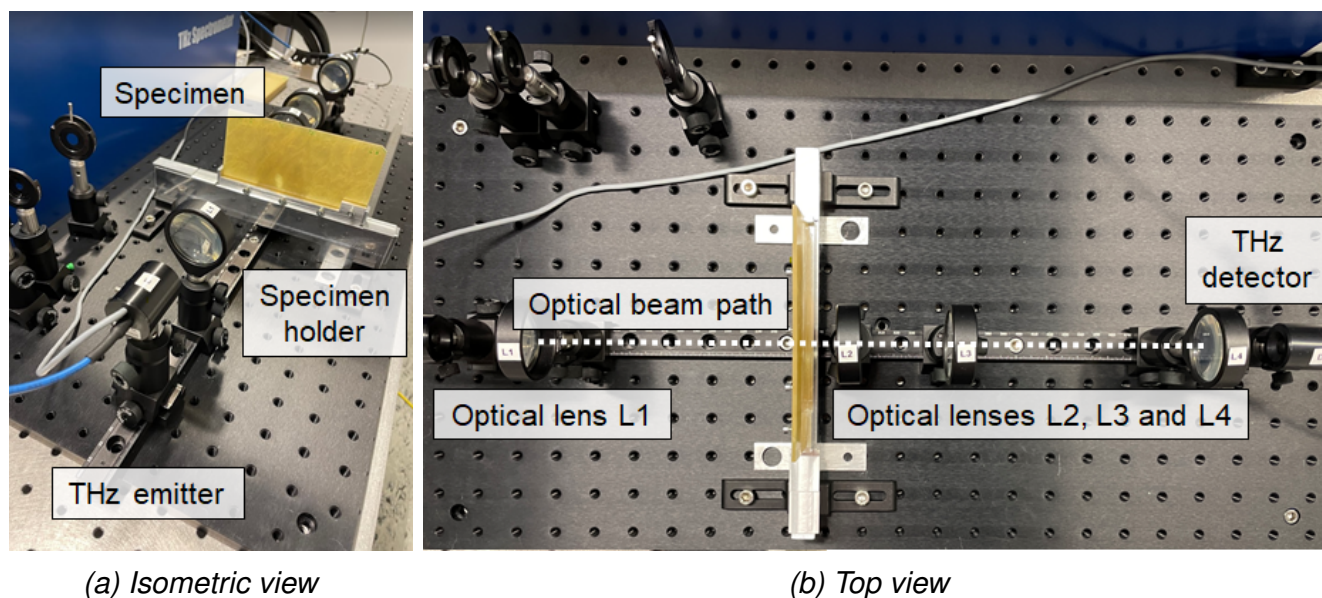


Figure 5.2: THz measurement setup including reference specimen and THz system

Two different DiCo-SMC prepreg materials with higher and lower nominal FMF (35 and 45 wt.-%) were provided by Fraunhofer ICT in addition to the standard nominal FMF of 41 wt.-% (cf. Table 2.1). Two or three layers of prepreg were stacked to form the initial charge. Different prepreg materials were combined to achieve as different FMFs as possible. The dimension of the cavity were 458 mm \times 458 mm. A full mold coverage was chosen to inhibit any material flow and to maintain the mostly planar isotropic fiber orientation from the prepreg production process. The mold was heated up to 145 °C and closed with a hydraulic press by Lauffer with a maximum press force of 500 kN. The pressure was maintained for 90 s before demolding.

After molding, the plates were cut into a total of 14 different reference specimens according to the external dimensions given in Figure 5.3. The chamfered edge defined the distinct orientation of the reference specimen. Six THz measurement regions were defined in every reference specimen. The standard diameter of the measurements regions was set to 10 mm for twelve reference specimens. Additionally, the six measurement regions of two reference specimens were THz measured with a beam diameter of 14 and 20 mm, respectively. The thickness of every measurement region was measured using a micrometer screw gauge Mitutoyo MDC-25SX with a maximum permissible error (MPE) of $\pm 2 \mu\text{m}$ and a digital numerical interval of 1 μm . THz measurements without any specimen (air measurements) were performed between the measurement of each specimen to obtain a current reference value (cf. Equation 5.1) and to compensate for a potential drift of the signal over time.

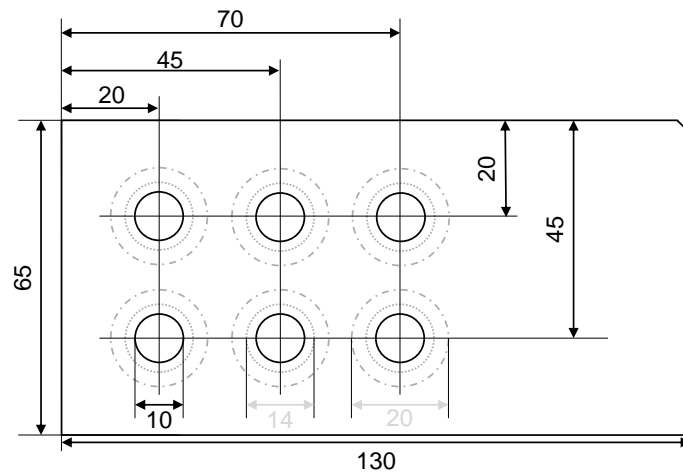


Figure 5.3: Technical drawing of DiCo-SMC reference specimen, including the circular THz measurement regions

After performing the THz measurements, the measurement regions were water jet cut for destructive determination of the FMF using TGA. The resin was burned at a temperature of 750 °C for a period of six hours.

Additionally to the 14 reference specimens within this work, the already existing optical parameters and referenced FMF of 18 measurement regions with a nominal thickness of 4 mm from a preliminary investigation of the author were further used (Bretz & Häfner et al. 2021). The DiCo-SMC from this investigation was based on the same resin formulation and production process. However, industrially produced nominal prepreg FMFs were different (41, 45 and 50 wt.-%). Dry glass fibers were added between the four prepreg layers of 12 measurement regions to broaden the range of investigated FMF. All measurement results for the 102 reference specimens are given in Table A2.1 in Appendix A2.

5.2.1.3 Data processing

Exemplary time domain signals are given in Figure 5.4a. Optical material parameter extraction from the recorded time domain signals was conducted using the commercial THz signal processing software TeraLyzer (Menlo Systems GmbH). The determined thickness measurement uncertainty was directly taken into account for the calculation of the optical parameters and its respective uncertainties. According to Bretz & Häfner et al. (2021), especially the refractive index n showed high correlation with the FMF. The refractive index is generally defined by:

$$n(f) = 1 + \frac{\zeta \cdot c}{2\pi f d} \quad , \quad 5.1$$

with the phase shift ζ of the signal with respect to the air measurement, the speed of light c , the frequency f and the material thickness d . All calculations of the frequency-dependent refractive indices for the different measurement regions were performed with the respective mean thickness of the measurement region and the calculated thickness uncertainty. TeraLyzer results were imported into MATLAB[®] for further data analysis.

5.2.2 Regression model

A linear regression model between the mean refractive index and the FMF in DiCo-SMC was already presented (Bretz & Häfner et al. 2021). This model allows for the non-destructive measurement of local FMF in DiCo-SMC. Furthermore, possible dependencies of nominal thickness changes are to be considered, so that the following regression model is investigated in this section:

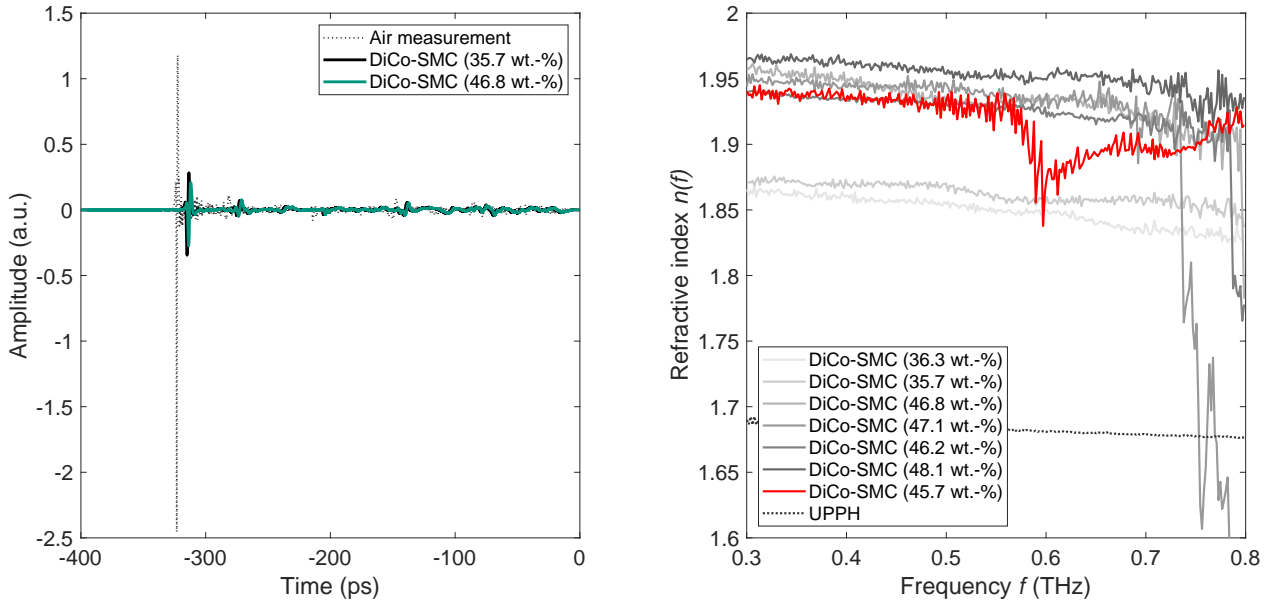
$$\hat{\xi}(\bar{n}, d) = \beta_0 + \beta_1 \cdot \bar{n} + \beta_2 \cdot d + \beta_{12} \cdot \bar{n} \cdot d \quad 5.2$$

The mean refractive index \bar{n} and the thickness d of a measurement region were chosen as independent variables for the estimate of the measurand $\hat{\xi}$ (local glass fiber mass fraction). An interaction term between \bar{n} and d was considered. The variables β_0 , β_1 , β_2 , and β_{12} describe the regression coefficients.

The mean refractive index \bar{n} was limited to the frequencies between 0.3 and 0.55 THz, because of the observed linear behavior up to 0.55 THz for all measurement regions. Exemplary calculated refractive indices over the frequency are given in Figure 5.4b for different DiCo-SMC and UPPH (0 wt.-% FMF).

Generally, a higher FMF leads to an optical denser medium, because glass is optically denser than UPPH. Initially, the calculated refractive index decreases approximately linearly for increasing frequencies. At higher frequencies, abrupt changes of the refractive index $n(f)$ are observed. This is due to THz receiver signals close to the noise level, which leads to failed calculations of $n(f)$. Generally, thicker and optical denser media absorb the electromagnetic waves stronger, which limits the spectrum for calculation of optical material properties.

Variables were normalized (z-score) for regression analysis. Measurement regions with the same nominal thickness showed strong multicollinearity in FMF and thickness (Bretz & Häfner et al. 2021). This effect is drastically reduced through the usage of multiple nominal thicknesses, as similar FMF exist for substantially different thicknesses (cf. Figure 5.5a). A significance level (p-value) of 1% was chosen for all regression analyses. The adjusted coefficient of determination (R_{adj}^2) was used to assess the model, penalizing a potential overfit of the model. Additionally, a k -fold cross-validation ($k = 10$) was performed to determine the *RMSE* on unseen data.



(a) THz time domain signal for different optical path lengths (b) Refractive index $n(f)$ over the frequency f in the THz spectrum

Figure 5.4: THz data of exemplary measurement regions

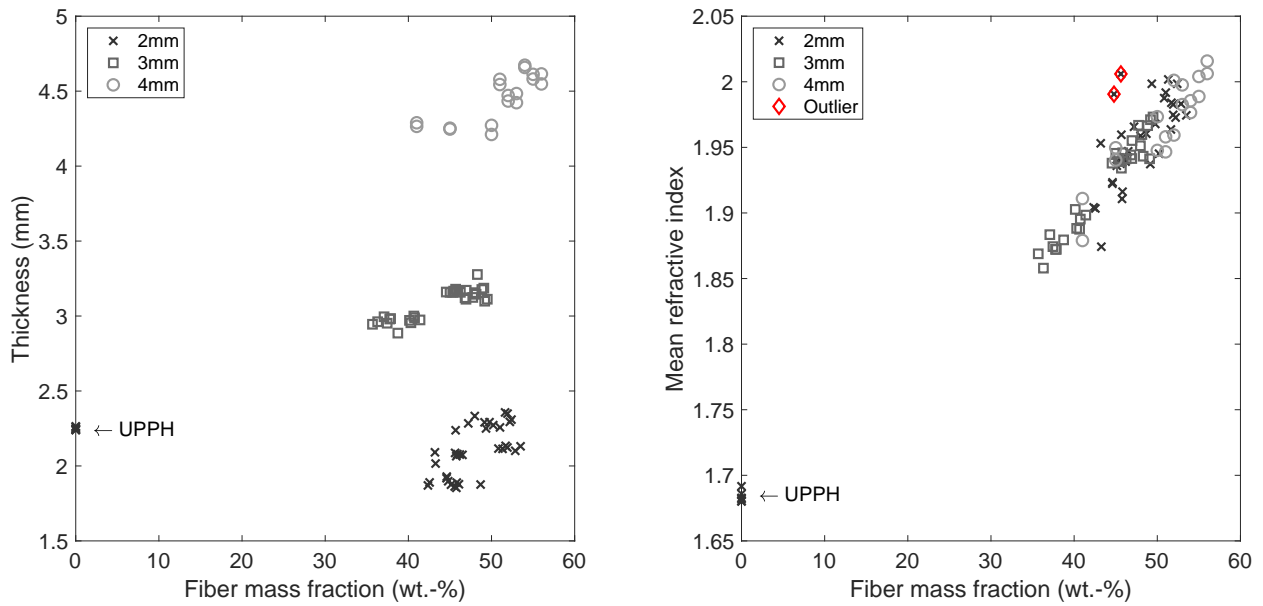
All 72 measurement regions investigated with a beam diameter of 10 mm as well as the 18 measurements regions from Bretz & Häfner et al. (2021) were initially included into the regression analysis. Thus, model (M1) was acquired (cf. Table 5.3). Basically, the measurement results of the refractive index of DiCo-SMC and UPPH confirm the linear character, as also illustrated in Figure 5.5b. However, Wietzke et al. (2007) demonstrated that extrapolations of optical parameters from multimaterials to pure materials can lead to questionable results.

For this reason, model (M2) was set up, which contains all data points previously described except for the six pure UPPH values. This measure simplifies model (M2) to only one independent variable (cf. Equation 5.3) and reduces the k -fold cross-validated $RMSE$ by more than 1 wt.-%. Model (M2) explicitly focuses on the FMFs of technical relevance, which likely occur due to process variations (cf. Section 5.2.4). Extrapolations are not viable for model (M2), which is exemplarily shown by the falsely predicted FMF $\hat{\xi}$ of 19.36 wt.-% for the mean measured refractive index of pure UPPH (cf. Appendix A3).

$$\hat{\xi}(\bar{n}) = \beta_0 + \beta_1 \cdot \bar{n} \quad 5.3$$

Two data points show substantially larger residuals (> 6 wt.-%) compared to all other data. These two outliers are highlighted in Figure 5.5b. The measured refractive index of those regions is larger than those of comparable measurement regions. This might indicate surface roughness, impurities due to the release agent or other foreign materials. Thus, these two

data points are excluded for a third regression analysis, leading to model (M3) with a cross-validated *RMSE* of 1.66 wt.-% (cf. Equation 5.3 and Table 5.3). This regression model and its residuals are illustrated in Figure 5.6. The restrictions regarding the limited value range for FMF apply analogously to (M2). Only (M3) will be considered in the further course of this work.



(a) Thickness over fiber mass fraction (b) Mean refractive index over fiber mass fraction

Figure 5.5: Distributions of fiber mass fraction, thickness and refractive index for different measurement regions; grouped according to nominal thickness; UPPH labeled

Table 5.3: Comparison of linear regression models

No.	DOFs	independent var.	Estimate	p-value	R^2_{adj}	k	<i>RMSE</i> (wt.-%)
(M1)	86	(intercept)	43.98	4.7e-102	0.95	10	3.14
		\bar{n}	10.97	1.7e-042			
		d	0.74	6.2e-002			
		$d \cdot \bar{n}$	-2.09	1.3e-004			
(M2)	82	(intercept)	46.57	2.8e-115	0.81	10	1.98
		\bar{n}	3.99	2.9e-031			
(M3)	80	(intercept)	46.74	1.0e-118	0.87	10	1.66
		\bar{n}	4.23	4.8-037			

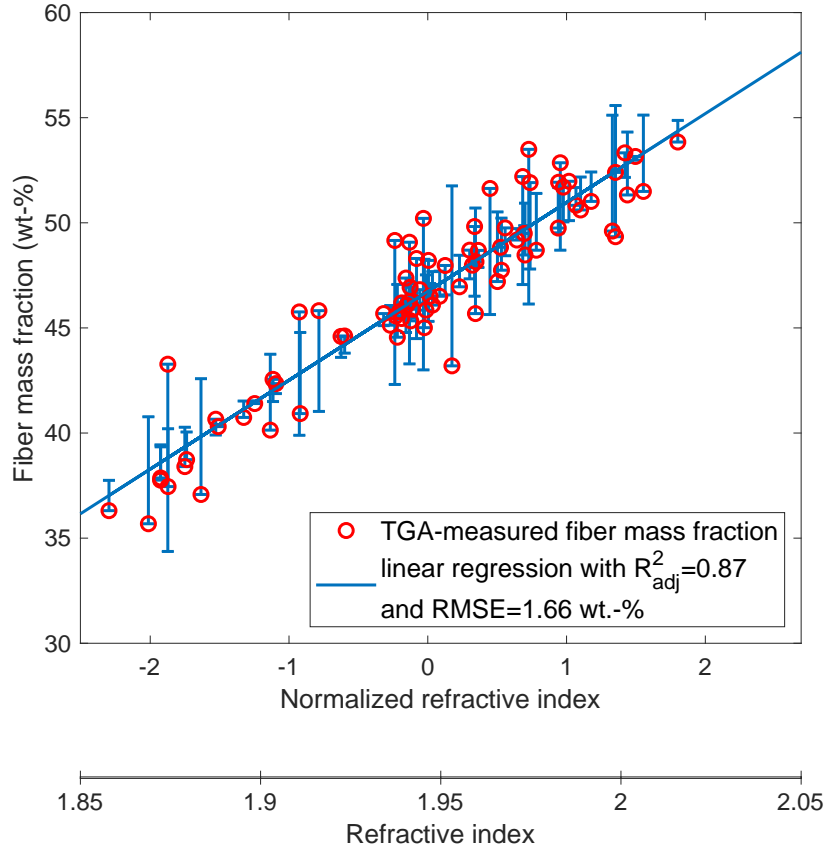


Figure 5.6: Linear regression of the fiber mass fraction based on the mean refractive index \bar{n} in the THz spectrum

5.2.3 THz measurement uncertainty

A linear regression model based on the averaged refractive index \bar{n} was established for non-destructively measuring the FMF (cf. Equation 5.3). According to Adunka (2000), empirical approximations are also subject to uncertainty, due to the estimation of the regression coefficients. Therefore, Equation 5.3 is considered as a function $\hat{\xi}(\bar{n}, \beta_0, \beta_1)$ for the uncertainty analysis. Thus, it follows for the combined uncertainty of fiber mass fraction $u_{\hat{\xi}}$, based on Equation 2.2:

$$u_{\hat{\xi}}^2(\bar{n}, \beta_0, \beta_1) = \left(\frac{\partial \hat{\xi}}{\partial \bar{n}} \right)^2 u_{\bar{n}}^2 + \left(\frac{\partial \hat{\xi}}{\partial \beta_0} \right)^2 u_{\beta_0}^2 + \left(\frac{\partial \hat{\xi}}{\partial \beta_1} \right)^2 u_{\beta_1}^2 + 2 \frac{\partial \hat{\xi}}{\partial \beta_0} \frac{\partial \hat{\xi}}{\partial \beta_1} u_{\beta_0, \beta_1} \quad , \quad 5.4$$

whereby $u_{\bar{n}}$ describes the mean based on all uncertainties of the refractive index $u_{n(f)}$ for all frequencies f between 0.3 and 0.55 THz. The uncertainties $u_{\beta_0}^2$, $u_{\beta_1}^2$, and u_{β_0, β_1} are obtained from the covariance matrix of coefficient estimates (cf. Equation 5.5). The results given capture the uncertainty of regression coefficients based on the linear regression performed in

Section 5.2.2 for regression model (M3). Further covariances are not considered.

$$\text{Cov}(\beta_0, \beta_1) = \begin{pmatrix} u_{\beta_0}^2 & u_{\beta_0, \beta_1} \\ u_{\beta_0, \beta_1} & u_{\beta_1}^2 \end{pmatrix} = \begin{pmatrix} 0.0326 & 0.0011 \\ 0.0011 & 0.0337 \end{pmatrix} \quad 5.5$$

The calculation of the frequency-dependent refractive index $n(f)$ is subject to a frequency-dependent uncertainty $u_{n(f)}$, which is determined directly in the software TeraLyzer using 25 repeated measurements. Additionally, the material thickness influences the calculation of the refractive index (cf. Equation 5.1). Here, the uncertainty of the thickness measurement of the DiCo-SMC $u_{c,d}$ is considered directly as an input in the software for the calculation of $u_{n(f)}$. For this purpose, the combined thickness measurement uncertainty $u_{c,d}$ was determined using a 3 mm thick, calibrated parallel gauge block¹ (u_{cal}) as well as 25 repeated measurements on the respective DiCo-SMC specimen ($u_{p,d}$) itself, according to Equation 5.6. Measurement results were bias corrected. Further uncertainties from material and production were neglected.

$$u_{c,d} = \sqrt{u_{\text{cal}}^2 + u_{p,d}^2} \quad 5.6$$

To project the uncertainty u_{ξ} onto the functional level in the form of the uncertainty of the estimated Young's modulus $u_{\hat{E}}$, it is assumed that an ideal DiCo-SMC specimen with a FMF of $\xi = 41$ wt.-% is measured using the proposed THz measurement model (measurement of the refractive index and propagation through the measurement model (M3)). This leads to a normal distribution of the measured FMF with the mean value $\mu_{\xi} = 41$ wt.-% and the standard deviation $s_{\xi} = u_{\xi}$. From this normal distribution, $n_s = 100,000$ samples are drawn for a Monte Carlo simulation (MCS). This corresponds to n_s randomly realized measurement results for the FMF of an ideal DiCo-SMC. Using Mori-Tanaka homogenization (cf. Section 2.2.5.1), the planar isotropic Young's modulus \hat{E} is calculated analytically for each of these n_s draws. The resulting distribution of \hat{E} is also normally distributed, so that the uncertainty $u_{\hat{E}}$ can be estimated.

The different uncertainty contributions and the resulting uncertainty budget are summarized in Table 5.4 for three different measurement regions (cf. no. 43, 55, and 79 in Table A2.1), whereby the coverage factor $k = 2$ was used for calculating the expanded measurement uncertainties U_{ξ} and $U_{\hat{E}}$.

¹Deutsche Akkreditierungsstelle (DAkkS) D-K-15089-01-00

Table 5.4: Uncertainty budget for Terahertz measurements of different fiber mass fractions [nominal fiber mass fraction]

	37.8 [35] wt.-%	46.9 [41] wt.-%	45.7 [45] wt.-%	Unit
u_{cal}		0.06		μm
$u_{\text{p},d}$	4.59	3.65	5.21	μm
$u_{\text{c},d}$	4.59	3.66	5.21	μm
<i>$u_{\text{c},d}$ serves as input to TeraLyzer to calculate $u_{\bar{n}}$</i>				
$u_{\bar{n}}$	0.00832	0.00339	0.00494	-
<i>$u_{\bar{n}}$ and Equation 5.5 serve as input to Equation 5.4 to calculate u_{ξ}</i>				
u_{ξ}	0.994	0.444	0.574	wt.-%
U_{ξ}	1.987	0.888	1.147	wt.-%
<i>u_{ξ} used for MCS and MT homogenization to calculate $u_{\hat{E}}$</i>				
$u_{\hat{E}}$	0.268	0.120	0.154	GPa
$U_{\hat{E}}$	0.536	0.239	0.309	GPa

5.2.4 Added value of Terahertz measurements

This section shows that using the THz measurement model significantly reduces the uncertainty in local material stiffness. So far, uncertainties in local FMF originating from the production process needed to be accepted because of lacking measurement technologies. The uncertainty in FMF originating from the production process served as a benchmark for the assessment.

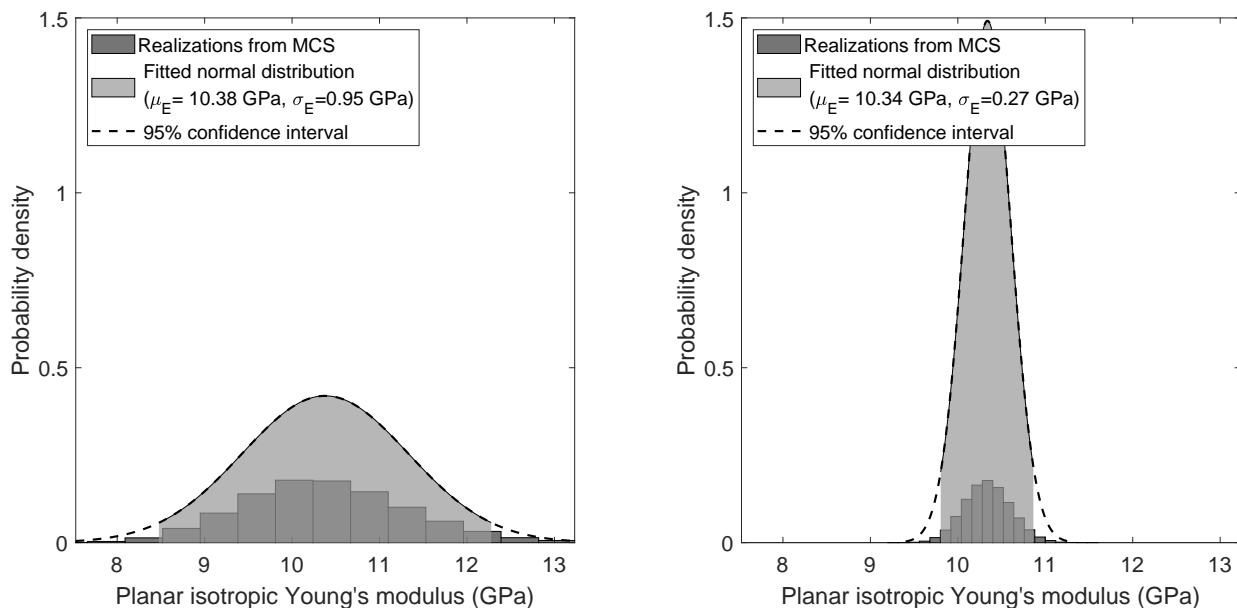
The uncertainty of the FMF related to the production process $u_{\xi,\text{prod}}$ was used for comparison to the THz measurement uncertainty u_{ξ} . The uncertainty $u_{\xi,\text{prod}}$ composes of the standard deviation of TGA-referenced measurement regions within the same reference specimen $s_{\xi,\text{TGA}}$ and a systematic deviation (bias) from the intended FMF (nominal value) b_{ξ} . Since reference specimens with different nominal FMF exist, the systematic deviations and the standard deviations are averaged over all specimens. Based on Table A2.1, leading to the results of Equation A2.1 for $\overline{s_{\xi,\text{TGA}}}$ and Equation A2.2 for $\overline{b_{\xi}}$ given in the Appendix A2, $u_{\xi,\text{prod}}$ is calculated for DiCo-SMC specimen with more than 3 layers according to:

$$u_{\xi,\text{prod}} = \sqrt{\overline{s_{\xi,\text{TGA}}}^2 + \overline{b_{\xi}}^2} = \sqrt{1.57^2 + 3.13^2} \text{ wt.-%} = 3.5 \text{ wt.-%} \quad 5.7$$

Only reference specimens with application-oriented nominal thicknesses of 3 and 4 mm were included in this calculation, so that the potential influence of extreme local outliers in FMF of a single prepreg layer was limited. Twelve measurement regions from Bretz & Häfner et al.

(2021) were not taken into account, as dry glass fibers were added manually. Previous studies of the FVF in DiCo-SMC showed comparable results (Trauth 2018). Therefore, using the THz measurement model enables a conservatively calculated reduction of the local FMF uncertainty by about 70% (cf. Table 5.4).

Mori-Tanaka homogenization and Monte Carlo simulation (MCS) allow to map FMF uncertainty onto the functional domain (uncertainty of Young's modulus, cf. Section 5.2.3). A comparable calculation of planar isotropic Young's modulus as already presented in the previous subsection was repeated for $\mu_\xi = 41$ wt.-% considering the standard deviation resulting from the production process $s_\xi = u_{\xi, \text{prod}}$. The result is illustrated in Figure 5.7a. For reference, Figure 5.7b shows the calculated distribution of Young's modulus based on the maximum observed measurement uncertainty $u_\xi = 0.994$ wt.-% (cf. Table 5.4). Again, the uncertainty of the local Young's modulus is reduced about 70%. However, if anisotropic fiber orientations are considered instead of the planar isotropic fiber orientation, the effect will be even stronger due to the stronger influence of oriented fiber fractions on Young's modulus (Bretz & Häfner et al. 2021).



(a) Uncertainty of fiber mass fraction from production process (b) Uncertainty of fiber mass fraction from THz measurement

Figure 5.7: Monte Carlo simulation and Mori-Tanaka homogenization of distributed fiber mass fractions in planar-isotropic DiCo-SMC

5.2.5 Measures for improved measurement time

Up to this point, the measurement times for each THz measurement region (MR) were too time-consuming for a large-scale in-line application with a time budget of one to three minutes.

For this reason, measures that increase the measurement speed or the area measured per time are evaluated in the subsections below. An overview of the three proposed measures is given in Table 5.5. For a change in beam diameter, two additional reference specimens were used (cf. Figure 5.3). These specimens and the respective MRs were not used to establish model (M3).

Table 5.5: Overview of measures for an improved THz measurement time

Measure	Assessment based on	Data generation	MR used in (M3)
Recording time window (RTW)	Influence on measurement uncertainty	Artificial shortening of six recordings in the time domain	yes
Averaging	Influence on measurement uncertainty	Recording of six regions with reduced averages	yes
Beam diameter	<i>RMSE</i> of estimated FMF	Six new measurement regions per diameter	no

The first two measures were applied to six measurement regions that were already used to establish the measurement model (M3). Therefore, the evaluation of these measures was based on the influence on the uncertainty contributions according to Equation 5.4. The results could then be compared to the existing reference measurements. Two additional reference specimens (cf. Figure 5.3) with enlarged diameters of the measurement regions were THz measured for the assessment of a changing beam diameter. Here, the *RMSE* of the FMF obtained using measurement model (M3) was considered for the assessment. An uncertainty contribution $u_{\bar{n}}$ for enlarged diameters comparable to measurements with a beam diameter of 10 mm was given for all MRs.

5.2.5.1 Reduced recording time window

The entire recording of a THz time domain signal is obtained by scanning the THz signal incrementally with the help of the THz detector at different points in time. Different incremental scans are realized by a mechanical change of the optical path length through the movement of a delay unit. A reduced recording time (RTW) proportionally reduces the measurement time as well. So far, a RTW of 400 ps was used, although the rise and fall of the maximum signal amplitude occurred within 20 ps (cf. Figure 5.4a). A shortened RTW implies a reduced number of recorded data, so that the resolution of the Fourier transform is also reduced. The resolution of the Fourier transform is calculated from the quotient f_s/N , with the sampling frequency f_s and the number of data points N used for the FFT. However, since the mean refractive index \bar{n} was chosen as feature for the measurement model, a reduced frequency resolution is expected to play a minor role.

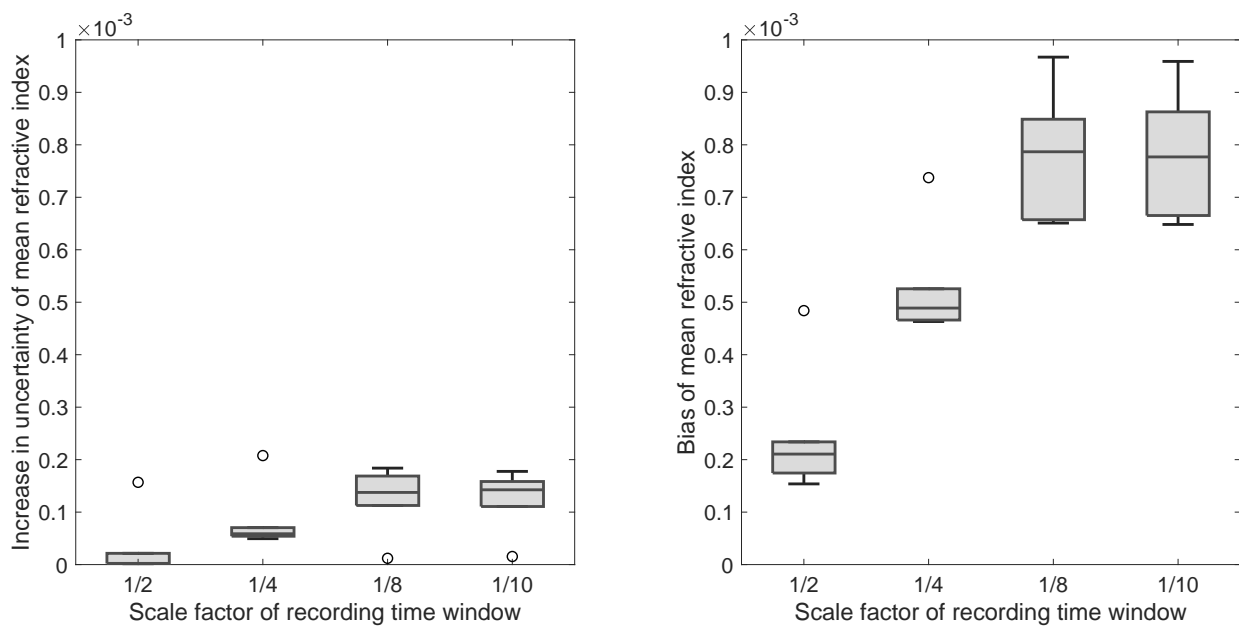
Therefore, the influence of a reduced RTW was systematically investigated by a stepwise reduction of information. The scale factor sf indicates the ratio of the trimmed RTW to the original RTW (400 ps). The respective air measurements were trimmed accordingly. The calculation of optical parameters follows the same principles as presented in Section 5.2.1 and 5.2.2. For each measurement region (MR) $k = \{1, \dots, 6\}$, the positive difference in uncertainty of the averaged refractive index for the scale factor sf was determined $\Delta u_{\bar{n}}$:

$$\Delta u_{\bar{n},k,sf} = u_{\bar{n},k,sf} - u_{\bar{n},k,sf=1} \tag{5.8}$$

In addition, the bias of the mean refractive index $b_{\bar{n}}$ was determined with respect to the reference measurement:

$$b_{\bar{n},k,sf} = |\bar{n}_{k,sf} - \bar{n}_{k,sf=1}| \tag{5.9}$$

Results are illustrated in Figure 5.8. Every boxplot summarizes the results for the $k = 6$ measurements regions. The observed influence is moderate compared to existing measurements (cf. Table 5.4 and Figure 5.6).



(a) Increased MU contribution of the mean refractive index $u_{\bar{n}}$ w.r.t. a RTW of 400 ps (b) Bias of the mean refractive index $b_{\bar{n}}$ w.r.t. a RTW of 400 ps

Figure 5.8: Influence of reduced recording time window (RTW) on the measurement uncertainty (MU) of the THz model

In order to determine the influences of the increased uncertainty contributions on the measurement result, the three realized results of the uncertainty analysis $u_{\bar{n}}$ from Table 5.4 were used. In the following equation, these realized results are denoted $u_{\bar{n},i}$ with $i = \{1, \dots, 3\}$. The for a reduced RTW corrected uncertainty $u_{\bar{n},sf,i}$ for different scale factors sf based on the i exemplary realizations led to:

$$u_{\bar{n},sf,i} = \sqrt{(\tilde{u}_{\bar{n},sf} + u_{\bar{n},i})^2 + \tilde{b}_{\bar{n},sf}^2} \quad 5.10$$

Here, the median values of the six MR, illustrated in the boxplots (cf. Figure 5.8), were used and are denoted by $\langle \tilde{\cdot} \rangle$. The results $u_{\bar{n},sf,i}$ were then subjected to Equation 5.4 to calculate the uncertainty $u_{\hat{\xi},sf,i}$. The differences to the respective uncertainties $u_{\hat{\xi}}$ from Table 5.4 are summarized as boxplots in Figure 5.10a for different scale factors. When comparing the results to existing uncertainties $u_{\hat{\xi}}$ in Table 5.4 for a full RTW of 400 ps, the results illustrate that an increase in measurement speed by a factor of 10 through a trimmed RTW is reasonable.

5.2.5.2 Reduced averaging

An increased measurement speed can also be achieved by averaging fewer waveforms. Since the recording of each waveform takes the same amount of time, a reduction in the number of averaged waveforms leads to a proportional reduction in measurement time. A disadvantage is that the signal quality, quantified by the SNR, can deteriorate. This is particularly relevant for higher THz frequencies, since these wavelengths are absorbed more strongly in the DiCo-SMC. However, since the mean refractive index \bar{n} relies on frequencies between 0.3 and 0.55 THz, a lower SNR and subsequent inaccurate calculation of the optical properties in higher THz frequency ranges can be tolerated.

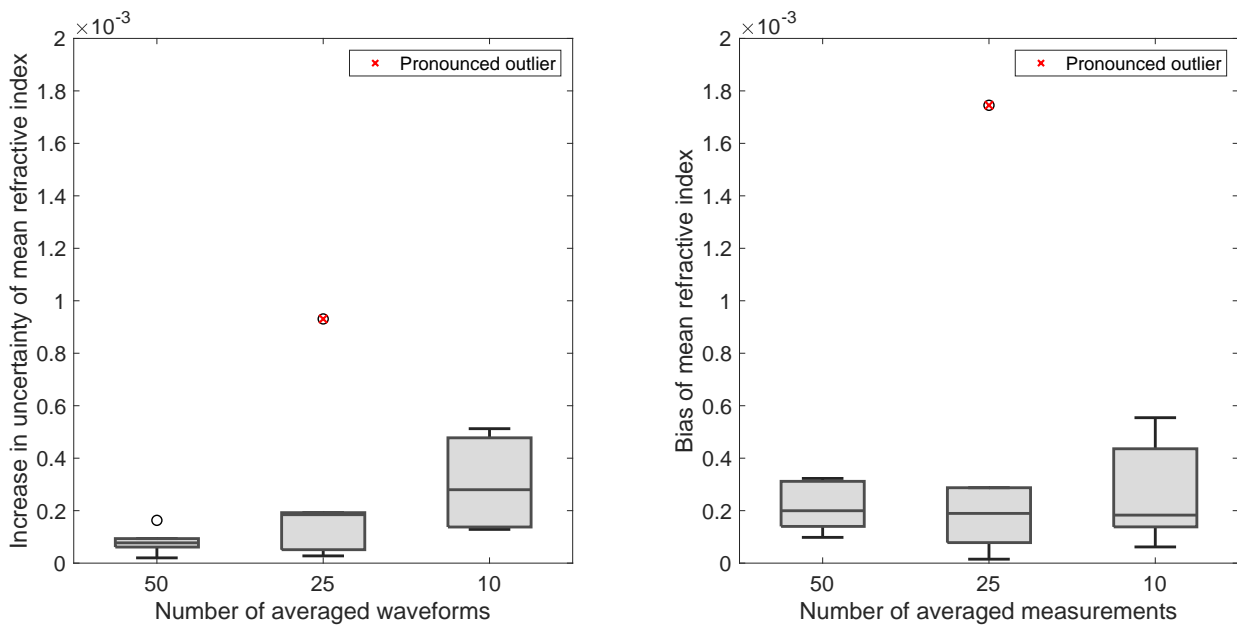
The same six MR from the previous subsection investigating the RTW were also used for this assessment. Before the TGA was performed, these six MRs were also measured with a stepwise reduced number of averages (50, 25, 10) in addition to the initial setting of 100 averages. The respective air measurements were conducted accordingly. The procedure for determining the optical properties remains as described in Section 5.2.1 and 5.2.2. Again, the positive difference in uncertainty of the mean refractive index for different numbers of measurements $m_{\text{avg}} = \{50; 25; 10\}$ to calculate the average was determined for the six MR $k = \{1, \dots, 6\}$:

$$\Delta u_{\bar{n},k,m_{\text{avg}}} = u_{\bar{n},k,m_{\text{avg}}} - u_{\bar{n},k,m_{\text{avg}}=100} \quad 5.11$$

In addition, the bias of the mean refractive index $b_{\bar{n}}$ was determined with respect to the reference measurement with 100 averages:

$$b_{\bar{n},k,m_{\text{avg}}} = |\bar{n}_{k,m_{\text{avg}}} - \bar{n}_{k,m_{\text{avg}}=100}| \quad 5.12$$

Results are illustrated in Figure 5.9. Every boxplot summarizes the results for the six measurements regions. The results range in the same order of magnitude as for a reduced RTW (cf. Figure 5.8) and are therefore also acceptable. However, a pronounced outlier was observed both for $\Delta u_{\bar{n},k,m_{\text{avg}}}$ and $b_{\bar{n},k,m_{\text{avg}}}$. Both identified outliers can be attributed to the same MR. Since the outliers no longer occurred with a further reduction of the number of averages, a random error can be assumed. Nevertheless, the results of this MR were used to estimate a worst case scenario for the uncertainty of the measurement model.



(a) Increased MU contribution of the mean refractive index $u_{\bar{n}}$ w.r.t. 100 averaged waveforms (b) Bias of the mean refractive index $b_{\bar{n}}$ w.r.t. 100 averaged waveforms

Figure 5.9: Influence of reduced averaging on the measurement uncertainty (MU) of the THz model

Similar to Equation 5.10, the averaging-corrected uncertainty $u_{\bar{n},m_{\text{avg}},i}$ for different averages m_{avg} , based on the i exemplary realizations from Table 5.4, was calculated according to:

$$u_{\bar{n},m_{\text{avg}},i} = \sqrt{(\tilde{u}_{\bar{n},m_{\text{avg}}} + u_{\bar{n},i})^2 + \tilde{b}_{\bar{n},m_{\text{avg}}}^2} \quad 5.13$$

Results were again subjected to Equation 5.4, leading to the boxplots displayed in Figure 5.10b. Based on the order of magnitude, which is the same as in Figure 5.10a, the reduction of waveform averaging is a viable measure for a reduced measurement time as well. Even if the values of the two outliers (cf. Figure 5.9) were chosen instead of the medians for a worst case estimate, this would only lead to a maximum uncertainty $u_{\xi} = 1.105 \text{ wt.-%}$, which is still well below the uncertainty $u_{\xi, \text{prod}}$ (cf. Equation 5.7).

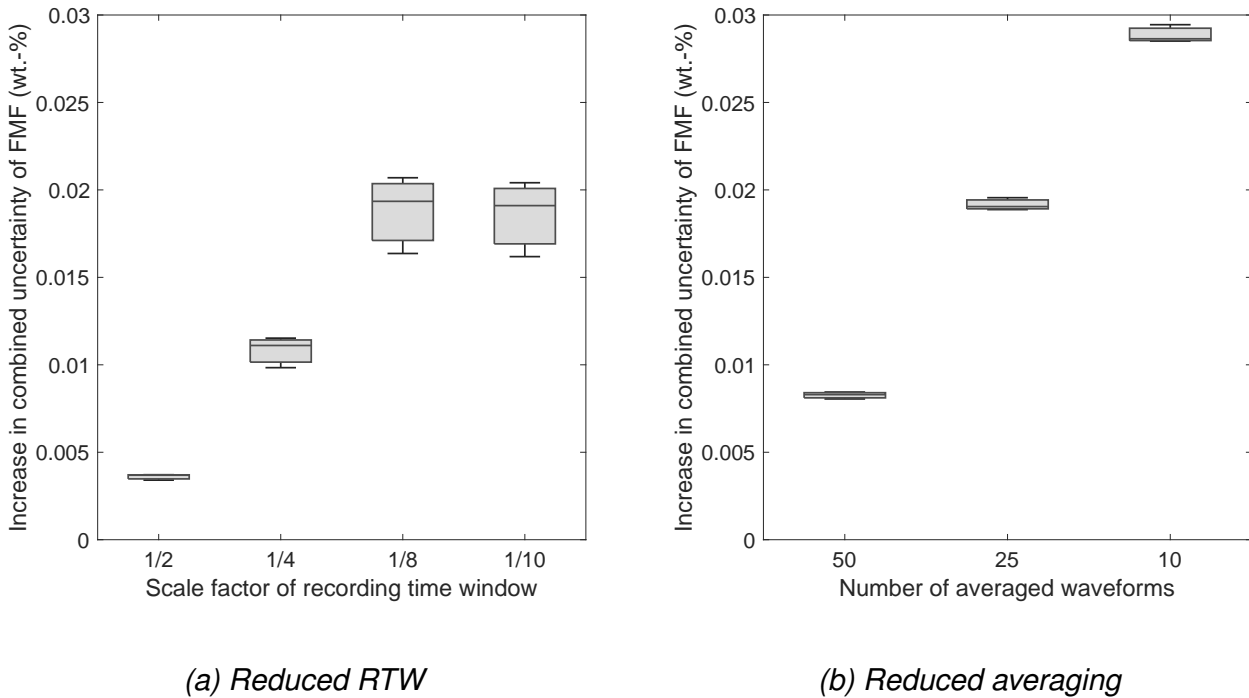


Figure 5.10: Influence on the combined uncertainty of the fiber mass fraction u_{ξ}

5.2.5.3 Reduced recording time window and averaging

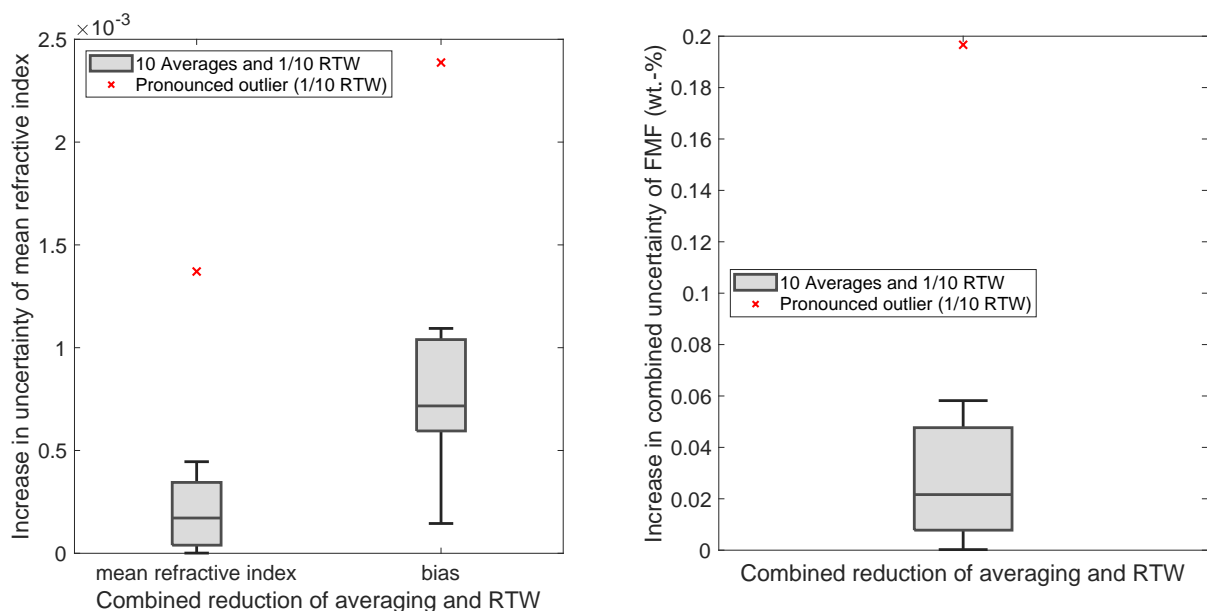
Since it was shown in the previous two subsections that a reduced RTW as well as fewer averages are tenable, the combination of both possibilities are examined here. For this purpose, the six MR, which were recorded using 10 averaged waveforms, were artificially trimmed with the scale factor $sf = 1/10$. Additionally, the pronounced outliers from Figure 5.9 were included in this investigation for a worst case estimate.

Analogously to the previous chapters, the positive difference in uncertainty of the mean refractive index $\Delta u_{\bar{n}}$ and the bias of the mean refractive index $b_{\bar{n}}$ were calculated with respect to the results at full RTW and 100 averaged waveforms:

$$\Delta u_{\bar{n}, k, m_{\text{avg}}, sf} = u_{\bar{n}, k, m_{\text{avg}}, sf} - u_{\bar{n}, k, m_{\text{avg}}=100, sf=1} \quad 5.14$$

$$b_{\bar{n},k,m_{\text{avg}},sf} = \left| \bar{n}_{k,m_{\text{avg}},sf} - \bar{n}_{k,m_{\text{avg}}=100,sf=1} \right| \quad 5.15$$

The results are presented in Figure 5.11a. The calculation of the corrected uncertainty $u_{\bar{n},m_{\text{avg}},sf}$ was followed by the calculation of the influence on u_{ξ} , summarized in Figure 5.11b. It turns out that the combination of both measures does not cause any significant interactions. A maximum increase of the uncertainty by 0.197 wt.-% follows in the worst case estimate when considering the pronounced outlier. Therefore, both measures can be combined to enable in-line deployment.



(a) Influence on the mean refractive index $u_{\bar{n}}$ and bias of refractive index $b_{\bar{n}}$

(b) Influence on the combined uncertainty of the fiber mass fraction u_{ξ}

Figure 5.11: Influence of combined reduced averaging and recording time window length (RTW) on the measurement uncertainty (MU) of the THz model

5.2.5.4 Increased beam diameter

Widening the measurement diameter of the THz beam is another way to increase the measured area per time. So far, a measurement diameter of 20 mm was used for mechanical characterization of DiCo-SMC in TGA (Trauth 2018; Trauth et al. 2021). Therefore, a transfer of the measurement model to this diameter is also aimed for. Additionally, an investigation with the measurement diameter of 14 mm is carried out as an interim step. Thus, an approximate twofold and fourfold increase of the measured area from the initial diameter of 10 mm was considered.

A similar SNR of the recordings with increased diameter compared to the standard diameter allowed the calculation of the refractive index for both enlarged measuring diameters. The uncertainty contribution $u_{\bar{n}}$ showed no deterioration compared to the measurements with the standard diameter of 10 mm. Thus, the refractive indices were used for the determination of the FMF according to (M3), cf. Table 5.3. Predicted FMF for the measurement diameter of 14 mm showed a $RMSE$ of 0.78 wt.-%. However, measured regions with a diameter of 20 mm showed a $RMSE$ of 3.17 wt.-%. In this case, three measured samples were in good agreement with the proposed measurement model. In contrast, three other samples show a significantly larger residual (cf. Figure 5.12).

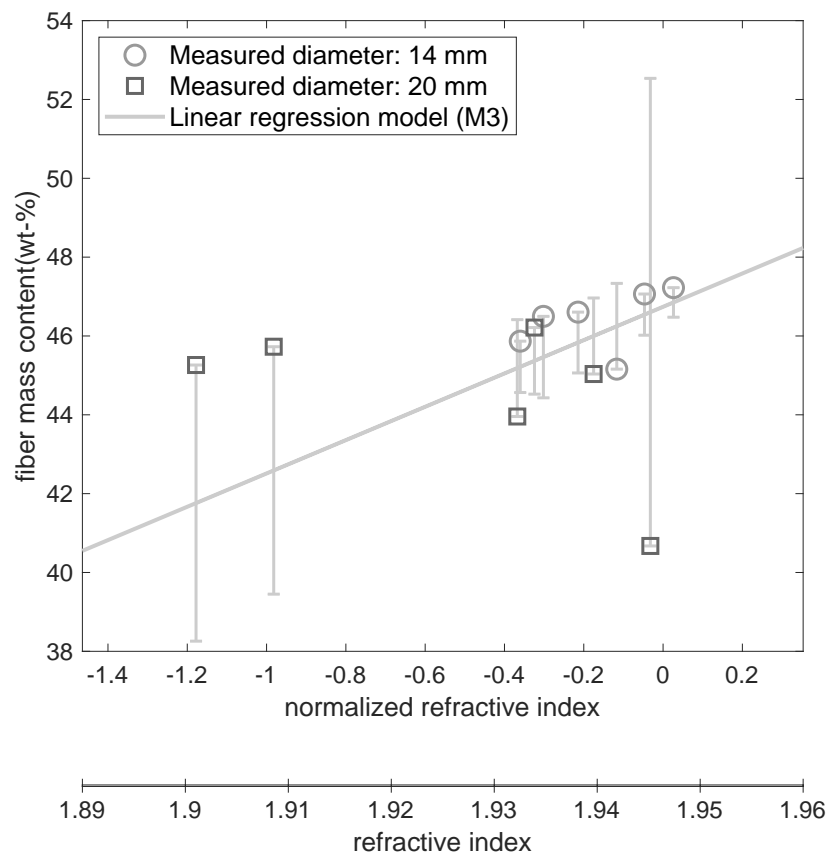


Figure 5.12: Residuals to Terahertz measurement model for different measurement diameters

Therefore, it is not possible to make a general statement on the transferability of the measurement models to any enlargement of the measurement diameters. However, since nine of twelve specimens with an increased measurement diameter were in good agreement with the existing measurement model, the deviations could also be attributed to poor surface quality or foreign materials. At this point, a larger sample size is necessary to be able to make a clear statement. In principle, an increase in the measurement diameter based on the resulting uncertainty component and the SNR is conceivable. However, measurement diameters are kept at 10 mm in the further course of this work.

5.3 Industrial image processing (IIP) for the measurement of Co-SMC positioning

In this section, an industrial camera is used to measure the pose of Co-SMC patches on DiCo-SMC. Existing works showed that the image contrast of Co-SMC patches on DiCo-SMC is sufficient for the detection of the patch centroid and orientation (cf. Section 3.2.1.4 and Bretz & Häfner et al. (2019)). The camera measurement process is divided into off-line and in-line steps so that measurement results can be obtained with high repeatability and short measurement times (cf. Figure 5.13). Furthermore, the measurement uncertainty for the position and orientation of the Co-SMC patch is determined on a component with the same dimensions as the flexural specimen used for validation (cf. Section 7.2.1.2).

5.3.1 Apparatus and methods

The following subsections describe the general experimental setup, the off-line camera calibration and the in-line image processing. Figure 5.13 illustrates the measurement process and gives a breakdown of the individual in- and off-line operations taken.

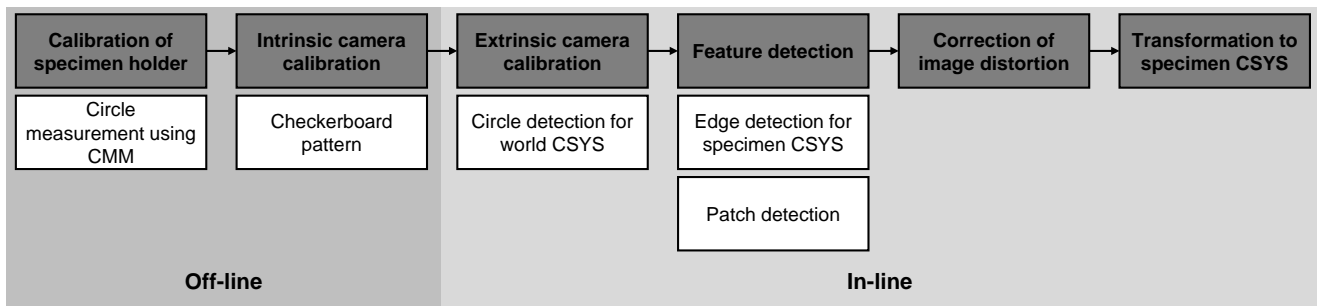
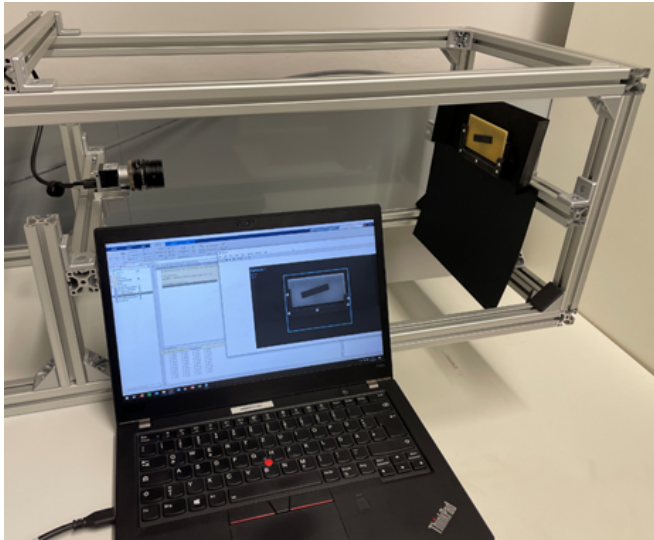


Figure 5.13: Classification and sequence of the camera measurement

5.3.1.1 Test rig and specimen holder

An available camera test rig designed at wbk was used for the optical measurement of the Co-SMC patches. A mono camera setup (Basler acA1920-40uc) with a Kowa lens (LM25HC 25mm/F1.4) was selected for the measurement task. The object distance was approximately 500 mm. The camera was connected to a notebook via USB 3.0 and controlled via MATLAB[®]. A 3D-printed holder was used to fix the specimens. The specimen holder served simultaneously as a calibration target defining the world coordinate system (world CSYS). For this purpose, laser-cut, white circles with a nominal diameter of 5 mm were glued onto the specimen holder. Test rig and specimen holder are depicted in Figure 5.14.



(a) Test rig



(b) Specimen holder

Figure 5.14: Measurement setup for image acquisition

5.3.1.2 Off-line calibration

Initially, the position and diameter of the attached circles were optically off-line measured using a CMM (Carl Zeiss OI-322). The white lower left circle was defined as the origin of the right-handed world coordinate system (CSYS). The positive axis x_w was further defined by the circle in the lower right (cf. Figure 5.15). Using these five calibrated world coordinates, the extrinsic camera parameters could individually be determined for every measurement according to the algorithm described in Heikkilä (2000). Additionally, five different poses of a checkerboard pattern served for the off-line determination of the intrinsic camera parameters using the MATLAB[®]-integrated function *estimateCameraParameters()*.

5.3.1.3 In-line image processing

The commercial software MATLAB[®] was also used for image processing. In recorded images, the calibration circles were first detected using the integrated function *imfindcircles()*. Thus, the point correspondences between calibrated world and image coordinates were determined. The right-handed specimen coordinate system was defined by the specimen edges of the chamfered corner, with the shorter side representing the positive x-axis of the specimen x_{spec} . The specimen edges were determined using the Canny edge detector and the Radon transform. The origin of the specimen CSYS was defined by the intersection of the regression lines. The Co-SMC patch on the specimen was segmented using binarization and subsequent morphological operations. Using the *regionprops()* function, the centroid and orientation features of the segmented patch were determined. The intrinsic parameters known from

checkerboard calibration were used to undistort image coordinates. Finally, the features were transformed into the specimen CSYS. Image acquisition and processing was performed on a notebook with an Intel® Core™ i5-8250U and without graphic card in less than 10 s.

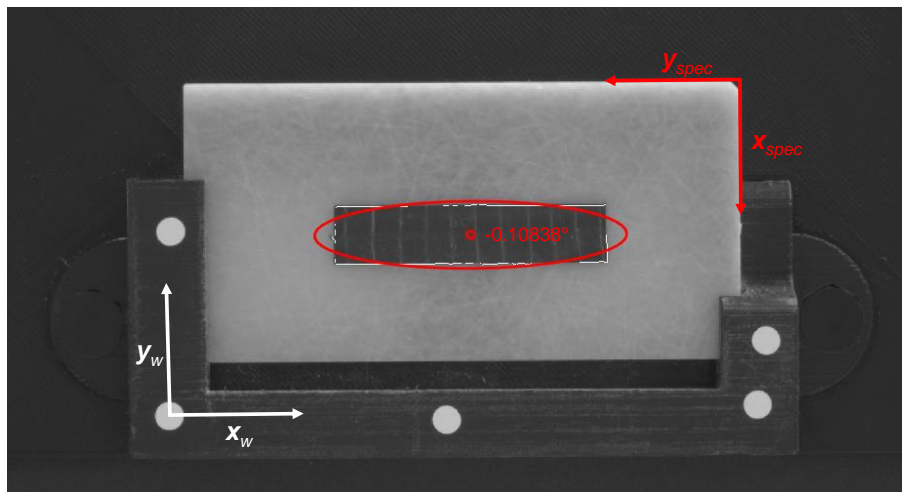


Figure 5.15: Exemplary world and specimen coordinate systems, patch segmentation and feature extraction

5.3.2 IIP measurement uncertainty

Image processing, as described in Section 5.3.1.3, was used to measure the centroid and the orientation of the Co-SMC patch on a specimen with the nominal dimensions specified in Table 7.9. The defined features of the patch were the x-coordinate of the patch centroid x_T , the respective y-coordinate y_T , and the mathematically positive rotation of the patch around the z-axis γ_T with respect to the specimen CSYS.

20 images under different lighting conditions were taken for an exemplary specimen. The intrinsic camera calibration was repeated five times. Similarly, the CMM measurements of the calibration circles to determine the world CSYS were repeated five times. Therefore, 25 different camera calibrations consisting of extrinsic and intrinsic parameters followed. In combination with the 20 captured images, 500 realized measurements of x_T , y_T , and γ_T were acquired. Thus, the means \bar{y}_{IIP} for the features and the respective standard uncertainties u_p were determined. The exemplary specimen was further optically calibrated using a total of six optical CMM measurements. For optimal contrast, the component was illuminated with a red, outer ring light and the base plate was transilluminated using white light. The origin of the specimen CSYS at the chamfered corner was determined by the intersection of the measured component edges. The edges of the patch were also identified using different edge filters within the software ZEISS CALYPSO. The intersections of the four measured patch edges defined the four corner points of the patch, from which the centroid and orientation were

subsequently determined. The calibration procedure lead to the mean $\bar{y}_{\text{CMM}} = x_{\text{cal}}$ and the standard uncertainty u_{cal} . Additionally, the bias $b = \bar{y}_{\text{IP}} - x_{\text{cal}}$ was calculated. u_w is neglected according to Deutsches Institut für Normung e.V. (2011b). The resulting uncertainty budget is given in Table 5.6a. Equation 2.7 and the respective coverage factor k for a 95.45% level of confidence based on the effective degrees of freedom ν_{eff} (JCGM100 2008, cf. Table 5.6b) were used for calculating the expanded measurement uncertainty U .

(a) Uncertainty budget				(b) Effective degrees of freedoms and coverage factors			
	x_T (mm)	y_T (mm)	γ_T (°)		x_T (mm)	y_T (mm)	γ_T (°)
x_{cal}	26.70	49.15	-0.63				
u_{cal}	0.02	0.02	0.10	$\nu_{u_{\text{cal}}}$		5	
u_p	0.04	0.06	0.02	ν_{u_p}		499	
$ b $	0.24	0.29	0.08	ν_b		6	
u_c	0.25	0.29	0.13	ν_{eff}	6	6	12
U	0.62	0.74	0.29	k	2.52	2.52	2.23

Table 5.6: Uncertainty budget of industrial image processing for Co-SMC patch measurement

5.4 Active thermography for the measurement of delaminations

In this section, thermographic images acquired by pulsed phase thermography (PPT) are used to quantify the size and position of delaminations in DiCo-SMC. Delaminations change the heat flow in a component and can therefore be visualized in thermographic images. A thermographic image analysis for delamination measurement is presented. Thermography has already been used to detect delaminations in many earlier studies (cf. Section 3.2.1.3). In contrast to the state of the art, the measurement uncertainty is quantified using artificial delaminations made out of a thin Teflon layer. The special characteristics for the detection of delaminations in CoDiCo-SMC is also discussed.

5.4.1 Apparatus and methods

The measurement setup as well as the data processing considering the hybrid material are presented in the two following subsections. Figure 5.16 illustrates the process for analyzing thermographic phasegrams and gives a breakdown of the individual in- and off-line operations taken.

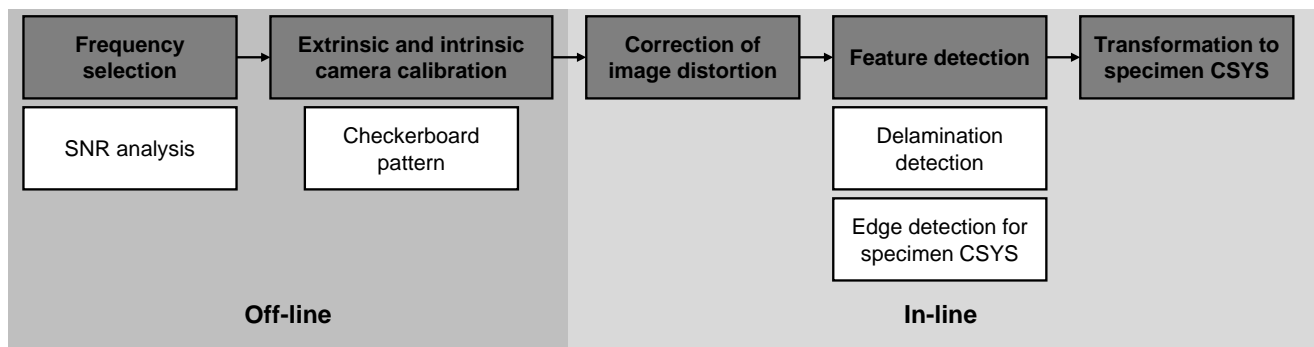


Figure 5.16: Classification and sequence of the pulsed phase thermography measurement

5.4.1.1 Measurement setup

In this work, the thermographic system, which is part of the multi-sensor system developed within the IRTG (Schäferling 2019), was further used. Both the IR camera and the pulsed heat source of the pulsed phase thermography (PPT) system were carried by a CNC portal. Figure 5.17 highlights the most important technical components.

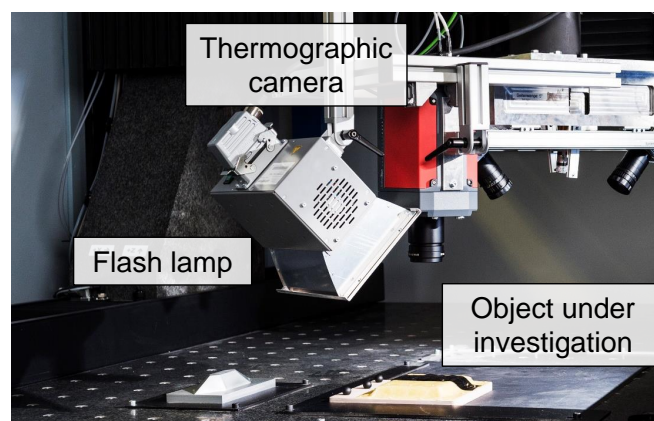


Figure 5.17: Measurement system for pulsed phase thermography

The system was developed and put into operation by the company edevis GmbH. A photographic flash (VH3-6000 from HENSEL-VISIT) thermally stimulated the object under examination. The maximum flash energy was 6 kJ. The heat flux was recorded by the ImagerIR 5385S thermal imaging camera (InfraTec GmbH) with a camera resolution of 320 x 246 pixels and 450 frames per second. The lens had a focal length of 25 mm, leading to an optimal object distance of 300 mm. With this setup, the sharp area contained all planes that were located at a distance of ± 6 mm from the focal point. The temperature evaluation of the specimen was observed for 60 s. A pulse delay triggered the flash 0.1 s after starting the recording. Post-processing using Discrete Fourier Transform (DFT) was performed using the commercial software DisplayIMG 6 from edevis. The specified frame rate and time window

resulted in a minimum recorded frequency of 0.017 Hz after Fourier transform. Amplitude and phasegrams were exported as grayscale images. Image post-processing was performed using MATLAB[®].

5.4.1.2 In-line Image processing

Delaminations can be detected in images that visualize the phase difference of the thermal wave in the material under investigation (phasegram of PPT, cf. Section 3.2.1.3). Phasegrams are more sensitive to thermal material properties than to geometric features. It has deeper probing capabilities than amplitude. (Busse et al. 1992) Non-uniform heating, reflections from the environment and variations in surface emissivity have a negligible effect on phase (Ibarra-Castanedo & Maldague 2004).

Since the CoDiCo-SMC is a hybrid material and the thermal properties of DiCo-SMC (GF) and Co-SMC (CF) are different, these differences also stand out in the image. Therefore, if a delamination is present in CoDiCo-SMC, ideally three different gray scale areas exist (DiCo-SMC, Co-SMC, delamination) in contrast to two for DiCo-SMC. These differences must be taken into account so that delaminations can also be detected and quantified in the hybrid material. A two level thresholding (binarization) was in most cases not sufficient for delamination detection in CoDiCo-SMC. Representative recorded phasegrams for a DiCo- and CoDiCo-SMC and their respective multilevel thresholding are illustrated in Figure 5.18a to 5.18d.

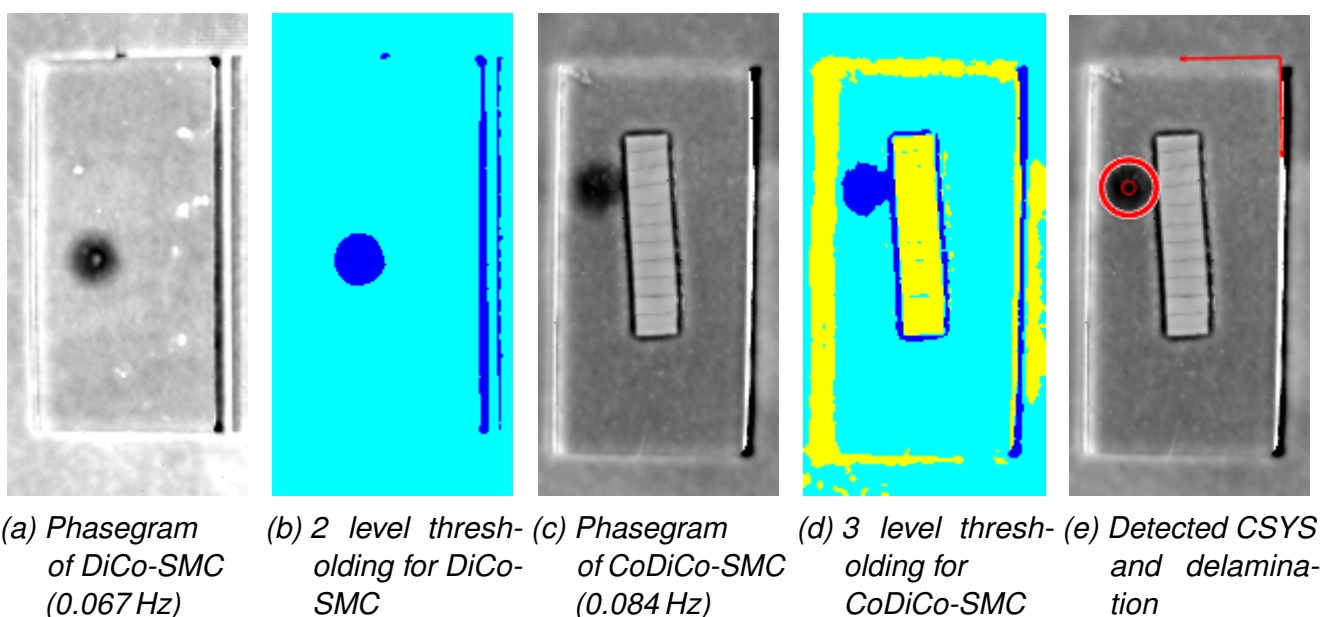


Figure 5.18: Multilevel image thresholding for detecting and measuring delaminations in grayscale phasegrams of CoDiCo-SMC

Initially, a phasegram frequency for a subsequent image processing was chosen based on SNR between delamination and background. These frequencies can be different based on the material system (cf. Figure 5.18a vs. 5.18c). Intrinsic and extrinsic camera parameters were calculated based on ten different poses of a checkerboard pattern using the MATLAB[®] routine for camera calibration. After undistorting the calibration images, an image scale describing the relationship between pixels and millimeters was determined with the help of the found point correspondences. These steps were not part of the in-line measurement procedure and conducted beforehand (off-line). Based on the camera calibration, the image distortion was in-line corrected for every recorded image. The phasegram region, in which the specimen was located (ROI), was cropped. This cropping excluded most parts of the background, which represented an additional gray value area in the image, from the image analysis. Subsequently, multilevel image thresholding was performed using the function *multithresh()*, so that the different gray value areas were segmented. Since delaminations were expected to be the darkest feature in the object because of their behavior as thermal barriers, the corresponding channel was selected. The respective channel was binarized and subsequently post-processed using morphological image operators. Delaminations were detected afterwards by the function *imfindcircles()*. A delamination was described by the coordinates of its centroid and its radius. Finally, the features were transformed into the specimen CSYS. The specimen CSYS was determined analogously to Section 5.3.1.3, by detecting and intersecting the two relevant specimen edges. A detected and measured delamination in the respective specimen CSYS is shown in Figure 5.18e for a CoDiCo-SMC. Image processing was performed on a notebook with an Intel[®] Core™ i5-8250U and without a dedicated graphic card in less than 5 s.

5.4.2 Measurement uncertainty of pulsed phase thermography

Thermographic image processing, as described Section 5.4.1.2, was used to measure the centroid and the radius of a circular delamination in a CoDiCo-SMC specimen with the nominal dimensions specified in Table 7.9. The delamination (Teflon, 130 μm thick) with a nominal radius of 10 mm was located at the centroid of the specimen, below the Co-SMC patch in a depth of 2 mm between two DiCo-SMC layers. The defined features of the delamination were the x-coordinate of the delamination centroid x_D , the respective y-coordinate y_D , and the radius r_D . The coordinates were given in the specimen CSYS.

The thermographic measurements were repeated 27 times, whereas the position of the specimen in the image was varied. The camera calibration was repeated five times. Thus, 135 different measurement results were obtained through the combination of individual measurements and calibrations. The means \bar{y}_{PPT} for the defined features and the respective standard uncertainties u_p were calculated. Five CT measurements were further used to

calibrate the exemplary specimen. CT reconstructions were analyzed using the commercial software VGSTUDIO MAX. The origin of the specimen CSYS at the chamfered corner was determined by the intersection of the three respective planes. Circles were fitted to the delamination in the CT reconstruction to determine the calibration values for the centroid and the radius. The calibration procedure lead to the mean $\bar{y}_{CT} = x_{cal}$ and the standard uncertainty u_{cal} . Additionally, the bias $b = \bar{y}_{CT} - x_{cal}$ was calculated. u_w was neglected according to Deutsches Institut für Normung e.V. (2011b). The resulting uncertainty budget is given in Table 5.7, using Equation 2.7 and the respective coverage factor based on ν_{eff} for calculating the expanded measurement uncertainty U .

<i>(a) Uncertainty budget</i>				<i>(b) Effective degrees of freedoms and coverage factors</i>			
	x_D (mm)	y_D (mm)	r_D (mm)		x_D (mm)	y_D (mm)	r_D (mm)
x_{cal}	29.38	54.28	10.22				
u_{cal}	0.16	0.24	0.15	$\nu_{u_{cal}}$		4	
u_p	1.81	3.75	1.07	ν_{u_p}		134	
$ b $	2.69	0.94	1.17	ν_b		5	
u_c	3.24	3.88	1.59	ν_{eff}	10	137	16
U	7.40	7.83	3.45	k	2.28	2.02	2.17

Table 5.7: Uncertainty budget of thermographic image processing for delamination measurement in a CoDiCo-SMC specimen with local Co-SMC reinforcement (cf. Table 7.9)

Six additional specimens were subjected to a measurement uncertainty analysis, following the same procedure. Delaminations of three different radii (5, 7, and 10 mm) were integrated into the DiCo-SMC at a nominal depth of 1 and 2 mm, respectively. The delaminations were completely buried beneath a local Co-SMC patch, so that the different thermal conductivities of DiCo and Co-SMC still needed to be considered when analyzing gray value differences in the phasegram. The uncertainty contributions of the quantities x_D and y_D showed no systematic deviations depending on the size or depth of the delamination. In accordance with expectations, delaminations closer to the surface showed lower uncertainty in the estimation of the radius. However, the actual radius of the delamination did not show any systematic influence on the uncertain estimate of the radius. The averaged results for the six additional specimens are summarized in Table 5.8. The detailed results for each of the six specimen are given in Appendix A4.

Table 5.7a and 5.8a show that the bias b for the measurement x_D is larger than for the measurement y_D . This can be explained by the uncertain estimation of the y-axis of the specimen, caused by the apparent phase jump in the phasegram (white area at the right edge of the specimen in Figure 5.18e). The phase jump occurred on this axis because of the

direction of excitation, in this case from left to right, by the flash lamp. The x-axis, which was aligned parallel to the direction of excitation, could be determined more precisely due to the absence of a phase jump. The difference in bias of x_D and y_D corresponded approximately to the width of the white phase jump (4 pixels ≈ 2 mm). An additional flash lamp perpendicular or opposite to the existing one could reduce this influence. The occurring difference of the uncertainty contribution u_p of x_D and y_D was caused by using a fixed image scale. With the use of a co-measured calibration target (cf. Figure 5.15), these contributions could be leveled and reduced. The measurement of the radius of a delamination is independent of a determined coordinate system. Thus, the uncertainty contribution u_p is smaller for radii compared to length measurements.

<i>(a) Uncertainty budget</i>				<i>(b) Effective degrees of freedoms and coverage factors</i>			
	x_D (mm)	y_D (mm)	r_D (mm)		x_D (mm)	y_D (mm)	r_D (mm)
u_{cal}	0.21	0.16	0.11	$\nu_{u_{cal}}$		4	
u_p	1.88	3.21	1.02	ν_{u_p}		134	
$ b $	2.69	0.70	0.94	ν_b		5	
u_c	3.29	3.28	1.40	ν_{eff}	11	139	22
U	7.40	6.63	2.96	k	2.25	2.02	2.13

Table 5.8: Uncertainty budget of thermographic image processing for delamination measurement in a CoDiCo-SMC specimen; delamination fully covered by Co-SMC layer

6 Methodology for in-line measurement propagation

This chapter presents a methodology to derive a functional statement, such as an individual component stiffness, from in-line measurement results within the production cycle time. In a first step, a parametrized simulation model is set up in which the different component-specific in-line measurements of manufacturing deviations are integrated. Thus, the component-specific function is assessed. Since the simulation models are computationally too expensive for an in-line deployment, the second part of the methodology presented uses surrogate models of the parameterized simulations for an in-line qualification.

6.1 Functional assessment of interacting manufacturing deviations

The FEM possesses the necessary prerequisites to model the influences of manufacturing deviations on component stiffness (cf. Section 2.3). Hereby, multiple manufacturing deviations and combined influences between those (interactions) can be considered. The integration of the in-line measurements into a parameterized FE model leads to a component-specific stiffness (simulation result). The comparison of this component-specific stiffness allows for a comparison with the component requirements or the ideally manufactured component. The general model set-up procedure and the quantification of occurring model uncertainties are described in the following.

6.1.1 FE model structure

The commercial software Abaqus™/Standard from Dassault Systèmes® was used to parametrically model CoDiCo-SMC specimens. Since component-specific measurement results have to be integrated into simulations, the Python™ interface of Abaqus can be used to both read in the measurement results and integrate them individually in the model setup. The component is always subjected to a reference load independently of the individually integrated manufacturing deviations. The general modeling approach and the integration of potential manufacturing deviations are presented in this section.

6.1.1.1 Geometry modeling and choice of element types

Linear and quadratic solid elements for the DiCo-SMC (Abaqus element types: C3D8 and C3D20) as well as continuum shell elements (CSE) for the Co-SMC (SC8R) were used. The DiCo- and Co-SMC were represented by two individual, perfectly bonded parts using Abaqus tie-constraints. Tie constraints also permit the connection of two surfaces through a geometric coupling when nodes do not lie on top of each other (A_Müller-Welt 2019). Thus, meshes of both parts did not need to be identical. Linear solid elements (C3D8) needed to be used because XFEM is only available for those elements in Abaqus™. Therefore, a

sufficient number of solid elements through the thickness direction needs to be considered when bending loads occur (Nasdala 2015). Several layers connected by tie-constraints each showed an almost identical behaviour for the use of shell or continuum shell elements. Due to the three-dimensional meshing when using CSE, it is easier to define connected surfaces of the individual layers for CSE instead of traditional shell elements. (A_Müller-Welt 2019) In order to ensure a sufficient fine meshing, convergence studies must be carried out.

6.1.1.2 Material modeling

Isotropic material behavior was assumed both for the glass fiber and the UPPH resin. A Mori-Tanaka homogenization based on orientation average (planar isotropic FOD) and fiber fraction was performed for calculating the linear elastic material properties of the DiCo-SMC (cf. Section 2.2.5.1 and A_Frontzek 2019). A maximum principal stress and strain criterion was chosen for the DiCo-SMC because of limited available material parameters. The maximum principle stress for different fiber fractions was determined with a least squares method based on experimental results (cf. Section 7.1.2.2).

The Co-SMC layer was modeled using five independent material parameters, describing a transverse isotropy. The respective engineering constants were defined in a local coordinate system for the elements of a Co-SMC layer. Failure in the Co-SMC layer was modeled using a publicly available Abaqus user subroutine of the Puck criterion (cf. Section 2.2.5.3).

The material parameters used are summarized in Table A5.1 in Appendix A5.

6.1.1.3 Manufacturing deviations

Void fraction was analytically integrated into the resin based on negligible mechanical properties of voids (Gross & Seelig 2018; A_Frontzek 2019) and the void volume fraction ϕ_{Void} . This led to equivalent isotropic mechanical properties for the bulk modulus K^* and the shear modulus G^* of:

$$K_{\text{UPPH}}^* = K_{\text{UPPH}} \left(1 - \frac{\phi_{\text{Void}}}{1 - \alpha(1 - \phi_{\text{Void}})} \right), \quad \text{with} \quad \alpha = \frac{1 + \nu_{\text{UPPH}}}{3(1 - \nu_{\text{UPPH}})} \quad 6.1$$

$$G_{\text{UPPH}}^* = G_{\text{UPPH}} \left(1 - \frac{\phi_{\text{Void}}}{1 - \beta(1 - \phi_{\text{Void}})} \right), \quad \text{with} \quad \beta = \frac{2(4 - 5\nu_{\text{UPPH}})}{15(1 - \nu_{\text{UPPH}})} \quad 6.2$$

Equation A1.4 and A1.5 in Appendix A1 can be used to calculate Young's modulus E^* and poisson ratio ν^* . The resulting isotropic resin properties were then as well used for the Mori-Tanaka (MT) homogenization of DiCo-SMC.

In order to be able to consider local differences in FMF in the DiCo-SMC, cylindrical measuring areas with the corresponding diameters of the THz beam (cf. Section 5.2.1) were included in the DiCo-SMC assembly. Separate partitions were defined for the measurement regions. This allowed the circular measurement regions to be finer meshed even in the case of a coarser meshing of the overall component. The measurement regions can be positioned variably on the DiCo-SMC component. However, real measurement data could only be obtained when the respective measurement region was not covered by Co-SMC. A local material stiffness can be defined in the measurement regions by means of MT homogenization. For the elements of the component outside the measurement regions, the material properties were assigned based on the average FMF measured in the component.

The Extended Finite Element Method (XFEM) was used to represent delaminations in the DiCo-SMC. The initial delamination was modeled as a shell and positioned within the solid elements of DiCo-SMC. Critical energy release rates were used in a Benzeggagh-Kenane (BK) law for a single scalar fracture criterion. Critical energy release rates were only available in fracture modes I and II for Co-SMC (Schober 2019). Thus, the critical release energy G_{IC} of DiCo-SMC was determined in a double cantilever beam (DCB) test (cf. Appendix A6).

Misorientations of the Co-SMC were integrated dependant on the dimensions of the Co-SMC reinforcement. For a full Co-SMC layer, the local coordinate system, in which the material properties were defined, was rotated by the respective misorientation for each element. Otherwise, if a patch reinforcement was part of the assembly, the respective Co-SMC part was rotated around its center. Local patch reinforcements can be further subjected to misplacements, which were realized through the respective displacements of the part in the assembly as well.

6.1.1.4 Storage of component characteristics

The characteristic information of a CoDiCo-SMC component was stored in a standardized .csv-format in the *characteristics file*. This allowed for a direct integration into the automated simulation workflow (cf. Section 6.1.1.5). The characteristic information was divided into external geometry information and intrinsic material properties. Not only were measurement results of measurement technologies under investigation considered in the file, but also the nominal values of other relevant component properties that were not yet the subject of in-line measurements. On the one hand, this enabled a straightforward sensitivity analysis with regard to the properties through direct incorporation into the simulation workflow. On the other hand, future results of measurement technologies can also be easily integrated and replace the nominal values of the respective quantities used in the simulation so far.

6.1.1.5 Simulation workflow

The overall simulation workflow is visualized in a program flow chart in Figure 6.1. The individual information of the component characterization was stored in the characteristics file. It was read into the function *main.py*. Necessary information is passed to the subfunctions for material homogenization and delamination mapping. Manufacturing deviations of the Co-SMC, however, were generated in the model assembly. The load case was also modeled in *main.py*. For different components and load cases, the function *main.py* needs to be individually modified. After the model generation, an *.inp*-file was obtained. This file described the respective component individually for submitting a tailored Abaqus job. It was either computed locally or on a high performance cluster. The result, stored in a *.odb*-file was also analyzed with a script, evaluating the relevant information regarding the individual fulfillment of the specified function of the component (stiffness, strength).

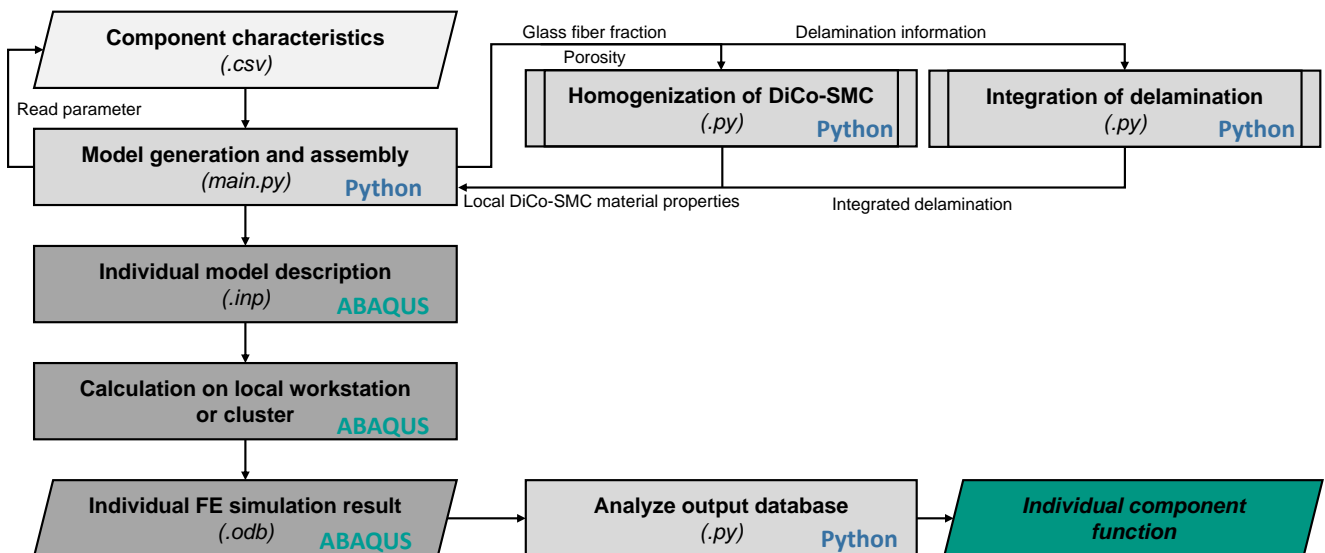


Figure 6.1: Program flow chart for component-individual FE simulations taking manufacturing deviations into account

6.1.2 Key metrics for assessment

An assessment of the deterministic simulation results was performed with the help of the systematic model deviation (bias) as root mean squared error (*RMSE*) of the function prediction (stiffness) based on in-line measurement data \hat{y}_{Sim} and the corresponding experimentally realized function y (Zhang 1993):

$$b_{\text{Sim}} = \text{RMSE} = \sqrt{\frac{\sum_{t=1}^T (y - \hat{y}_{\text{Sim}})^2}{T}} \quad 6.3$$

Similar to the coefficient of variation, a normalization was performed using the mean experimental results \bar{y} to achieve comparability between different load cases:

$$CV_{RMSE} = \frac{RMSE}{\bar{y}} \quad 6.4$$

6.1.3 Uncertainty of the FE model

The inherent uncertainty of the function prediction model must be addressed. In the scope of this thesis, the discretization $u_{\text{Sim,D}}$ and input uncertainty $u_{\text{Sim,I}}$ were considered for the stiffness uncertainty. A strength uncertainty was not assessed within this scope. The further two uncertainty sources presented in Section 2.1.4.4 (solution and modeling error) were not considered in detail because of their typically small influence (Lord & Wright 2003). Furthermore, the systematic model deviation (bias) needed to be taken into account, so that the combined uncertainty follows (JCGM100 2008; Deutsches Institut für Normung e.V. 2011b; Häfner 2017) :

$$u_{\text{c,Sim}} = \sqrt{u_{\text{Sim,I}}^2 + u_{\text{Sim,D}}^2 + b_{\text{Sim}}^2} \quad 6.5$$

The bias b was determined by the $RMSE$ between predicted and realized function (cf. Equation 6.3).

6.1.3.1 Determination of the standard uncertainty due to input quantities

In the context of this work, a distinction shall be made between two different types of input variables for determining the input uncertainty $u_{\text{Sim,I}}$. These were, on the one hand, the uncertainties of the material properties and, on the other hand, the uncertainties of the in-line measurement technologies (cf. Chapter 5). A collection of the potentially relevant uncertainty contributions for a CoDiCo-SMC component is given in Table 6.1. This set holds for the measurement technologies used in this thesis, the respective material modeling and the model assembly. The uncertainty contributions were quantified in terms of standard uncertainties. Both literature sources and own calculations were used in accordance with JCGM100 (2008) (cf. Table A5.2 and A5.3).

Initially, a screening of the collected potentially relevant uncertainty contributions was performed in order to identify the most relevant uncertainty contributions in advance and thus keep the simulation effort reasonable. Here, it is generally useful to vary a single input factor by its standard uncertainty (one factor at a time), while leaving the other input factors at their target level (Häfner 2017). Input factors leading to minor deviations from the simulated reference Young's modulus were discarded. Subsequently, the simulative determination of $u_{\text{Sim,I}}$ was performed according to JCGM101 (2008). For an efficient and at the same time

Table 6.1: Selection of relevant uncertainty contributions of the input quantities for the FE simulation (uncertainties from in-line measurement technologies highlighted in gray)

Stiffness: DiCo-SMC	Stiffness: Co-SMC	Co-SMC patch	Delamination
u_{ξ}	$u_{\phi,CF}$	u_{x_T}	$u_{A,D}$
$u_{\phi,Void}$	$u_{E,CF,\parallel}$	u_{y_T}	u_{x_D}
$u_{E,GF}$	$u_{E,CF,\perp}$	u_{γ_T}	u_{y_D}
$u_{v,GF}$	$u_{G,CF,\perp\parallel}$	u_{d_T}	
$u_{E,UPPH}$	$u_{v,CF,\perp\parallel}$		
$u_{v,UPPH}$	$u_{E,UPPH}$		
	$u_{v,UPPH}$		

random coverage of the entire experimental space, a latin hypercube sampling (LHS) was used instead of a Monte Carlo method (MCM). Here, the function *lhs()* from the Python™ package *pyDOE* allowed for a distribution of the parameters according to their probability density function (PDF) while minimizing correlations. The size of the LHS was chosen to be larger than ten times the number of input parameters remaining after the screening (Loeppky et al. 2009). All input variables were assumed to be independent. Outputs were expected to be normally distributed. Thus, fitting a normal distribution to the outputs allowed for estimating the uncertainty of the output (standard deviation).

Depending on the combination of manufacturing deviations, the uncertainty contributions of the individual input variables may vary due to the anisotropic material properties of fiber composites. For this reason, representative test specimen configurations (combinations of manufacturing deviations) must be selected.

6.1.3.2 Determination of the standard uncertainty due to discretization

The most reliable method to quantify the uncertainty of the discretization $u_{Sim,D}$ is the comparison of the FE result of the selected mesh with a reference simulation using the finest possible mesh (Grätsch & Bathe 2005). A representative component configuration must also be selected at this point, since a defined nominal geometry is a prerequisite for this method.

Due to the automated model construction, meshing of an identical component always leads to the same mesh. Therefore, $u_{Sim,D}$ was directly determined by the difference of the Young's modulus with the used discretization E_D and the Young's modulus with the finest possible discretization for reference $E_{D,ref}$:

$$u_{Sim,D} = b_{Sim,D} = E_D - E_{D,ref}$$

6.2 In-line qualification of the functional assessment

When deviations from the target state occur in the production of FRPs, a decision must be made whether the component can still meet the functional requirements. Up to now, this has been accomplished mainly based on defined tolerances, without checking the actual realized function (cf. Chapter 1). Parametrized FE simulations, as presented in the previous chapter (Section 6.1), are able to make functional statements based on digital representations of component and material. However, the computing times are too high to be considered for an in-line use in production.

This leads to the requirement for real-time predictions of the function of composites in order to make the FE simulation (digital twin) usable for decisions in quality assurance while adhering to the cycle time. The approach of data-driven models, as surrogate models of the parameterized FE models, offers the possibility of a real-time function prediction.

For this purpose, virtual input-output relations were generated by the described FE model (cf. Equation 6.7). Virtually realized measurement results of component states served as input quantities. The predicted (simulated) component function (stiffness \hat{E}_l) based on these quantities represented the main output. Additionally, the influence of the manufacturing deviations on the strength, expressed as the stress exposure \hat{E}_l , was included.

$$\hat{\mathbf{y}}_l = \left[\hat{E}_l, \hat{f}_{E,l} \right] = f(\boldsymbol{\omega}_l) = f(\xi_l, \phi_{\text{Void},l}, x_{T,l}, y_{T,l}, \gamma_{T,l}, A_{D,l}, x_{D,l}, y_{D,l}) \quad 6.7$$

The $l = \{1, \dots, L\}$ sets of combined $\omega_{i,l}$ manufacturing deviations were generated using Latin Hypercube Sampling (LHS). For the realization of a specific manufacturing deviation ω_i , either the corresponding PDF or a rectangular distribution for the respective value range was chosen. It was assumed that the occurrences of considered manufacturing deviations in production were not correlated with each other.

For a sufficient coverage of the high-dimensional space of possible manufacturing deviations, a sufficiently large number of sets L needs to be calculated (Bellman 1961; Loeppky et al. 2009).

6.2.1 Selection of data-driven surrogate models

In the following, Kriging surrogate models and artificial neural networks (ANN) were selected based on existing, successfully implemented surrogate models (cf. Section 3.2.4). Both approaches fulfill the requirement of a prediction adherent to the *cycle time*. Both types of models also process *vectorial (multidimensional) inputs*, so that a set l of combined manufacturing deviations ω_l can be used as input. Compared to the available, user-friendly

library¹ for implementing different Kriging model approaches for scalar and vectorial outputs (Bouhleb et al. 2019), the ANN has the additional advantage that different *binary cases* (specimen compositions) can be discerned in a single model. The Python™ deep learning API Keras was chosen for ANN model creation. Using an ANN allowed for the direct learning of different stiffnesses or strengths in different component regions. For a Kriging model approach, multiple models needed to be trained for the respective desired output size. However, the advantage of the Kriging model is the *inherent uncertainty information*, whereas this information has to be provided by the multiple generation of different models based on slightly altered training data sets for ANNs (Coral et al. 2016). Furthermore, it was necessary that the functional predictions, after being transferred to data-driven surrogate models, reproduce the real component behavior as precisely as possible (*precision*), with low systematic deviation (bias). The basic suitability has also already been demonstrated for both types of surrogate model (cf. Section 3.2.4). A high degree of *robustness* of the surrogate model was required, so that the function prediction is only slightly sensitive to uncertain input variables (in-line measurement results). This requirement is the subject of the measurement uncertainty analysis (cf. Section 6.2.4)

Modeling approach	Cycle time	Vectorial in-/output	Binary cases	Inherent uncertainty information	Precision	Robustness
Kriging	●	●	○	●	●	Section 6.2.4
ANN	●	●	●	○	●	Section 6.2.4

Table 6.2: Comparison of ANNs and Kriging models for data-driven surrogate modeling and their suitability with regard to the defined requirements: fulfilled (●), not fulfilled (○)

6.2.2 Model training

Generally, virtual training data (input-output relation of FE simulations) within the whole experimental space of expected manufacturing deviations is needed for both types of surrogate models (cf. Section 6.2). FE simulation results were additionally generated as test data and compared to the surrogate model prediction. However, slightly different approaches were considered to take the respective advantages into account and are described in the remainder of this section.

6.2.2.1 Kriging model

Discrete (binary) compositions of a component exist when considering DiCo- and CoDiCo-SMC as well as delaminations. Thus, four independent training sets (training subsets) were

¹Bouhleb, M.A.; Hwang, J.T.; Bartoli, N.; Lafage, R.; Morlier, J.; Martins, J. R. R. A., *SMT: Surrogate Modeling Toolbox*. <https://smt.readthedocs.io/en/latest/> (accessed on Jan. 5, 2022).

chosen for the four essential specimen compositions (DiCo-SMC, DiCo-SMC with delamination, CoDiCo-SMC, CoDiCo-SMC with delamination). Equation 6.8 displays row-wise the output values for the four essential specimen compositions, with the stiffness (here: Young's modulus E), the Puck damage criteria $f_{E,\text{Puck,FF}}$, $f_{E0,\text{Puck}}$, and $f_{E1,\text{Puck}}$ (Verein Deutscher Ingenieure e.V. 2006) in the Co-SMC, as well as the stress exposure $f_{E,0}$, and $f_{E,1}$ to $f_{E,M}$ in the M different measurement regions of the DiCo-SMC. An individual Kriging model needs to be trained for every row in the matrix.

$$\hat{\mathbf{y}}_{\text{Kr}} = \begin{bmatrix} \hat{\mathbf{y}}_{\text{DiCo}} \\ \hat{\mathbf{y}}_{\text{DiCo,Delam.}} \\ \hat{\mathbf{y}}_{\text{CoDiCo}} \\ \hat{\mathbf{y}}_{\text{CoDiCo,Delam.}} \end{bmatrix} = \begin{bmatrix} \hat{E} & 0 & 0 & 0 & \hat{f}_{E,0} & \hat{f}_{E,1} & \dots & \hat{f}_{E,M} \\ \hat{E} & 0 & 0 & 0 & \hat{f}_{E,0} & \hat{f}_{E,1} & \dots & \hat{f}_{E,M} \\ \hat{E} & \hat{f}_{E0,\text{Puck}} & \hat{f}_{E1,\text{Puck}} & \hat{f}_{E,\text{Puck,FF}} & \hat{f}_{E,0} & \hat{f}_{E,1} & \dots & \hat{f}_{E,M} \\ \hat{E} & \hat{f}_{E0,\text{Puck}} & \hat{f}_{E1,\text{Puck}} & \hat{f}_{E,\text{Puck,FF}} & \hat{f}_{E,0} & \hat{f}_{E,1} & \dots & \hat{f}_{E,M} \end{bmatrix} \quad 6.8$$

Iterative reduction of model uncertainty First, an iterative approach was chosen for training a Kriging model, making use of the inherent uncertainty information. Even when training data is evenly distributed, regions with a higher model uncertainty exist. An iterative training approach aimed to prevent regions of high uncertainty by explicitly choosing those regions as training data for a next training iteration t . Therefore, an initial training set \mathbf{T}_1 five times the input size was generated based on LHS. Afterwards, multiple rounds of consecutive training iterations were conducted based on a search for the regions with the highest variances. A subsequent generation of optimal training data \mathbf{T}_t and re-training with those newly generated FE data was performed at the points with the highest variances. However, evaluating and assessing the variances for the existing Kriging model using a full factorial design would drastically increase the runtime. Therefore, a grid search based on a LHS with a sufficient high number G is proposed for evaluating the local variances of the existing Kriging model. The regularized squared variances of all output values of an essential specimen composition e were calculated for $g = \{1, \dots, G\}$ specimen realizations according to Equation 6.9 in order to find these configurations for each of the four surrogate model compositions (cf. Equation 6.8) which offer the most potential for improvement in training iteration t . The size of the additional training sets was chosen to be 80. The procedure was repeated until no further improvements were achieved in the test set \mathbf{P}_1 (convergence, cf. Section 6.2.3). Regularization was performed because of the existing scale differences for stiffness and failure criteria. Squared variances were chosen following the idea of least squares.

$$S_{t,e,g}^2 = S^2(E)_{t,e,g} + \sum_{k=1}^3 S^2(f_{E,\text{Puck},k})_{t,e,g} + \sum_{k=0}^M S^2(f_{E,k})_{t,e,g} \quad 6.9$$

Direct approach The size of each training set was directly chosen to be the size after convergence was achieved in the iterative approach. This approach brings the advantage of evenly distributed training data within the experimental space. The respective output values were independently generated for the four essential specimen compositions based on the FE simulations.

6.2.2.2 Artificial neural network

The training data set for the neural network was composed according to the **direct approach** of the four training subsets (cf. Section 6.2.2.1). However, from this training data set, 20% of the data were randomly retained as a development (validation) set to adjust the hyperparameters (Ripley 1996). The ReLU (Rectified Linear Unit) activation function was chosen. The loss function was chosen as the mean squared error (MSE), based on best practice for regression problems (Reed & Marks 1998). The ANN was trained in 1500 epochs with a batch size of 50. Early stopping was triggered if no significant improvements were identified in 20 consecutive epochs to prevent overfitting. Adam was used as optimization algorithm. Since ANNs are able to differentiate between classes (Aggarwal 2018), Equation 6.8 simplifies for the ANN to equation Equation 6.10, directly integrating the different potential specimen compositions. The row vector represents the output neurons of the ANN.

$$\hat{\mathbf{y}}_{\text{ANN}} = \left[\hat{E} \quad \hat{f}_{E0,\text{Puck}} \quad \hat{f}_{E1,\text{Puck}} \quad \hat{f}_{E,\text{Puck,FF}} \quad \hat{f}_{E,0} \quad \hat{f}_{E,1} \quad \dots \quad \hat{f}_{E,M} \right] \quad 6.10$$

6.2.3 Model assessment

Three different data sets served for assessing the performance of both surrogate models. A first test set P_1 was generated using LHS to evaluate the performance over the evenly distributed, whole parameter space. It was 20% of the size of the training set for each specimen composition. Additionally, the performance of the surrogate model was evaluated based on a set of virtual experiments P_2 and physical experiments P_3 . The comparison to physical experiments allowed a direct statement on the prediction performance and the suitability for an application in the real world. However, the surrogate model was trained on virtual data. Therefore, the comparison to the deterministic virtual experiments was also used. This allowed a statement about the general ability of the surrogate model to describe the parameter space of technical relevance based on the FE simulations. As a key metrics, the *RMSE* was used analogously to Equation 6.3 again to calculate the difference between the function prediction of the surrogate model \hat{y}_{SM} and the test set \hat{y}_{test} , dependent on the test sets $P_i = \{P_1; P_2; P_3\}$ and its respective number of data points K_i , in Equation 6.11. The variable \hat{y}_{SM} refers to the scalar prediction, such as the Young's modulus, of a surrogate model (cf. Equation 6.8 and 6.10). Occurring differences between b_{P_2} and b_{P_3} are due to an

insufficient description of reality by the FE simulation. Differences between b_{P_1} and b_{P_2} give conclusion about the local validity of the model in comparison to the generalizability over the whole parameter space.

$$b_{P_i} = RMSE(P_i) = \sqrt{\frac{\sum_{k=1}^{K_i} (\hat{y}_{test,i,k} - \hat{y}_{SM,i,k})^2}{K_i}}, \text{ for } \begin{cases} i = \{1;2;3\} \\ \hat{y}_{test,i} = \{\hat{y}_{Sim,P_1}; \hat{y}_{Sim,P_2}; y_{P_3}\} \end{cases} \quad 6.11$$

Analogously to Equation 6.4, the relative bias $CV_{RMSE}(P_i)$ is determined by normalization using the averaged output of a test data set $\bar{y}_{test,i}$.

6.2.4 Uncertainty of the surrogate models

Uncertainties of surrogate models consist firstly of the uncertainties of the input variables $u_{SM,I}$ and of the surrogate model itself based on the available training data $u_{SM,T}$ (Coral et al. 2016). Furthermore, the systematic model deviation, described by equation Equation 6.11, has to be considered (Zhang 1993). Overall, the combined uncertainty of a surrogate model $u_{c,SM}$, neglecting correlations of the individual terms, follows:

$$u_{c,SM} = \sqrt{u_{SM,I}^2 + u_{SM,T}^2 + b^2} \quad 6.12$$

The next two subsections describe the determination of the uncertainty contributions $u_{SM,I}$ and $u_{SM,T}$ in more detail.

6.2.4.1 Determination of the standard uncertainty due to model training data

Due to the inherent uncertainty information in Kriging models, different approaches were taken for ANN and Kriging model.

Artificial neural network The influence of data variability, i.e. the dependence on the training data, is not directly apparent for an ANN. Coral et al. (2016) proposed the training of an ANN committee, the repeated realization of slightly different ANNs based on random changes on training data.

For this purpose, the L sets of training data, based on LHS, were used (cf. Section 6.2.2). These were extended by $M = 0.1 \cdot L$ randomly generated additional training data via MCM. From the totally available set $T = T_L \cup T_M$ for model training, $r = \{1, \dots, R\}$ random combinations for L -sized training sets were drawn in a bootstrapping method. With these combinations, R realizations of ANN were generated. Propagation of the overall C test sets then led to

normally distributed function predictions \hat{y}_{SM} , from which the mean and standard deviation were estimated. The standard uncertainty due to model training data was then determined by averaging the C different standard deviations:

$$u_{SM,T,ANN} = \frac{1}{C} \sum_{i=1}^C u_{SM,T,i} \quad 6.13$$

The procedure is visualized in Figure 6.2.

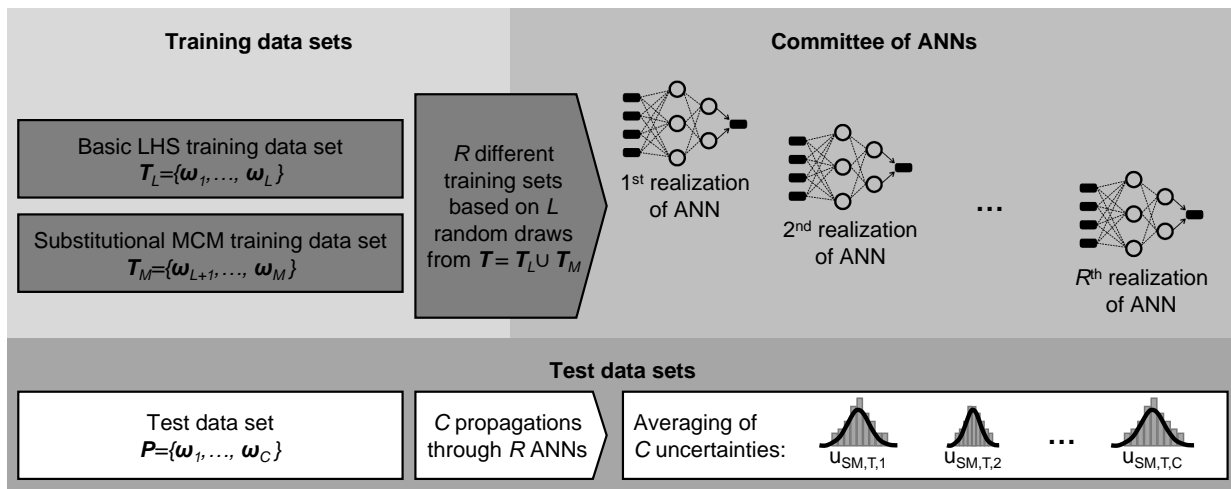


Figure 6.2: Determination of the standard uncertainty due to model training data for an artificial neural network, own illustration based on Coral et al. (2016)

Kriging model Based on the given training data, the results of the existing Kriging model were subject to locally different, but quantified uncertainties. Similar to the methodology for iterative reduction of model uncertainty presented in Section 6.2.2.1, the mean uncertainty of the $g = \{1, \dots, G\}$ randomly generated data points using LHS were used to quantify the training uncertainty:

$$u_{SM,T,Kriging} = \frac{1}{G} \sum_{i=1}^G u_{SM,T,i} \quad 6.14$$

6.2.4.2 Determination of the standard uncertainty due to input quantities

The same quantities describing in-line measurements, that were already considered for the measurement uncertainty analysis of the FE simulation, were considered again (cf. Table 6.1 and Appendix A8). At this point, a screening for most influential quantities was omitted, since the evaluation of the surrogate models was significantly faster than the calculation of the FE simulation. According to their PDF, $q = \{1, \dots, Q\}$ different combinations of realized input

variables for each configuration from the test data set P were drawn and propagated through the surrogate models (ANN and Kriging model), based on the training set T_L . Thus, C different normal distributions for the function prediction of the test data followed. Again, $u_{SM,I}$ was determined by the mean value of the standard deviation.

Additionally, Häfner & Biehler et al. (2018) suggested to directly propagate the input variables through the ANN committee. Thus, a joint (merged) determination of $u_{SM,T}$ and $u_{SM,I}$ based on $R \cdot Q$ realizations is obtained. This procedure was followed within this work to determine the ANN uncertainty.

7 Application of function-oriented measurements for CoDiCo-SMC

The presented research approach was evaluated in two experimental applications, representing two different load cases of a CoDiCo-SMC specimen. Generally, the experimental and simulation setup as well as the results of the FE models and the surrogate models are described in both cases.

7.1 Pre-study on tensile specimens

The simplest test specimen imaginable, a tensile specimen with a full Co-SMC layer, was used to demonstrate the basic suitability of adaptive FE modeling and surrogate modeling. Measurement results were not considered for the first test specimen because of the full Co-SMC layer.

7.1.1 Experimental design

An overview of the requirements for the test specimen, the specimens manufactured, and the experimental procedure is given in this section.

7.1.1.1 Specimen selection and geometry

The first validation specimen, a CoDiCo-SMC tensile specimen with combined manufacturing deviations, builds upon the existing work of Schäferling et al. (2019). The tensile test specimens were further selected to satisfy the following requirements:

- 1) Reproducibility of the different test specimen configurations
- 2) Sufficient number of specimens for statistical validation of scattering material properties
- 3) Phenomenological description of the influence of manufacturing deviations (effects of defects)
- 4) Validation of the simulation model under a simple stress state
- 5) Validation of the surrogate modeling methodology

The following manufacturing deviations in DiCo-SMC and CoDiCo-SMC tensile specimens were considered:

- 1) Deviating fiber mass fraction in DiCo-SMC
- 2) Delamination in DiCo-SMC
- 3) Delamination at CoDiCo interface
- 4) Misorientation of Co-SMC layer

A component-specific quantification of the manufacturing deviations with corresponding measurement technology was not carried out on these pre-study test specimens, since the validation of the simulation model was the main focus.

7.1.1.2 Manufactured configurations

DiCo-SMC prepregs with varying, nominal FFM ξ_{nom} (41, 45, and 50 wt.-%) were manufactured and stacked to a nominal thickness of 2 mm (two layers of DiCo-SMC). A full Co-SMC layer (nominal thickness: 0.3 mm) was added optionally in the stacking process on top of the DiCo-SMC stack to produce hybrid specimen. Artificial delaminations of varying lengths were optionally integrated over the entire width of the specimen between the two DiCo-SMC layers (abbreviation: M) or between the CoDiCo interface (abbreviation: T). They consisted of a 130 μm thick Teflon (PTFE) foil. The mold cavity (458 x 458 mm²) was heated up to 145°C, fully covered with tailored prepreg material and closed with a maximum hydraulic press force of 500 kN for 90 s. Rectangular coupon specimen (200 x 15 mm², cf. Figure 7.1b), according to the recommendations by Trauth (2018) for CoDiCo-SMC, were waterjet cut from all plates. Misorientations of the Co-SMC layer (10° and 20°) were realized by waterjet cutting. Different tensile specimens with varying nominal manufacturing deviations were realized (cf. Table 7.1).¹ Each configuration consisted of at least 15 samples. The mean thickness of every configuration was calculated based on three measurements per specimen.

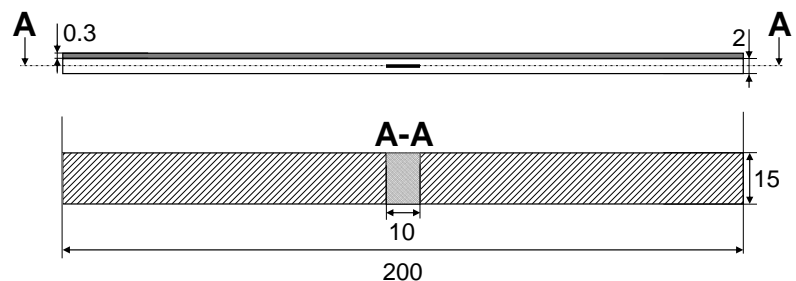
7.1.1.3 Experimental procedure

Tensile tests were performed on a Zmart.Pro universal testing machine by ZwickRoell (load cell capacity of 200 kN). The hydraulic clamping length was 50 mm at each side of the specimen. Sandpaper was used as a clamping aid instead of glued end tabs. A clamped specimen is shown in Figure 7.1a. Every specimen was preloaded up to 100 N before being loaded until fracture with a nominal loading rate of 1 mm/min. Young's modulus was determined using a least squares method in a strain range between 0.05% and 0.25% (Deutsches Institut für Normung e.V. 2019). Tensile strength was defined by an abrupt load drop of 8 MPa to account for an early failure of the Co-SMC under certain manufacturing deviations. Failure was only evaluated when the specimen failed at sufficient distance from the clamping area. At least five specimens were considered for the evaluation of tensile strength for every configuration.

¹An additional horizontal line is added to Table 7.1 to separate specimens 17 to 20. For these specimens, the delamination was located between Co- and DiCo-SMC.

Table 7.1: Manufactured tensile specimen configurations; Delamination in DiCo-SMC (M); Delamination at CoDiCo interface (T); standard deviation given in square brackets

No.	Abbrev.	ξ_{nom} (wt.-%)	Co-SMC angle ($^{\circ}$)	Delamination size (mm ²)	Mean thickness (mm)
1	41	41	-	-	1.76 [0.03]
2	41.M10	41	-	10 x 15	1.90 [0.03]
3	41.M20	41	-	20 x 15	1.89 [0.03]
4	41.0	41	0	-	2.26 [0.02]
5	41.0.M10	41	0	10 x 15	2.09 [0.02]
6	41.10	41	10	-	2.19 [0.04]
7	41.20	41	20	-	2.22 [0.02]
8	41.20.M20	41	20	20 x 15	2.14 [0.04]
9	45.M10	45	-	10 x 15	2.32 [0.02]
10	45.20	45	20	-	2.36 [0.02]
11	50	50	-	-	2.49 [0.02]
12	50.M20	50	-	20 x 15	2.49 [0.03]
13	50.0	50	0	-	2.55 [0.06]
14	50.0.M20	50	0	20 x 15	2.61 [0.04]
15	50.20	50	20	-	2.73 [0.05]
16	50.20.M20	50	20	20 x 15	2.14 [0.06]
17	41.0.T10	41	0	10 x 15	2.12 [0.03]
18	41.0.T20	41	0	20 x 15	2.14 [0.04]
19	41.20.T20	41	20	20 x 15	2.14 [0.05]
20	50.20.T20	50	20	20 x 15	2.72 [0.05]



(a) Clamped CoDiCo-SMC tensile specimen (b) Nominal geometry of a CoDiCo-SMC tensile specimen; including a delamination in the DiCo-SMC of 10 mm length (M10)

Figure 7.1: Tensile test setup and geometry of the tensile specimen

7.1.2 General observations

Basic findings about the influence of (combined) manufacturing deviations in CoDiCo-SMC are described in the following.

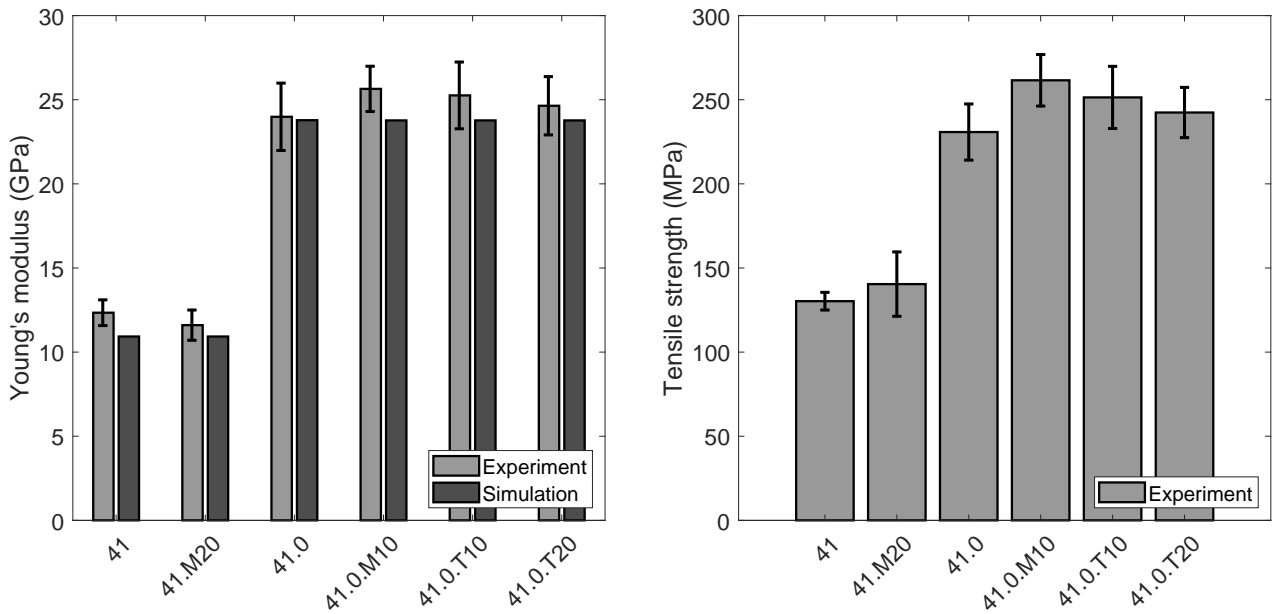
7.1.2.1 Combined delamination and carbon fiber misorientation

A delamination showed a negligible influence on the stiffness and strength for DiCo-SMC as well as CoDiCo-SMC specimens in the uniaxial tensile test (cf. Figure 7.2). This behavior can be mechanically explained by a parallel connection of two beam elements. The evaluation of the simulated Young's modulus also showed no difference in stiffness in the presence of delamination.¹

However, if a delamination was combined with a Co-SMC misorientation, both stiffness and strength were reduced not only as a result of the suboptimal loading of the continuous fibers, but also due to a smaller distance of the delamination to the Co-SMC (cf. delamination position "M" vs. "T" in Figure 7.3). The non-fiber-parallel force flow in the Co-SMC led to a bulging and twisting, which was more severe with a smaller residual thickness ("T"). The twisting and bulging induced local stress concentrations. Ultimately, inter fiber fracture (IFF, cf. Figure 7.4b) occurred instead of fiber fracture (FF, cf. Figure 7.4a). The regions of increased maximum principal stress in Figure 7.4c are consistent with the observed failure type and location (cf. Figure 7.4b).

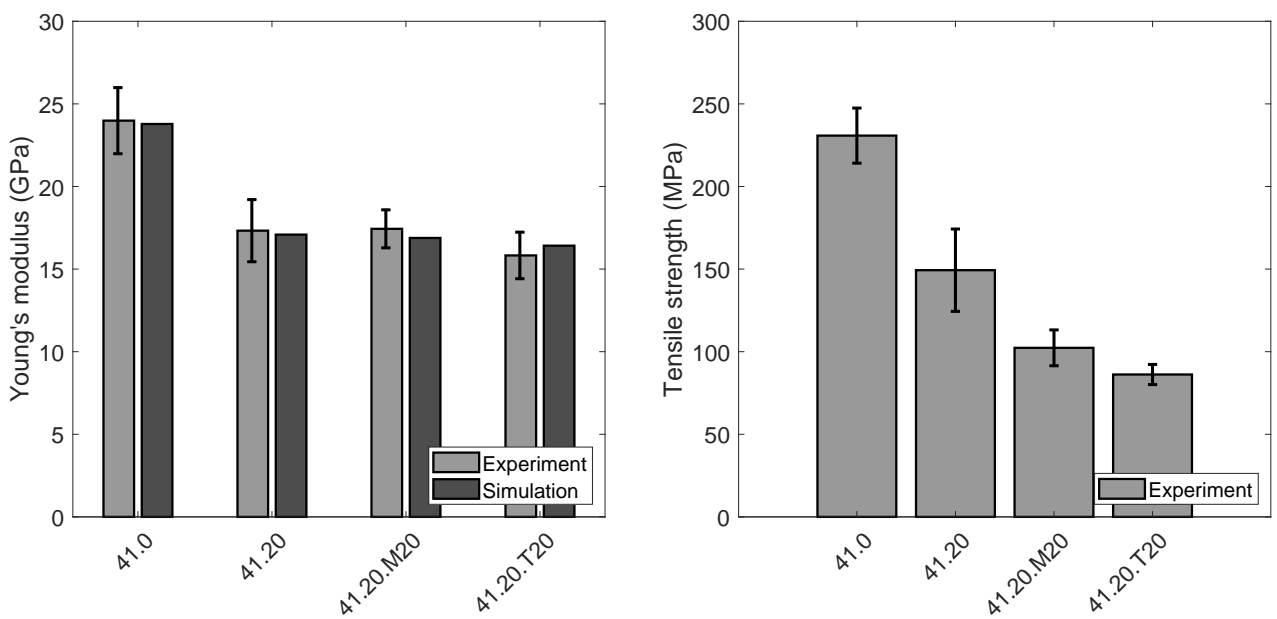
The results show that the criticality of delaminations should be evaluated depending on the load case, so that a general rejection could possibly be avoided in a function-oriented consideration. However, if a Co-SMC misorientation is present, delaminations below the Co-SMC are to be classified as very critical, due to a twisting and bulging occurring in the Co-SMC. In this case, CoDiCo-SMC failed even earlier than a pure DiCo-SMC. Nevertheless, the possibility remains that delaminations could be tolerated in DiCo-SMC as long as they are not on the load path and below the Co-SMC reinforcement.

¹The model setup presented in Chapter 6 using XFEM does not allow the representation of delaminations at the interface between Co- and DiCo-SMC. Nevertheless, in order to verify the phenomenological observations of combined manufacturing delaminations in tensile specimens, an alternative modeling was considered. Here, fixed nodal connections between the DiCo and CoDiCo-SMC were locally removed to represent a delamination (A_Müller-Welt 2019). Component stiffnesses could also be represented well with this technique. A drawback, however, is that strengths cannot be determined due to singularities at the boundaries between existing and removed nodal connections.



(a) Young's modulus for a delamination as the only manufacturing deviation (b) Tensile strength for a delamination as the only manufacturing deviation

Figure 7.2: Influence of a single delamination on tensile properties



(a) Combined influence on Young's modulus (b) Combined influence on tensile strength

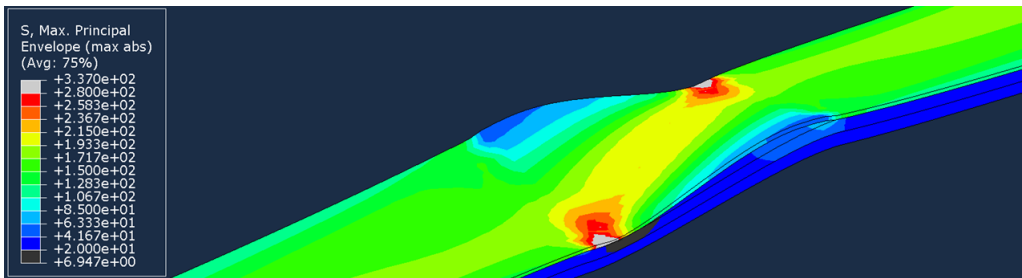
Figure 7.3: Influence of Co-SMC misorientation and delamination on tensile properties



(a) Fiber fracture of Co-SMC (41.0.T20)



(b) Inter fiber fracture of Co-SMC (41.20.T20)



(c) Simulated stress distribution in 41.20.T20 (displacements scaled by a factor of 25)

Figure 7.4: Observed damages in tensile specimen with combined manufacturing deviations

7.1.2.2 Tensile strength for varying glass fiber fraction

The tensile strengths for pure DiCo-SMC specimens with nominal 41 and 50 wt.% FMF were evaluated to determine the influence of varying glass fiber fractions on the strength. Figure 7.5 also includes the mean and standard deviation (SD) from the investigations of Trauth (2018) in addition to the boxplots of the experimental results of this test series. Trauth (2018) considered as well a planar isotropic fiber orientation distribution of the same material formulation. Overall, a linear increase in strength with reasonable deviations was observed ($RMSE = 6.58 \text{ MPa}$, $R_{\text{adj}}^2 = 0.884$).

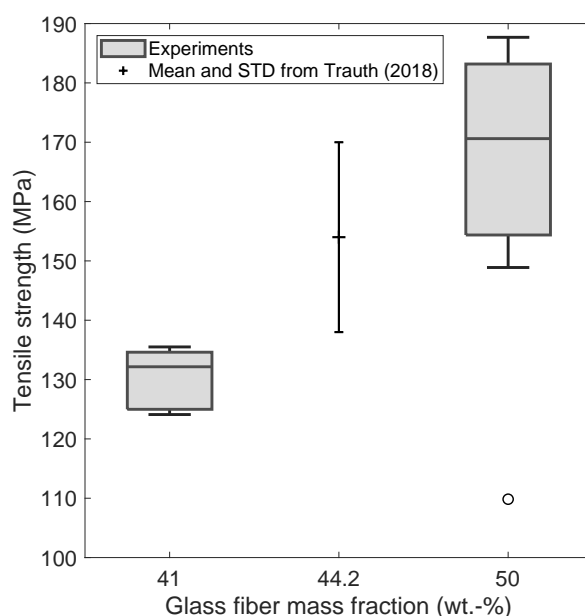


Figure 7.5: Experimental results for the tensile strength of DiCo-SMC with varying glass fiber mass fraction; supplemented by results from Trauth (2018)

7.1.3 FE model

The CoDiCo-SMC tensile specimen was FE modeled with a total length of 120 mm and a width of 15 mm. At each side, 10 mm were reserved for clamping resulting in ROI lengths of 100 mm for both experiments and simulations. The DiCo-SMC model thickness was individually adjusted according to the mean measured specimen thickness (cf. Table 7.1). The thickness of the Co-SMC layer was kept at its nominal thickness of 0.3 mm. Both edges across the width of the specimen in the clamping areas (CA) were connected with a reference point (RP, cf. Figure 7.6). One reference point was fixed, while the second reference point was loaded with a longitudinal force of 1500 N. Four different measurement regions (MR, 15 mm in diameter) for assigning local GF fractions were defined. These four regions of varying GF fraction and an integrated delamination are visualized in Figure 7.6.

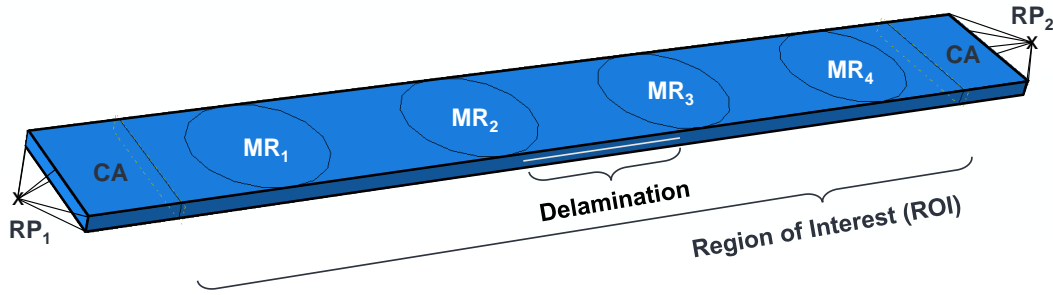


Figure 7.6: Model assembly for DiCo-SMC tensile specimen FE model, including local measurement regions for GF fractions and a delamination

The element side length was 0.77 mm (7500 elements in the ROI). A convergence study showed no significant further increase of strain energy after 3350 elements in the ROI (cf. Figure A7.1). The used material parameters are given in Appendix A5. The Young's modulus was calculated using the simulated strain energy W (*ALLSE* in Abaqus) by:

$$E = \frac{1}{2} \frac{F^2 l}{WA} \quad 7.1$$

The force at failure was extrapolated using the stretch factor f_s both for Co- and DiCo-SMC ($F_{\max,Co}$, $F_{\max,DiCo}$). The minimum was used to calculate the respective tensile strength R^+ :

$$R^+ = \frac{\min(F_{\max,Co}, F_{\max,DiCo})}{A} \quad 7.2$$

7.1.4 Assessment of the FE model

In accordance with the simulation methodology using XFEM to represent delamination in DiCo-SMC (cf. Section 6.1), only the first 16 configurations from Table 7.1 were used to assess the FE model in the remainder of this section. The systematic deviation (bias) as well as a complete uncertainty analysis based on the input quantities is investigated.

7.1.4.1 Systematic deviations to the experiments

The experimental results for the Young's modulus of these configurations are compared to the simulated results in Figure 7.7. Across all configurations, the *RMSE* was 1.34 GPa ($CV_{RMSE} = 7.8\%$). However, it is noticeable that the Young's modulus of the configurations with 50 wt.-% FMF (configurations no. 11 to 16 in Table 7.1) was systematically overestimated. This is not the case for the configurations with 41 and 45 wt.-%. These configurations exhibited a significantly lower *RMSE* of 0.65 GPa ($CV_{RMSE} = 3.8\%$) compared to the configurations 11 to 16 ($RMSE = 1.88$ GPa, $CV_{RMSE} = 10.8\%$). This leads to the assumption that fibers were

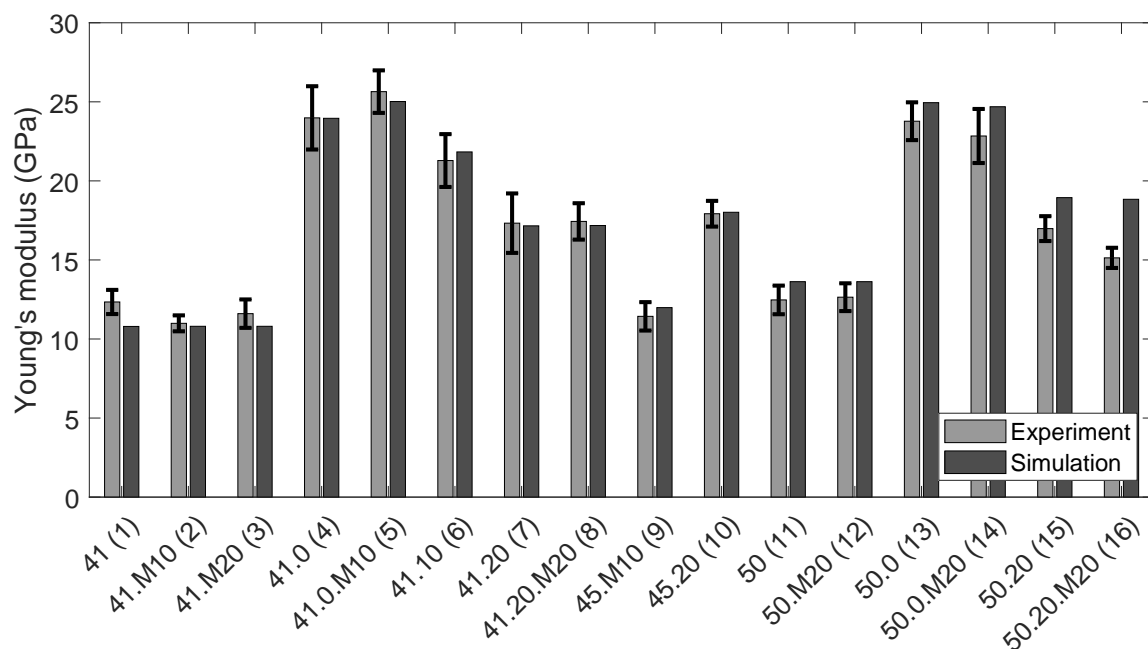


Figure 7.7: Experimental and simulated Young's modulus for CoDiCo-SMC tensile specimen; error bars indicate one standard deviation; configuration no. in parenthesis

not sufficiently impregnated for those high fiber content of 50 wt.%. Thus, the analytically predicted material properties no longer held. Overall, it can be stated that the FE model predicted the stiffness well for the first 16 configurations.

The experimental results for tensile strength are compared with the simulated results in Figure 7.8. Reasonable results could only be obtained for configurations of pure DiCo-SMC or with high Co-SMC misorientations of 20°. The nominal longitudinal tensile strength of the Co-SMC led to an overestimation of this specific hybrid material composition (cf. configuration 41.0). The material properties used were determined for a Co-SMC specimen with 1 mm thickness (Trauth 2018) in contrast to the single layer Co-SMC used here.

The failure was well described for the configuration 41.20.M20, especially when taking into account configuration 41.20. The delamination lead to a bulging of the specimen, similar to Figure 7.4c, which locally increased the stress concentration and lead to an earlier failure. In this case, the longitudinal tensile strength had less influence on failure due to the existing stress state and the misorientation (cf. Section 2.2.5.3).

The existing deviations between simulation and experiment for pure DiCo-SMC and delamination indicate that further micromechanical effects exist, which cannot be correctly represented by the purely geometric integration of delamination into a homogenized DiCo-SMC material.

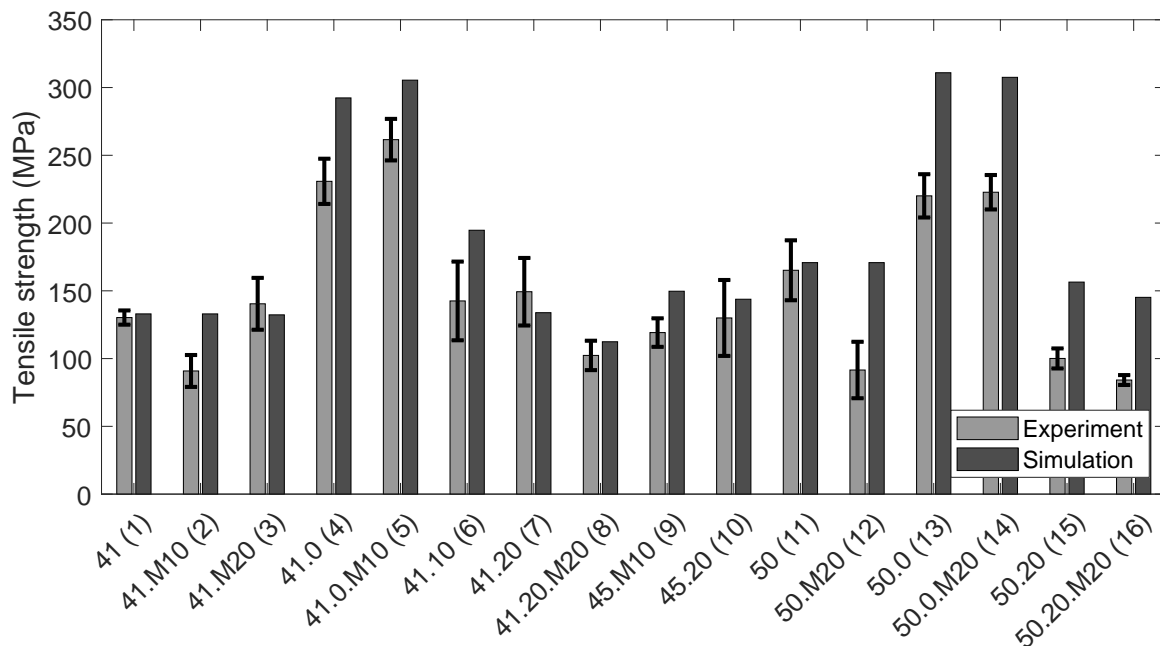


Figure 7.8: Experimental and simulated tensile strength for CoDiCo-SMC tensile specimen; error bars indicate one standard deviation; configuration no. in parenthesis

Since the experimental tensile strength of the CoDiCo-SMC specimen with 50 wt.% was even lower than the strength of comparable configurations with 41 wt.%, the hypothesis that the material was too dry for this FMF (insufficient fiber impregnation) was confirmed.

Overall, the implemented simulation model including material modeling, simulation setup and existing material parameters allowed only limited conclusions about the influence of manufacturing deviations on strength. Basic tendencies for CoDiCo-SMC specimen were in agreement with the experimental results. Reliable failure strength values could not be obtained for all configurations. Even if the six configurations with 50 wt.-% are excluded from analysis, a $RMSE$ of 34.3 MPa ($CV_{RMSE} = 22.9\%$) still remained. The calculation of the bias is summarized for both Young's modulus and tensile strength in Table 7.2. CV_{RMSE} is given in percentage for easier comparison between E and R^+ .

Table 7.2: Systematic deviations (bias) of the FE simulation for CoDiCo-SMC tensile specimen; CV_{RMSE} given in percentage

Included configurations for calculation of	No. 1 to 16		No. 1 to 10		No. 11 to 16	
	E (GPa)	R^+ (MPa)	E (GPa)	R^+ (MPa)	E (GPa)	R^+ (MPa)
$RMSE$	1.34	50.2	0.65	34.3	1.88	64.2
CV_{RMSE} (%)	7.8	33.8	3.8	22.9	10.8	44.3

7.1.4.2 Uncertainty analysis

Five different specimen configurations were considered for the uncertainty analysis. Different FMF in the DiCo-SMC as well as different Co-SMC patch orientations were considered. Based on the screening analysis (one factor at a time) of all potential input uncertainty contributions¹ (cf. Table 6.1), nine input parameters could be neglected based on their relative significance below 0.5% for all representative specimen configurations under investigation. Thus, six to eight parameters remained dependent on the configuration (cf. Table 7.3). The influence of voids was of minor relevance as long as the Co-SMC layer is mostly loaded in fiber direction. The measurement uncertainty for Co-SMC patch orientation lost drastically of relevance for strong misorientations due to the generally reduced reinforcement effect of the Co-SMC layer. In contrast, the FVF and thickness of the Co-SMC layer were of highest relevance. Input variables that describe the properties of the prepreg as a realization of the prepreg manufacturing process (ξ , ϕ_{CF} , d_T) contributed significantly to the uncertainties. The inherent material uncertainties of the raw materials (E_{GF} , $E_{CF,\parallel}$, E_{UPPH}) were less important, especially for perfectly oriented Co-SMC layers

Table 7.3: Screening analysis: Relative influence of one standard deviation on Young's modulus for different configurations; remaining input parameters highlighted in gray; according to A_Debowski 2020

Input parameter	Configuration				
	41.0.M10	41.10.M20	41.20.M20	45.0.M20	45.10.M20
ξ	2.2 %	2.7 %	3.7 %	2.3 %	2.8 %
ϕ_{Void}	-0.3 %	-0.4 %	-0.6 %	-0.3 %	-0.4 %
E_{GF}	1.3 %	1.6 %	2.1 %	1.5 %	1.7 %
E_{UPPH}	2.7 %	3.4 %	4.8 %	2.6 %	3.3 %
ϕ_{CF}	6.4 %	5.6 %	4.2 %	6.1 %	5.4 %
$E_{CF,\parallel}$	2.7 %	2.2 %	1.2 %	2.6 %	2.1 %
d_T	6.5 %	5.2 %	2.9 %	6.2 %	4.9 %
γ_T	-0.2 %	-2.5 %	-3.0 %	-0.1 %	-2.3 %

As a next step, the remaining parameters were subjected to the LHS based on their input uncertainties, which led to normal distributed realizations for the Young's modulus of different configurations. An exemplary realization of the uncertain Young's modulus including the fitted normal distribution is given in Figure 7.9a for configuration 41.0.M20. The highlighted area covers occurring values for the Young's modulus with 95% confidence. Simulated and experimental standard deviations are of similar size (cf. Figure 7.9b). Simulations could not

¹Displacements of the full Co-SMC layer (x_T , y_T) and displacements of the delamination along the width direction of the specimen were not considered in this study.

be compared to experiments for the last two simulated configurations. These configurations were added to virtually investigate the influence of the input parameters for a different FMF. Experimental and simulated standard uncertainties decreased with increasing CF misorientation. This reaffirmed the high contribution of existing uncertainties of the Co-SMC properties (ϕ_{CF} and d_T).

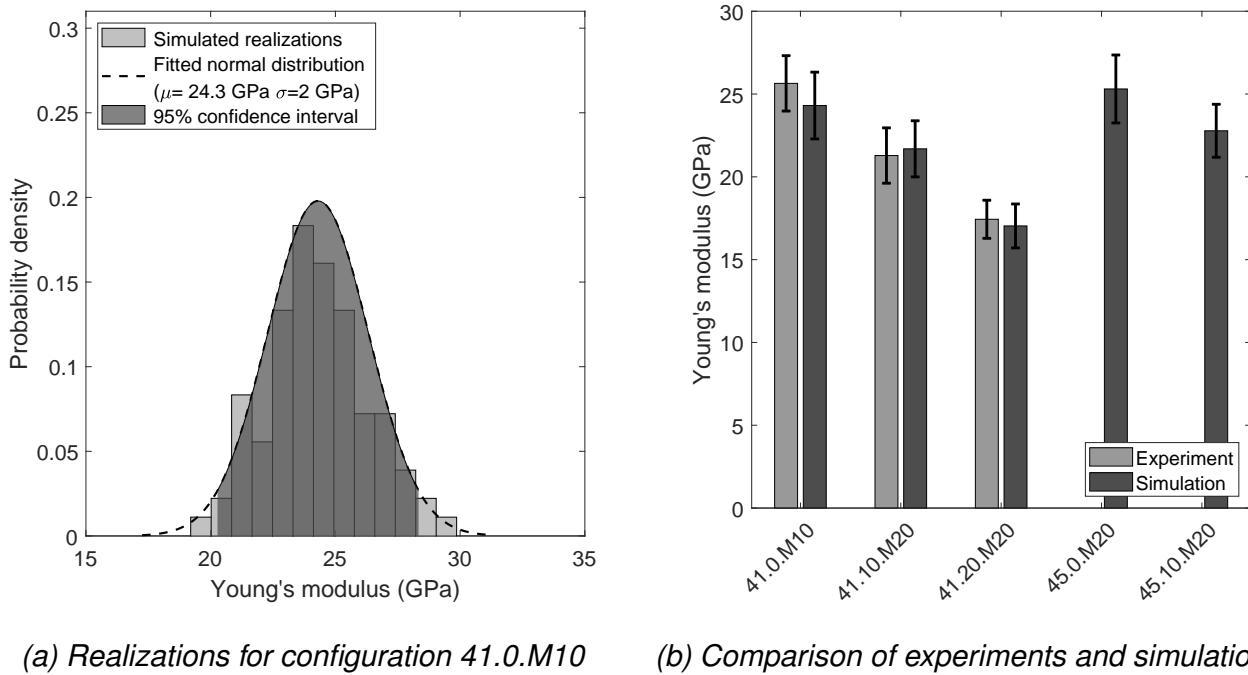


Figure 7.9: Simulated and experimental uncertainties of Young's modulus for CoDiCo-SMC tensile specimen; error bars indicate one standard deviation

Additionally, the influence of measurable (ξ , ϕ_{Void} , γ_T) and non-measurable input quantities (E_{GF} , E_{UPPH} , $E_{CF,\parallel}$, ϕ_{CF} , d_T) was investigated in a separate analysis. The uncertainty contribution of the respective group was calculated based on the results of a LHS. Overall, the uncertainty caused by non-measurable input quantities was substantially larger, as given in Table 7.4.

Table 7.4: Uncertainty contributions for measurable and non-measurable input quantities (tensile specimen)

Configuration	Uncertainty of		Overall
	measurable	non-measurable	
DiCo	330 MPa	849 MPa	911 MPa
CoDiCo	276 MPa	2058 MPa	2077 MPa

The overall uncertainty budget according to Equation 6.5 is given in Table 7.5, using a coverage factor $k = 2$ for calculating the expanded uncertainty U_{Sim} . A reference simulation with 30,000 elements in the ROI was conducted to determine $u_{\text{Sim,D}}$. The bias b was calculated as the *RMSE* of the configuration with 41 and 45 wt.-% FMF (cf. Section 7.1.3). Remarkably, the uncertainties of the input parameters $u_{\text{Sim,I}}$ dominated the combined uncertainties for all configurations. For reference, the expanded uncertainty U_{Sim} of configuration 41.0.M10 is approximately 17.4% of its expected Young's modulus.

Table 7.5: Uncertainty budget for FE simulation of Young's modulus of CoDiCo-SMC tensile specimen (MPa)

	41.0.M10	41.10.M20	41.20.M20	45.0.M20	45.10.M20
$u_{\text{Sim,I}}$	2016	1695	1326	2051	1601
$u_{\text{Sim,D}}$	5.3	0.3	1	3.2	0.1
$ b $			646		
$u_{\text{c,Sim}}$	2117	1813	1475	2151	1727
U_{Sim}	4234	3627	2951	4301	3453

7.1.5 Surrogate model

The general model setup and training procedure is presented in the following two subsections for both surrogate modeling cases.

7.1.5.1 Kriging model

Four different training subsets were considered for training the different specimen compositions. The size of the experimental design was initially determined to be five times the number of considered input parameters for each specimen composition (cf. Table A8.1), leading to training sets of 55 to 70 specimen configurations for each composition (total sum: 250) to initialize the iterative training approach. Further training data was added in iterations based on the methodology described in Section 6.2.2.1.

The size of the experimental design for a direct training approach was determined by the number of training data after convergence was achieved in the iterative approach.

7.1.5.2 Artificial neural network

A fully connected multilayer perceptron was set up. Each of the 21 input neurons was representing one parameter of the characteristics file for the FE simulation. Three hidden layers were used, each consisting of 18 neurons. The output layer was modeled with 9

neurons, as described in Equation 6.10. Thus, a total of 1251 parameters needed to be trained.

7.1.6 Assessment of surrogate models

This section compares the direct and iterative training approaches, evaluates the systematic deviations, and closes with an uncertainty analysis.

7.1.6.1 Iterative training

The iterative training results are compared to a reference model trained on the same number of training data, both for ANN and Kriging model (cf. Figure 7.10). The overall sum of training data (810) was determined based on an assumed convergence of the Young's modulus. In each iteration, the ANN was trained on the same training data as the Kriging model. As expected, the ANN model performance was initially inferior compared to the reference ANN model trained on more data, both for Young's modulus and tensile strength. This was not observed for the Kriging model. Here, the initial model already performed about 1% better than the reference model for predicting Young's modulus. However, a repeated, second direct training led to comparable results for the direct Kriging model approach ($CV_{RMSE} = 2.1\%$ for Young's modulus and 4.7% for tensile strength).

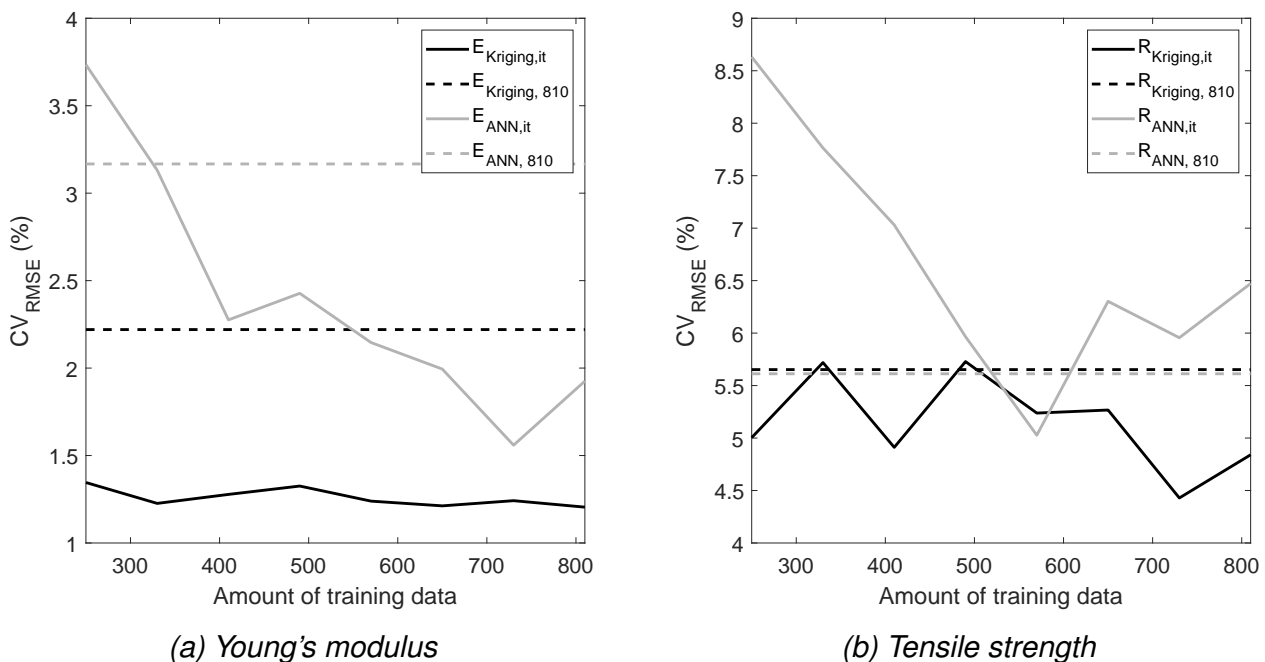


Figure 7.10: Evolution of surrogate model bias based on iterative (it) training data generation for tensile specimen

Overall, the Kriging model improves only marginally in the iterative training approach. Therefore, it can be assumed that the Kriging model already converged considering only the initial training data set. An improvement over the iterations is observable for the ANN due to the higher number of degrees of freedom. At this point, no added value from the iterative training can be determined when the uncertainty analysis of the surrogate models is considered (cf. Section 7.1.6.3). The final models, based on the iterative training, were further used.

7.1.6.2 Systematic deviation

Table 7.6 gives the $RMSE$ as well as CV_{RMSE} of the surrogate models for four different test data sets (cf. Section 6.2.3). When compared to the first test set, the Kriging model predicted the Young's modulus better compared to the ANN. Kriging model and ANN showed a similar performance in predicting tensile strength, with a slight advantage for the Kriging model. Both surrogate models seem to be generally suited to map adaptive FE simulations displaying manufacturing deviations.

Table 7.6: Systematic deviations (bias) of the surrogate models for CoDiCo-SMC tensile specimen

	Kriging model		ANN	
	E (GPa)	R^+ (MPa)	E (GPa)	R^+ (MPa)
$RMSE(\mathbf{P}_1)$	0.20	6.63	0.32	8.86
$CV_{RMSE}(\mathbf{P}_1)$ (%)	1.2	4.8	1.9	6.5
$RMSE(\mathbf{P}_2)$	0.10	26.00	0.42	30.04
$CV_{RMSE}(\mathbf{P}_2)$ (%)	0.5	13.9	2.4	16.1
$RMSE(\mathbf{P}_3)$	1.37	35.88	1.00	21.40
$CV_{RMSE}(\mathbf{P}_3)$ (%)	8.0	24.1	5.8	27.2
$RMSE(\mathbf{P}_3^*)$	0.65	24.99	0.47	23.10
$CV_{RMSE}(\mathbf{P}_3^*)$ (%)	3.8	16.7	2.8	15.4

However, the bias in tensile strength was worse compared to the bias in Young's modulus. The performance of both models slightly decreased when the second test set \mathbf{P}_2 (virtual experiments) was considered. In this test set, only three distinct FMF in DiCo-SMC were considered, which significantly limited the covered parameter space. The bias substantially increased when considering physical experiments (\mathbf{P}_3). However, the relative deviation is of similar magnitude as for the FE simulation itself (cf. configurations No. 1 to 16 in Table 7.1). Since the FE simulation was already unable to describe the behavior of the test specimens with an excessive fiber content, this is inevitably also to be expected for the surrogate models, which were trained on these FE simulations. For this reason, the comparison to \mathbf{P}_3^* was drawn, which consists of physical experimental data of the test specimens with 41 and 45

wt.-% FMF. In particular, the systematic deviation of Young's modulus is significantly reduced. The systematic deviation of the tensile strength is also reduced, but still remains at a higher level.

The computational effort for the functional prediction was drastically reduced by using the surrogate models. A single FE simulation took 57 s on a system with 3.3 GHz clock speed (Intel® Core™ i5-6600). The same configuration was evaluated in less than 0.01 s using the surrogate models.

7.1.6.3 Uncertainty analysis

Table 7.7 shows the overall uncertainty budget for Young's modulus according to the different test data sets following Equation 6.12 with a coverage factor $k=2$. Uncertainties of the models based on training and input variables hold for all test data sets. The uncertainties for the ANN were combined (Häfner & Biehler et al. 2018). The low uncertainty of the Kriging model based on the training data is noteworthy. A lower overall uncertainty is achieved for the Kriging model due to the significantly lower contributions of the Kriging model terms $u_{SM,I}$ and $u_{SM,T}$ compared to the terms of the ANN. In both cases, the model-related uncertainties contribute significantly to the overall uncertainty.

Table 7.7: Uncertainty budget for surrogate modeled Young's modulus of CoDiCo-SMC tensile specimen (MPa)

	Kriging model				ANN			
	P_1	P_2	P_3	P_3^*	P_1	P_2	P_3	P_3^*
$u_{SM,I}$		691 {	684			2296 {	1161	
$u_{SM,T}$			98				1908	
$ b $	200	95	1374	647	321	420	1001	473
$u_{c,SM}$	719	697	1538	947	2318	2334	2505	2344
U_{SM}	1439	1394	3076	1893	4637	4668	5009	4688

7.2 Multi-axial stress state in flexural specimens

A modified CoDiCo-SMC flexural specimen was used for fully evaluating the proposed workflow of a function-oriented quality assurance. Specimens were individually measured and results forwarded to the respective FE and surrogate model.

7.2.1 Experimental design

An updated overview of the requirements for the specimen is given. Based on these requirements, a modified flexural specimen was designed to account for a similar sensitivity with respect to all manufacturing deviations under investigation. Manufactured configurations are presented.

7.2.1.1 Specimen selection

The second validation specimen should additionally be characterized by all measurement technologies proposed in Chapter 5. Furthermore, it should be possible to perform physical experiments with a sufficient high number of samples. The requirements for the second validation specimen can therefore be formulated as follows:

- 1) Reproducibility of the nominal test specimen configurations
- 2) Sufficient number of specimens to account for scattering material properties
- 3) Increased complexity of the stress state in the component compared to tensile tests
- 4) Utilization of real measurement results
- 5) Comparable sensitivity to different manufacturing deviations (cf. Section 7.2.1.2)

The first two requirements limited the design space to planar test specimens so that material and tooling costs can be kept within reasonable limits.

Two established planar specimen geometries from material science are generally suitable to realize a multi-axial stress state, as an increase in complexity compared to tensile tests. Biaxial tensile testing of cruciform specimens is a method for determining material parameters under a multi-axial stress state. However, the design, manufacturing, and experiments involve increased effort, especially for CoDiCo-SMC (Schemmann et al. 2018). In contrast, rectangular flexural specimens are easier to manufacture. However, the classical flexural test avoids the occurrence of complex stress states by choosing the ratio of support span to thickness L/d in such way that the normal stresses induced by the bending moment dominate the shear stresses (ASTM International D30.04 Committee 2015b). According to the standard, the ratio should be 32:1. Trauth (2018) confirmed this value for CoDiCo-SMC. It was also experimentally shown that relevant shear stresses are induced in the flexural specimen if this ratio is not reached. The shear stresses increased further with a decreasing ratio L/d .

Thus, deliberately undershooting the recommendations also leads to a multi-axial stress state. Since both potential specimen choices involve a test specimen and not a real product, the relative stiffness in relation to the stiffness of a defined ideal configuration needed to be used for the functional evaluation. Based on the comparison in Table 7.8, the modified flexural specimen was selected as the second validation specimen.

Table 7.8: Comparison of test specimen alternatives for the validation of the function-oriented measurement of CoDiCo-SMC

Legend:		
● suitable		
◐ partially suitable		
○ not suitable		
	Biaxial tensile specimen	Modified flexural specimen
Multi-axial stress state	●	●
Simple manufacturing	◐	●
Production volume	◐	●
Moderate experimental effort	○	●
Functional assessment	◐	◐

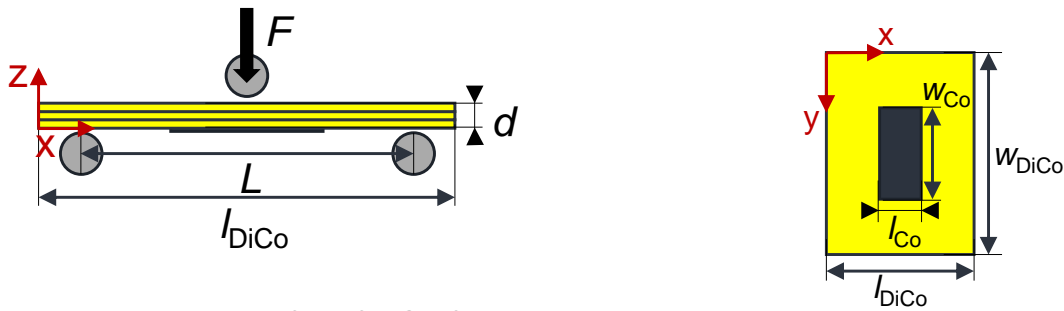
To obtain and use real measurement results from all measurement technologies presented in Chapter 5, only a local Co-SMC reinforcement was to be used in contrast to the first validation specimen. The high absorption coefficient of carbon fibers only allowed the application of the developed THz measurement model (cf. Equation 5.3) for quantifying the FMF of GF DiCo-SMC. However, the use of local reinforcements is in line with the material philosophy presented in Chapter 1, so that the practical relevance is maintained.

A similar sensitivity with respect to the three principal manufacturing deviations under investigation (FMF of DiCo-SMC, Co-SMC pose consisting of rotation and translation, and delamination in DiCo-SMC) was ensured by a suitable specimen design (cf. Section 7.2.1.2).

7.2.1.2 Specimen design and geometry

The three-point flexural test (cf. Figure 7.11a) was identified as a suitable testing principle for a specimen based on the first four criteria in Section 7.2.1.1. The sensitivity of the specimen stiffness with respect to the manufacturing deviations under investigation should be as similar as possible (cf. fifth criterion in Section 7.2.1.1) to improve evaluation capabilities in later steps. The following section describes the optimization approach for the chosen specimen design.

A three-point flexural specimen is defined by its length l , width w , thickness d , and support span L (cf. Figure 7.11b). The support span is further defined by $L = 0.8 \cdot l$. (ASTM International D30.04 Committee 2015b)



(a) Loading diagram for a CoDiCo-SMC, in accordance with ASTM International D30.04 Committee (2015b)

(b) General dimensions of a CoDiCo-SMC flexural specimen

Figure 7.11: Description of a three-point bending setup

The design parameters of patch length l_{Co} and patch width w_{Co} were added since a hybrid component, consisting of a Co-SMC patch applied to the DiCo-SMC base specimen, was considered. The Co-SMC patch placement on the bottom of the specimen intended to stress the CF under tensile load. According to the aforementioned research of Trauth (2018), $L = 40$ mm and $d = 3$ mm were set to limit the design space. Due to the chosen aspect ratio, substantial shear stress components are expected under a bending load. The Co-SMC length $l_{Co} \in [10$ mm, 30 mm], the width of Co-SMC $w_{Co} \in [5$ mm, 60 mm] and the width of DiCo-SMC $w_{DiCo} \in [35$ mm, 100 mm] remained as design parameters. Furthermore, the following constraint was set to ensure sufficient THz measurement points: $w_{Co} \leq 0.6 \cdot w_{DiCo}$.

The component function was defined as the flexural modulus E_f as an attribute of the component stiffness:

$$E_f = \frac{L^3 F}{4u_z w_{DiCo} d^3} \quad 7.3$$

Five exemplary manifestations of manufacturing deviations were defined for being able to evaluate the sensitivity of the component stiffness with respect to different manufacturing deviations. The representative manifestations as well as the ideal, delamination-free configuration with a FMF of 41 wt.-% and a central placement of the Co-SMC ($x_T = 0.5 \cdot l_{DiCo}$, $y_T = 0.5 \cdot w_{DiCo}$, $\gamma_T = 0^\circ$) on the line of maximum deflection are shown in Figure 7.12. The unidirectional carbon fibers of the Co-SMC are aligned along the component length (x-coordinate). The chosen manufacturing deviations consist of a rotation of the Co-SMC by $\gamma_T = -10^\circ$, the displacement of the Co-SMC from the central position by 10 mm each in the length and width directions

($\Delta x_T = \Delta y_T = 10$ mm), the increase (45 wt.-%) and decrease (35 wt.-%) of the FMF in the DiCo-SMC, and the consideration of a delamination with an area of 400 mm² in 1 mm depth in the DiCo-SMC.

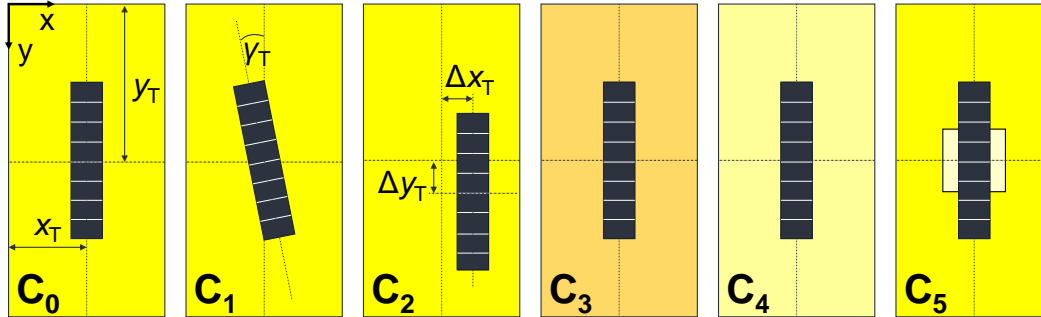


Figure 7.12: Comparison of the ideal manufactured flexural specimen C_0 in contrast to representative manufacturing deviations; C_1 : Co-SMC misorientation; C_2 : Co-SMC misplacement; C_3 : increased DiCo-SMC FMF; C_4 : decreased DiCo-SMC FMF; C_5 : delamination in DiCo-SMC

Different combinations of design parameters led to different sensitivities to manufacturing deviations. A specimen with similar sensitivities to various manufacturing deviations was sought to clearly quantify the influences of these deviations. The following objective function (cf. Equation 7.4) ensured a component function as equally sensitive as possible to the $i = \{1, \dots, 5\}$ different manufacturing deviations in the defined design space:

$$\max(f(w_{\text{DiCo}}, w_{\text{Co}}, l_{\text{Co}})) = \max \left(\frac{1}{\sigma_{E_f}} \sum_{i=1}^5 \underbrace{\left| \frac{E_{f,i} - E_{f,0}}{E_{f,0}} \right|}_{E_{f,\text{rel},i}} \right) \quad 7.4$$

The denominator σ_{E_f} punishes large differences in sensitivity regarding different manufacturing deviations and was defined by:

$$\sigma_{E_f}(w_{\text{DiCo}}, w_{\text{Co}}, l_{\text{Co}}) = \sqrt{\frac{1}{4} \sum_{i=1}^5 \left| E_{f,\text{rel},i} - \bar{E}_{f,\text{rel}} \right|^2}, \quad \text{with } \bar{E}_{f,\text{rel}} = \frac{1}{5} \sum_{i=1}^5 E_{f,\text{rel},i} \quad 7.5$$

An initial data set was generated to find suitable regions of design parameter combinations according to Equation 7.4. Here, the design space was covered by its eight corner points and 92 further design parameter combinations (100 design parameter combinations in total). Furthermore, the general simulation model workflow presented in Section 6.1, parameterized for integrating potential manufacturing deviations, was extended by a parametrization of the three design parameters. Specifics to the FE model of the flexural specimen are given

in Section 7.2.4. Considering manufacturing deviations and design parameters, the value of the objective function (Equation 7.4) was initially determined for 100 design parameter combinations, each evaluated for the six defined manifestations of manufactured quality (cf. Figure 7.12). Particularly good results were obtained for $l_{Co} \leq 15$ mm, $w_{Co} \geq 30$ mm, and $w_{DiCo} \geq 75$ mm. Thus, this reduced design space was refined with 50 further random design parameter combinations generated by LHS. Based on these results, the design parameters were further restricted to $l_{Co} = 10$ mm and $w_{DiCo} \geq 85$ mm. The finally remaining design space was covered using a full factorial design with 23 additional design parameter combinations. Here, a step size of 5 mm was chosen for the design parameters to obtain specimens that can be manufactured well manually. The results for the objective function of all 173 investigated design parameter combinations are illustrated in Figure 7.13.

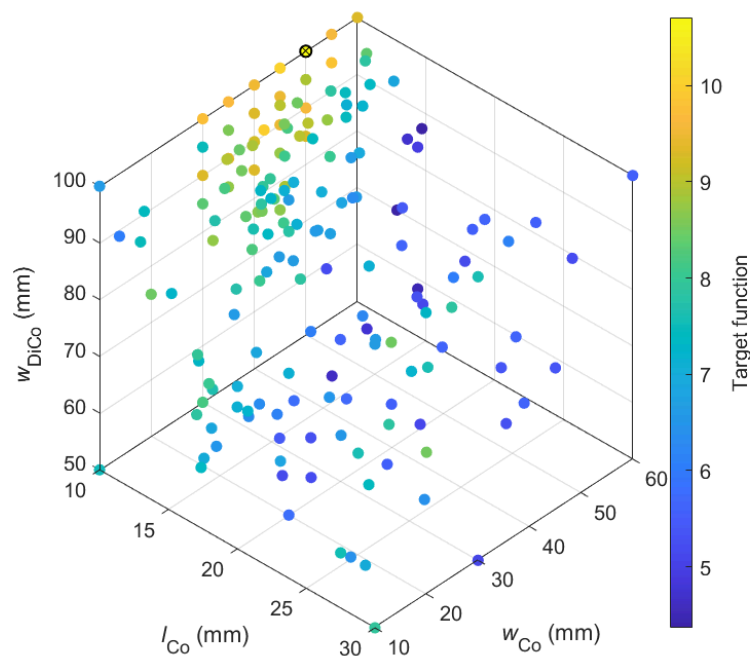


Figure 7.13: Result of the objective function for different design parameter combinations

The dimensions of the specimen design with the most similar sensitivity regarding the representative manufacturing deviations from Figure 7.12 are given in Table 7.9.

Table 7.9: Dimensioning of flexural specimen according to Equation 7.4; length l_{DiCo} and thickness d given for completeness

l_{DiCo}	w_{DiCo}	l_{Co}	w_{Co}	d
50 mm	100 mm	10 mm	50 mm	3 mm

7.2.1.3 Manufactured configurations

Different combinations of manufacturing deviations were to be realized compared to an ideal state of a component to systematically investigate and evaluate the influence of combined manufacturing deviations. A combination of nominally defined manufacturing deviations is referred to in the following as configuration. An exact reproduction of the identical component was not possible due to statistical process variations, both in the semifinished product and in the co-molding process. For statistical validation of the results, each nominal combination of manufacturing deviations was produced at least three times.

The listed manufacturing deviations were considered in the experimental design, taking into account manual and reproducible manufacturing as well as a feasible description in the FE simulations (cf. Figure 7.12):

- 1) Deviating fiber mass fraction in DiCo-SMC
- 2) Translation of the Co-SMC patch
- 3) Rotation of the Co-SMC patch
- 4) Delamination in DiCo-SMC

The first three manufacturing deviations are generally described by a continuous range of values. In contrast, the presence of a delamination is a binary problem. However, if a delamination exists, it is also characterized by continuous quantities for its size and position.

The manufactured configurations are given in Table 7.10, including the intended, nominal FMF ξ_{nom} based on prepreg material.

Table 7.10: Manufactured flexural specimen configurations for CoDiCo-SMC (C_i) and DiCo-SMC (D_i) with given nominal manufacturing deviations

No.	Abbrev.	ξ_{nom} (wt.-%)	$\hat{\xi}$ (wt.-%)	Δx_T (mm)	Δy_T (mm)	$\Delta \gamma_T$ (mm)	r_D (mm)	Δx_D (mm)	Δy_D (mm)
1	C_0	41	46.2	0	0	0	0	0	0
2	C_1	41	46.5	0	0	-10	0	0	0
3	C_2	41	48.6	10	10	0	0	0	0
4	C_5	41	45.3	0	0	0	7	0	0
5	D_1	41	48.1	-	-	-	-	-	-
6	D_2	41	49.2	-	-	-	7	0	0
7	D_3	35	41.7	-	-	-	-	-	-
8	D_4	41	48.5	-	-	-	-	-	-
9	D_5	45	49.8	-	-	-	-	-	-
10	D_6	?	44.6	-	-	-	-	-	-

The configurations D_3 to D_6 were produced from a second batch production of prepreg material. Special focus was given to varying FMF in pure DiCo-SMC to clearly verify the potentials of the THz measurements. D_6 was produced from prepreg material with unknown nominal FMF. Thus, ξ_{nom} is unknown for D_6 and marked with a question mark (?) in Table 7.10. Additionally, the mean realized FMF $\hat{\xi}$ for each configuration, based on THz measurements, is given. Substantial differences were observed compared to the intended FMF.

7.2.2 Measurement procedure

The areal measurements of the optical and thermographic methods were carried out on the flexural specimen in exactly the same way as described in Chapter 5. The same specimen geometry as presented here was already used in both cases for the measurement uncertainty analysis. However, suitable locations had to be selected for the local THz measurement in order to quantify the glass fiber fractions in the specimen within a reasonable amount of time. Therefore, considering the component function, three measurement regions with a diameter of 10 mm were chosen on the line of maximum deflection. Since Co-SMC patches and delamination change the optical path length, the THz regression model loses its validity when traveling through those mediums. For this reason, two additional measurement regions with an offset to the line of maximum deflection were selected to ensure three valid measuring points, even if Co-SMC patches or delaminations were present and optionally, displaced and rotated. The circular measurement regions are given in Figure 7.14. An additional rail was designed to serve as specimen holder in the existing measurement setup (cf. Figure 5.2) to measure the specimen at the defined measurement regions.

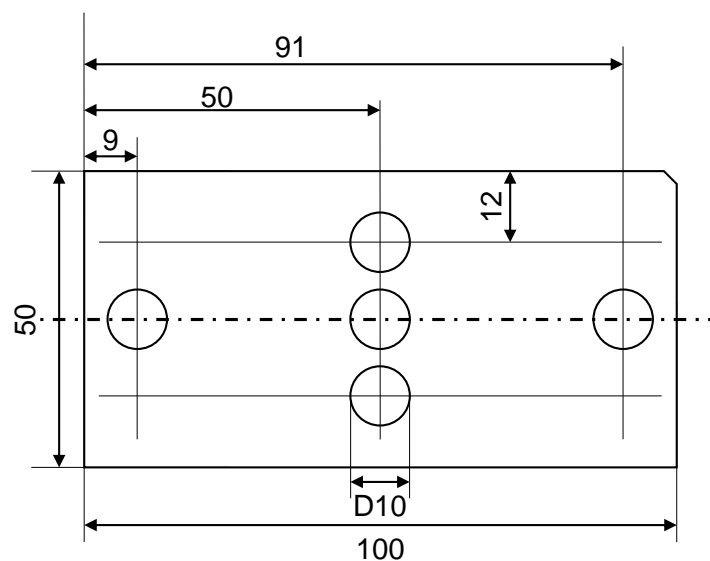


Figure 7.14: Technical drawing of circular THz measurement regions in the flexural specimen

7.2.2.1 Experimental procedure

A flexural test according to the setup shown in Figure 7.11a was performed on a ZwickRoell universal testing machine with a maximum load cell capacity of 20 kN at a loading speed of 5 mm/min. The test setup is shown Figure 7.15.

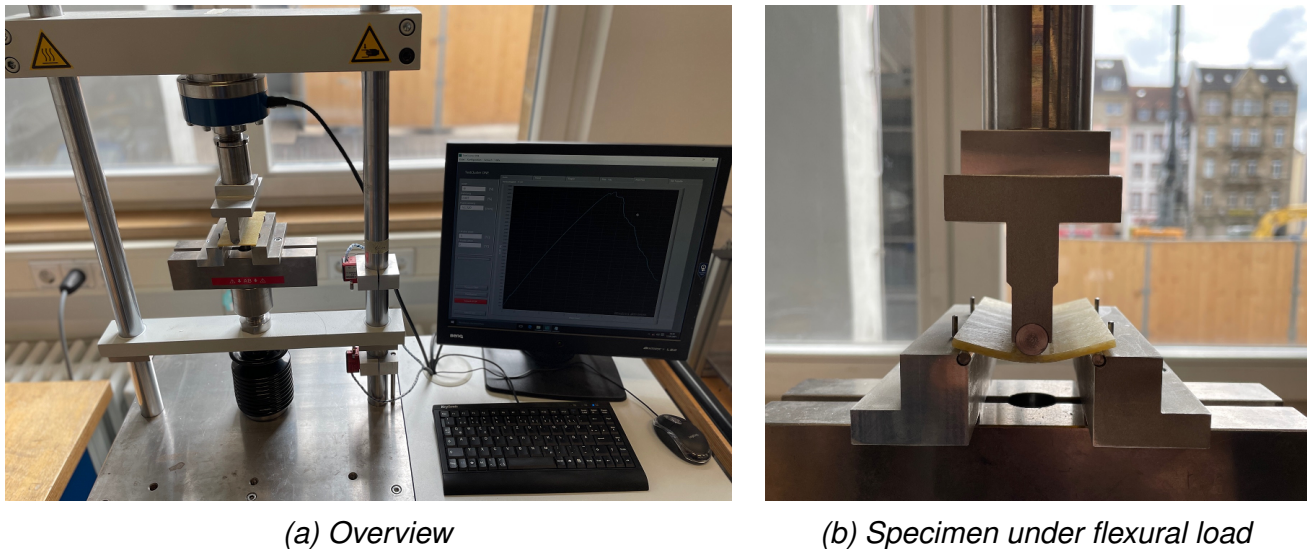


Figure 7.15: Flexural test setup

Force and displacement were recorded with a frequency of 50 Hz. The flexural modulus was evaluated between 0.05% and 0.25% strain (Deutsches Institut für Normung e.V. 2011a), excluding the first 0.7 mm of displacement because settling was observed. It should be emphasized at this point that the flexural moduli determined are not comparable with the flexural modulus or the Young's modulus according to the norm, since the support distances were deliberately reduced. Nevertheless, the comparability within these components is given, so that the flexural modulus can be understood as a function of the component.

7.2.3 General observations

General observations of the experiments conducted are described, taking into account obtained measurement results as well.

7.2.3.1 Underperformance of CoDiCo-SMC

The averaged experimental bending moduli of the four known nominal configurations of CoDiCo-SMC and, as an example, the result for D_1 are plotted in Figure 7.16. It is noticeable that the configuration C_0 fell significantly short of the expected stiffness of about 12.5 GPa for an ideal specimen. The specimens were even less stiff than the D_1 configuration. This can be attributed to high stresses in the interface between Co- and DiCo-SMC. High stresses

occurred locally due to the different material stiffnesses, so that failure occurred at this location. In the experiments, interface damage was observed even at comparatively low forces of less than 2 kN. Due to the Co-SMC patch being pressed into the DiCo-SMC in reality, the residual thickness of the remaining DiCo-SMC was lower compared to a pure DiCo-SMC specimen.

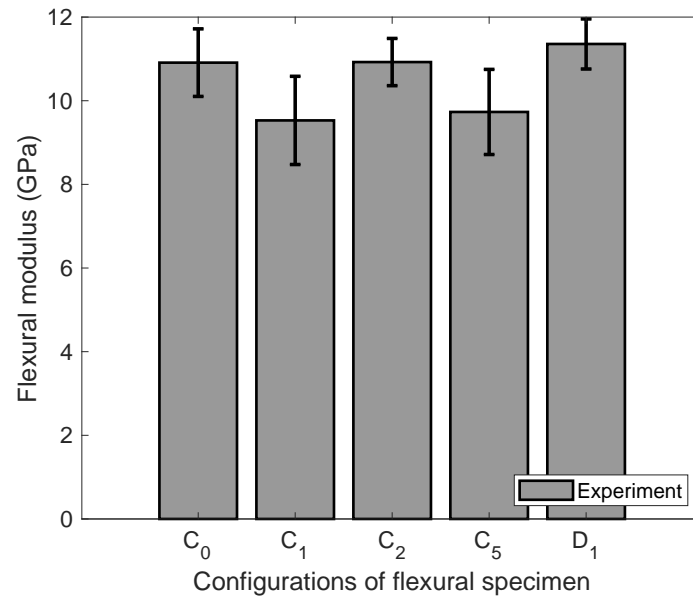
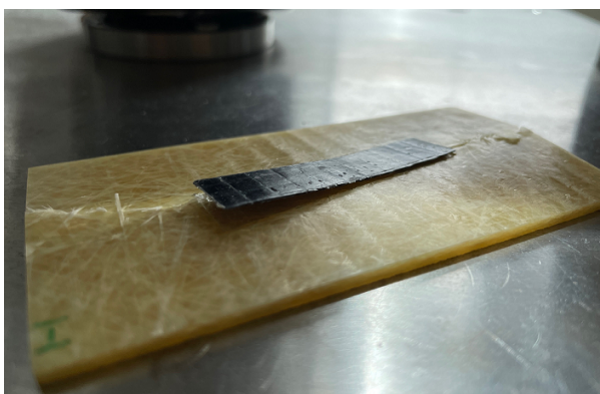
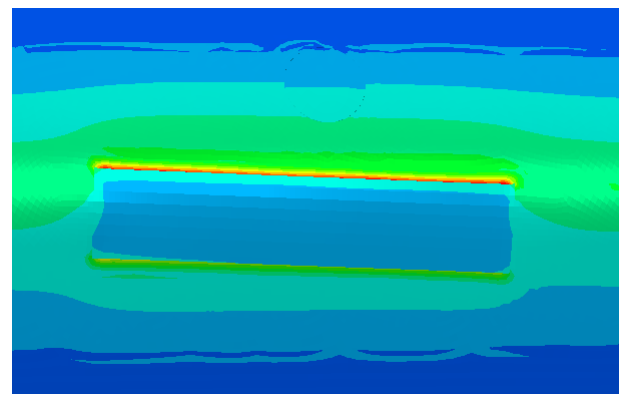


Figure 7.16: Observed underperformance of CoDiCo-SMC compared to DiCo-SMC

Figure 7.17a shows an exemplary failed CoDiCo-SMC specimen. Damage initially occurred at the interface and the Co-SMC thus no longer carried the load. This can also be seen from the fact that the Co-SMC was not damaged. Qualitatively, the increased stresses (maximum principle stress) at the interface region are illustrated in Figure 7.17b.



(a) Co-SMC interface damage in CoDiCo-SMC flexural specimen



(b) Increased stresses at interface regions, qualitatively depicted (red indicates higher stresses)

Figure 7.17: Failure mechanism of CoDiCo-SMC specimen

7.2.3.2 Influence of variations in fiber mass fraction

Figure 7.18a shows the force-displacement curves of the individual specimens of configuration D_3 . Configuration D_3 was chosen for closer examination because the observed flexural moduli scatter in a high range of about 3 GPa. The flexural moduli are also given as bar graphs in Figure 7.18b. The mean THz-measured FMF are given within the individual bars. All measured FMF of the realized configuration D_3 are clearly above the nominal fiber fraction of 35 wt.-%. However, the third specimen had a considerably lower FMF than the other specimens of the configuration. The lower FMF causes the significant lower flexural modulus leading to the overall large spread in D_3 .

This result was tested for generalizability. Figure 7.19a shows the experimentally determined flexural modulus over the nominal FMF for all DiCo-SMC specimen. Large scattering was observed, leading to no significant correlation between nominal FMF and individual flexural modulus. In contrast, the measured FMF in the five MRs per DiCo-SMC specimen were averaged and led to a linear correlation with a $R_{\text{adj}}^2 = 0.446$ (p-value $< 1.6 \cdot 10^{-4}$). Furthermore, only considering MRs on the line of maximum deflection further improved both statistical values ($R_{\text{adj}}^2 = 0.486$, p-value $< 1 \cdot 10^{-4}$).

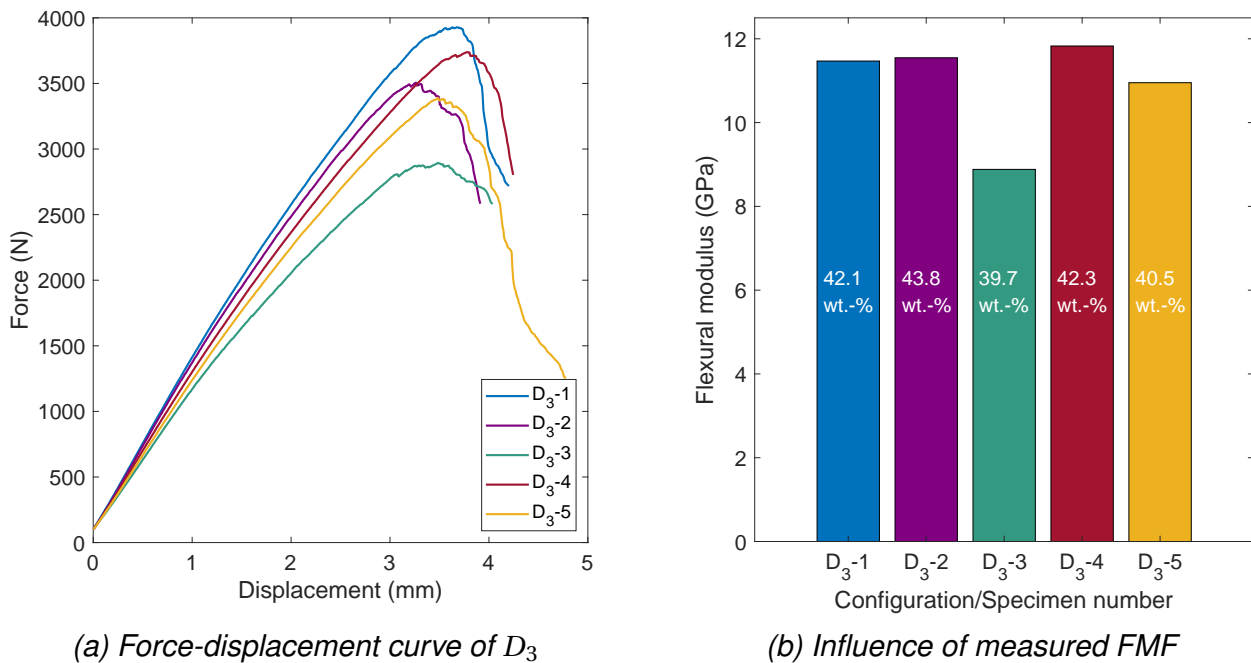


Figure 7.18: Flexural testing and THz measurement results for D_3

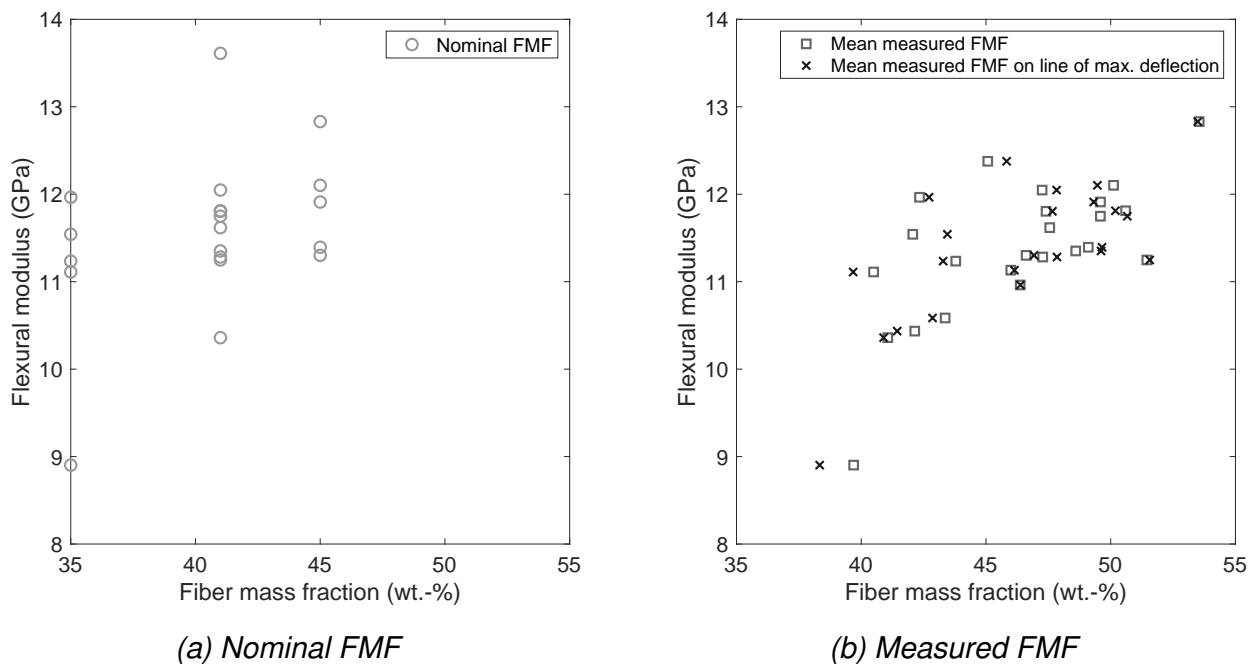


Figure 7.19: Correlations between FMF and flexural modulus

7.2.4 FE Model

The CoDiCo-SMC flexural specimen was FE modeled according to the dimensions given in Table 7.9. However, the DiCo-SMC model thickness was individually adjusted according to the mean measured specimen thickness. The thickness of the local Co-SMC patch was kept at its nominal thickness. At each side along the y-axis of the specimen, 5 mm were reserved as a support surface. The five MRs, illustrated in Figure 7.14, were integrated as separate partitions so that the mesh size could be easily adjusted locally while maintaining a broader mesh in the general DiCo-SMC body. Measurement results of local FMF were used for creating a locally different stiffness based on a planar isotropic FOD and MT homogenization. The stiffness of the DiCo-SMC outside of the MR was calculated accordingly using the mean measured FMF. MRs covered by the Co-SMC or containing a delamination cannot be used for the THz measurement model and are therefore not created when located under a Co-SMC patch. Potential delaminations were integrated into the DiCo-SMC using XFEM. An exemplary model assembly is given in Figure 7.20. Here, two MR were covered by the Co-SMC patch and are therefore not contained in the model assembly. The Co-SMC patch is depicted only for reference, as it is generally placed on the bottom of the specimen (cf. Section 7.2.1.2).

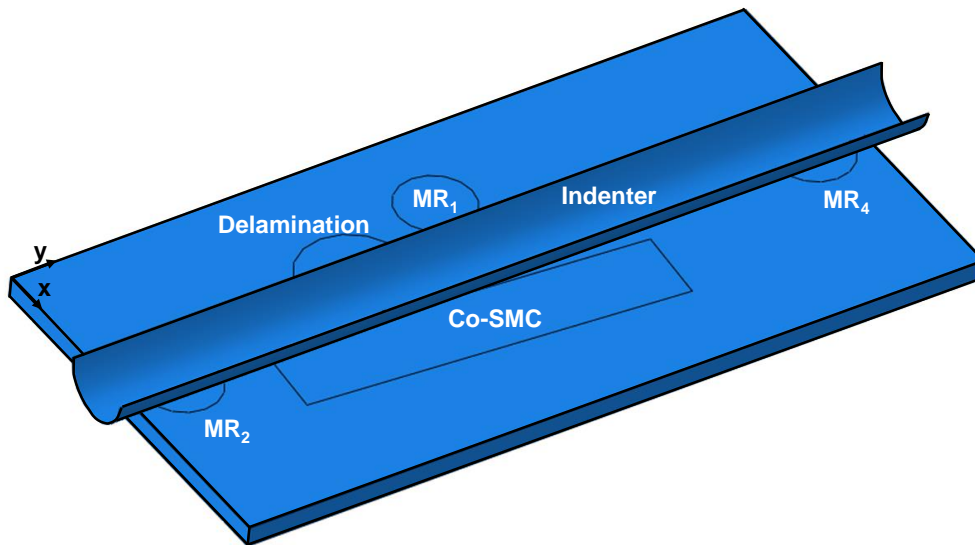


Figure 7.20: Exemplary model assembly for CoDiCo-SMC flexural specimen FE model, including local measurement regions for GF fractions and a delamination

The load was applied using a rigid indenter being moved in the direction of the negative z-axis. The physical supports were modeled by displacement boundary conditions to reduce the computational effort. The contact between DiCo-SMC and supports as well as indenter was modeled frictionless. Since a linear-elastic material behavior was assumed, a target deflection of the flexural specimen of 1 mm was specified to achieve reasonable computation times. Due to the target conflict between local material penetration of the contact surfaces and applied displacement when using the penalty method, minimal deviations for the realized displacement occurred. For the evaluation of simulation results, the actual realized displacement was used. Generally, the element side length was specified in the support surface (2 mm), the MRs (1.5 mm), and for Co-SMC patches and delaminations (1.25 mm). Other mesh sizes of the DiCo-SMC were not specified, but a smooth transition in element size ensured. Twelve elements were considered along the thickness direction of the DiCo-SMC. This led to approximately 30,000 elements for a CoDiCo-SMC specimen, slightly influenced by the size and position of the delamination as well as the orientation and position of the Co-SMC patch. A convergence study was performed (cf. Figure A7.2). The used material parameters are given in Appendix A5. The simulated flexural modulus was calculated according to Equation 7.3, using the realized displacement. The force at failure was extrapolated using the stretch factor f_s based on the maximum strain and Puck criterion.

7.2.5 Assessment of the FE model

The systematic deviation (bias) to the experiments is assessed. Additionally, the overall uncertainty budget for the FE model is calculated.

7.2.5.1 Systematic deviations to the experiments

The averaged experimental results of the different configurations are compared to the averaged individual simulation results, based on the individual measurement results for each specimen, in Figure 7.21. Additionally, the simulation result for the nominal specification of each configuration is given. Generally, it should be noted that the realized FMF were significantly higher than the nominally intended FMF (cf. Table 7.10). This led to consistently higher stiffness predictions by the simulations based on the measurement results.

The underperformance of the CoDiCo-SMC, already indicated in Section 7.2.3.1, is evident here. Due to the high stresses and the failure in the interface, the load could not be transferred to the Co-SMC. High deviations of partly more than 40% resulted (cf. C_1 in Figure 7.21), so that the model is not suitable for a real prediction of the stiffnesses of CoDiCo-SMC for this load case. The deviations were smaller for the configuration C_2 , since the Co-SMC was translated out of the bending line. Thus, a residual load-bearing capacity of the Co-SMC was retained in this case. The mean simulated flexural modulus based on measurement results for the configuration C_5 , including a delamination, was 38.6% higher than the respective experimental results (13.49 GPa vs. 9.73 GPa, cf. Figure 7.21). This discrepancy between simulation and experiment is even higher than the one for the reference configuration C_0 (14.06 GPa compared to 10.91 GPa, leading to 28.9% relative deviation). Overall, a $RMSE$ of 3.54 GPa ($CV_{RMSE} = 0.34$) was observed for individually propagated measurement results of the CoDiCo-SMC flexural specimens.

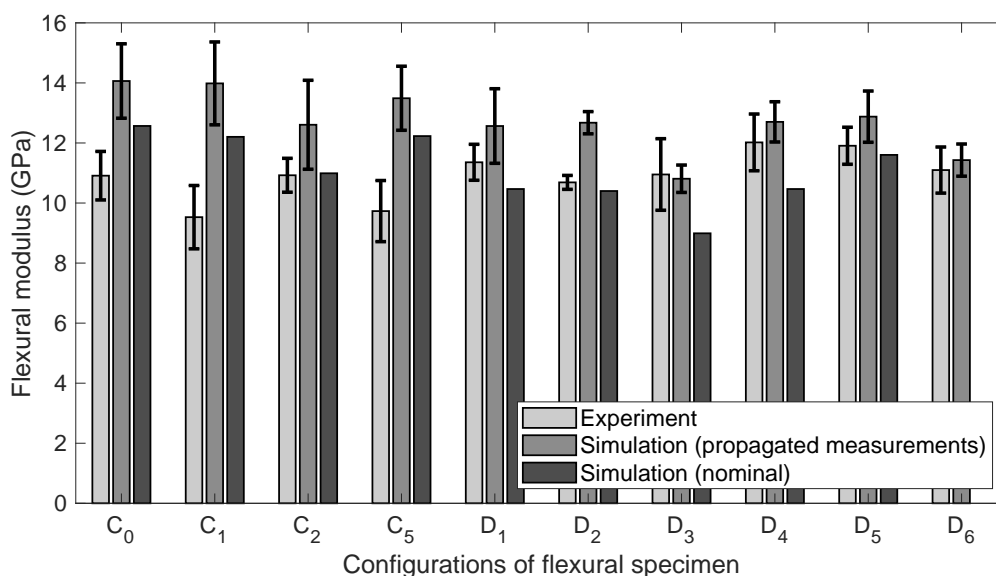


Figure 7.21: Experimental and simulated flexural modulus for CoDiCo-SMC flexural specimen; error bars indicate one standard deviation

When considering the DiCo-SMC, it should be noted that the real FMF for the configurations D_1 , D_2 , D_4 , and D_5 were close to 50 wt.-%. Here, also based on comparable results for tensile tests with such high FMF, it is suspected that sufficient impregnation of the fibers was no longer guaranteed (cf. Section 7.1.4.1). When comparing D_1 and D_2 , it should nevertheless be noted that the slightly increased FMF for D_2 overcompensates for the effect of stiffness reduction due to delamination in the simulation. Whether the stiffness reduction was caused by delamination or by a higher degree of defective fiber impregnation could not be evaluated at this point. The configurations D_3 and D_6 exhibited a FMF closer to the specified FMF for the DiCo-SMC by Fraunhofer ICT (41 wt.-%). Here, the influence on the functional level due to the occurring manufacturing deviations (deviating FMF) could be explained well by the simulations with propagated measurement results. This becomes particularly clear when the experimental results are compared with the simulation results of the nominal properties and the real measured properties. By taking into account the individual measurement results, the $RMSE$ could be reduced by 16% from 1.42 GPa ($CV_{RMSE} = 0.124$) to 1.19 GPa ($CV_{RMSE} = 0.105$), considered over all configurations for DiCo-SMC.

Due to the dominating stress concentrations in the interface, an evaluation of the flexural strength for CoDiCo-SMC was not performed. Furthermore, the predicted failure forces for DiCo-SMC also show an $RMSE$ of 2.35 kN ($CV_{RMSE} = 0.44$), so that a suitable prediction of the failure cannot be guaranteed using currently available material data (maximum stress or strain criterion) for this load case.

7.2.5.2 Uncertainty analysis

Three different specimen configurations were considered for the uncertainty screening, investigating the influences of the hybrid material as well as limiting the computational effort to a reasonable extent. Two CoDiCo-SMC with varying patch orientations as well as a DiCo-SMC were investigated.

According to the one factor at a time approach (cf. Section 6.1.3.1), seven factors could be excluded from further analysis due to their negligible influence of less than 0.5%. The uncertainty contributions of six factors (ξ , ϕ_{Void} , d_T , E_{GF} , E_{UPPH} , ν_{UPPH}) were to be considered further because they exceeded the defined threshold. In addition, variations in the results based on the factors that determined the meshing of the DiCo-SMC body could also be identified. These were the factors describing the Co-SMC and delamination properties. Since the influences of these factors were mixed with changes in meshes, they were also considered further. The remaining factors after screening and their relative influence are listed in Table 7.11. It should also be noted at this point that a varying component stiffness additionally influences the solution of the contact problem. Again, it is visible that the parameters of the

DiCo-SMC gained importance when the enhanced stiffness effect by the Co-SMC patch was reduced.

Table 7.11: Screening analysis: Relative influence of one standard deviation on flexural modulus for different configurations; most relevant input parameters highlighted in gray

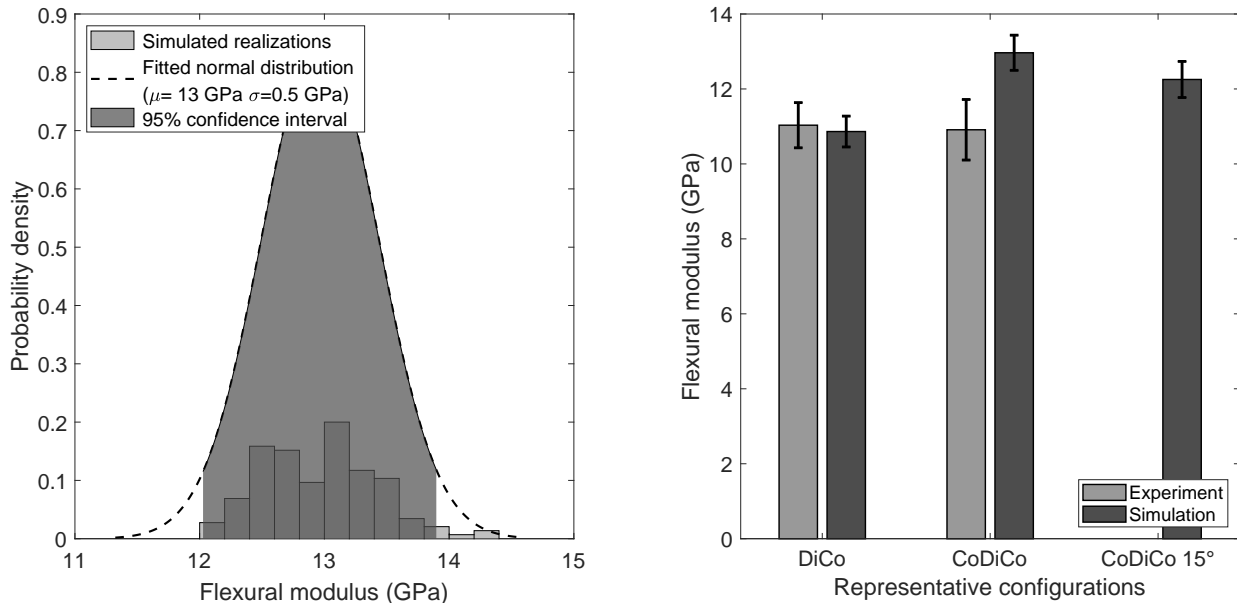
Input parameter	Configuration		
	DiCo	CoDiCo	CoDiCo 15°
ξ	2.53 %	2.13 %	2.00 %
ϕ_{Void}	-1.29 %	-0.95 %	-1.27 %
d_{T}	-	0.54 %	0.48 %
γ_{T}	-	0.32 %	-0.32 %
x_{T}	-	0.99 %	-0.12 %
y_{T}	-	1.23 %	0.54 %
r_{D}	-	-0.12 %	-0.88 %
x_{D}	-	-0.24 %	-0.55 %
y_{D}	-	1.08 %	-0.51 %
E_{GF}	3.21 %	2.96 %	2.63 %
E_{UPPH}	0.71 %	0.97 %	1.25 %
ν_{UPPH}	0.52 %	0.25 %	0.46 %

The remaining parameters were afterwards subjected to an LHS, leading to normal distributed realizations of the flexural modulus for the three different configurations. Exemplary realizations for an ideal CoDiCo-SMC specimen are given in Figure 7.22a. The simulated and experimental results are compared in Figure 7.22b. Both in experiment and simulation, the uncertainty of the hybrid component was higher compared to the pure DiCo-SMC. However, experimental standard deviations were higher than those determined by simulation, indicating that not all physical relevant aspects were covered by the simulation parameters.

Measurable (ξ , ϕ_{Void} , γ_{T} , x_{T} , y_{T} , r_{D} , x_{D} , y_{D}) and non-measurable input quantities (d_{T} , E_{GF} , E_{UPPH} , ν_{UPPH}) were discerned in two following LHS. The uncertainty contributions of the respective groups followed and are given in Table 7.12. The uncertainties of used non-measurable input quantities to the overall larger uncertainty contribution, both for DiCo- and CoDiCo-SMC.

A coverage factor $k=2$ was used to calculate the expanded uncertainty U_{Sim} based on $u_{\text{c,Sim}}$ according to Equation 2.3 and 6.5. The results are given in Table 7.13. Here, the systematic deviations determined the overall uncertainty. The uncertainty of non-measurable input quantities was the second largest influence (cf. Table 7.12). A reference simulation with at least 44,000 elements determined $u_{\text{Sim,D}}$. The bias b corresponded to the results of

Section 7.2.5.1. For reference, the expanded uncertainty U_{Sim} of a DiCo-SMC configuration is approximately 23% of its expected value. This ratio is drastically increased for CoDiCo-SMC to 55% due to its significant bias.



(a) Realizations of ideal CoDiCo-SMC simulation (b) Comparison of experiments and simulations

Figure 7.22: Simulated and experimental uncertainties of flexural modulus; error bars indicate one standard deviation

Table 7.12: Uncertainty contributions for and measurable and non-measurable input quantities (flexural specimen)

Configuration	Uncertainty of		Overall
	measurable	non-measurable	
DiCo	167 MPa	372 MPa	411 MPa
CoDiCo	234 MPa	430 MPa	469 MPa

Table 7.13: Uncertainty budget for FE simulation of flexural specimen (MPa)

	CoDiCo	DiCo
$u_{Sim,I}$	469	411
$u_{Sim,D}$	181	60
$ b $	3538	1190
$u_{c,Sim}$	3574	1260
U_{Sim}	7147	2520

7.2.5.3 Added value

Even if the advantages of measuring the characteristics of DoDiCo-SMC in practice could not be demonstrated due to the neglected interface modeling, the advantage shall be highlighted simulatively using a typical manufacturing deviation. Typical manufacturing deviations for a Co-SMC patch of comparable dimensions, consisting of a patch rotation by 2° and a displacement of 3 mm each in x- and y-direction from the nominal configuration (Fengler & Schäferling et al. 2019), lead to a simulated reduction of the stiffness by 443 MPa for the considered ideal flexural specimen. A higher fiber content of 1.5%, caused by random variations in production processes, compensates this stiffness loss again, so that the original stiffness requirement would still be met.

7.2.6 Surrogate model

Both surrogate model setups and training procedures are given in the following two subsections for the flexural specimen load case.

7.2.6.1 Kriging model

Again, four different training subsets were used for training the different specimen compositions. For testing the iterative reduction of model uncertainty, a Kriging model was initialized based on a training set of 200 specimen configurations, taking into account five times the numbers of input quantities for each specimen composition (cf. Table A8.2). Further promising training data was added in subsequent iterations (cf. Section 6.2.2.1).

The size of the experimental design for a direct training approach was based on the size of training data after convergence was achieved in the iterative approach.

7.2.6.2 Artificial neural network

A fully connected multilayer perceptron with 20 input neurons was used. The three hidden layers consisted each of 18 neurons, while the output consisted of 11 neurons. Thus, a total of 1271 parameters needed to be trained.

7.2.7 Assessment of surrogate models

This section compares the direct and iterative training approaches, evaluates the systematic deviations, and closes with an uncertainty analysis.

7.2.7.1 Iterative training

For both, the ANN and the Kriging models, the iterative training results are opposed to a respective reference model based on a directly LHS-generated training set (size: 1400 data points) in Figure 7.23.

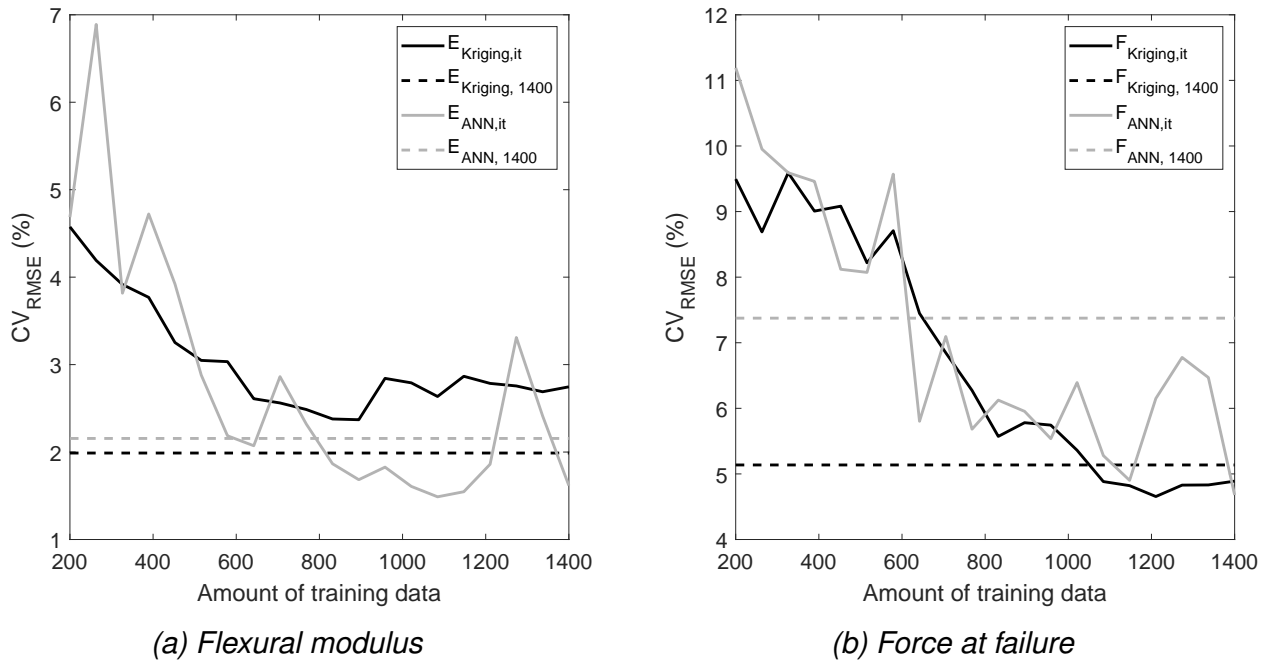


Figure 7.23: Evolution of surrogate model bias based on iterative (it) training data generation for flexural specimen

Training data was the same for ANN and Kriging model at each iteration. The ANN and Kriging model performance was initially inferior compared to the reference ANN model trained on more data, both for Young's modulus and force at failure. Contrary to Figure 7.10, more training data was needed as well for the Kriging model to converge. Overall, iterative training proves to be useful to incrementally improve the surrogate model performance. The final models, based on the iterative training, were further used.

7.2.7.2 Systematic deviation

$RMSE$ and CV_{RMSE} are opposed for the three different test data sets in Table 7.14. The ANN showed slight advantages for the first test set P_1 , both in stiffness and strength. Nonetheless, both surrogate models seem further to be generally suited for this load case as well. The $RMSE$ of both models roughly doubled when the second test set P_2 (virtual experiments) was considered. This test set significantly limits the covered parameters space, because only three distinct FMF in DiCo-SMC were considered (cf. Table 7.10). As discussed in Section 7.2.5.1, the failure prediction based on available material data in FE simulations was not matching

experimental results. Therefore, the bias substantially increased as well for the surrogate models when considering physical experiments (P_3). Generally, the bias in strength was significantly worse compared to the bias of Young's modulus for all test sets.

Table 7.14: Systematic deviations (bias) of the surrogate models for flexural specimen

	Kriging model		ANN	
	E (GPa)	F^+ (N)	E (GPa)	F^+ (N)
$RMSE(P_1)$	0.32	111	0.19	107
$CV_{RMSE}(P_1)$ (%)	2.7	4.9	1.6	4.7
$RMSE(P_2)$	0.50	264	0.28	285
$CV_{RMSE}(P_2)$ (%)	4.4	11.6	2.5	12.5
$RMSE(P_3)$	2.03	2290	2.35	2283
$CV_{RMSE}(P_3)$ (%)	18.3	46.9	21.2	46.7

A single FE simulation for a CoDiCo-SMC specimen took mostly between 15 and 25 minutes on the KIT High Performance Computing (HPC) using Intel® Xeon Gold 6230 processors. The same configuration was evaluated in less than 0.01 s using the surrogate models.

7.2.7.3 Uncertainty analysis

The overall uncertainty budget according to the different test data sets is given for the Young's modulus in Table 7.15, following Equation 2.3 and 6.12 with a coverage factor $k=2$. Uncertainties of the models based on training and input variables hold for all test data sets. Again, the Kriging model uncertainties related to input quantities and model training were considerably lower than the uncertainty for the ANN. However, the overall uncertainty was similar for both models. The bias dominated the model-related uncertainties for P_3 .

Table 7.15: Uncertainty budget for surrogate modeled flexural modulus of CoDiCo-SMC flexural specimen (MPa)

	Kriging model			ANN		
	P_1	P_2	P_3	P_1	P_2	P_3
$u_{SM,I}$	237	150	184	428	187	369
$u_{SM,T}$						
$ b $	320	496	2028	188	284	2354
$u_{c,SM}$	398	550	2042	467	514	2393
U_{SM}	797	1100	4084	935	1027	4785

8 Discussion and outlook

In this chapter, the presented approach for a function-oriented quality assurance of hybrid SMCs is discussed based on the guiding research questions (cf. Section 1.3). The requirements specified in Section 3.1 to determine the research deficit are considered as well. Both, the suitability of the measurement technologies alone (cf. Chapter 5) and the integration of the measurement results into the function-oriented evaluation routine, consisting of FE simulation and surrogate model (cf. Chapter 7), are discussed. Finally, an outlook of further research questions within the field is given.

8.1 Discussion

The research goal of this thesis is to develop a function-oriented quality assurance for a hybrid SMC (CoDiCo-SMC). In the following, the derived research questions are critically discussed to evaluate the achievement of the goal. Here, it is as well referred to the requirements defined in Section 3.1 (highlighted in bold).

In-line measurements: *Is it possible to quantify common manufacturing deviations of hybrid sheet molding compound within the cycle time?*

Different measurement technologies were successfully **applied to CoDiCo-SMC** and **multiple defects** were quantified. All measurements technologies used adhere to the cycle time (**in-line integration**).

Deviations of the FMF in DiCo-SMC could be measured non-destructively for the first time. THz spectroscopy in transmission mode was used for this purpose. A linear regression model allowed the quantification of deviations of the local FMF with a measurement uncertainty of less than 1 wt.-% for a measurement diameter of 10 mm. This result represented a significant information gain compared to the uncertainty of the local FMF resulting from the production process (3.5 wt.-%). Until now, only CT with the help of critically discussed, subjective gray value limits was available as a non-destructive measurement technology alternative for the FMF. The established regression model was successfully used for the existing material formulation within the IRTG, independent of the production batch. However, a change in the material formulation, by changing the resin mixture or the glass fibers, inevitably leads to a change in the optical parameters. This potential change has not been taken into account up to this point. Significant experimental effort is involved to generate the measurement model. Specimens have to be produced, THz-measured, and TGA-referenced. This effort must currently be taken again to react to material changes. Investigations to reduce the measurement time showed that both the recording time window (RTW) and the total number of averaged waveforms can be reduced to one tenth of the initial value. The combination

of both methods reduces the time required for one measurement to 0.5 s. A transferability to changed measurement diameters is expected to hold according to the results and the existing physical conditions, but could not be clearly confirmed in the performed experiments. With the present in-line THz measurement technology, it is therefore possible to measure a large number of ROIs on a component in a cycle time less than 90 s. However, the total number is limited by the handling operations required to align the component in the beam path. Furthermore, parallel alignment of the surface normal of the component and the beam path must be ensured. Curved component segments were not considered.

The pose of a Co-SMC patch on a DiCo-SMC was determined using industrial image processing (IIP). Due to the systematic separation of in-line and off-line calibration, the measurement could be performed with high repeatability and low measurement uncertainty. Thus, the corresponding individual measurement results per component are available for further use. The requirements of the measurement technology do not exceed the state of the art at this point, since only planar specimens were investigated and carbon fiber (CF) misorientations within the patch, such as undulations or fiber wavinesses, were not considered. However, those questions have already been answered by the state of the art and appropriate solutions can be referred to if needed.

Pulsed phase thermography (PPT) was used to record phasegrams of CoDiCo-SMC specimens. Due to different thermal conductivity coefficients, both Co- and DiCo-SMC as well as delaminations were distinguished from each other based on their gray value differences. An automated workflow using multilevel thresholding allowed for the quantification of the location and position of potential delaminations. For the first time, the measurement uncertainty evaluation of the PPT was performed with inserted PTFE delaminations instead of blind holes. When inspecting other material combinations, parameters of the algorithm have to be adapted.

Since voids could not be systematically and reliably integrated into the specimen within the co-moulding process, they were excluded from the metrological consideration in the context of this work. It should be referred to CT as an existing measurement technology, even if it currently cannot meet the cycle time requirements.

The screening analyses carried out showed that additional attention should be paid to the manufacturing deviations of the Co-SMC (patch thickness and CF fraction). Respective measurement technologies have not been investigated in the context of this work.

Parametrized simulations: *Do simulations with imported measurement results of manufacturing deviations represent the material behavior of hybrid sheet molding compound accurately?*

Tserpes et al. (2016) already demonstrated the advantages of integrating CT-based measurement results (voids) into FE simulations. In this work, several measurement results regarding manufacturing deviations obtained by in-line measurement technologies were integrated into FE simulations (**measurement results as input quantities**). In particular, the measurement of FMF by THz spectroscopy reduced the *RMSE* between experimental and simulated Young's modulus for DiCo-SMC flexural specimen by 16% (cf. Section 7.2.5). The integration of varying Co-SMC poses into the model assembly represented these manufacturing deviations well, as the validation for tensile specimen showed (cf. Figure 7.7). The interface damages between Co- and DiCo-SMC for the flexural specimens did not allow a clear statement at this point for the second validation specimen. The influence of measured delaminations on the stiffness could not be represented with sufficient accuracy using XFEM. The simulated stiffness reduction (**simulation as functional assessment**) for flexural specimens was much lower for delaminations than the one observed in the experiment (average deviation of 38.6% for C_5 in Figure 7.21). Not considered so far, but promising for further development of the model, is the use of measurement results on the Co-SMC (thickness and CF fraction). The foundations were laid by the appropriate structuring of the characteristics file for the adaptive generation of the model assembly. Likewise, void fractions were analytically considered in the model assembly and measurement results, if available, can be used.

It should be critically noted that the component strength could only be insufficiently displayed. This was particularly evident for the flexural specimens. The use of more complex, material-specific damage modeling (Schemmann 2018; Görthofer et al. 2019) could remedy this shortcoming for DiCo-SMC. However, the bonding of Co- and DiCo-SMC requires an appropriate model approach as well if the interface is subjected to significant stresses.

Overall, it can be stated that the integration of the measurement results of FMF (cf. Section 7.2.5), of Co-SMC poses (cf. Section 7.1.2), and of voids (Tserpes et al. 2016) is advantageous to predict the component-specific stiffness. Due to the insufficient agreement between simulated and real stiffnesses for delaminations, a function-oriented consideration of delaminations cannot yet be recommended. More advanced material models need to be used to predict component failure.

In-line surrogate model: *Can virtual training data, generated from simulations, be used to achieve real-time capability of the functional assessment?*

The component characteristics, written to a standardized .csv-file, were used in this work for the script-based generation of the individual FE model. This file served as well as a direct input for the surrogate models. To evaluate the basic capability of the selected surrogate models to represent the parametrized FE simulations, the test data set P_1 was utilized. This

test set consisted of purely virtually generated input-output relations. For both load cases considered, a model was found that represented the respective test data set with a CV_{RMSE} of less than 2% in stiffness and less than 5% for material failure (cf. Table 7.6 and 7.14). A fundamental advantage between ANN and Kriging model could not be determined at this point.

Thus, it can be concluded that the material behavior as a function of different manufacturing deviations could generally be learned and assessed by the surrogate models (**real-time applicability**). However, since more complex damage modeling is recommended, this verification must be carried out again if the modeling approach is changed.

Measurement uncertainty: *Do the measurement uncertainties of the in-line measurement technologies, the simulation and the surrogate model allow for an industrial application?*

Even though no tolerated industrial component is yet available for the new material class of CoDiCo-SMC, a discussion regarding the suitability of the **measurement technologies** is to be carried out based on Equation 8.1 (German Association of the Automotive Industry 2011):

$$Q_{MS} = \frac{2 \cdot U}{TOL} \leq 15\% \quad 8.1$$

By rearranging Equation 8.1 with respect to the tolerance TOL (cf. Equation A9.1), the product specifications can be determined for which the respective measurement technology with the expanded uncertainty U would be suited considering the capability ratio Q_{MS} . The detailed calculation can be found in Table A9.1 in the Appendix A9. However, the tolerances to be demanded according to the measurement capability cannot be accepted industrially. If such tolerances were to be accepted, the function of the component would have to be regarded as significantly restricted or even unserviceable. Therefore, the maturity level of the measurement technologies does not meet industrial standards from the perspective of German Association of the Automotive Industry (2011). However, it should be noted that at least for the non-destructive in-line measurement of FMF, no alternative in-line measurement technology exists and a significant reduction in the local uncertainty of FMF compared to the production process was achieved.

High safety factors (> 1.5) in the product design of FRPs are considered because of uncertainties in the production process and of material properties (Schürmann 2007). These safety factors and the expanded uncertainty of the FE simulated stiffness relative to the expected product function (stiffness) are used to discuss the applicability in an industrial setting. For both the tensile specimen and the DiCo-SMC flexural specimen, the expanded **uncertainty of the FE simulation** U_{Sim} was approximately 20% of the expected stiffness. This means

that even components that satisfy only a safety factor of 1.2 after measurement of the function still meet a one-sided tolerance limit (minimum stiffness) with a probability of 97.7% (cf. Appendix A10). Using the function-oriented measurements, necessary safety factors in the dimensioning of components can be adapted and reduced to meet industry-specific requirements. However, the application-specific load cases must be considered. Within the scope of this work, the influences of Co-SMC patch poses and FMF of the DiCo-SMC were successfully **validated in experiments**.

Surrogate models, trained on aforementioned FE models and using **measurement results as input quantities**, were used to accelerate the functional evaluation to adhere to the cycle time in production. Influences of manufacturing deviations on the component function, distributed over the entire parameter space, could be successfully trained. The expanded **uncertainty of the surrogate models** U_{SM} was determined in compliance with JCGM100 (2008) and approximately of similar size as U_{Sim} . Controversially, the determined uncertainties for the Kriging model were lower than expected based on the results for the FE simulation (cf. Table 7.5 and 7.7) and compared to the ANN (cf. Table 7.7 and 7.15). Here, it should be noted that the FE models reacted more sensitively to uncertain input variables than the Kriging models in the analysis of measurement uncertainty ($u_{Sim,I}$ compared to $u_{SM,I}$). This observation can be attributed to two factors. First, uncertainties of the material parameters were no longer considered in the surrogate models to limit the training effort. However, the uncertain material parameters were found to contribute significantly to the uncertainty (cf. Table 7.4 and 7.12). Second, in the context of this work, the training sets for the surrogate models were directly created from the global value domains (cf. Table A8.1 and A8.2). The intended uniform coverage of the experimental space by means of LHS leads to larger distances between two sets of combined manufacturing deviations $\omega_{i,l}$ and $\omega_{i,l+1}$ than the distance between two statistical realizations of a set $\omega_{i,l}$ based on measurement uncertainties of measurement technologies. Consequently, the trained surrogate models cannot correctly represent the influences of local variations due to uncertain input quantities. This is to be judged as extremely critical and excludes an application in the industrial field at present. A remedy could be an extension of the LHS generated global training data by adding the material parameters in the training set and additionally extending this initial training set by adding local statistical fluctuations of the measured input quantities for each $\omega_{i,l}$. Thus, the training effort would be significantly increased.

In conclusion, especially the Terahertz measurement technology contributed to a reduction in the uncertainty of the component characteristics. Although every measurement technology quantified the respective manufacturing deviations successfully, no measurement technology met so far the requirements regarding measurement uncertainties in the automotive industry

according to German Association of the Automotive Industry (2011). Integrating measurement results into parametrized FE simulations helps to reduce safety factors based on the expanded uncertainty U_{Sim} . The uncertainty U_{SM} is of similar size as U_{Sim} . However, the uncertainty contribution $u_{\text{SM},I}$ needs further efforts for covering uncertainties of material parameters and local variations of input quantities.

As an overall assessment, it can be concluded that the first three research questions were confirmed. First, three different in-line measurement technologies (terahertz spectroscopy, pulsed phase thermography, industrial camera) allowed for the quantification of common manufacturing deviations in CoDiCo-SMC. Second, the integration of the measurement results for FMF, Co-SMC poses, and voids led to a component-specific stiffness prediction. Third, the material behavior as a function of different manufacturing deviations was learned by two different surrogate models. Considering the fourth research question, it must be noted that the measurement uncertainties of the measurement technologies do not meet industrial requirements. However, the measurement uncertainty consideration of the FE simulation and the surrogate models showed that the approach offers great potential for the reduction of common safety factors.

8.2 Outlook

As indicated by the prior discussion, further research directions could be identified and are described in this section. First, three specific aspects for the further development of the presented methodology related to CoDiCo-SMC are presented. Subsequently, a broader outlook on the use of function-oriented measurement results is given.

Measurement technologies The integration of a physical model based on a rule of mixture (Jördens & Scheller & Wietzke et al. 2010) could allow easy transferability of the THz measurement model to other material formulations. Robots could further be used to automate fast handling operations of the component in the THz beam path. This handling would also have the advantage that the same measurement regions can be measured in different orientations. Thus, additional conclusions on the fiber orientation distribution can be drawn (Jördens & Scheller & Wietzke et al. 2010).

The material class CoDiCo-SMC further showed a high sensitivity with respect to manufacturing deviations of the Co-SMC patches, which have not been further quantified so far. A promising measurement technology here is an eddy current system to quantify variations of the CF fraction via changing impedances. Since thickness variations of the Co-SMC were also observed, an information fusion between impedance and local material thickness would probably have to be performed. Ideally, the in-line measurement technology should be integrated into the prepreg production process.

Material modeling for FE simulation Further research approaches can be used to incorporate material-specific damage modeling and local fiber orientations into the FE models. Here, the works from other IRTG subprojects (Schemmann (2018) and Meyer et al. (2020)) are particularly suited. Additionally, appropriate interface models between Co- and DiCo-SMC are needed to model delaminations inbetween.

Surrogate modeling For the training of the surrogate models, material parameters and local variations of the input variables should additionally be considered in the training data to obtain a better estimation of the respective uncertainty contribution. Precisely quantified uncertainties help to strengthen the acceptance of those black box models.

The continuous integration and use of product knowledge in production is key for further improving production performance by function-oriented measurements. The use of structural simulations and sensitivity analyses in the design process should not only be limited to adjustable design parameters for achieving the most robust design possible (Fengler & Schäferling et al. 2019), but should also be used to directly quantify the influence of relevant manufacturing deviations (Franz et al. 2021). Thus, the design process can also be used directly to identify requirements for necessary measurement technologies and measurement locations (ROIs) for functionally relevant manufacturing deviations in accordance with Figure 4.1.

9 Conclusion

The use of fiber-reinforced polymers (FRPs) increases steadily on global scale. The combination of discontinuous SMC (DiCo-SMC) and continuous SMC (Co-SMC) in a new, hybrid material class (CoDiCo-SMC) promises reasonable manufacturing costs as well as high local stiffness and strength. Traditionally, harsh requests for defect-free FRP components, leading to high quality requirements, are a cost driver in this industry. Further, occurring manufacturing deviations jeopardize the fulfillment of the functionality of manufactured components.

To overcome these limitations, an approach for a component-specific, function-oriented in-line quality assurance is proposed. For this type of quality assurance, in-line measurement results are integrated into functional models, such as finite element (FE) models. Surrogate models of these functional models accelerate the evaluation to adhere to the cycle time within production.

In the present work, component-specific, function-oriented in-line quality assurance was exemplarily implemented for the new CoDiCo-SMC material class. Three different measurement technologies were used to quantify three relevant manufacturing deviations (glass fiber fraction, Co-SMC patch pose, delamination). THz spectroscopy was used for the first time to in-line measure local variations of the glass fiber fraction in DiCo-SMC. Pulsed phase thermography was used to quantify delamination and an industrial camera to measure Co-SMC patch pose. For each measurement technology, the measurement uncertainty was quantified according to the “International Guide to the Expression of Uncertainty in Measurement (GUM)”. The measurement results were further processed in a parameterized FE model and aggregated to a functional prediction. Using the measurement results and respective FE-modeled functions, surrogate models were trained through input-output relations. Within this work, the predicted component function is also understood as measurement. Hence, the measurement uncertainties of both FE models and surrogate models were determined.

The presented approach was validated using two exemplary test specimens. The results show that in particular the measurements of local glass fiber fractions and the Co-SMC patch pose allow conclusions to be drawn on the component-specific stiffness. The determined measurement uncertainties do currently not allow for an industrial application. Making use of component-specific functional information in production allows to reduce common safety factors during the design phase of FRP components.

List of own publications

- Bretz, L. & Gärtner, A. & Häfner, B. & Lanza, G. (2021). „Fiber Orientation Evaluation of Intrinsically Manufactured Metal-CFRP Hybrid Structures by Data Fusion of Pulsed Phase Thermography and Laser Light Section“. Proceedings of the Conference Future Production of Hybrid Structures 2020 (Wolfsburg, Germany, Sept. 23, 2020). Springer, pp. 241–252. DOI: 10.1007/978-3-662-62924-6.
- Bretz, L. & Günther, F. & Häfner, B. & Herrmann, H.-G. & Jost, H. & Kretschmar, V. & Lanza, G. & Pohl, M. & Schwarz, M. & Stommel, M. & Summa, J. (2021). „Einfluss, Detektion und Vorhersage von Defekten in großserientauglichen Hybridverbunden für Metall/CFK-Leichtbautragstrukturen“. *Intrinsische Hybridverbunde für Leichtbautragstrukturen*. Ed. by J. Fleischer. Berlin: Springer Vieweg, pp. 80–120. DOI: 10.1007/978-3-662-62833-1.
- Bretz, L. & Günther, F. & Jost, H. & Schwarz, M. & Kretschmar, V. & Pohl, M. & Weiser, L. & Häfner, B. & Summa, J. & Herrmann, H.-G. & Stommel, M. & Lanza, G. (2020). „Design & quality assurance of intrinsic hybrid metal-CFRP lightweight structures“. Online Proceedings of the 4th International Conference Hybrid 2020 Materials and Structures (Karlsruhe, Germany, Apr. 28–29, 2020). Deutsche Gesellschaft für Materialkunde e.V., pp. 144–156. URL: <https://hybrid2020.dgm.de/the-conference/proceedings/> (Accessed: Jan. 5, 2022).
- Bretz, L. & Häfner, B. & Lanza, G. (2019). „Funktionsorientierte Inline-Messtechnik von Faserverbunden“, *wt Werkstatttechnik online* 11/12, pp. 816–821. DOI: 10.37544/1436-4980-2019-11-12-18.
- Bretz, L. & Häfner, B. & Lanza, G. (2021). „Non-destructive measurement of fiber mass content of glass fiber sheet molding compound using Terahertz radiation“, *Measurement* 168, Article 108386. DOI: 10.1016/j.measurement.2020.108386.
- Bretz, L. & Hinze, T. & Häfner, B. & Lanza, G. (2019). „Evaluation of anomaly detection capabilities using a non-orthogonal camera angle in pulse-phase thermography“. Online Proceedings of the 2nd CIRP Conference on Composite Material Parts Manufacturing (CCMPM 2019) (Sheffield, United Kingdom, Oct. 10–11, 2019). Elsevier, pp. 308–313. DOI: 10.1016/j.procir.2019.09.032.
- Bretz, L. & Wilke, M. & Häfner, B. & Lanza, G. (2020). „Comparison of anomaly detection capabilities of pulse phase thermography in transmission and reflection setup on Sheet Molding Compound“. Online Proceedings of the 4th International Conference Hybrid 2020 Materials and Structures (Karlsruhe, Germany, Apr. 28–29, 2020). Deutsche Gesellschaft für Materialkunde e.V., pp. 108–115. URL: <https://hybrid2020.dgm.de/the-conference/proceedings/> (Accessed: Jan. 5, 2022).

- Fengler, B. & Schäferling, M. & Schäfer, B. & Bretz, L. & Lanza, G. & Häfner, B. & Hrymak, A. & Kärger, L. (2019). „Manufacturing uncertainties and resulting robustness of optimized patch positions on continuous-discontinuous fiber reinforced polymer structures“, *Composite Structures* 213, pp. 47–57. DOI: 10.1016/j.compstruct.2019.01.063.
- Meyer, N. & Schöttl, L. & Bretz, L. & Hrymak, A. N. & Kärger, L. (2020). „Direct Bundle Simulation approach for the compression molding process of Sheet Molding Compound“, *Composites Part A: Applied Science and Manufacturing* 132, Article 105809. DOI: 10.1016/j.compositesa.2020.105809.

References

References according to the scheme (A_<last name> <year>) refer to Bachelor and Master Theses at the wbk Institute of Production Science, which were supervised by the author of this dissertation.

A_Debowski 2020

Debowski, K. (2020). „Messunsicherheitsanalyse der struktursimulierten, mechanischen Eigenschaften eines defektbehafteten Zugstabs aus hybridem SMC“. Bachelor Thesis, Karlsruhe Institute of Technology (KIT). Karlsruhe: wbk Institute of Production Science.

A_Frontzek 2019

Frontzek, J. (2019). „Integration von Messdaten in eine Homogenisierungsroutine zur strukturmechanischen Simulation von Sheet Molding Compound“. Bachelor Thesis, Karlsruhe Institute of Technology (KIT). Karlsruhe: wbk Institute of Production Science.

A_Koch 2020

Koch, D. (2020). „Metamodellierung der mechanischen Eigenschaften eines defektbehafteten, hybriden Sheet Molding Compound unter Zugbelastung“. Bachelor Thesis, Karlsruhe Institute of Technology (KIT). Karlsruhe: wbk Institute of Production Science.

A_Müller-Welt 2019

Müller-Welt, P. (2019). „Automatisierte Delaminationsparameteranalyse eines endloskohlenstofffaserverstärkten Sheet Molding Compounds“. Master Thesis, Karlsruhe Institute of Technology (KIT). Karlsruhe: wbk Institute of Production Science.

Adunka 2000

Adunka, F. (2000). *Meßunsicherheiten: Theorie und Praxis*. 2. Ed. Essen: Vulkan.

Advani & Tucker 1987

Advani, S. G. & Tucker, C. L. I. (1987). „The Use of Tensors to Describe and Predict Fiber Orientation in Short Fiber Composites“, *Journal of Rheology* 31.8, pp. 751–784. DOI: 10.1122/1.549945.

Aggarwal 2018

Aggarwal, C. C. (2018). *Neural Networks and Deep Learning: A Textbook*. 1. Ed. Cham: Springer International Publishing. DOI: /10.1007/978-3-319-94463-0.

Amenabar et al. 2011

Amenabar, I.; Mendikute, A.; López-Arraiza, A.; Lizaranzu, M. & Aurrekoetxea, J. (2011). „Comparison and analysis of non-destructive testing techniques suitable for delamination inspection in wind turbine blades“, *Composites Part B: Engineering* 42.5, pp. 1298–1305. DOI: 10.1016/j.compositesb.2011.01.025.

ASTM International D30.04 Committee 2015a

ASTM International D30.04 Committee (2015a). *Standard Test Methods for Constituent Content of Composite Materials*. ASTM E3171-15. West Conshohocken: ASTM International. URL: <https://www.astm.org/d3171-15.html> (Accessed: Jan. 5, 2022).

ASTM International D30.04 Committee 2015b

ASTM International D30.04 Committee (2015b). *Standard Test Methods for Standard Test Method for Flexural Properties of Polymer Matrix Composite Materials*. ASTM D7264/D7264M-15. West Conshohocken: ASTM International. URL: https://www.astm.org/d7264_d7264m-15.html (Accessed: Jan. 5, 2022).

ASTM International D30.06 Committee 2013

ASTM International D30.06 Committee (2013). *Standard Test Method for Mode I Interlaminar Fracture Toughness of Unidirectional Fiber-Reinforced Polymer Matrix Composites*. ASTM D5528-13. West Conshohocken: ASTM International. URL: <https://www.astm.org/d5528-13.html> (Accessed: Jan. 5, 2022).

ASTM International E07.10 Committee 2017

ASTM International E07.10 Committee (2017). *Standard Guide for Nondestructive Testing of Polymer Matrix Composites Used in Aerospace Applications*. ASTM E2533-17. West Conshohocken: ASTM International. URL: <https://www.astm.org/e2533-17.html> (Accessed: Jan. 5, 2022).

ASTM International E37.01 Committee 2020

ASTM International E37.01 Committee (2020). *Standard Test Method for Compositional Analysis by Thermogravimetry*. ASTM E1131-20. West Conshohocken: ASTM International. URL: <https://www.astm.org/e1131-20.html> (Accessed: Jan. 5, 2022).

Barbero 2013

Barbero, E. J. (2013). *Finite element analysis of composite materials using Abaqus*. 1. Ed. Cleveland: CRC Press. DOI: 10.1201/b14788.

Bauernhansel 2016

Bauernhansel, T. (2016). *Leichtbau im Maschinen-, Anlagen-, und Gerätebau*. Stuttgart: Fraunhofer Institute for Manufacturing Engineering and Automation IPA (Fraunhofer IPA). URL: <http://publica.fraunhofer.de/dokumente/N-441527.html> (Accessed: Jan. 5, 2022).

Bellman 1961

Bellman, R. (1961). *Adaptive Control Processes: A Guided Tour*. Princeton: Princeton University Press. URL: <http://www.jstor.org/stable/j.ctt183ph6v> (Accessed: Jan. 5, 2022).

Benaicha et al. 2015

Benaicha, M.; Jalbaud, O.; Hafidi Alaoui, A. & Burtschell, Y. (2015). „Correlation between the

mechanical behavior and the ultrasonic velocity of fiber-reinforced concrete“, *Construction and Building Materials* 101.1, pp. 702–709. DOI: 10.1016/j.conbuildmat.2015.10.047.

Benveniste 1987

Benveniste, Y. (1987). „A new approach to the application of Mori-Tanaka’s theory in composite materials“, *Mechanics of Materials* 6.2, pp. 147–157. DOI: 10.1016/0167-6636(87)90005-6.

Berger 2019

Berger, D. (2019). *Qualitätssicherung von textilen Kohlenstofffaser-Preforms mittels prozess-integrierter Wirbelstromsensor-Arrays*. Dissertation, Karlsruhe Institute of Technology (KIT). Düren: Shaker. DOI: 10.5445/IR/1000090870.

Bertram et al. 2016

Bertram, B.; Pinter, P. & Weidenmann, K. A. (2016). „Non-destructive determination of the local fiber volume content in flat AL(OH)₃-filled SMC parts from X-ray projections“. Online Proceedings of the 17th European Conference on Composite Materials (ECCM17) (Munich, Germany, June 26–30, 2016). European Society for Composite Materials. URL: <https://www.carbon-connected.de/Group/ECCM17-.17th.European.Conference.on.Composite.Materials/4-Exp/Start/Accordion?perPage=10&page=5> (Accessed: Jan. 5, 2022).

Beyerer 2016

Beyerer, J. (2016). *Machine Vision - Automated Visual Inspection: Theory, Practice and Applications*. Ed. by F. Puente León & C. Frese. 1. Ed. Berlin: Springer. DOI: 10.1007/978-3-662-47794-6.

Böhlke & Kärger et al. 2016

Böhlke, T.; Kärger, L.; Weidenmann, K. A.; Seelig, T. & Henning, F. (2016). „Integrated engineering of continuous-discontinuous long fiber reinforced polymer (CoDiCo-FRP) structures in the framework of the International Research Training Group GRK 2078“. Presentation on the 5th Congress on Composite Simulation (Hamburg, Germany, Feb. 25, 2016). URL: <https://www.composite-simulation.de/?ID=Rueckblick> (Accessed: Jan. 5, 2022).

Böhlke & Henning et al. 2019

Böhlke, T.; Henning, F.; Hrymak, A.; Kärger, L.; Weidenmann, K. A. & Wood, J. T. (2019). *Continuous–Discontinuous Fiber-Reinforced Polymers – An integrated Engineering Approach*. 1. Ed. Munich: Carl Hanser. DOI: 10.3139/9781569906934.

Bouhleb et al. 2019

Bouhleb, M. A.; Hwang, J. T.; Bartoli, N.; Lafage, R.; Morlier, J. & Martins, J. R. (2019). „A Python surrogate modeling framework with derivatives“, *Advances in Engineering Software* 135, Article 102662. DOI: 10.1016/j.advengsoft.2019.03.005.

Brabandt 2018

Brabandt, D. (2018). *Qualitätssicherung von textilen Kohlenstofffaser-Preforms mittels optischer Messtechnik*. Dissertation, Karlsruhe Institute of Technology (KIT). Düren: Shaker. DOI: 10.5445/IR/1000085135.

Brasington et al. 2021

Brasington, A.; Sacco, C.; Halbritter, J.; Wehbe, R. & Harik, R. (2021). „Automated fiber placement: A review of history, current technologies, and future paths forward“, *Composites Part C: Open Access* 6, Article 100182. DOI: 10.1016/j.jcomc.2021.100182.

Bretz & Häfner et al. 2019

Bretz, L.; Häfner, B. & Lanza, G. (2019). „Funktionsorientierte Inline-Messtechnik von Faserverbunden“, *wt Werkstatttechnik online* 11/12, pp. 816–821. DOI: 10.37544/1436-4980-2019-11-12-18.

Bretz & Häfner et al. 2021

Bretz, L.; Häfner, B. & Lanza, G. (2021). „Non-destructive measurement of fiber mass content of glass fiber sheet molding compound using Terahertz radiation“, *Measurement* 168, Article 108386. DOI: 10.1016/j.measurement.2020.108386.

Bretz & Hinze et al. 2019

Bretz, L.; Hinze, T.; Häfner, B. & Lanza, G. (2019). „Evaluation of anomaly detection capabilities using a non-orthogonal camera angle in pulse-phase thermography“. Online Proceedings of the 2nd CIRP Conference on Composite Material Parts Manufacturing (CCMPM 2019) (Sheffield, United Kingdom, Oct. 10–11, 2019). Elsevier, pp. 308–313. DOI: 10.1016/j.procir.2019.09.032.

Brylka 2017

Brylka, B. (2017). *Charakterisierung und Modellierung der Steifigkeit von langfaserverstärktem Polypropylen*. Dissertation, Karlsruhe Institute of Technology (KIT). Karlsruhe: KIT Scientific Publishing. DOI: 10.5445/KSP/1000070061.

Bücheler 2018

Bücheler, D. (2018). *Locally continuous-fiber reinforced sheet molding compound*. Dissertation, Karlsruhe Institute of Technology (KIT). Stuttgart: Fraunhofer. DOI: 10.5445/IR/1000079163.

Bücheler & Henning 2016

Bücheler, D. & Henning, F. (2016). „Hybrid resin improves position and alignment of continuously reinforced prepreg during compression co-molding with sheet molding compound“. Online Proceedings of the 17th European Conference on Composite Materials (ECCM17) (Munich, Germany, June 26–30, 2016). European Society for Composite Materials. URL: <https://www.carbon-connected.de/Group/ECCM17-.17th.European.Conference>.

on.Composite.Materials/5-MT/Start/Accordion?perPage=10&page=18 (Accessed: Jan. 5, 2022).

Bücheler & Kaiser et al. 2016

Bücheler, D.; Kaiser, A. & Henning, F. (2016). „Using Thermogravimetric Analysis to Determine Carbon Fiber Weight Percentage of Fiber-Reinforced Plastics“, *Composites Part B: Engineering* 106, pp. 218–223. DOI: 10.1016/j.compositesb.2016.09.028.

Busse et al. 1992

Busse, G.; Wu, D. & Karpen, W. (1992). „Thermal wave imaging with phase sensitive modulated thermography“, *Journal of Applied Physics* 71.8, pp. 3962–3965. DOI: 10.1063/1.351366.

Cherif 2016

Cherif, C. (2016). *Textile Materials for Lightweight Constructions*. 1. Ed. Berlin: Springer. DOI: 10.1007/978-3-662-46341-3.

Chu & Majumdar 2012

Chu, S. & Majumdar, A. (2012). „Opportunities and challenges for a sustainable energy future“, *Nature* 488, pp. 294–303. DOI: 10.1038/nature11475.

Colombo & Vergani 2014

Colombo, C. & Vergani, L. (2014). „Influence of delamination on fatigue properties of a fibreglass composite“, *Composite Structures* 107, pp. 325–333. DOI: 10.1016/j.compstruct.2013.07.028.

Coral et al. 2016

Coral, R.; Flesch, C. A.; Penz, C. A.; Roisenberg, M. & Pacheco, A. (2016). „A Monte Carlo-Based Method for Assessing the Measurement Uncertainty in the Training and Use of Artificial Neural Networks“, *Metrology and Measurement Systems* 23.2, pp. 281–294. DOI: 10.1515/mms-2016-0015.

Corbridge et al. 2017

Corbridge, D.; Harper, L.; De Focatiis, D. & Warrior, N. (2017). „Compression moulding of composites with hybrid fibre architectures“, *Composites Part A: Applied Science and Manufacturing* 95, pp. 87–99. DOI: 10.1016/j.compositesa.2016.12.018.

Deutsches Institut für Normung e.V. 2011a

Deutsches Institut für Normung e.V. (2011a). *Fibre-reinforced plastic composites – Determination of flexural properties*. DIN EN ISO 14125:2011-05. Berlin: Beuth. URL: <https://www.beuth.de/en/standard/din-en-iso-14125/139335738> (Accessed: Jan. 5, 2022).

Deutsches Institut für Normung e.V. 2011b

Deutsches Institut für Normung e.V. (2011b). *Geometrical product specifications (GPS) – Coordinate measuring machines (CMM): Technique for determining the uncertainty of*

- measurement – Part 3: Use of calibrated workpieces or measurement standards*. DIN EN ISO 15530-3:2011-10. Berlin: Beuth. URL: <https://www.iso.org/standard/53627.html> (Accessed: Jan. 5, 2022).
- Deutsches Institut für Normung e.V. 2019
- Deutsches Institut für Normung e.V. (2019). *Plastics - Determination of tensile properties - Part 1: General principles*. DIN EN ISO 527-1:2019-12. Berlin: Beuth. URL: <https://www.beuth.de/en/standard/din-en-iso-527-1/306958894> (Accessed: Jan. 5, 2022).
- Deutsches Institut für Normung e.V. 2020
- Deutsches Institut für Normung e.V. (2020). *Plastics – Thermogravimetry (TG) of polymers – Part 1: General principles*. DIN EN ISO 11358-1:2020-12. Berlin: Beuth. URL: <https://www.beuth.de/en/draft-standard/din-en-iso-11358-1/331048123> (Accessed: Jan. 5, 2022).
- Dey et al. 2017
- Dey, S.; Mukhopadhyay, T. & Adhikari, S. (2017). „Metamodel based high-fidelity stochastic analysis of composite laminates: A concise review with critical comparative assessment“, *Composite Structures* 171, pp. 227–250. DOI: 10.1016/j.compstruct.2017.01.061.
- Domininghaus 2012
- Domininghaus, H. (2012). *Kunststoffe : Eigenschaften und Anwendungen*. Ed. by P. Elsner; P. Eyerer & T. Hirth. 8. Ed. Berlin: Springer. DOI: 10.1007/978-3-642-16173-5.
- Donaldson & Miracle 2001
- Donaldson, S. L. & Miracle, D. B. (2001). *ASM Handbook Vol 21: Composites*. 10. Ed. Novelty: ASM International.
- Dong 2016
- Dong, C. (2016). „Effects of Process-Induced Voids on the Properties of Fibre Reinforced Composites“, *Journal of Materials Science & Technology* 32.7, pp. 597–604. DOI: 10.1016/j.jmst.2016.04.011.
- Dong et al. 2015
- Dong, J.; Kim, B.; Locquet, A.; McKeon, P.; Declercq, N. & Citrin, D. (2015). „Nondestructive evaluation of forced delamination in glass fiber-reinforced composites by terahertz and ultrasonic waves“, *Composites Part B: Engineering* 79, pp. 667–675. DOI: 10.1016/j.compositesb.2015.05.028.
- Duan et al. 2012
- Duan, Y.; Servais, P.; Genest, M.; Ibarra-Castanedo, C. & Maldague, X. P. V. (2012). „ThermoPoD: A reliability study on active infrared thermography for the inspection of composite material“, *Journal of Mechanical Science and Technology* 26.7, pp. 1985–1991. DOI: 10.1007/s12206-012-0510-8.

Eshelby 1957

Eshelby, J. D. (1957). „The determination of the elastic field of an ellipsoidal inclusion, and related problems“, *Proceedings of the Royal Society A* 241.1226, pp. 147–157. DOI: 10.1098/rspa.1957.0133.

Essig 2018

Essig, W. (2018). *Ganzheitliche Betrachtung zur zerstörungsfreien Prüfung von thermoplastischen CFK-Tapes mittels Luftultraschall*. Dissertation, University of Stuttgart. Stuttgart: Institut für Kunststofftechnik.

Esward et al. 2003

Esward, T.; Lord, G. & Wright, L. (2003). *Model Validation in Continuous Modelling*. NPL Report. CMSC 29/03. Teddington: National Physical Laboratory. URL: <https://eprintspublications.npl.co.uk/2857/> (Accessed: Jan. 5, 2022).

European Alliance for SMC/BMC 2016

European Alliance for SMC/BMC (2016). *Design for success - A design & technology manual for SMC/BMC*. Brussels: European Alliance for SMC/BMC. URL: <https://smcbmc-europe.org/design-for-success.php> (Accessed: Jan. 5, 2022).

European Commission 2019

European Commission (2019). *Communication from the Commission to the European Parliament, the European Council, the Council, the European Economic and Social Committee and the Committee of the Regions - The European Green Deal*. URL: <https://eur-lex.europa.eu/legal-content/EN/TXT/?uri=CELEX%3A52019DC0640> (Accessed: Jan. 5, 2022).

Fengler & Kärger et al. 2018

Fengler, B.; Kärger, L.; Henning, F. & Hrymak, A. (2018). „Multi-Objective Patch Optimization with Integrated Kinematic Draping Simulation for Continuous–Discontinuous Fiber-Reinforced Composite Structures“, *Journal of Composites Science* 2.2, Article 22. DOI: 10.3390/jcs2020022.

Fengler & Schäferling et al. 2019

Fengler, B.; Schäferling, M.; Schäfer, B.; Bretz, L.; Lanza, G.; Häfner, B.; Hrymak, A. & Kärger, L. (2019). „Manufacturing uncertainties and resulting robustness of optimized patch positions on continuous-discontinuous fiber reinforced polymer structures“, *Composite Structures* 213, pp. 47–57. DOI: 10.1016/j.compstruct.2019.01.063.

Fischer et al. 2019

Fischer, B.; Sarasini, F.; Tirillò, J.; Touchard, F.; Chocinski-Arnault, L.; Mellier, D.; Panzer, N.; Sommerhuber, R.; Russo, P.; Papa, I.; Loprestó, V. & Ecault, R. (2019). „Impact damage assessment in biocomposites by micro-CT and innovative air-coupled detection of

- laser-generated ultrasound“, *Composite Structures* 210, pp. 922–931. DOI: 10.1016/j.compstruct.2018.12.013.
- Fish & Belytschko 2007
- Fish, J. & Belytschko, T. (2007). *A first course in finite elements*. Reprinted with corrections. Chichester: Wiley, p. 319. URL: <https://www.wiley.com/en-us/A+First+Course+in+Finite+Elements-p-9780470035801> (Accessed: Jan. 5, 2022).
- Franz et al. 2019a
- Franz, M.; Schleich, B. & Wartzack, S. (2019a). „Influence of layer thickness variations on the structural behaviour of optimised fibre reinforced plastic parts“. Online Proceedings of the 2nd CIRP Conference on Composite Material Parts Manufacturing (CCMPM 2019) (Sheffield, United Kingdom, Oct. 10–11, 2019). Elsevier, pp. 26–31. DOI: 10.1016/j.procir.2019.09.034.
- Franz et al. 2019b
- Franz, M.; Schleich, B. & Wartzack, S. (2019b). „Variation Analysis of Design Parameters of Fibre-Reinforced Plastic Parts“. Proceedings of the Design Society: International Conference on Engineering Design (Delft, Netherlands, Aug. 5–10, 2019). Cambridge University Press, pp. 2725–2734. DOI: 10.1017/dsi.2019.279.
- Franz et al. 2021
- Franz, M.; Schleich, B. & Wartzack, S. (2021). „Tolerance management during the design of composite structures considering variations in design parameters“, *The International Journal of Advanced Manufacturing Technology* 113, pp. 1753–1770. DOI: 10.1007/s00170-020-06555-5.
- Fries 2018
- Fries, T.-P. (2018). „Extended Finite Element Methods (XFEM)“. *Encyclopedia of Continuum Mechanics*. Ed. by H. Altenbach & A. Öchsner. Berlin: Springer, pp. 1–10. DOI: 10.1007/978-3-662-53605-6_17-1.
- Gao et al. 2019
- Gao, W.; Haitjema, H.; Fang, F.; Leach, R.; Cheung, C.; Savio, E. & Linares, J. (2019). „On-machine and in-process surface metrology for precision manufacturing“, *CIRP Annals* 68, pp. 843–866. DOI: 10.1016/j.cirp.2019.05.005.
- German Association of the Automotive Industry 2011
- German Association of the Automotive Industry (2011). *Quality Management in the Automotive Industry - Capability of Measurement Processes*. VDA Band 5.1:2011-07. Frankfurt: Henrich Druck und Medien GmbH.
- Görthofer et al. 2019
- Görthofer, J.; Meyer, N.; Pallicity, T. D.; Schöttl, L.; Trauth, A.; Schemmann, M.; Hohberg, M.; Pinter, P.; Elsner, P.; Henning, F.; Hrymak, A.; Seelig, T.; Weidenmann, K. A.; Kärger, L.

& Böhlke, T. (2019). „Virtual process chain of sheet molding compound: Development, validation and perspectives“, *Composites Part B: Engineering* 169, pp. 133–147. DOI: 10.1016/j.compositesb.2019.04.001.

Grätsch & Bathe 2005

Grätsch, T. & Bathe, K.-J. (2005). „A posteriori error estimation techniques in practical finite element analysis“, *Computers & Structures* 83.4, pp. 235–265. DOI: 10.1016/j.compstruc.2004.08.011.

Grimberg et al. 2013

Grimberg, R.; Šturm, R. & Grum, J. (2013). „Nondestructive evaluation and characterization of fiber reinforced composites using non-contact ultrasound transducers“. Online Proceedings of the 12th International Conference of the Slovenian Society for Non-Destructive Testing (Portorož, Slovenia, Sept. 4–6, 2013). NDT.net, Article 16084. URL: <https://www.ndt.net/search/docs.php3?id=16084> (Accessed: Jan. 5, 2022).

Groß et al. 2018

Groß, L.; Herwig, A.; Berg, D.; Schmidt, C.; Denkena, B.; Horst, P. & Meiners, D. (2018). „Production-based design of a hybrid load introduction element for thin-walled CFRP Structures“, *Production Engineering* 12.2, pp. 113–120. DOI: 10.1007/s11740-018-0821-4.

Gross & Seelig 2018

Gross, D. & Seelig, T. (2018). *Fracture Mechanics: With an Introduction to Micromechanics*. 3. Ed. Berlin: Springer. DOI: 10.1007/978-3-319-71090-7.

Häfner 2017

Häfner, B. (2017). *Lebensdauerprognose in Abhängigkeit der Fertigungsabweichungen bei Mikroverzahnungen*. Dissertation, Karlsruhe Institute of Technology (KIT). Karlsruhe: Shaker.

Häfner & Biehler et al. 2018

Häfner, B.; Biehler, M.; Wagner, R. & Lanza, G. (2018). „Comparison of anomaly detection capabilities of pulse phase thermography in transmission and reflection setup on Sheet Molding Compound“. Online Proceedings of the 15th CIRP Conference on Computer Aided Tolerancing (Milan, Italy, June 13–11, 2018). Elsevier, pp. 155–160. DOI: 10.1016/j.procir.2018.04.031.

Häfner & Lanza 2017

Häfner, B. & Lanza, G. (2017). „Function-oriented measurements and uncertainty evaluation of micro-gears for lifetime prognosis“, *CIRP Annals* 66.1, pp. 475–478. DOI: 10.1016/j.cirp.2017.04.065.

Ham & Popovics 2015

Ham, S. & Popovics, J. S. (2015). „Application of contactless ultrasound toward automated

- inspection of concrete structures“, *Automation in Construction* 58, pp. 155–164. DOI: 10.1016/j.autcon.2015.07.018.
- Hartmann & Weckenmann 2014
- Hartmann, W. & Weckenmann, A. (2014). „Verifying the functional ability of microstructured surfaces by model-based testing“, *Measurement Science and Technology* 25.9, Article 094012. DOI: 10.1088/0957-0233/25/9/094012.
- Hauck et al. 2014
- Hauck, J.; Kremling, S.; Stich, D. & Heidemeyer, P. (2014). „Prüfung von Kunststoffbauteilen mittels Terahertz-Technologie: Der Weg von der Transmissionszur Reflexionsanordnung“. Online Proceedings of DGZfP-Jahrestagung 2014 (Potsdam, Germany, May 26–28, 2014). NDT.net, Article 17411. URL: <https://www.ndt.net/search/docs.php3?id=17411> (Accessed: Jan. 5, 2022).
- Heikkilä 2000
- Heikkilä, J. (2000). „Geometric camera calibration using circular control points“, *IEEE Transactions on Pattern Analysis and Machine Intelligence* 22.10, pp. 1066–1077. DOI: 10.1109/34.879788.
- Hürkamp et al. 2019
- Hürkamp, A.; Lorenz, R.; Behrens, B.-A. & Dröder, K. (2019). „Computational Manufacturing for Multi-Material Lightweight Parts“. Online Proceedings of the 2nd CIRP Conference on Composite Material Parts Manufacturing (CCMPM 2019) (Sheffield, United Kingdom, Oct. 10–11, 2019). Elsevier, pp. 102–107. DOI: 10.1016/j.procir.2019.09.041.
- Ibarra-Castanedo & Maldague 2004
- Ibarra-Castanedo, C. & Maldague, X. (2004). „Pulsed phase thermography reviewed“, *Quantitative InfraRed Thermography Journal* 1.1, pp. 47–70. DOI: 10.3166/qirt.1.47-70.
- Im et al. 2020
- Im, K.-H.; Kim, S.-K.; Jung, J.-A.; Cho, Y.-T.; Woo, Y.-D. & Chiou, C.-P. (2020). „NDE Terahertz Wave Techniques for Measurement of Defect Detection on Composite Panels of Honeycomb Sandwiches“, *Electronics* 9.9, Article 1360. DOI: 10.3390/electronics9091360.
- Imkamp & Berthold 2009
- Imkamp, D. & Berthold, J. (2009). „Schneller, sicherer, genauer – Roadmap Fertigungsmesstechnik 2020 (Teil1)“, *QZ - Qualität und Zuverlässigkeit* 54.5, pp. 36–39. URL: <https://www.qz-online.de/a/article/article-292139> (Accessed: Jan. 5, 2022).
- JCGM100 2008
- JCGM100 (2008). *Evaluation of measurement data — Guide to the expression of uncer-*

tainty in measurement (GUM). Joint Committee for Guides in Metrology. URL: <https://www.bipm.org/en/committees/jc/jcgm/publications> (Accessed: Jan. 5, 2022).

JCGM101 2008

JCGM101 (2008). *Evaluation of measurement data - Supplement 1 to the "Guide to the expression of uncertainty in measurement" - Propagation of distributions using a Monte Carlo method*. Joint Committee for Guides in Metrology. URL: <https://www.bipm.org/en/committees/jc/jcgm/publications> (Accessed: Jan. 5, 2022).

JCGM200 2012

JCGM200 (2012). *International vocabulary of metrology — Basic and general concepts and associated terms (VIM)*. Joint Committee for Guides in Metrology. URL: <https://www.bipm.org/en/committees/jc/jcgm/publications> (Accessed: Jan. 5, 2022).

Jördens & Scheller & Wietzke et al. 2010

Jördens, C.; Scheller, M.; Wietzke, S.; Romeike, D.; Jansen, C.; Zentgraf, T.; Wiesauer, K.; Reisecker, V. & Koch, M. (2010). „Terahertz spectroscopy to study the orientation of glass fibres in reinforced plastics“, *Composites Science and Technology* 70.3, pp. 472–477. DOI: 10.1016/j.compscitech.2009.11.022.

Jördens & Scheller & Wichmann et al. 2009

Jördens, C.; Scheller, M.; Wichmann, M.; Mikulics, M.; Wiesauer, K. & Koch, M. (2009). „Terahertz birefringence for orientation analysis“, *Applied Optics* 48.11, pp. 2037–2044. DOI: 10.1364/AO.48.002037.

Karabutov & Podymova 2014

Karabutov, A. & Podymova, N. (2014). „Quantitative analysis of the influence of voids and delaminations on acoustic attenuation in CFRP composites by the laser-ultrasonic spectroscopy method“, *Composites Part B: Engineering* 56, pp. 238–244. DOI: 10.1016/j.compositesb.2013.08.040.

Kehrer & Pinter et al. 2017

Kehrer, L.; Pinter, P. & Böhlke, T. (2017). „Mean and full field homogenization of artificial long fiber reinforced thermoset polymers“. Online Proceedings of the 88th Annual Meeting in Applied Mathematics and Mechanics (Weimar, Germany, Mar. 6–10, 2017). Wiley, pp. 603–604. DOI: 10.1002/pamm.201710271.

Kehrer & Wicht et al. 2018

Kehrer, L.; Wicht, D.; Wood, J. T. & Böhlke, T. (2018). „Dynamic mechanical analysis of pure and fiber-reinforced thermoset- and thermoplastic-based polymers and free volume-based viscoelastic modeling“, *GAMM-Mitteilungen* 41.1, Article e201800007. DOI: 10.1002/gamm.201800007.

Kehrer 2019

Kehrer, M. L. (2019). *Thermomechanical Mean-Field Modeling and Experimental Char-*

- acterization of Long Fiber-Reinforced Sheet Molding Compound Composites*. Dissertation, Karlsruhe Institute of Technology (KIT). Karlsruhe: KIT Scientific Publishing. DOI: 10.5445/KSP/1000093328.
- Knops 2008
Knops, M. (2008). *Analysis of Failure in Fiber Polymer Laminates: The Theory of Alfred Puck*. 1. Ed. Berlin: Springer. DOI: 10.1007/978-3-540-75765-8.
- Kosse 2018
Kosse, P. (2018). *Modellierung der Messunsicherheit der dreidimensionalen Erfassung von Faserverbundkunststoff-Preforms*. Dissertation, RWTH Aachen University. Aachen: Apprimus.
- Kosse et al. 2014
Kosse, P.; Fürtjes, T. & Schmitt, R. (2014). „Digitalisierung dreidimensionaler CFK-Halbzeuge zur Fehlstellenklassifizierung am Beispiel der Faserwelligkeit“. Online Proceedings of Forum Bildverarbeitung 2014 (Regensburg, Germany, Nov. 27–28, 2014). KIT Scientific Publishing, pp. 141–151. DOI: 10.1002/pamm.201710271.
- Krämer et al. 2014
Krämer, A.; Lin, S.; Brabandt, D.; Böhlke, T. & Lanza, G. (2014). „Quality Control in the Production Process of SMC Lightweight Material“. Online Proceedings of the 47th CIRP Conference on Manufacturing Systems (Windsor, Canada, Apr. 28–30, 2014). Elsevier, pp. 772–777. DOI: 10.1002/pamm.201710271.
- Krumbholz et al. 2009
Krumbholz, N.; Hochrein, T.; Vieweg, N.; Hasek, T.; Kretschmer, K.; Bastian, M.; Mikulics, M. & Koch, M. (2009). „Monitoring polymeric compounding processes inline with THz time-domain spectroscopy“, *Polymer Testing* 28.1, pp. 30–35. DOI: 10.1016/j.polymeresting.2008.09.009.
- Kruth et al. 2011
Kruth, J.; Bartscher, M.; Carmignato, S.; Schmitt, R.; De Chiffre, L. & Weckenmann, A. (2011). „Computed tomography for dimensional metrology“, *CIRP Annals* 60.2, pp. 821–842. DOI: 10.1016/j.cirp.2011.05.006.
- Lanza et al. 2019
Lanza, G.; Häfner, B.; Schild, L.; Berger, D.; Eschner, N.; Wagner, R. & Zaiß, M. (2019). „In-Line Measurement Technology and Quality Control“. *Metrology*. Ed. by W. Gao. Singapore: Springer, pp. 399–433. DOI: 10.1007/978-981-10-4938-5_14.
- Lee et al. 2020
Lee, J.; Lee, Y.-J. & Shim, C.-S. (2020). „Probabilistic prediction of mechanical characteristics of corroded strands“, *Engineering Structures* 203, Article 109882. DOI: 10.1016/j.engstruct.2019.109882.

Léonard et al. 2017

Léonard, F.; Stein, J.; Soutis, C. & Withers, P. (2017). „The quantification of impact damage distribution in composite laminates by analysis of X-ray computed tomograms“, *Composites Science and Technology* 152, pp. 139–148. DOI: 10.1016/j.compscitech.2017.08.034.

Lightfoot et al. 2017

Lightfoot, J.; Wisnom, M. & Potter, K. (2017). „Examination of drape-induced defects using computer X-ray tomography“. Online Proceedings of the 19th International Conference on Composite Materials (ICCM19) (Montreal, Canada, July 28–Feb. 2, 2013). Concordia Centre for Composites, Article LIG80130. URL: <http://www.iccm-central.org/Proceedings/ICCM19proceedings/> (Accessed: Jan. 5, 2022).

Little et al. 2012

Little, J. E.; Yuan, X. & Jones, M. I. (2012). „Characterisation of voids in fibre reinforced composite materials“, *NDT & E International* 46, pp. 122–127. DOI: 10.1016/j.ndteint.2011.11.011.

Loeppky et al. 2009

Loeppky, J. L.; Sacks, J. & Welch, W. J. (2009). „Choosing the Sample Size of a Computer Experiment: A Practical Guide“, *Technometrics* 51.4, pp. 366–376. DOI: 10.1198/TECH.2009.08040.

Lord & Wright 2003

Lord, G. & Wright, L. (2003). *Uncertainty Evaluation in Continuous Modelling*. NPL Report. CMSC 31/03. Teddington: National Physical Laboratory. URL: <https://eprintspublications.npl.co.uk/2900/> (Accessed: Jan. 5, 2022).

Maldague 2001

Maldague, X. P. V. (2001). *Theory and practice of infrared technology for nondestructive testing*. Ed. by K. Chang. New York: Wiley.

Manta et al. 2019

Manta, A.; Gresil, M. & Soutis, C. (2019). „Infrared thermography for void mapping of a graphene/epoxy composite and its full-field thermal simulation“, *Fatigue & Fracture of Engineering Materials & Structures* 42.7, pp. 1441–1453. DOI: 10.1111/ffe.12980.

Mathes & Witten 2013

Mathes, V. & Witten, E. (2013). *Handbuch Faserverbundkunststoffe/Composites: Grundlagen, Verarbeitung, Anwendungen*. 4. Ed. Wiesbaden: Springer Vieweg. DOI: 10.1007/978-3-658-02755-1.

May 2020

May, D. (2020). *Integrierte Produktentwicklung mit Faser-Kunststoff-Verbunden*. 1. Ed. Berlin: Springer. DOI: 10.1007/978-3-662-60286-7.

Mehdikhani et al. 2018

Mehdikhani, M.; Steensels, E.; Standaert, A.; Vallons, K.; Gorbatikh, L. & Lomov, S. (2018). „Multi-scale digital image correlation for detection and quantification of matrix cracks in carbon fiber composite laminates in the absence and presence of voids controlled by the cure cycle“, *Composites Part B: Engineering* 154, pp. 138–147. DOI: 10.1016/j.compositesb.2018.07.006.

Meng et al. 2021

Meng, X.; Feng, J.; Pai, N.; Zequan, H.; Kaiyuan, L.; Cheng, Z. & Yazhen, Z. (2021). „Effects of filler type and aging on self-sensing capacity of cement paste using eddy current-based nondestructive detection“, *Measurement* 182, Article 109708. DOI: 10.1016/j.measurement.2021.109708.

Meola & Carlomagno 2010

Meola, C. & Carlomagno, G. M. (2010). „Impact damage in GFRP: New insights with infrared thermography“, *Composites Part A: Applied Science and Manufacturing* 41.12, pp. 1839–1847. DOI: 10.1016/j.compositesa.2010.09.002.

Mesogitis et al. 2014

Mesogitis, T.; Skordos, A. & Long, A. (2014). „Uncertainty in the manufacturing of fibrous thermosetting composites: A review“, *Composites Part A: Applied Science and Manufacturing* 57, pp. 67–75. DOI: 10.1016/j.compositesa.2013.11.004.

Meyer et al. 2020

Meyer, N.; Schöttl, L.; Bretz, L.; Hrymak, A. N. & Kärger, L. (2020). „Direct Bundle Simulation approach for the compression molding process of Sheet Molding Compound“, *Composites Part A: Applied Science and Manufacturing* 132, Article 105809. DOI: 10.1016/j.compositesa.2020.105809.

Mizukami & Watanabe 2018

Mizukami, K. & Watanabe, Y. (2018). „A simple inverse analysis method for eddy current-based measurement of through-thickness conductivity of carbon fiber composites“, *Polymer Testing* 69, pp. 320–324. DOI: 10.1016/j.polymertesting.2018.05.043.

Montanini 2010

Montanini, R. (2010). „Quantitative determination of subsurface defects in a reference specimen made of Plexiglas by means of lock-in and pulse phase infrared thermography“, *Infrared Physics & Technology* 53.5, pp. 363–371. DOI: 10.1016/j.infrared.2010.07.002.

Mori & Tanaka 1973

Mori, T. & Tanaka, K. (1973). „Average stress in matrix and average elastic energy of materials with misfitting inclusions“, *Acta Metallurgica* 21.5, pp. 571–574. DOI: 10.1016/0001-6160(73)90064-3.

Naresh et al. 2020

Naresh, K.; Khan, K.; Umer, R. & Cantwell, W. (2020). „The use of X-ray computed tomography for design and process modeling of aerospace composites: A review“, *Materials & Design* 190, Article 108553. DOI: 10.1016/j.matdes.2020.108553.

Nasdala 2015

Nasdala, L. (2015). *FEM-Formelsammlung Statik und Dynamik: Hintergrundinformationen, Tipps und Tricks*. 3. Ed. Wiesbaden: Springer Vieweg. DOI: 10.1007/978-3-658-06630-7.

Neitzel et al. 2014

Neitzel, M.; Mitschang, P. & Breuer, U. (2014). *Handbuch Verbundwerkstoffe: Werkstoffe, Verarbeitung, Anwendung*. Ed. by Federation of Reinforced Plastics. 2. Ed. Munich: Carl Hanser. DOI: 10.3139/9783446436978.

Neto 2015

Neto, M. A. (2015). *Engineering Computation of Structures: The Finite Element Method*. Ed. by A. Amaro; L. Roseiro; J. Cirne & R. Leal. 1. Ed. Cham: Springer. DOI: 10.1007/978-3-319-17710-6.

Nüßler & Jonuscheit 2021

Nüßler, D. & Jonuscheit, J. (2021). „Terahertz based non-destructive testing (NDT)“, *tm - Technisches Messen* 88.4, pp. 199–210. DOI: doi:10.1515/teme-2019-0100.

Pangboonyanon et al. 2016

Pangboonyanon, W.; Zaiß, M.; Fleischer, J. & Lanza, G. (2016). „Optimization of process chain for continuous-discontinuous long fiber reinforced polymer structures“. Online Proceedings of the 17th European Conference on Composite Materials (ECCM17) (Munich, Germany, June 26–30, 2016). European Society for Composite Materials. URL: <https://www.carbon-connected.de/Group/ECCM17-.17th.European.Conference.on.Composite.Materials/5-MT/Start/Accordion?perPage=10&page=15> (Accessed: Jan. 5, 2022).

Park et al. 2014

Park, B.; An, Y.-K. & Sohn, H. (2014). „Visualization of hidden delamination and debonding in composites through noncontact laser ultrasonic scanning“, *Composites Science and Technology* 100, pp. 10–18. DOI: 10.1016/j.compscitech.2014.05.029.

Pfrommer et al. 2018

Pfrommer, J.; Zimmerling, C.; Liu, J.; Kärger, L.; Henning, F. & Beyerer, J. (2018). „Optimisation of manufacturing process parameters using deep neural networks as surrogate models“. Online Proceedings of the 51st CIRP Conference on Manufacturing Systems (Stockholm, Sweden, May 16–18, 2018). Elsevier, pp. 426–431. DOI: 10.1016/j.procir.2018.03.046.

Pinter 2018

Pinter, P. (2018). *Microstructure characterization of continuous-discontinuous fibre reinforced Polymers based on volumetric images*. Dissertation, Karlsruhe Institute of Technology (KIT). Karlsruhe: KIT Scientific Publishing. DOI: 10.5445/IR/1000084499.

Puck et al. 2002

Puck, A.; Kopp, J. & Knops, M. (2002). „Guidelines for the determination of the parameters in Puck’s action plane strength criterion“, *Composites Science and Technology* 62.3, pp. 371–378. DOI: 10.1016/S0266-3538(01)00202-0.

Reden & Schüppel 2019

Reden, T. von & Schüppel, D. (2019). „Entwicklungen hin zu kostengünstigem CFK“, *Lightweight Design* 12, pp. 60–63. DOI: 10.1007/s35725-018-0071-6.

Reed & Marks 1998

Reed, R. D. & Marks, R. J. (1998). *Neural Smithing: Supervised Learning in Feedforward Artificial Neural Networks*. Cambridge: MIT Press. URL: <https://mitpress.mit.edu/books/neural-smithing> (Accessed: Jan. 5, 2022).

Rieh 2021

Rieh, J.-S. (2021). *Introduction to Terahertz Electronics*. 1. Ed. Cham: Springer International Publishing. DOI: 10.1007/978-3-030-51842-4.

Ripley 1996

Ripley, B. D. (1996). *Pattern recognition and neural networks*. 1. Ed. Cambridge: Cambridge University Press. DOI: 10.1017/CB09780511812651.

Ryu et al. 2016

Ryu, C.-H.; Park, S.-H.; Kim, D.-H.; Jhang, K.-Y. & Kim, H.-S. (2016). „Nondestructive evaluation of hidden multi-delamination in a glass-fiber-reinforced plastic composite using terahertz spectroscopy“, *Composite Structures* 156, pp. 338–347. DOI: 10.1016/j.composit.2015.09.055.

Samborski et al. 2019

Samborski, S.; Gliszczyński, A.; Rzeczkowski, J. & Wiacek, N. (2019). „Mode I Interlaminar Fracture of Glass/Epoxy Unidirectional Laminates. Part I: Experimental Studies“, *Materials* 12.10, Article 1607. DOI: 10.3390/ma12101607.

Schäferling 2019

Schäferling, M. (2019). *Development of a data fusion-based multi-sensor system for hybrid sheet molding compound*. Dissertation, Karlsruhe Institute of Technology (KIT). Düren: Shaker. DOI: 10.5445/IR/1000093417.

Schäferling et al. 2019

Schäferling, M.; Häfner, B.; Lanza, G.; Trauth, A.; Weidenmann, K. A. & Thompson, M. (2019). „Effects of defects in hybrid sheet moulding compound – Evaluation of defects and

the impact on mechanical properties“, *Materials Science & Engineering Technology* 50.11, pp. 1317–1325. DOI: 10.1002/mawe.201800139.

Schemmann 2018

Schemmann, M. (2018). *Biaxial characterization and mean-field based damage modeling of sheet molding compound composites*. Dissertation, Karlsruhe Institute of Technology (KIT). Karlsruhe: KIT Scientific Publishing. DOI: 10.5445/KSP/1000084270.

Schemmann et al. 2018

Schemmann, M.; Lang, J.; Helfrich, A.; Seelig, T. & Böhlke, T. (2018). „Cruciform Specimen Design for Biaxial Tensile Testing of SMC“, *Journal of Composites Science* 2.1, Article 12. DOI: 10.3390/jcs2010012.

Schipp et al. 1992

Schipp, C.; Röber, S.; Zachmann, H. & Seferis, J. (1992). „Determination of the fiber content in polymer composites by means of X-ray absorption-measurements“, *Journal of Applied Polymer Science* 44.9, pp. 1631–1634. DOI: 10.1002/app.1992.070440917.

Schmidt et al. 2017

Schmidt, C.; Denkena, B.; Groß, L. & Völtzer, K. (2017). „Concept for Automated Production of CFRP-metal Hybrid Compounds Integrated in an Automated Fiber Placement Process“. Online Proceedings of the 10th CIRP Conference on Intelligent Computation in Manufacturing Engineering (Ischia, Italy, July 20–22, 2016). Elsevier, pp. 56–61. DOI: 10.1016/j.procir.2016.06.046.

Schober 2019

Schober, M. (2019). *On the characterization and modeling of interfaces in fiber reinforced polymer structures*. Dissertation, Karlsruhe Institute of Technology (KIT). Stuttgart: Fraunhofer. DOI: 10.5445/IR/1000100455.

Schöttl & Dörr et al. 2020

Schöttl, L.; Dörr, D.; Pinter, P.; Weidenmann, K. A.; Elsner, P. & Kärger, L. (2020). „A novel approach for segmenting and mapping of local fiber orientation of continuous fiber-reinforced composite laminates based on volumetric images“, *NDT & E International* 110, Article 102194. DOI: 10.1016/j.ndteint.2019.102194.

Schöttl & Kolb et al. 2020

Schöttl, L.; Kolb, P.; Liebig, W. V.; Weidenmann, K. A.; Inal, K. & Elsner, P. (2020). „Crack characterization of discontinuous fiber-reinforced composites by using micro-computed tomography: Cyclic in-situ testing, crack segmentation and crack volume fraction“, *Composites Communications* 21, Article 100384. DOI: 10.1016/j.coco.2020.100384.

Schöttl & Weidenmann et al. 2021

Schöttl, L.; Weidenmann, K. A.; Sabiston, T.; Inal, K. & Elsner, P. (2021). „Fiber bundle tracking method to analyze sheet molding compound microstructure based on computed

- tomography images“, *NDT & E International* 117, Article 102370. DOI: 10.1016/j.ndteint.2020.102370.
- Schuh et al. 2014
- Schuh, G.; Korthals, K. & Arnoscht, J. (2014). „Contribution of Body Lightweight Design to the Environmental Impact of Electric Vehicles“. Online Proceedings of WGP Congress 2012 (Berlin, Germany, June 27–28, 2012). Trans Tech Publications Ltd., pp. 329–347. DOI: 10.4028/www.scientific.net/AMR.907.329.
- Schürmann 2007
- Schürmann, H. (2007). *Konstruieren mit Faser-Kunststoff-Verbunden*. 2. Ed. Berlin: Springer. DOI: 10.1007/978-3-540-72190-1.
- Schwenke & Franke 2007
- Schwenke, H. & Franke, M. (2007). „Bestimmung der Unsicherheit von Messungen mit KMG – Status und Ausblick“, *PTB-Mitteilungen* 117.4, pp. 363–371. DOI: 10.7795/310.20070499.
- Sinsbeck 2017
- Sinsbeck, M. (2017). *Uncertainty Quantification for Expensive Simulations - Optimal Surrogate Modeling under Time Constraints*. Dissertation, University of Stuttgart. Stuttgart: Opus. DOI: 10.18419/opus-9206.
- Stamopoulos et al. 2016
- Stamopoulos, A.; Tserpes, K.; Prucha, P. & Vavrik, D. (2016). „Evaluation of porosity effects on the mechanical properties of carbon fiber-reinforced plastic unidirectional laminates by X-ray computed tomography and mechanical testing“, *Journal of Composite Materials* 50.15, pp. 2087–2098. DOI: 10.1177/0021998315602049.
- Stark & Damerau 2018
- Stark, R. & Damerau, T. (2018). „Digital Twin“. *CIRP Encyclopedia of Production Engineering*. Ed. by S. Chatti & T. Tolio. Berlin: Springer, pp. 1–8. DOI: 10.1007/978-3-642-35950-7_16870-1.
- Talreja 2015
- Talreja, R. (2015). „Manufacturing defects in composites and their effects on performance“. *Polymer Composites in the Aerospace Industry*. Ed. by P. Irving & C. Soutis. Cambridge: Woodhead Publishing, pp. 99–113. DOI: 10.1016/B978-0-85709-523-7.00005-0.
- Technical Committee ISO/TC 135 2005
- Technical Committee ISO/TC 135 (2005). *Non-destructive testing – General terms and definitions*. ISO/TS 18173:2005-01. Geneva: International Organization for Standardization (ISO). URL: <https://www.iso.org/standard/40735.html> (Accessed: Jan. 5, 2022).
- Trauth et al. 2021
- Trauth, A.; Kehrer, L.; Pinter, P.; Weidenmann, K. A. & Böhlke, T. (2021). „On the effective

elastic properties based on mean-field homogenization of sheet molding compound composites“, *Composites Part C: Open Access* 4, Article 100089. DOI: 10.1016/j.jcomc.2020.100089.

Trauth 2018

Trauth, A. (2018). *Characterisation and modelling of continuous-discontinuous sheet moulding compound composites for structural applications*. Dissertation, Karlsruhe Institute of Technology (KIT). Karlsruhe: KIT Scientific Publishing. DOI: 10.5445/KSP/1000097160.

Tserpes et al. 2016

Tserpes, K.; Stamopoulos, A. & Pantelakis, S. (2016). „A numerical methodology for simulating the mechanical behavior of CFRP laminates containing pores using X-ray computed tomography data“, *Composites Part B: Engineering* 102, pp. 122–133. DOI: 10.1016/j.compositesb.2016.07.019.

Verein Deutscher Ingenieure e.V. 2006

Verein Deutscher Ingenieure e.V. (2006). *Development of FRP components - Analysis*. VDI 2014 Part 3:2006-09. Berlin: Beuth. URL: <https://www.beuth.de/en/technical-rule/vdi-2014-blatt-3/71840061> (Accessed: Jan. 5, 2022).

Wagner 2020

Wagner, R. (2020). *Strategien zur funktionsorientierten Qualitätsregelung in der Serienproduktion*. Dissertation, Karlsruhe Institute of Technology (KIT). Düren: Shaker. DOI: 10.5445/IR/1000124008.

Wagner et al. 2020

Wagner, R.; Häfner, B.; Biehler, M. & Lanza, G. (2020). „Digital DNA in quality control cycles of high-precision products“, *CIRP Annals* 69.1, pp. 373–376. DOI: 10.1016/j.cirp.2020.03.020.

Wang & Zhong et al. 2020

Wang, B.; Zhong, S.; Lee, T.-L.; Fancey, K. & Mi, J. (2020). „Non-destructive testing and evaluation of composite materials/structures: A state-of-the-art review“, *Advances in Mechanical Engineering* 12.4, Article 1687814020913761. DOI: 10.1177/1687814020913761.

Wang & Wu et al. 2021

Wang, T.; Wu, D.; Chen, W. & Yang, J. (2021). „Detection of delamination defects inside carbon fiber reinforced plastic laminates by measuring eddy-current loss“, *Composite Structures* 268, Article 114012. DOI: 10.1016/j.compstruct.2021.114012.

Webersen et al. 2016

Webersen, M.; Johannesmann, S.; Claes, L. & Henning, B. (2016). „Characterization of continuous-fiber reinforced thermoplastics using thermoacoustically excited ultrasonic Lamb waves“. Online Proceedings of 2016 IEEE International Ultrasonics Symposium (IUS)

- (Tours, France, Sept. 18–21, 2016). IEEE, Article 16443523. DOI: 10.1109/ULTSYM.2016.7728585.
- Weckenmann & Hartmann 2013
- Weckenmann, A. & Hartmann, W. (2013). „Function-oriented method for the definition and verification of microstructured surfaces“, *Precision Engineering* 37.3, pp. 684–693. DOI: 10.1016/j.precisioneng.2013.01.013.
- Weckenmann & Hartmann 2015
- Weckenmann, A. & Hartmann, W. (2015). „A model- and simulation-based approach for tolerancing and verifying the functional capability of micro/nano-structured workpieces“, *Measurement* 76, pp. 70–79. DOI: 10.1016/j.measurement.2015.08.010.
- Wendt et al. 2007
- Wendt, K.; Keck, C. & Schwenke, H. (2007). „Prüfprozesseignung von Inline-Messtechnik im Karosseriebau“, *PTB-Mitteilungen* 117.4, pp. 417–424. DOI: 10.7795/310.20070499.
- Wietzke et al. 2007
- Wietzke, S.; Jansen, C.; Rutz, F.; Mittleman, D. & Koch, M. (2007). „Determination of additive content in polymeric compounds with terahertz time-domain spectroscopy“, *Polymer Testing* 26.5, pp. 614–618. DOI: 10.1016/j.polymertesting.2007.03.002.
- Witten & Mathes 2019
- Witten, E. & Mathes, V. (2019). *Der Markt für Glasfaserverstärkte Kunststoffe (GFK) 2019*. Frankfurt: AVK Industrievereinigung Verstärkte Kunststoffe e. V. (AVK). URL: https://www.avk-tv.de/files/20190911_avk_marktbericht_2019_final.pdf (Accessed: Jan. 5, 2022).
- Yang & He 2016
- Yang, R. & He, Y. (2016). „Optically and non-optically excited thermography for composites: A review“, *Infrared Physics & Technology* 75, pp. 26–50. DOI: 10.1016/j.infrared.2015.12.026.
- Zaiß & Demmerle et al. 2017
- Zaiß, M.; Demmerle, J.; Oergele, J.-N. & Lanza, G. (2017). „New Concepts for Quality Assurance of Lightweight Material“. Online Proceedings of the 1st CIRP Conference on Composite Material Parts Manufacturing (Karlsruhe, Germany, June 8–9, 2017). Elsevier, pp. 259–264. DOI: 10.1016/j.procir.2017.03.224.
- Zaiß & Jank et al. 2017
- Zaiß, M.; Jank, M.-H.; Netzelmann, U.; Waschkes, T.; Rabe, U.; Herrmann, H.-G.; Thompson, M. & Lanza, G. (2017). „Use of Thermography and Ultrasound for the Quality Control of SMC Lightweight Material Reinforced by Carbon Fiber Tapes“. Online Proceedings of the 10th CIRP Conference on Intelligent Computation in Manufacturing Engineering (Ischia, Italy, July 20–22, 2016). Elsevier, pp. 33–38. DOI: 10.1016/j.procir.2016.06.039.

Zhang et al. 2018

Zhang, H.; Grosse, C. U.; Avdelidis, N. P.; Grager, J.-C.; Sfarra, S.; Ibarra-Castanedo, C. & Maldague, X. P. V. (2018). „A novel optical air-coupled ultrasound NDE sensing technique compared with infrared thermographic NDT on impacted composite materials“. Online Proceedings of SPIE Defense + Commercial Sensing 2018 (Orlando, United States, Apr. 15–15, 2018). SPIE, pp. 201–208. DOI: 10.1117/12.2303494.

Zhang 1993

Zhang, P. (1993). „Model Selection Via Multifold Cross Validation“, *The Annals of Statistics* 21.1, pp. 299–313. URL: <http://www.jstor.org/stable/3035592> (Accessed: Jan. 5, 2022).

List of figures

1.1	Advantages and disadvantages of continuous and discontinuous sheet molding compound	2
1.2	Cost-efficient design and manufacturing process for fiber-reinforced polymers	4
1.3	Structure of this thesis	6
2.1	Integration levels of production-integrated metrology	9
2.2	Principle of a SMC prepreg plant	15
2.3	Compression molding of SMC components	16
2.4	Principle of a unidirectional prepreg plant	17
2.5	Production process of CoDiCo-SMC components	18
2.6	Overview of common NDT technologies	21
2.7	Representative volume element of a unidirectional lamina	22
3.1	Comparison of response surfaces and emulators	45
4.1	Fundamental concept for the function-oriented quality assurance of FRP components	50
4.2	Methodological solution approach for a function-oriented quality assurance of hybrid sheet molding compounds	51
5.1	Proposed measurement technologies and respective measurands for CoDiCo-SMC	55
5.2	THz measurement setup including reference specimen and THz system	57
5.3	Technical drawing of DiCo-SMC reference specimen	58
5.4	THz data of exemplary measurement regions	60
5.5	Distributions of fiber mass fraction, thickness and refractive index for different measurement regions	61
5.6	Linear regression of the fiber mass fraction based on the mean refractive index \bar{n} in the THz spectrum	62
5.7	Monte Carlo simulation and Mori-Tanaka homogenization of distributed fiber mass fractions in planar-isotropic DiCo-SMC	65
5.8	Influence of reduced recording time window (RTW) on the measurement uncertainty (MU) of the THz model	67
5.9	Influence of reduced averaging on the measurement uncertainty (MU) of the THz model	69
5.10	Influence on the combined uncertainty of the fiber mass fraction u_{ξ}	70

5.11	Influence of combined reduced averaging and recording time window length (RTW) on the measurement uncertainty (MU) of the THz model	71
5.12	Residuals to Terahertz measurement model for different measurement diameters	72
5.13	Classification and sequence of the camera measurement	73
5.14	Measurement setup for image acquisition	74
5.15	Exemplary world and specimen coordinate systems, patch segmentation and feature extraction	75
5.16	Classification and sequence of the pulsed phase thermography measurement	77
5.17	Measurement system for pulsed phase thermography	77
5.18	Multilevel image thresholding for detecting and measuring delaminations in grayscale phasegrams of CoDiCo-SMC	78
6.1	Program flow chart for component-individual FE simulations taking manufacturing deviations into account	85
6.2	Determination of the standard uncertainty due to model training data for an artificial neural network	93
7.1	Tensile test setup and geometry of the tensile specimen	97
7.2	Influence of a single delamination on tensile properties	99
7.3	Influence of Co-SMC misorientation and delamination on tensile properties	99
7.4	Observed damages in tensile specimen with combined manufacturing deviations	100
7.5	Experimental results for the tensile strength of DiCo-SMC with varying glass fiber mass fraction	101
7.6	Model assembly for DiCo-SMC tensile specimen FE model	102
7.7	Experimental and simulated Young's modulus for CoDiCo-SMC tensile specimen	103
7.8	Experimental and simulated tensile strength for CoDiCo-SMC tensile specimen	104
7.9	Simulated and experimental uncertainties of Young's modulus for CoDiCo-SMC tensile specimen	106
7.10	Evolution of surrogate model bias based on iterative training data generation for tensile specimen	108
7.11	Description of a three-point bending setup	113
7.12	Comparison of the ideal manufactured flexural specimen in contrast to representative manufacturing deviations	114
7.13	Result of the objective function for different design parameter combinations	115

7.14	Technical drawing of circular THz measurement regions in the flexural specimen	117
7.15	Flexural test setup	118
7.16	Observed underperformance of CoDiCo-SMC compared to DiCo-SMC	119
7.17	Failure mechanism of CoDiCo-SMC specimen	119
7.18	Flexural testing and THz measurement results for D_3	120
7.19	Correlations between FMF and flexural modulus	121
7.20	Exemplary model assembly for CoDiCo-SMC flexural specimen FE model	122
7.21	Experimental and simulated flexural modulus for CoDiCo-SMC flexural specimen	123
7.22	Simulated and experimental uncertainties of flexural modulus	126
7.23	Evolution of surrogate model bias based on iterative training data generation for flexural specimen	128
A6.1	DCB specimen and experimental setup	177
A6.2	Results of DCB experiments for DiCo-SMC	178
A7.1	Convergence study for FE model of tensile specimen	179
A7.2	Convergence study for FE model of flexural specimen	180

List of tables

2.1	Composition of discontinuous UPPH GF Sheet Molding Compound	18
2.2	Composition of continuous UPPH CF Sheet Molding Compound	19
2.3	Overview of manufacturing deviations in CoDiCo-SMC	20
3.1	Overview of relevant research for a function-oriented quality assurance of hybrid SMCs	47
5.1	Comparison of measurement technologies for quantifying manufacturing deviations in CoDiCo-SMC	53
5.3	Comparison of linear regression models	61
5.4	Uncertainty budget for Terahertz measurements of different fiber mass fractions	64
5.5	Overview of measures for an improved THz measurement time	66
5.6	Uncertainty budget of industrial image processing for Co-SMC patch measurement	76
5.7	Uncertainty budget of thermographic image processing for delamination measurement in a CoDiCo-SMC specimen with local Co-SMC reinforcement	80
5.8	Uncertainty budget of thermographic image processing for delamination measurement in a CoDiCo-SMC specimen; delamination fully covered by Co-SMC layer	81
6.1	Selection of relevant uncertainty contributions of the input quantities for the FE simulation	87
6.2	Comparison of ANNs and Kriging models for data-driven surrogate modeling	89
7.1	Manufactured tensile specimen configurations	97
7.2	Systematic deviations (bias) of the FE simulation for CoDiCo-SMC tensile specimen	104
7.3	Screening analysis for FEM uncertainty of tensile specimens	105
7.4	Uncertainty contributions for measurable and non-measurable input quantities (tensile specimen)	106
7.5	Uncertainty budget for FE simulation of Young's modulus of CoDiCo-SMC tensile specimen	107
7.6	Systematic deviations (bias) of the surrogate models for CoDiCo-SMC tensile specimen	109
7.7	Uncertainty budget for surrogate modeled Young's modulus of CoDiCo-SMC tensile specimen	110

7.8	Comparison of test specimen alternatives for the validation of the function-oriented measurement of CoDiCo-SMC	112
7.9	Dimensioning of flexural specimen	115
7.10	Manufactured flexural specimen configurations for CoDiCo-SMC (C_i) and DiCo-SMC (D_i) with given nominal manufacturing deviations	116
7.11	Screening analysis for FEM uncertainty of flexural specimens	125
7.12	Uncertainty contributions for and measurable and non-measurable input quantities (flexural specimen)	126
7.13	Uncertainty budget for FE simulation of flexural specimen	126
7.14	Systematic deviations (bias) of the surrogate models for flexural specimen	129
7.15	Uncertainty budget for surrogate modeled flexural modulus of CoDiCo-SMC flexural specimen	129
A2.1	Individual measurement results of DiCo-SMC reference specimens	170
A2.1	Individual measurement results of DiCo-SMC reference specimens	171
A3.1	Mean refractive index and normalized values (z-score) for UPPH measurement regions	172
A4.1	Uncertainty budget of thermographic image processing for delamination measurement (nominal radius of 5 mm) in a CoDiCo-SMC specimen	173
A4.2	Uncertainty budget of thermographic image processing for delamination measurement (nominal radius of 7 mm) in a CoDiCo-SMC specimen	173
A4.3	Uncertainty budget of thermographic image processing for delamination measurement (nominal radius of 10 mm) in a CoDiCo-SMC specimen	173
A5.1	Material parameters for FE simulations	174
A5.2	Considered input quantities for FE simulations of tensile specimen	175
A5.3	Considered input quantities for FE simulations of flexural specimen	176
A8.1	Considered value domains of input quantities for surrogate model training of (tensile specimen)	181
A8.2	Considered value domains of input quantities for surrogate model training of (flexural specimen)	181
A9.1	Required minimum tolerances based on German Association of the Automotive Industry (2011)	182

Appendix

A1 Further equations for DiCo-SMC homogenization

Hill's polarization tensor \mathbb{P}^{ud} for a prolate spheroidal inclusion in an isotropic medium is given in Mandel notation by Brylka (2017):

$$\mathbb{P}^{\text{ud}} = \begin{bmatrix} r & m & m & 0 & 0 & 0 \\ m & k+p & k-p & 0 & 0 & 0 \\ m & k-p & k+p & 0 & 0 & 0 \\ 0 & 0 & 0 & 2p & 0 & 0 \\ 0 & 0 & 0 & 0 & 2q & 0 \\ 0 & 0 & 0 & 0 & 0 & 2q \end{bmatrix} \quad \text{A1.1}$$

The coefficients k, r, m, p, q of Equation A1.1 are calculated based on the elastic constants of the matrix G_{M} and K_{M} , and the aspect ratio a of the fibers (Brylka 2017):

$$\begin{aligned} k &= \frac{G_{\text{M}}(7h(a) - 2a^2 - 4a^2h(a)) + 3K_{\text{M}}(h(a) - 2a^2 + 2a^2h(a))}{8(1-a^2)G_{\text{M}}(4G_{\text{M}} + 3K_{\text{M}})}, \\ m &= \frac{(G_{\text{M}} + 3K_{\text{M}})(2a^2 - h(a) - 2a^2h(a))}{4G_{\text{M}}(1-a^2)(4G_{\text{M}} + 3K_{\text{M}})}, \\ r &= \frac{G_{\text{M}}(6 - 5h(a) - 8a^2 + 8a^2h(a) + 3K_{\text{M}}(h(a) - 2a^2 + 2a^2h(a)))}{2G_{\text{M}}(1-a^2)(4G_{\text{M}} + 3K_{\text{M}})}, \\ p &= \frac{G_{\text{M}}(15h(a) - 2a^2 - 12a^2h(a)) + 3K_{\text{M}}(3h(a) - 2a^2)}{16G_{\text{M}}(1-a^2)(4G_{\text{M}} + 3K_{\text{M}})}, \\ q &= \frac{2G_{\text{M}}(4 - 3h(a) - 2a^2) + 3K_{\text{M}}(2 - 3h(a) + 2a^2 - 3a^2h(a))}{8G_{\text{M}}(1-a^2)(4G_{\text{M}} + 3K_{\text{M}})}, \\ h(a) &= \frac{a(a\sqrt{a^2-1} - \text{arccosh}(a))}{(a^2-1)^{3/2}}. \end{aligned} \quad \text{A1.2}$$

The coefficients of Equation 2.10 are calculated based on the components of the transverse isotropic tensor \mathbb{A} (Kehrer & Pinter et al. 2017; Advani & Tucker 1987):

$$\begin{aligned} b_1 &= A_{1111}^* + A_{2222}^* - 2A_{1122}^* - 4A_{1212}^*, \\ b_2 &= A_{1122}^* - A_{2233}^*, \\ b_3 &= A_{1212}^* + \frac{A_{2233}^* - A_{2222}^*}{2}, \\ b_4 &= A_{2233}^*, \\ b_5 &= \frac{A_{2222}^* - A_{2233}^*}{2}. \end{aligned} \quad \text{A1.3}$$

For isotropic materials, the bulk modulus K can be written as:

$$K = \frac{E}{3(1 - 2\nu)} \quad \text{A1.4}$$

Similarly, the shear modulus G reads for isotropic materials as:

$$G = \frac{E}{2(1 + 2\nu)} \quad \text{A1.5}$$

A2 THz measurements results of DiCo-SMC reference specimens

Table A2.1 gives the nominal FMF ξ_{nom} according to the settings of the prepreg production process, the TGA-measured FMF $\hat{\xi}_{\text{TGA}}$, the bias $|b_{\xi,i}|$ for each measurement section i , the bias $|\overline{b_{\xi,k}}|$ for each reference specimen k , the standard deviation $s_{\hat{\xi}_{\text{TGA},k}}$ for each reference specimen k , the mean thickness measurements \overline{d} using a micrometer screw gauge based on at least five measurements, the set beam diameter during the THz measurements, and the THz-measured mean refractive index \overline{n} between 0.3 and 0.55 THz. Measurement regions used for calculating the measurement uncertainty were measured 25 times.

The uncertainty of the FMF related to the production process $u_{\xi,\text{prod}}$ is calculated according to Equation 5.7. Hereby, the mean standard deviation of TGA-referenced measurement regions within the same reference specimen $\overline{s_{\hat{\xi}_{\text{TGA}}}}$ is calculated according to Equation A2.1:

$$\overline{s_{\hat{\xi}_{\text{TGA}}}} = \frac{1}{7} \sum_{k=8}^{14} s_{\hat{\xi}_{\text{TGA},k}} = 1.57 \text{ wt.-%} \quad \text{A2.1}$$

The mean systematic deviation (bias) from the intended FMF (nominal value) $\overline{b_{\xi}}$ is calculated according to Equation A2.2:

$$\overline{b_{\xi}} = \frac{1}{10} \sum_{k=8}^{17} |\overline{b_{\xi,k}}| = 3.13 \text{ wt.-%} \quad \text{A2.2}$$

Table A2.1: Individual measurement results of DiCo-SMC reference specimens (No. 85 to 102 from Bretz & Häfner et al. (2021))

No. k of ref. specimen	No. i	ξ_{nom} (wt.-%)	$\hat{\xi}_{\text{TGA}}$ (wt.-%)	$ b_{\xi,i} $ (wt.-%)	$\overline{ b_{\xi,k} }$ (wt.-%)	$s_{\xi,\text{TGA},k}$ (wt.-%)	\bar{d} (mm)	Beam diameter (mm)	\bar{n}
1	1	0	0	0			2.260	10	1.6859
	2	0	0	0			2.250	10	1.6916
	3	0	0	0	0	0	2.264	10	1.6828
	4	0	0	0	0	0	2.246	10	1.6820
	5	0	0	0	0	0	2.241	10	1.6804
	6	0	0	0	0	0	2.239	10	1.6801
2	7	35	44.61	9.61			1.929	10	1.9233
	8	35	44.79	9.79			1.898	10	1.9906
	9	35	46.08	11.08	10.65	1.59	1.878	10	1.9406
	10	35	45.13	10.13	10.65	1.59	1.875	10	1.9360
	11	35	48.69	13.69	10.65	1.59	1.876	10	1.9604
	12	35	44.60	9.60	10.65	1.59	1.918	10	1.9223
3	13	38	45.77	7.77			1.854	10	1.9385
	14	38	42.35	4.35			1.870	10	1.9042
	15	38	42.55	4.55	6.22	1.67	1.890	10	1.9035
	16	38	45.82	7.82	6.22	1.67	1.889	10	1.9162
	17	38	45.57	7.57	6.22	1.67	1.863	10	1.9375
	18	38	43.27	5.27	6.22	1.67	2.016	10	1.8743
4	19	41	45.76	4.76			2.065	10	1.9108
	20	41	46.19	5.19			2.076	10	1.9392
	21	41	46.51	5.51	4.53	1.19	2.074	10	1.9470
	22	41	45.62	4.62	4.53	1.19	2.087	10	2.0060
	23	41	45.89	4.89	4.53	1.19	2.079	10	1.9422
	24	41	43.20	2.20	4.53	1.19	2.091	10	1.9531
5	25	43	50.83	7.83			2.116	10	1.9875
	26	43	51.32	8.32			2.114	10	2.0018
	27	43	52.86	9.86	9.02	0.99	2.101	10	1.9832
	28	43	51.70	8.70	9.02	0.99	2.134	10	1.9840
	29	43	53.49	10.49	9.02	0.99	2.131	10	1.9744
	30	43	51.91	8.91	9.02	0.99	2.123	10	1.9748
6	31	45	45.68	0.68			2.238	10	1.9596
	32	45	47.21	2.21			2.284	10	1.9657
	33	45	52.20	7.20	3.97	2.28	2.294	10	1.9727
	34	45	49.16	4.16	3.97	2.28	2.291	10	1.9372
	35	45	50.21	5.21	3.97	2.28	2.272	10	1.9452
	36	45	49.34	4.34	3.97	2.28	2.250	10	1.9985
7	37	50	51.02	1.02			2.257	10	1.9917
	38	50	49.76	0.24			2.292	10	1.9679
	39	50	47.98	2.02	0.79	1.65	2.333	10	1.9588
	40	50	51.93	1.93	0.79	1.65	2.349	10	1.9827
	41	50	52.40	2.4	0.79	1.65	2.309	10	1.9985
	42	50	51.63	1.63	0.79	1.65	2.357	10	1.9637
8	43	35	37.76	2.76			2.980	10	1.8722
	44	35	37.86	2.86			2.983	10	1.8723
	45	35	40.66	5.66	3.40	1.87	3.000	10	1.8876
	46	35	40.74	5.74	3.40	1.87	2.988	10	1.8953
	47	35	37.08	2.08	3.40	1.87	2.995	10	1.8835
	48	35	36.31	1.31	3.40	1.87	2.962	10	1.8579
9	49	39	38.74	0.26			2.886	10	1.8795
	50	39	40.14	1.14			2.971	10	1.9027
	51	39	41.40	2.40	0.05	2.11	2.974	10	1.8984
	52	39	40.30	1.30	0.05	2.11	2.955	10	1.8882
	53	39	37.45	1.55	0.05	2.11	2.952	10	1.8743
	54	39	35.68	3.32	0.05	2.11	2.945	10	1.8689

Table A2.1: Individual measurement results of DiCo-SMC reference specimens (No. 85 to 102 from Bretz & Häfner et al. (2021))

No. k of ref. specimen	No. i	ξ_{nom} (wt.-%)	$\hat{\xi}_{\text{TGA}}$ (wt.-%)	$ b_{\xi,i} $ (wt.-%)	$\overline{ b_{\xi,k} }$ (wt.-%)	$s_{\hat{\xi},\text{TGA},k}$ (wt.-%)	\bar{d} (mm)	Beam diameter (mm)	\bar{n}
10	55	41	46.93	5.93	7.21	1.19	3.112	10	1.9415
	56	41	49.08	8.08			3.186	10	1.9413
	57	41	49.18	8.18			3.099	10	1.9711
	58	41	49.49	8.49			3.112	10	1.9732
	59	41	47.74	6.74			3.124	10	1.9668
	60	41	46.82	5.82			3.122	10	1.9442
11	61	41	45.87	4.87	5.41	0.77	3.122	14	1.9325
	62	41	47.23	6.23			3.117	14	1.9474
	63	41	46.61	5.61			3.104	14	1.9381
	64	41	45.16	4.16			3.063	14	1.9419
	65	41	46.50	5.50			3.064	14	1.9348
	66	41	47.06	6.06			3.068	14	1.9446
12	67	41	45.26	4.26	3.48	2.01	3.100	20	1.9010
	68	41	43.96	2.96			3.074	20	1.9322
	69	41	45.73	4.73			3.079	20	1.9086
	70	41	45.03	4.03			3.093	20	1.9397
	71	41	40.67	0.33			3.134	20	1.9452
	72	41	46.21	5.21			3.073	20	1.9339
13	73	42.33	47.97	5.97	4.02	1.44	3.156	10	1.9512
	74	42.33	45.34	3.34			3.158	10	1.9417
	75	42.33	44.56	2.56			3.160	10	1.9379
	76	42.33	45.85	3.85			3.170	10	1.9459
	77	42.33	46.25	4.25			3.158	10	1.9413
	78	42.33	48.14	6.14			3.145	10	1.9598
14	79	45	45.68	0.68	1.71	1.59	3.179	10	1.9342
	80	45	45.01	0.01			3.158	10	1.9455
	81	45	46.96	1.96			3.172	10	1.9552
	82	45	48.84	3.84			3.177	10	1.9666
	83	45	45.45	0.45			3.166	10	1.9392
	84	45	48.30	3.30			3.277	10	1.9433
15	85	41	40.93	0.07	1.34	-	4.265	8	1.9110
	86	41	38.40	2.60			4.289	8	1.8790
16	87	45	47.37	2.37	1.94	-	4.247	8	1.9404
	88	45	46.51	1.51			4.253	8	1.9497
17	89	50	48.47	1.53	2.73	-	4.211	8	1.9734
	90	50	46.08	3.92			4.272	8	1.9477
18	91	51	48.21	2.79	2.55	-	4.544	8	1.9466
	92	51	48.70	2.30			4.579	8	1.9580
19	93	52	49.82	2.18	1.76	-	4.471	8	1.9594
	94	52	53.33	1.33			4.434	8	2.0011
20	95	53	49.61	3.39	3.32	-	4.484	8	1.9976
	96	53	49.75	3.25			4.423	8	1.9826
21	97	54	48.70	5.30	3.67	-	4.673	8	1.9765
	98	54	51.97	2.03			4.658	8	1.9856
22	99	55	53.16	1.84	3.12	-	4.581	8	2.0040
	100	55	50.61	4.39			4.612	8	1.9888
23	101	56	51.49	4.51	3.34	-	4.548	8	2.0062
	102	56	53.84	2.16			4.615	8	2.0158

A3 Assessment of THz regression model (M2)

The mean refractive indices and the normalized values for the six measurement regions of UPPH are given in Table A3.1.

Table A3.1: Mean refractive index and normalized values (z-score) for UPPH measurement regions

	\bar{n}	z-score
UPPH ₁	1.6859	-6.7655
UPPH ₂	1.6916	-6.6155
UPPH ₃	1.6828	-6.8455
UPPH ₄	1.6820	-6.8646
UPPH ₅	1.6804	-6.9061
UPPH ₆	1.6801	-6.9157
$\overline{\text{UPPH}}$	1.6838	-6.8188

The mean z-score for UPPH from Table A3.1 is used with the coefficient estimates for (M2) from Table 5.3, leading to the following false extrapolation for UPPH:

$$46.57 \text{ wt.-%} + 3.99 \cdot (-6.8188) \text{ wt.-%} \approx 19.36 \text{ wt.-%} \neq 0 \text{ wt.-%}$$

A3.1

A4 Further uncertainty budgets for PPT of delaminations

<i>(a) Delamination depth of 1 mm</i>				<i>(b) Delamination depth of 2 mm</i>			
	x_D (mm)	y_D (mm)	r_D (mm)		x_D (mm)	y_D (mm)	r_D (mm)
x_{cal}	30.79	53.21	5.21	x_{cal}	25.11	54.12	5.19
u_{cal}	0.13	0.17	0.09	u_{cal}	0.1	0.12	0.07
u_p	1.68	3.25	0.84	u_p	1.85	2.84	1.19
$ b $	3.51	1.24	1.04	$ b $	3.13	0.62	0.77
u_c	3.89	3.48	1.34	u_c	3.63	2.91	1.42

Table A4.1: Uncertainty budget of thermographic image processing for delamination measurement (nominal radius of 5 mm) in a CoDiCo-SMC specimen

<i>(a) Delamination depth of 1 mm</i>				<i>(b) Delamination depth of 2 mm</i>			
	x_D (mm)	y_D (mm)	r_D (mm)		x_D (mm)	y_D (mm)	r_D (mm)
x_{cal}	31.24	53.68	7.17	x_{cal}	29.72	53.68	7.19
u_{cal}	0.25	0.25	0.14	u_{cal}	0.27	0.08	0.11
u_p	1.96	2.91	0.51	u_p	2.03	3.72	1.05
$ b $	3.44	0.05	1.21	$ b $	1.86	1.25	0.74
u_c	3.96	2.92	1.32	u_c	2.77	3.93	1.29

Table A4.2: Uncertainty budget of thermographic image processing for delamination measurement (nominal radius of 7 mm) in a CoDiCo-SMC specimen

<i>(a) Delamination depth of 1 mm</i>				<i>(b) Delamination depth of 2 mm</i>			
	x_D (mm)	y_D (mm)	r_D (mm)		x_D (mm)	y_D (mm)	r_D (mm)
x_{cal}	27.99	49.46	10.23	x_{cal}	33.97	55.03	10.23
u_{cal}	0.34	0.13	0.15	u_{cal}	0.14	0.22	0.08
u_p	1.49	2.57	0.63	u_p	2.27	3.89	1.93
$ b $	3.36	0.90	1.61	$ b $	0.88	0.11	0.29
u_c	3.69	2.73	1.73	u_c	2.44	3.90	1.95

Table A4.3: Uncertainty budget of thermographic image processing for delamination measurement (nominal radius of 10 mm) in a CoDiCo-SMC specimen

A5 List of simulation parameters

Table A5.1: Material parameters for FE simulations

Parameter	Symbol	Value	Reference
<i>DiCo-SMC properties</i>			
Glass fiber mass fraction	ξ	41 wt.-%	Trauth 2018
Glass fiber aspect ratio	a	1881	Görthofer et al. 2019
Fiber density	ρ_{GF}	2.6 g/cm ³	Trauth 2018
Matrix density	ρ_{UPPH}	1.14 g/cm ³	Trauth 2018
Fiber Young's modulus	E_{GF}	73 GPa	Görthofer et al. 2019
Fiber Poisson's ratio	ν_{GF}	0.22	Görthofer et al. 2019
Matrix Young's modulus	E_{UPPH}	3.06 GPa	Görthofer et al. 2019
Matrix Poisson's ratio	ν_{UPPH}	0.3	Görthofer et al. 2019
<i>Co-SMC properties</i>			
Carbon fiber volume fraction	ϕ_{CF}	48 vol.-%	Trauth 2018
Thickness	d_T	0.3 mm	A_Debowski 2020
Young's modulus (\parallel)	$E_{Co,\parallel}$	110.1 GPa	Trauth 2018
Young's modulus (\perp)	$E_{Co,\perp}$	8.3 GPa	Trauth 2018
Shear modulus ($\perp \parallel$)	$G_{Co,\perp\parallel}$	3.77 GPa	Schürmann 2007
Shear modulus ($\perp \perp$)	$G_{Co,\perp\perp}$	2.19 GPa	Schürmann 2007
Poisson's ratio ($\perp \parallel$)	$\nu_{Co,\perp\parallel}$	0.27	Schürmann 2007
Poisson's ratio ($\perp \perp$)	$\nu_{Co,\perp\perp}$	0.33	Schürmann 2007
Longitudinal tensile strength	R_{\parallel}^+	1424 MPa	Trauth 2018
Longitudinal compression strength	R_{\parallel}^-	567 MPa	Trauth 2018
Transverse tensile strength	R_{\perp}^+	34 MPa	Trauth 2018
Transverse compression strength	R_{\perp}^-	163 MPa	Trauth 2018
Shear strength	$R_{\perp\parallel}$	79 MPa	Verein Deutscher Ingenieure e.V. 2006
Puck inclination parameter	$p_{\perp\parallel}^+$	0.35	Verein Deutscher Ingenieure e.V. 2006
Puck inclination parameter	$p_{\perp\parallel}^-$	0.3	Verein Deutscher Ingenieure e.V. 2006
Puck inclination parameter	$p_{\perp\perp}^+$	0.3	Verein Deutscher Ingenieure e.V. 2006
Puck inclination parameter	$p_{\perp\perp}^-$	0.3	Verein Deutscher Ingenieure e.V. 2006
Parameter for Puck weakening factor	m	0.5	Verein Deutscher Ingenieure e.V. 2006
Parameter for Puck weakening factor	s	0.5	Verein Deutscher Ingenieure e.V. 2006

Table A5.2: Considered input quantities for FE simulations of tensile specimen; intervals and standard uncertainties given in same units as their corresponding nominal value

Input quantity	Distribution	Nominal value	Interval	Standard uncertainty	Reference
ξ	normal	41 wt.-%	-	2.25	based on Bretz & Häfner et al. 2021
ϕ_{Void}	uniform	2 vol.-%	[0, 4]	1.16	based on Talreja 2015
ϕ_{CF}	normal	48 wt.-%	-	2.5	Trauth 2018
d_{T}	normal	0.314 mm	-	0.042	A_Debowski 2020
γ_{T}	normal	0°	[-2, 2]	1.16	Fengler & Schäferling et al. (2019)
l_{D}	uniform	20 mm	[15, 25]	2.89	Assumption
x_{D}	uniform	0 mm	[-5,5]	2.89	Assumption
E_{GF}	uniform	73 GPa	[66.5, 79.5]	3.8	Görthofer et al. 2019, EduPack 2021 ¹
ν_{GF}	uniform	0.22	[0.21, 0.23]	0.006	Görthofer et al. 2019, EduPack 2021
E_{UPPH}	uniform	3.06 GPa	[2.07, 4.41]	0.675	Görthofer et al. 2019, EduPack 2021
ν_{UPPH}	uniform	0.3	[0.29, 0.31]	0.006	Görthofer et al. 2019, EduPack 2021
$E_{\text{CF},\parallel}$	uniform	230 GPa	[225, 260]	10.1	Schürmann 2007, EduPack 2021
$E_{\text{CF},\perp}$	uniform	28 GPa	[24, 34]	2.9	Schürmann 2007, EduPack 2021
$G_{\text{CF},\perp,\parallel}$	uniform	50 GPa	[45, 55]	2.9	Schürmann 2007, EduPack 2021
ν_{CF}	uniform	0.23	[0.2, 0.23]	0.009	Schürmann 2007

Standard deviations are considered as standard uncertainties for normal distributions. The standard uncertainty for a uniform distribution on the interval $[a_-, a_+]$ is calculated by (JCGM100 2008):

$$u = \frac{a_+ - a_-}{2\sqrt{3}} \quad \text{A5.1}$$

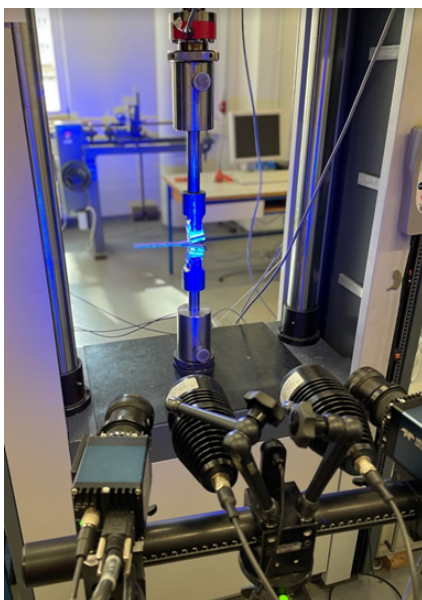
¹Ansys (CES) Granta EduPack 2021. <https://www.ansys.com/de-de/products/materials/granta-edupack> (accessed on Jan. 5, 2022).

Table A5.3: Considered input quantities for FE simulation of flexural specimen; intervals and standard uncertainties given in same units as their corresponding nominal value; measured quantities highlighted in gray

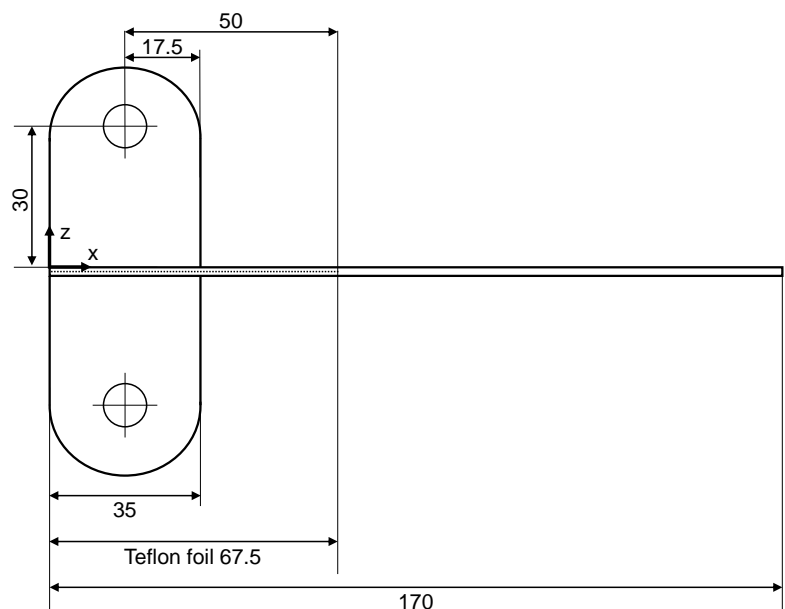
Input quantity	Distribution	Nominal value	Interval	Standard uncertainty	Reference
ξ	normal	41 wt.-%	-	0.994	Table 5.4
ϕ_{Void}	uniform	2 vol.-%	[0, 4]	1.16	based on Talreja 2015
ϕ_{CF}	normal	48 wt.-%	-	2.5	Trauth 2018
d_{T}	normal	0.314 mm	-	0.042	A_Debowski 2020
γ_{T}	normal	0°	-	0.13	Table 5.6
x_{T}	normal	0 mm	-	0.25	Table 5.6
y_{T}	normal	0 mm	-	0.29	Table 5.6
r_{D}	normal	7 mm	-	1.59	Table 5.7
x_{D}	normal	0 mm	-	3.24	Table 5.7
y_{D}	normal	0 mm	-	3.88	Table 5.7
E_{GF}	uniform	73 GPa	[66.5, 79.5]	3.8	Görthofer et al. 2019, EduPack 2021
ν_{GF}	uniform	0.22	[0.21, 0.23]	0.006	Görthofer et al. 2019, EduPack 2021
E_{UPPH}	uniform	3.23 GPa	[3.06, 3.4]	0.1	Kehrer & Wicht et al. 2018 Görthofer et al. 2019
ν_{UPPH}	uniform	0.34	[0.3, 0.385]	0.025	Kehrer & Wicht et al. 2018 Görthofer et al. 2019
$E_{\text{CF},\parallel}$	uniform	230 GPa	[225, 260]	10.1	Schürmann 2007, EduPack 2021
$E_{\text{CF},\perp}$	uniform	28 GPa	[24, 34]	2.9	Schürmann 2007, EduPack 2021
$G_{\text{CF},\perp\parallel}$	uniform	50 GPa	[45, 55]	2.9	Schürmann 2007, EduPack 2021
ν_{CF}	uniform	0.22	[0.2, 0.23]	0.009	Schürmann 2007

A6 Critical energy release rate for DiCo-SMC

The standard ASTM International D30.06 Committee (2013) was used for the experimental determination of the critical energy release rate G_{IC} of Dico-SMC. The geometry of the test specimen is shown in Figure A6.1b. The 2 mm thick test specimens were manufactured with a fully covered mold. Thus, the planar isotropy of the glass fiber DiCo-SMC. A 0.13 mm thick Teflon film with a length of 67.5 mm was placed in the middle of the two SMC layers before compression molding. It defined the initial crack length a_0 in the double cantilever beam (DCB) test. Two loading blocks were bonded to the specimens. The force of the Zmart-Pro universal testing machine by ZwickRoell was introduced via the loading blocks, with one rotational degree of freedom remaining. To open the matrix pockets at the end of the Teflon foil, the specimens were pre-loaded with 15 N. During the test, loading blocks were pulled apart in the z-direction at a defined speed of 20 mm/min. An ARAMIS camera system from GOM GmbH was used to track the crack growth (cf. Figure A6.1a). It was coupled with the force-displacement output of the testing machine. Each image taken by the camera system provided local strain values of corresponding points along the crack propagation line. The crack was assumed to have reached a certain point at a local strain rate of 1%. The distance between individual points was 2 mm.



(a) Experimental setup



(b) Technical drawing of DCB specimen

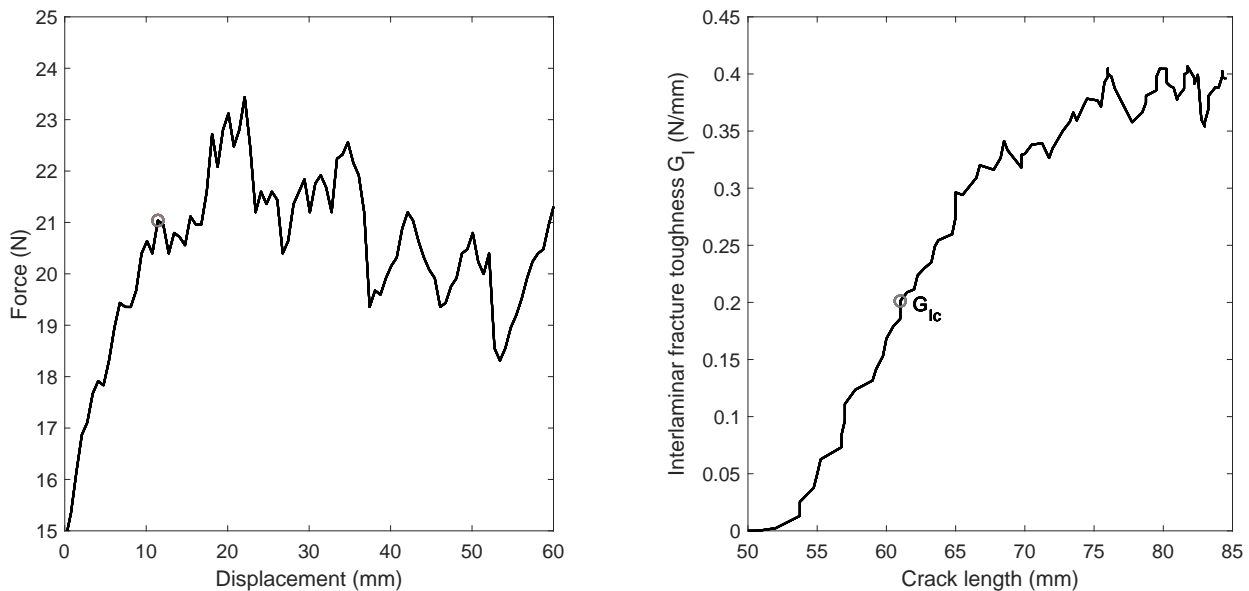
Figure A6.1: DCB specimen and experimental setup

The crack length a , the force P , the displacement δ and the specimen width b are used according to Equation A6.1. In addition, a correction factor F is introduced to account for shortening

of the lever and tilting of the force application. (ASTM International D30.06 Committee 2013)

$$G_I = \frac{3P\delta}{2ba} \cdot F \quad \text{A6.1}$$

The averaged force-displacement curve of the eight DCB specimens is shown in Figure A6.2a. Crack growth occurred exclusively in the plane of the initial crack. The critical energy release rate G_{IC} can be estimated at the point where the force no longer increases linearly (ASTM International D30.06 Committee 2013). Averaged over all specimens, it is 0.201 N/mm (cf. Figure A6.2b), which is in accordance to the order of magnitude for unidirectional GF/epoxy laminae (Samborski et al. 2019).

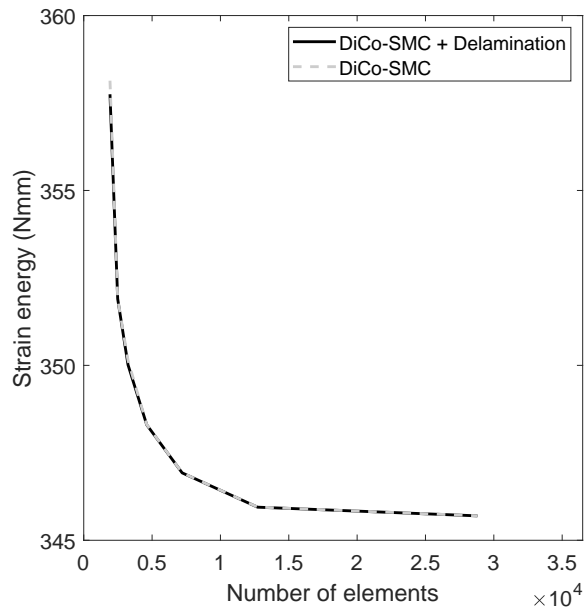


(a) Averaged force-displacement curve of the DCB experiment

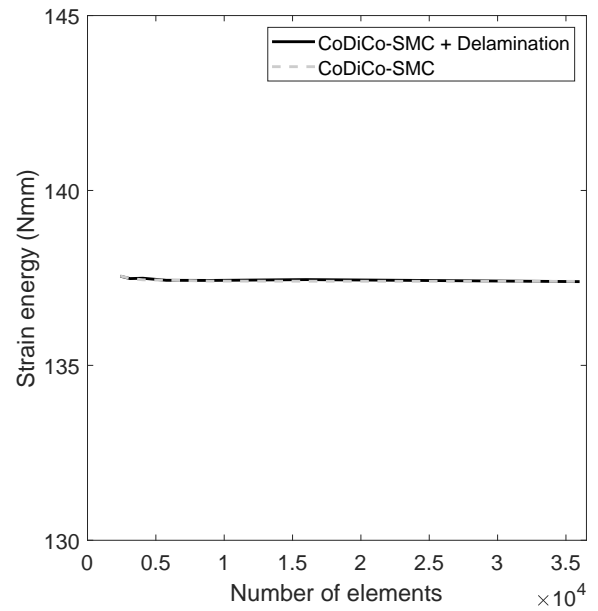
(b) Energy release rate over the crack length with an initial crack length $a_0=50$ mm

Figure A6.2: Results of DCB experiments for DiCo-SMC

A7 Convergence study of finite element simulations

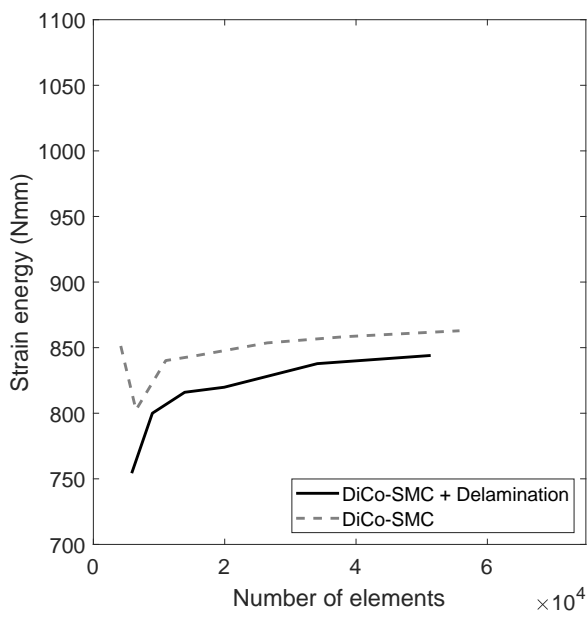


(a) *DiCo-SMC tensile specimen*

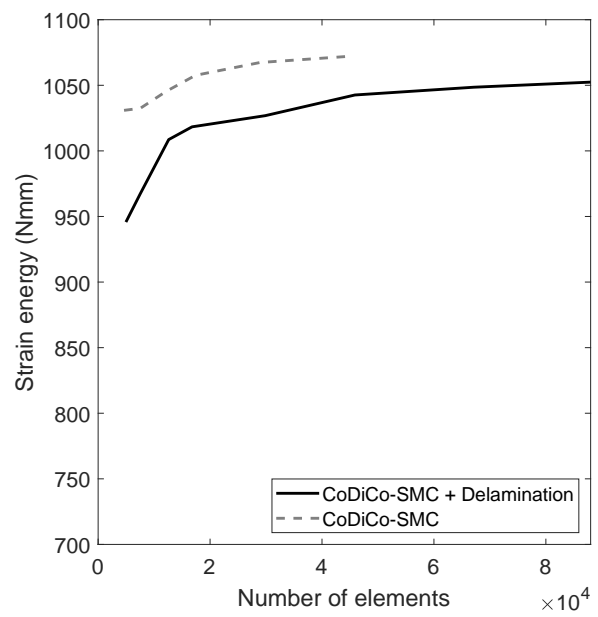


(b) *CoDiCo-SMC tensile specimen*

Figure A7.1: Convergence study for FE model of tensile specimen (force-controlled)



(a) DiCo-SMC flexural specimen



(b) CoDiCo-SMC flexural specimen

Figure A7.2: Convergence study for FE model of flexural specimen (displacement-controlled)

A8 Input quantities for surrogate model training

Table A8.1: Considered (x) value domains of input quantities for surrogate model training (tensile specimen); uniform distribution assumed for obtaining training data within the whole experimental space (A_Koch 2020)

Considered input quantity for composition	DiCo-SMC	DiCo-SMC and delamination	CoDiCo-SMC	CoDiCo-SMC and delamination	Value domain
ξ_0	x	x	x	x	[30, 55] wt.-%
ξ_{MR_1}	x	x	x	x	[30, 55] wt.-%
ξ_{MR_2}	x	x	x	x	[30, 55] wt.-%
ξ_{MR_3}	x	x	x	x	[30, 55] wt.-%
ξ_{MR_4}	x	x	x	x	[30, 55] wt.-%
$\phi_{Void,0}$	x	x	x	x	[0, 5] vol.-%
ϕ_{Void,MR_1}	x	x	x	x	[0, 5] vol.-%
ϕ_{Void,MR_2}	x	x	x	x	[0, 5] vol.-%
ϕ_{Void,MR_3}	x	x	x	x	[0, 5] vol.-%
ϕ_{Void,MR_4}	x	x	x	x	[0, 5] vol.-%
d_{DiCo}	x	x	x	x	[1.75, 2.5] mm
γ_T			x	x	[0, 20] °
l_D		x		x	[5, 50] mm
x_D		x		x	[-25, 25] mm

Table A8.2: Considered (x) value domains of input quantities for surrogate model training (flexural specimen); uniform distribution assumed for obtaining training data within the whole experimental space

Considered input quantity for composition	DiCo-SMC	DiCo-SMC and delamination	CoDiCo-SMC	CoDiCo-SMC and delamination	Value domain
ξ_{MR_1}	x	x	x	x	[30, 55] wt.-%
ξ_{MR_2}	x	x	x	x	[30, 55] wt.-%
ξ_{MR_3}	x	x	x	x	[30, 55] wt.-%
ξ_{MR_4}	x	x	x	x	[30, 55] wt.-%
ξ_{MR_5}	x	x	x	x	[30, 55] wt.-%
ϕ_{Void}	x	x	x	x	[0, 5] vol.-%
d_{DiCo}	x	x	x	x	[2.4, 3.5] mm
Δx_T			x	x	[-10, 10] mm
Δy_T			x	x	[-10, 10] mm
γ_T			x	x	[-15, 15] °
Δx_D		x		x	[-15, 15] mm
Δy_D		x		x	[-35, 35] mm
r_D		x		x	[0, 10] mm

A9 Requirements according to VDA 5.1

Equation 8.1 can be rearranged to:

$$TOL_{\min} \geq \frac{2 \cdot U \cdot 100\%}{15\%} \quad \text{A9.1}$$

Table A9.1 gives the calculated minimum tolerances TOL_{\min} according to Equation A9.1 based on the results from the measurement uncertainty analyses (Table 5.4, Table 5.7, Table 5.6).

Table A9.1: Required minimum tolerances based on German Association of the Automotive Industry (2011)

	ξ (wt.-%)	x_T (mm)	y_T (mm)	γ_T (mm)	x_D (mm)	y_D (mm)	r_D (mm)
U	1.987	0.62	0.74	0.29	7.40	7.83	3.45
TOL_{\min}	26.493	8.27	9.87	3.87	98.67	104.40	46.00

A10 Required safety factors using function-oriented measurements

The following section serves to ensure the understanding of the discussion of the safety factor in Chapter 8. As an example, the expanded uncertainty U_{Sim} of the tensile tests for 41.0.M10 is used, which is about 17.4% of the mean realized stiffness \bar{E} (cf. Section 7.1.4.2). Furthermore, a safety factor f_{Safe} of 1.2 is assumed with respect to the minimum required stiffness E_{min} .

Assuming that the measurement results are normally distributed with the uncertainty $u = u_{\text{c,Sim}}$ around the measured value \hat{y} , the probability that the function is fulfilled can be calculated according Equation A10.1, using Equation A10.2 and A10.3.

$$P(x \geq E_{\text{min}}) = \int_{E_{\text{min}}}^{\infty} \frac{1}{\sqrt{2\pi}u} e^{-\frac{(x-\hat{y})^2}{2u^2}} dx = 0.97725 \quad \text{A10.1}$$

$$\hat{y} = \bar{E} = f_{\text{Safe}} \cdot E_{\text{min}} = 1.2 \cdot E_{\text{min}} \quad \text{A10.2}$$

$$u = u_{\text{c,Sim}} = \frac{U_{\text{Sim}}}{2} \approx \frac{0.174 \cdot \bar{E}}{2} = \frac{0.174 \cdot 1.2 \cdot E_{\text{min}}}{2} \approx 0.1 \cdot E_{\text{min}} \quad \text{A10.3}$$

Forschungsberichte aus dem wbk
Institut für Produktionstechnik
Karlsruher Institut für Technologie (KIT)

Bisher erschienene Bände:

Band 0

Dr.-Ing. Wu Hong-qi

Adaptive Volumenstromregelung mit Hilfe von drehzahlgeregelten Elektroantrieben

Band 1

Dr.-Ing. Heinrich Weiß

**Fräsen mit Schneidkeramik - Verhalten des System
Werkzeugmaschine-Werkzeug-Werkstück und Prozessanalyse**

Band 2

Dr.-Ing. Hans-Jürgen Stierle

**Entwicklung und Untersuchung hydrostatischer Lager für die
Axialkolbenmaschine**

Band 3

Dr.-Ing. Herbert Hörner

Untersuchung des Geräuschverhaltens druckgeregelter Axialkolbenpumpen

Band 4

Dr.-Ing. Rolf-Dieter Brückbauer

**Digitale Drehzahlregelung unter der besonderen Berücksichtigung
von Quantisierungseffekten**

Band 5

Dr.-Ing. Gerhard Staiger

Graphisch interaktive NC-Programmierung von Drehteilen im Werkstattbereich

Band 6

Dr.-Ing. Karl Peters

**Ein Beitrag zur Berechnung und Kompensation von Positionierfehlern an
Industrierobotern**

Band 7

Dr.-Ing. Paul Stauss

Automatisierte Inbetriebnahme und Sicherung der Zuverlässigkeit und Verfügbarkeit numerisch gesteuerter Fertigungseinrichtungen

Band 8

Dr.-Ing. Günter Möckesch

Konzeption und Realisierung eines strategischen, integrierten Gesamtplanungs- und -bearbeitungssystems zur Optimierung der Drehteilorganisation für auftragsbezogene Drehereien

Band 9

Dr.-Ing. Thomas Oestreicher

Rechnergestützte Projektierung von Steuerungen

Band 10

Dr.-Ing. Thomas Selinger

Teilautomatisierte werkstattnahe NC-Programmerstellung im Umfeld einer integrierten Informationsverarbeitung

Band 11

Dr.-Ing. Thomas Buchholz

Prozessmodell Fräsen, Rechnerunterstützte Analyse, Optimierung und Überwachung

Band 12

Dr.-Ing. Bernhard Reichling

Lasergestützte Positions- und Bahnvermessung von Industrierobotern

Band 13

Dr.-Ing. Hans-Jürgen Lesser

Rechnergestützte Methoden zur Auswahl anforderungsgerechter Verbindungselemente

Band 14

Dr.-Ing. Hans-Jürgen Lauffer

Einsatz von Prozessmodellen zur rechnerunterstützten Auslegung von Räumwerkzeugen

Band 15

Dr.-Ing. Michael C. Wilhelm

Rechnergestützte Prüfplanung im Informationsverbund moderner Produktionssysteme

Band 16

Dr.-Ing. Martin Ochs

Entwurf eines Programmsystems zur wissensbasierten Planung und Konfigurierung

Band 17

Dr.-Ing. Heinz-Joachim Schneider

Erhöhung der Verfügbarkeit von hochautomatisierten Produktionseinrichtungen mit Hilfe der Fertigungsleittechnik

Band 18

Dr.-Ing. Hans-Reiner Ludwig

Beanspruchungsanalyse der Werkzeugschneiden beim Stirnplanfräsen

Band 19

Dr.-Ing. Rudolf Wieser

Methoden zur rechnergestützten Konfigurierung von Fertigungsanlagen

Band 20

Dr.-Ing. Edgar Schmitt

Werkstattsteuerung bei wechselnder Auftragsstruktur

Band 21

Dr.-Ing. Wilhelm Enderle

Verfügbarkeitssteigerung automatisierter Montagesysteme durch selbsttätige Behebung prozessbedingter Störungen

Band 22

Dr.-Ing. Dieter Buchberger

Rechnergestützte Strukturplanung von Produktionssystemen

Band 23

Prof. Dr.-Ing. Jürgen Fleischer

Rechnerunterstützte Technologieplanung für die flexibel automatisierte Fertigung von Abkanteilen

Band 24

Dr.-Ing. Lukas Loeffler

Adaptierbare und adaptive Benutzerschnittstellen

Band 25

Dr.-Ing. Thomas Friedmann

Integration von Produktentwicklung und Montageplanung durch neue rechnergestützte Verfahren

Band 26

Dr.-Ing. Robert Zurrin

Variables Formhonen durch rechnergestützte Hornprozesssteuerung

Band 27

Dr.-Ing. Karl-Heinz Bergen

Langhub-Innenrundhonen von Grauguss und Stahl mit einem elektromechanischem Vorschubsystem

Band 28

Dr.-Ing. Andreas Liebisch

Einflüsse des Festwalzens auf die Eigenspannungsverteilung und die Dauerfestigkeit einsatzgehärteter Zahnräder

Band 29

Dr.-Ing. Rolf Ziegler

Auslegung und Optimierung schneller Servopumpen

Band 30

Dr.-Ing. Rainer Bartl

Datenmodellgestützte Wissensverarbeitung zur Diagnose und Informationsunterstützung in technischen Systemen

Band 31

Dr.-Ing. Ulrich Golz

Analyse, Modellbildung und Optimierung des Betriebsverhaltens von Kugelgewindetrieben

Band 32

Dr.-Ing. Stephan Timmermann

Automatisierung der Feinbearbeitung in der Fertigung von Hohlformwerkzeugen

Band 33

Dr.-Ing. Thomas Noe

Rechnergestützter Wissenserwerb zur Erstellung von Überwachungs- und Diagnoseexpertensystemen für hydraulische Anlagen

Band 34

Dr.-Ing. Ralf Lenschow

Rechnerintegrierte Erstellung und Verifikation von Steuerungsprogrammen als Komponente einer durchgängigen Planungsmethodik

Band 35

Dr.-Ing. Matthias Kallabis

Räumen gehärteter Werkstoffe mit kristallinen Hartstoffen

Band 36

Dr.-Ing. Heiner-Michael Honeck

Rückführung von Fertigungsdaten zur Unterstützung einer fertigungsgerechten Konstruktion

Band 37

Dr.-Ing. Manfred Rohr

Automatisierte Technologieplanung am Beispiel der Komplettbearbeitung auf Dreh-/Fräszellen

Band 38

Dr.-Ing. Martin Steuer

Entwicklung von Softwarewerkzeugen zur wissensbasierten Inbetriebnahme von komplexen Serienmaschinen

Band 39

Dr.-Ing. Siegfried Beichter

Rechnergestützte technische Problemlösung bei der Angebotserstellung von flexiblen Drehzellen

Band 40

Dr.-Ing. Thomas Steitz

Methodik zur marktorientierten Entwicklung von Werkzeugmaschinen mit Integration von funktionsbasierter Strukturierung und Kostenschätzung

Band 41

Dr.-Ing. Michael Richter

Wissensbasierte Projektierung elektrohydraulischer Regelungen

Band 42

Dr.-Ing. Roman Kuhn

Technologieplanungssystem Fräsen. Wissensbasierte Auswahl von Werkzeugen, Schneidkörpern und Schnittbedingungen für das Fertigungsverfahren Fräsen

Band 43

Dr.-Ing. Hubert Klein

Rechnerunterstützte Qualitätssicherung bei der Produktion von Bauteilen mit frei geformten Oberflächen

Band 44

Dr.-Ing. Christian Hoffmann

Konzeption und Realisierung eines fertigungsintegrierten Koordinatenmessgerätes

Band 45

Dr.-Ing. Volker Frey

Planung der Leittechnik für flexible Fertigungsanlagen

Band 46

Dr.-Ing. Achim Feller

Kalkulation in der Angebotsphase mit dem selbsttätig abgeleiteten Erfahrungswissen der Arbeitsplanung

Band 47

Dr.-Ing. Markus Klaiber

Produktivitätssteigerung durch rechnerunterstütztes Einfahren von NC-Programmen

Band 48

Dr.-Ing. Roland Minges

Verbesserung der Genauigkeit beim fünffachsignen Fräsen von Freiformflächen

Band 49

Dr.-Ing. Wolfgang Bernhart

Beitrag zur Bewertung von Montagevarianten: Rechnergestützte Hilfsmittel zur kostenorientierten, parallelen Entwicklung von Produkt und Montagesystem

Band 50

Dr.-Ing. Peter Ganghoff

Wissensbasierte Unterstützung der Planung technischer Systeme: Konzeption eines Planungswerkzeuges und exemplarische Anwendung im Bereich der Montagesystemplanung

Band 51

Dr.-Ing. Frank Maier

Rechnergestützte Prozessregelung beim flexiblen Gesenkbiegen durch Rückführung von Qualitätsinformationen

Band 52

Dr.-Ing. Frank Debus

Ansatz eines rechnerunterstützten Planungsmanagements für die Planung in verteilten Strukturen

Band 53

Dr.-Ing. Joachim Weinbrecht

Ein Verfahren zur zielorientierten Reaktion auf Planabweichungen in der Werkstattregelung

Band 54

Dr.-Ing. Gerd Herrmann

Reduzierung des Entwicklungsaufwandes für anwendungsspezifische Zellenrechnersoftware durch Rechnerunterstützung

Band 55

Dr.-Ing. Robert Wassmer

Verschleissentwicklung im tribologischen System Fräsen: Beiträge zur Methodik der Prozessmodellierung auf der Basis tribologischer Untersuchungen beim Fräsen

Band 56

Dr.-Ing. Peter Uebelhoer

Inprocess-Geometriemessung beim Honen

Band 57

Dr.-Ing. Hans-Joachim Schelberg

Objektorientierte Projektierung von SPS-Software

Band 58

Dr.-Ing. Klaus Boes

Integration der Qualitätsentwicklung in featurebasierte CAD/CAM-Prozessketten

Band 59

Dr.-Ing. Martin Schreiber

Wirtschaftliche Investitionsbewertung komplexer Produktionssysteme unter Berücksichtigung von Unsicherheit

Band 60

Dr.-Ing. Ralf Steuernagel

Offenes adaptives Engineering-Werkzeug zur automatisierten Erstellung von entscheidungsunterstützenden Informationssystemen

Band 62

Dr.-Ing. Uwe Schauer

Qualitätsorientierte Feinbearbeitung mit Industrierobotern: Regelungsansatz für die Freiformflächenfertigung des Werkzeug- und Formenbaus

Band 63

Dr.-Ing. Simone Loeper

Kennzahlengestütztes Beratungssystem zur Verbesserung der Logistikleistung in der Werkstattfertigung

Band 64

Dr.-Ing. Achim Raab

Räumen mit hartstoffbeschichteten HSS-Werkzeugen

Band 65,

Dr.-Ing. Jan Erik Burghardt

Unterstützung der NC-Verfahrenskette durch ein bearbeitungs-elementorientiertes, lernfähiges Technologieplanungssystem

Band 66

Dr.-Ing. Christian Tritsch

Flexible Demontage technischer Gebrauchsgüter: Ansatz zur Planung und (teil-)automatisierten Durchführung industrieller Demontageprozesse

Band 67

Dr.-Ing. Oliver Eitrich

Prozessorientiertes Kostenmodell für die entwicklungsbegleitende Vorkalkulation

Band 68

Dr.-Ing. Oliver Wilke

Optimierte Antriebskonzepte für Räummaschinen - Potentiale zur Leistungssteigerung

Band 69

Dr.-Ing. Thilo Sieth

Rechnergestützte Modellierungsmethodik zerspantechnologischer Prozesse

Band 70

Dr.-Ing. Jan Linnenbuenger

Entwicklung neuer Verfahren zur automatisierten Erfassung der geometrischen Abweichungen an Linearachsen und Drehschwenkköpfen

Band 71

Dr.-Ing. Mathias Klimmek

Fraktionierung technischer Produkte mittels eines frei beweglichen Wasserstrahlwerkzeuges

Band 72

Dr.-Ing. Marko Hartel

Kennzahlenbasiertes Bewertungssystem zur Beurteilung der Demontage- und Recyclingeignung von Produkten

Band 73

Dr.-Ing. Jörg Schaupp

Wechselwirkung zwischen der Maschinen- und Hauptspindelantriebsdynamik und dem Zerspanprozess beim Fräsen

Band 74

Dr.-Ing. Bernhard Neisius

Konzeption und Realisierung eines experimentellen Telemanipulators für die Laparoskopie

Band 75

Dr.-Ing. Wolfgang Walter

Erfolgsversprechende Muster für betriebliche Ideenfindungsprozesse. Ein Beitrag zur Steigerung der Innovationsfähigkeit

Band 76

Dr.-Ing. Julian Weber

Ein Ansatz zur Bewertung von Entwicklungsergebnissen in virtuellen Szenarien

Band 77

Dr.-Ing. Dipl. Wirtsch.-Ing. Markus Posur

Unterstützung der Auftragsdurchsetzung in der Fertigung durch Kommunikation über mobile Rechner

Band 78

Dr.-Ing. Frank Fleissner

Prozessorientierte Prüfplanung auf Basis von Bearbeitungsobjekten für die Kleinserienfertigung am Beispiel der Bohr- und Fräsbearbeitung

Band 79

Dr.-Ing. Anton Haberkern

Leistungsfähigere Kugelgewindetriebe durch Beschichtung

Band 80

Dr.-Ing. Dominik Matt

Objektorientierte Prozess- und Strukturinnovation (OPUS)

Band 81

Dr.-Ing. Jürgen Andres

Robotersysteme für den Wohnungsbau: Beitrag zur Automatisierung des Mauerwerkbaus und der Elektroinstallation auf Baustellen

Band 82

Dr.-Ing. Dipl.Wirtschaftsing. Simone Riedmiller

Der Prozesskalender - Eine Methodik zur marktorientierten Entwicklung von Prozessen

Band 83

Dr.-Ing. Dietmar Tilch

Analyse der Geometrieparameter von Präzisionsgewinden auf der Basis einer Least-Squares-Estimation

Band 84

Dr.-Ing. Dipl.-Kfm. Oliver Stiefbold

Konzeption eines reaktionsschnellen Planungssystems für Logistikketten auf Basis von Software-Agenten

Band 85

Dr.-Ing. Ulrich Walter

Einfluss von Kühlschmierstoff auf den Zerspansprozess beim Fräsen: Beitrag zum Prozessverständnis auf Basis von zerspantechnischen Untersuchungen

Band 86

Dr.-Ing. Bernd Werner

Konzeption von teilautonomer Gruppenarbeit unter Berücksichtigung kultureller Einflüsse

Band 87

Dr.-Ing. Ulf Osmers

Projektieren Speicherprogrammierbarer Steuerungen mit Virtual Reality

Band 88

Dr.-Ing. Oliver Doerfel

Optimierung der Zerspantechnik beim Fertigungsverfahren Wälzstossen: Analyse des Potentials zur Trockenbearbeitung

Band 89

Dr.-Ing. Peter Baumgartner

Stufenmethode zur Schnittstellengestaltung in der internationalen Produktion

Band 90

Dr.-Ing. Dirk Vossmann

Wissensmanagement in der Produktentwicklung durch Qualitätsmethodenverbund und Qualitätsmethodenintegration

Band 91

Dr.-Ing. Martin Plass

Beitrag zur Optimierung des Honprozesses durch den Aufbau einer Honprozessregelung

Band 92

Dr.-Ing. Titus Konold

Optimierung der Fünffachsfräsbearbeitung durch eine kennzahlenunterstützte CAM-Umgebung

Band 93

Dr.-Ing. Jürgen Brath

Unterstützung der Produktionsplanung in der Halbleiterfertigung durch risikoberücksichtigende Betriebskennlinien

Band 94

Dr.-Ing. Dirk Geisinger

Ein Konzept zur marktorientierten Produktentwicklung

Band 95

Dr.-Ing. Marco Lanza

Entwurf der Systemunterstützung des verteilten Engineering mit Axiomatic Design

Band 96

Dr.-Ing. Volker Hüntrup

Untersuchungen zur Mikrostrukturierbarkeit von Stählen durch das Fertigungsverfahren Fräsen

Band 97

Dr.-Ing. Frank Reinboth

Interne Stützung zur Genauigkeitsverbesserung in der Inertialmesstechnik: Beitrag zur Senkung der Anforderungen an Inertialsensoren

Band 98

Dr.-Ing. Lutz Trender

Entwicklungsintegrierte Kalkulation von Produktlebenszykluskosten auf Basis der ressourcenorientierten Prozesskostenrechnung

Band 99

Dr.-Ing. Cornelia Kafka

Konzeption und Umsetzung eines Leitfadens zum industriellen Einsatz von Data-Mining

Band 100

Dr.-Ing. Gebhard Selinger

Rechnerunterstützung der informellen Kommunikation in verteilten Unternehmensstrukturen

Band 101

Dr.-Ing. Thomas Windmüller

Verbesserung bestehender Geschäftsprozesse durch eine mitarbeiterorientierte Informationsversorgung

Band 102

Dr.-Ing. Knud Lembke

Theoretische und experimentelle Untersuchung eines bistabilen elektrohydraulischen Linearantriebs

Band 103

Dr.-Ing. Ulrich Thies

Methode zur Unterstützung der variantengerechten Konstruktion von industriell eingesetzten Kleingeräten

Band 104

Dr.-Ing. Andreas Schmäzle

Bewertungssystem für die Generalüberholung von Montageanlagen –Ein Beitrag zur wirtschaftlichen Gestaltung geschlossener Facility- Management-Systeme im Anlagenbau

Band 105

Dr.-Ing. Thorsten Frank

Vergleichende Untersuchungen schneller elektromechanischer Vorschubachsen mit Kugelgewindetrieb

Band 106

Dr.-Ing. Achim Agostini

Reihenfolgeplanung unter Berücksichtigung von Interaktionen: Beitrag zur ganzheitlichen Strukturierung und Verarbeitung von Interaktionen von Bearbeitungsobjekten

Band 107

Dr.-Ing. Thomas Barrho

Flexible, zeitfenstergesteuerte Auftragseinplanung in segmentierten Fertigungsstrukturen

Band 108

Dr.-Ing. Michael Scharer

Quality Gate-Ansatz mit integriertem Risikomanagement

Band 109

Dr.-Ing. Ulrich Suchy

Entwicklung und Untersuchung eines neuartigen Mischkopfes für das Wasser Abrasivstrahlschneiden

Band 110

Dr.-Ing. Sellal Mussa

Aktive Korrektur von Verlagerungsfehlern in Werkzeugmaschinen

Band 111

Dr.-Ing. Andreas Hühsam

Modellbildung und experimentelle Untersuchung des Wälzschälprozesses

Band 112

Dr.-Ing. Axel Plutowsky

Charakterisierung eines optischen Messsystems und den Bedingungen des Arbeitsraums einer Werkzeugmaschine

Band 113

Dr.-Ing. Robert Landwehr

Konsequent dezentralisierte Steuerung mit Industrial Ethernet und offenen Applikationsprotokollen

Band 114

Dr.-Ing. Christoph Dill

Turbulenzreaktionsprozesse

Band 115

Dr.-Ing. Michael Baumeister

Fabrikplanung im turbulenten Umfeld

Band 116

Dr.-Ing. Christoph Gönzheimer

Konzept zur Verbesserung der Elektromagnetischen Verträglichkeit (EMV) in Produktionssystemen durch intelligente Sensor/Aktor-Anbindung

Band 117

Dr.-Ing. Lutz Demuß

Ein Reifemodell für die Bewertung und Entwicklung von Dienstleistungsorganisationen: Das Service Management Maturity Modell (SMMM)

Band 118

Dr.-Ing. Jörg Söhner

Beitrag zur Simulation zerspanungstechnologischer Vorgänge mit Hilfe der Finite-Element-Methode

Band 119

Dr.-Ing. Judith Elsner

Informationsmanagement für mehrstufige Mikro-Fertigungsprozesse

Band 120

Dr.-Ing. Lijing Xie

Estimation Of Two-dimension Tool Wear Based On Finite Element Method

Band 121

Dr.-Ing. Ansgar Blessing

Geometrischer Entwurf mikromechatronischer Systeme

Band 122

Dr.-Ing. Rainer Ebner

Steigerung der Effizienz mehrachsiger Fräsprozesse durch neue Planungsmethoden mit hoher Benutzerunterstützung

Band 123

Dr.-Ing. Silja Klinkel

Multikriterielle Feinplanung in teilautonomen Produktionsbereichen – Ein Beitrag zur produkt- und prozessorientierten Planung und Steuerung

Band 124

Dr.-Ing. Wolfgang Neithardt

Methodik zur Simulation und Optimierung von Werkzeugmaschinen in der Konzept- und Entwurfsphase auf Basis der Mehrkörpersimulation

Band 125

Dr.-Ing. Andreas Mehr

Hartfeinbearbeitung von Verzahnungen mit kristallinen diamantbeschichteten Werkzeugen beim Fertigungsverfahren Wälzstoßen

Band 126

Dr.-Ing. Martin Gutmann

Entwicklung einer methodischen Vorgehensweise zur Diagnose von hydraulischen Produktionsmaschinen

Band 127

Dr.-Ing. Gisela Lanza

Simulative Anlaufunterstützung auf Basis der Qualitätsfähigkeiten von Produktionsprozessen

Band 128

Dr.-Ing. Ulf Dambacher

Kugelgewindetrieb mit hohem Druckwinkel

Band 129

Dr.-Ing. Carsten Buchholz

Systematische Konzeption und Aufbau einer automatisierten Produktionszelle für pulverspritzgegossene Mikrobauteile

Band 130

Dr.-Ing. Heiner Lang

Trocken-Räumen mit hohen Schnittgeschwindigkeiten

Band 131

Dr.-Ing. Daniel Nesges

Prognose operationeller Verfügbarkeiten von Werkzeugmaschinen unter Berücksichtigung von Serviceleistungen

Im Shaker Verlag erschienene Bände:

Band 132

Dr.-Ing. Andreas Bechle

Beitrag zur prozesssicheren Bearbeitung beim Hochleistungsfertigungsverfahren Wälzschälen

Band 133

Dr.-Ing. Markus Herm

Konfiguration globaler Wertschöpfungsnetzwerke auf Basis von Business Capabilities

Band 134

Dr.-Ing. Hanno Tritschler

Werkzeug- und Zerspanprozessoptimierung beim Hartfräsen von Mikrostrukturen in Stahl

Band 135

Dr.-Ing. Christian Munzinger

Adaptronische Strebe zur Steifigkeitssteigerung von Werkzeugmaschinen

Band 136

Dr.-Ing. Andreas Stepping

Fabrikplanung im Umfeld von Wertschöpfungsnetzwerken und ganzheitlichen Produktionssystemen

Band 137

Dr.-Ing. Martin Dyck

Beitrag zur Analyse thermische bedingter Werkstückdeformationen in Trockenbearbeitungsprozessen

Band 138

Dr.-Ing. Siegfried Schmalzried

Dreidimensionales optisches Messsystem für eine effizientere geometrische Maschinenbeurteilung

Band 139

Dr.-Ing. Marc Wawerla

Risikomanagement von Garantieleistungen

Band 140

Dr.-Ing. Ivesa Buchholz

Strategien zur Qualitätssicherung mikromechanischer Bauteile mittels multisensorieller Koordinatenmesstechnik

Band 141

Dr.-Ing. Jan Kotschenreuther

Empirische Erweiterung von Modellen der Makrozerspannung auf den Bereich der Mikrobearbeitung

Band 142

Dr.-Ing. Andreas Knödel

Adaptronische hydrostatische Drucktascheneinheit

Band 143

Dr.-Ing. Gregor Stengel

Fliegendes Abtrennen räumlich gekrümmter Strangpressprofile mittels Industrierobotern

Band 144

Dr.-Ing. Udo Weismann

Lebenszyklusorientiertes interorganisationelles Anlagencontrolling

Band 145

Dr.-Ing. Rüdiger Pabst

Mathematische Modellierung der Wärmestromdichte zur Simulation des thermischen Bauteilverhaltens bei der Trockenbearbeitung

Band 146

Dr.-Ing. Jan Wieser

Intelligente Instandhaltung zur Verfügbarkeitssteigerung von Werkzeugmaschinen

Band 147

Dr.-Ing. Sebastian Haupt

Effiziente und kostenoptimale Herstellung von Mikrostrukturen durch eine Verfahrenskombination von Bahnerosion und Laserablation

Band 148

Dr.-Ing. Matthias Schlipf

Statistische Prozessregelung von Fertigungs- und Messprozess zur Erreichung einer variabilitätsarmen Produktion mikromechanischer Bauteile

Band 149

Dr.-Ing. Jan Philipp Schmidt-Ewig

Methodische Erarbeitung und Umsetzung eines neuartigen Maschinenkonzeptes zur produktflexiblen Bearbeitung räumlich gekrümmter Strangpressprofile

Band 150

Dr.-Ing. Thomas Ender

Prognose von Personalbedarfen im Produktionsanlauf unter Berücksichtigung dynamischer Planungsgrößen

Band 151

Dr.-Ing. Kathrin Peter

**Bewertung und Optimierung der Effektivität von Lean Methoden
in der Kleinserienproduktion**

Band 152

Dr.-Ing. Matthias Schopp

Sensorbasierte Zustandsdiagnose und -prognose von Kugelgewindetrieben

Band 153

Dr.-Ing. Martin Kipfmüller

Aufwandsoptimierte Simulation von Werkzeugmaschinen

Band 154

Dr.-Ing. Carsten Schmidt

**Development of a database to consider multi wear mechanisms
within chip forming simulation**

Band 155

Dr.-Ing. Stephan Niggeschmidt

**Ausfallgerechte Ersatzteilbereitstellung im Maschinen- und Anlagenbau
mittels lastabhängiger Lebensdauerprognose**

Band 156

Dr.-Ing. Jochen Conrad Peters

**Bewertung des Einflusses von Formabweichungen in der
Mikro-Koordinatenmesstechnik**

Band 157

Dr.-Ing. Jörg Ude

**Entscheidungsunterstützung für die Konfiguration
globaler Wertschöpfungsnetzwerke**

Band 158

Dr.-Ing. Stefan Weiler

Strategien zur wirtschaftlichen Gestaltung der globalen Beschaffung

Band 159

Dr.-Ing. Jan Rühl

Monetäre Flexibilitäts- und Risikobewertung

Band 160

Dr.-Ing. Daniel Ruch

Positions- und Konturerfassung räumlich gekrümmter Profile auf Basis bauteilimmanenter Markierungen

Band 161

Dr.-Ing. Manuel Tröndle

Flexible Zuführung von Mikrobauteilen mit piezoelektrischen Schwingförderern

Band 162

Dr.-Ing. Benjamin Viering

Mikroverzahnungsnormal

Band 163

Dr.-Ing. Chris Becke

Prozesskrafttrichtungsangepasste Frässtrategien zur schädigungsarmen Bohrungsbearbeitung an faserverstärkten Kunststoffen

Band 164

Dr.-Ing. Patrick Werner

Dynamische Optimierung und Unsicherheitsbewertung der lastabhängigen präventiven Instandhaltung von Maschinenkomponenten

Band 165

Dr.-Ing. Martin Weis

Kompensation systematischer Fehler bei Werkzeugmaschinen durch self-sensing Aktoren

Band 166

Dr.-Ing. Markus Schneider

Kompensation von Konturabweichungen bei gerundeten Strangpressprofilen durch robotergestützte Führungswerkzeuge

Band 167

Dr.-Ing. Ester M. R. Ruprecht

Prozesskette zur Herstellung schichtbasierter Systeme mit integrierten Kavitäten

Band 168

Dr.-Ing. Alexander Broos

Simulationsgestützte Ermittlung der Komponentenbelastung für die Lebensdauerprognose an Werkzeugmaschinen

Band 169

Dr.-Ing. Frederik Zanger

Segmentspannbildung, Werkzeugverschleiß, Randschichtzustand und Bauteileigenschaften: Numerische Analysen zur Optimierung des Zerspanungsprozesses am Beispiel von Ti-6Al-4V

Band 170

Dr.-Ing. Benjamin Behmann

Servicefähigkeit

Band 171

Dr.-Ing. Annabel Gabriele Jondral

Simulationsgestützte Optimierung und Wirtschaftlichkeitsbewertung des Lean-Methodeneinsatzes

Band 172

Dr.-Ing. Christoph Ruhs

Automatisierte Prozessabfolge zur qualitätssicheren Herstellung von Kavitäten mittels Mikrobahnerosion

Band 173

Dr.-Ing. Steven Peters

Markoffsche Entscheidungsprozesse zur Kapazitäts- und Investitionsplanung von Produktionssystemen

Band 174

Dr.-Ing. Christoph Kühlewein

Untersuchung und Optimierung des Wälzschälverfahrens mit Hilfe von 3D-FEM-Simulation – 3D-FEM Kinematik- und Spannbildungssimulation

Band 175

Dr.-Ing. Adam-Mwanga Dieckmann

Auslegung und Fertigungsprozessgestaltung sintergefügter Verbindungen für μ MIM-Bauteile

Band 176

Dr.-Ing. Heiko Hennrich

Aufbau eines kombinierten belastungs- und zustandsorientierten Diagnose- und Prognosesystems für Kugelgewindetriebe

Band 177

Dr.-Ing. Stefan Herder

Piezoelektrischer Self-Sensing-Aktor zur Vorspannungsregelung in adaptronischen Kugelgewindetriebe

Band 178

Dr.-Ing. Alexander Ochs

Ultraschall-Strömungsgreifer für die Handhabung textiler Halbzeuge bei der automatisierten Fertigung von RTM-Bauteilen

Band 179

Dr.-Ing. Jürgen Michna

Numerische und experimentelle Untersuchung zerspanungsbedingter Gefügeumwandlungen und Modellierung des thermo-mechanischen Lastkollektivs beim Bohren von 42CrMo4

Band 180

Dr.-Ing. Jörg Elser

Vorrichtungsfreie räumliche Anordnung von Fügepartnern auf Basis von Bauteilmarkierungen

Band 181

Dr.-Ing. Katharina Klimscha

Einfluss des Fügespalts auf die erreichbare Verbindungsqualität beim Sinterfügen

Band 182

Dr.-Ing. Patricia Weber

Steigerung der Prozesswiederholbarkeit mittels Analyse akustischer Emissionen bei der Mikrolaserablation mit UV-Pikosekundenlasern

Band 183

Dr.-Ing. Jochen Schädel

Automatisiertes Fügen von Tragprofilen mittels Faserwickeln

Band 184

Dr.-Ing. Martin Krauß

Aufwandsoptimierte Simulation von Produktionsanlagen durch Vergrößerung der Geltungsbereiche von Teilmodellen

Band 185

Dr.-Ing. Raphael Moser

Strategische Planung globaler Produktionsnetzwerke

Bestimmung von Wandlungsbedarf und Wandlungszeitpunkt mittels multikriterieller Optimierung

Band 186

Dr.-Ing. Martin Otter

Methode zur Kompensation fertigungsbedingter Gestaltabweichungen für die Montage von Aluminium Space-Frame-Strukturen

Band 187

Dr.-Ing. Urs Leberle

Produktive und flexible Gleitförderung kleiner Bauteile auf phasenflexiblen Schwingförderern mit piezoelektrischen 2D-Antriebselementen

Band 188

Dr.-Ing. Johannes Book

Modellierung und Bewertung von Qualitätsmanagementstrategien in globalen Wertschöpfungsnetzwerken

Band 189

Dr.-Ing. Florian Ambrosy

Optimierung von Zerspanungsprozessen zur prozesssicheren Fertigung nanokristalliner Randschichten am Beispiel von 42CrMo4

Band 190

Dr.-Ing. Adrian Kölmel

Integrierte Messtechnik für Prozessketten unreifer Technologien am Beispiel der Batterieproduktion für Elektrofahrzeuge

Band 191

Dr.-Ing. Henning Wagner

Featurebasierte Technologieplanung zum Preforming von textilen Halbzeugen

Band 192

Dr.-Ing. Johannes Gebhardt

Strukturoptimierung von in FVK eingebetteten metallischen Lasteinleitungselementen

Band 193

Dr.-Ing. Jörg Bauer

Hochintegriertes hydraulisches Vorschubsystem für die Bearbeitung kleiner Werkstücke mit hohen Fertigungsanforderungen

Band 194

Dr.-Ing. Nicole Stricker

Robustheit verketteter Produktionssysteme

Robustheitsevaluation und Selektion des Kennzahlensystems der Robustheit

Band 195

Dr.-Ing. Anna Sauer

Konfiguration von Montagelinien unreifer Produkttechnologien am Beispiel der Batteriemontage für Elektrofahrzeuge

Band 196

Dr.-Ing. Florian Sell-Le Blanc

Prozessmodell für das Linearwickeln unrunder Zahnspulen

Ein Beitrag zur orthozyklischen Spulenwickeltechnik

Band 197

Dr.-Ing. Frederic Förster

Geregeltes Handhabungssystem zum zuverlässigen und energieeffizienten Handling textiler Kohlenstofffaserzuschnitte

Band 198

Dr.-Ing. Nikolay Boev

Numerische Beschreibung von Wechselwirkungen zwischen Zerspanprozess und Maschine am Beispiel Räumen

Band 199

Dr.-Ing. Sebastian Greinacher

Simulationsgestützte Mehrzieloptimierung schlanker und ressourceneffizienter Produktionssysteme

Band 200

Dr.-Ing. Benjamin Häfner

Lebensdauerprognose in Abhängigkeit der Fertigungsabweichungen bei Mikroverzahnungen

Band 201

Dr.-Ing. Stefan Klotz

Dynamische Parameteranpassung bei der Bohrungsherstellung in faserverstärkten Kunststoffen unter zusätzlicher Berücksichtigung der Einspannsituation

Band 202

Dr.-Ing. Johannes Stoll

Bewertung konkurrierender Fertigungsfolgen mittels Kostensimulation und stochastischer Mehrzieloptimierung

Anwendung am Beispiel der Blechpaketfertigung für automobiler Elektromotoren

Band 203

Dr.-Ing. Simon-Frederik Koch

Fügen von Metall-Faserverbund-Hybridwellen im Schleuderverfahren
ein Beitrag zur fertigungsgerechten intrinsischen Hybridisierung

Band 204

Dr.-Ing. Julius Ficht

Numerische Untersuchung der Eigenspannungsentwicklung für sequenzielle Zerspanungsprozesse

Band 205

Dr.-Ing. Manuel Baumeister

Automatisierte Fertigung von Einzelblattstapeln in der Lithium-Ionen-Zellproduktion

Band 206

Dr.-Ing. Daniel Bertsch

Optimierung der Werkzeug- und Prozessauslegung für das Wälzschälen von Innenverzahnungen

Band 207

Dr.-Ing. Kyle James Kippenbrock

Deconvolution of Industrial Measurement and Manufacturing Processes for Improved Process Capability Assessments

Band 208

Dr.-Ing. Farboud Bejnoud

Experimentelle Prozesskettenbetrachtung für Räumbauteile am Beispiel einer einsatzgehärteten PKW-Schiebemuffe

Band 209

Dr.-Ing. Steffen Dosch

Herstellungsübergreifende Informationsübertragung zur effizienten Produktion von Werkzeugmaschinen am Beispiel von Kugelgewindetrieben

Band 210

Dr.-Ing. Emanuel Moser

Migrationsplanung globaler Produktionsnetzwerke

Bestimmung robuster Migrationspfade und risiko-effizienter Wandlungsbefähiger

Band 211

Dr.-Ing. Jan Hochdörffer

Integrierte Produktallokationsstrategie und Konfigurationssequenz in globalen Produktionsnetzwerken

Band 212

Dr.-Ing. Tobias Arndt

Bewertung und Steigerung der Prozessqualität in globalen Produktionsnetzwerken

Band 213

Dr.-Ing. Manuel Peter

Unwuchtminimale Montage von Permanentmagnetrotoren durch modellbasierte Online-Optimierung

Band 214

Dr.-Ing. Robin Kopf

Kostenorientierte Planung von Fertigungsfolgen additiver Technologien

Band 215

Dr.-Ing. Harald Meier

**Einfluss des Räumens auf den Bauteilzustand in der Prozesskette
Weichbearbeitung – Wärmebehandlung – Hartbearbeitung**

Band 216

Dr.-Ing. Daniel Brabandt

**Qualitätssicherung von textilen Kohlenstofffaser-Preforms mittels
optischer Messtechnik**

Band 217

Dr.-Ing. Alexandra Schabunow

**Einstellung von Aufnahmeparametern mittels projektionsbasierter Qualitäts-
kenngrößen in der industriellen Röntgen-Computertomographie**

Band 218

Dr.-Ing. Jens Bürgin

Robuste Auftragsplanung in Produktionsnetzwerken
Mittelfristige Planung der variantenreichen Serienproduktion unter Unsicherheit
der Kundenauftragskonfigurationen

Band 219

Dr.-Ing. Michael Gerstenmeyer

**Entwicklung und Analyse eines mechanischen Oberflächenbehandlungs-
verfahrens unter Verwendung des Zerspanungswerkzeuges**

Band 220

Dr.-Ing. Jacques Burtscher

**Erhöhung der Bearbeitungsstabilität von Werkzeugmaschinen durch
semi-passive masseneinstellbare Dämpfungssysteme**

Band 221

Dr.-Ing. Dietrich Berger

**Qualitätssicherung von textilen Kohlenstofffaser-Preforms mittels prozess-
integrierter Wirbelstromsensor-Arrays**

Band 222

Dr.-Ing. Fabian Johannes Ballier

Systematic gripper arrangement for a handling device in lightweight production processes

Band 223

Dr.-Ing. Marielouise Schäferling, geb. Zaiß

Development of a Data Fusion-Based Multi-Sensor System for Hybrid Sheet Molding Compound

Band 224

Dr.-Ing. Quirin Spiller

Additive Herstellung von Metallbauteilen mit dem ARBURG Kunststoff-Freiformen

Band 225

Dr.-Ing. Andreas Spohrer

Steigerung der Ressourceneffizienz und Verfügbarkeit von Kugelgewindetrieben durch adaptive Schmierung

Band 226

Dr.-Ing. Johannes Fisel

Veränderungsfähigkeit getakteter Fließmontagesysteme

Planung der Fließbandabstimmung am Beispiel der Automobilmontage

Band 227

Dr.-Ing. Patrick Bollig

Numerische Entwicklung von Strategien zur Kompensation thermisch bedingter Verzüge beim Bohren von 42CrMo4

Band 228

Dr.-Ing. Ramona Pfeiffer, geb. Singer

Untersuchung der prozessbestimmenden Größen für die anforderungsgerechte Gestaltung von Pouchzellen-Verpackungen

Band 229

Dr.-Ing. Florian Baumann

Additive Fertigung von endlosfaserverstärkten Kunststoffen mit dem ARBURG Kunststoff-Freiform Verfahren

Band 230

Dr.-Ing. Tom Stähr

Methodik zur Planung und Konfigurationsauswahl skalierbarer Montagesysteme – Ein Beitrag zur skalierbaren Automatisierung

Band 231

Dr.-Ing. Jan Schwennen

Einbringung und Gestaltung von Lasteinleitungsstrukturen für im RTM-Verfahren hergestellte FVK-Sandwichbauteile

Band 232

Dr.-Ing. Sven Coutandin

Prozessstrategien für das automatisierte Preforming von bebinderten textilen Halbzeugen mit einem segmentierten Werkzeugsystem

Band 233

Dr.-Ing. Christoph Liebrecht

Entscheidungsunterstützung für den Industrie 4.0-Methodeneinsatz
Strukturierung, Bewertung und Ableitung von Implementierungsreihenfolgen

Band 234

Dr.-Ing. Stefan Treber

Transparenzsteigerung in Produktionsnetzwerken
Verbesserung des Störungsmanagements durch verstärkten Informationsaustausch

Band 235

Dr.-Ing. Marius Dackweiler

Modellierung des Fügewickelprozesses zur Herstellung von leichten Fachwerkstrukturen

Band 236

Dr.-Ing. Fabio Echsler Minguillon

Prädiktiv-reaktives Scheduling zur Steigerung der Robustheit in der Matrix-Produktion

Band 237

Dr.-Ing. Sebastian Haag

Entwicklung eines Verfahrensablaufes zur Herstellung von Batteriezellstapeln mit großformatigem, rechteckigem Stapelformat und kontinuierlichen Materialbahnen

Band 238

Dr.-Ing. Raphael Wagner

Strategien zur funktionsorientierten Qualitätsregelung in der Serienproduktion

Band 239

Dr.-Ing. Christopher Ehrmann

Ausfallfrüherkennung von Ritzel-Zahnstangen- Trieben mittels Acoustic Emission

Band 240

Dr.-Ing. Janna Hofmann

Prozessmodellierung des Fünf-Achs-Nadelwickelns zur Implementierung einer trajektoriebasierten Drahtzugkraftregelung

Band 241

Dr.-Ing. Andreas Kuhnle

**Adaptive Order Dispatching based on Reinforcement Learning
Application in a Complex Job Shop in the Semiconductor Industry**

Band 242

Dr.-Ing. Andreas Greiber

**Fertigung optimierter technischer Oberflächen durch eine
Verfahrenskombination aus Fliehkraft-Tauchgleitschleifen und Laserablation
Prozesseinflüsse und Prozessauslegung**

Band 243

Dr.-Ing. Jan Niclas Eschner

**Entwicklung einer akustischen Prozessüberwachung zur
Porenbestimmung im Laserstrahlschmelzen**

Band 244

Dr.-Ing. Sven Roth

**Schädigungsfreie Anbindung von hybriden FVK/Metall-Bauteilen an
metallische Tragstrukturen durch Widerstandspunktschweißen**

Band 245

Dr.-Ing. Sina Kathrin Peukert

**Robustheitssteigerung in Produktionsnetzwerken mithilfe eines integrierten
Störungsmanagements**

Band 246

Dr.-Ing. Alexander Jacob

Hochiterative Technologieplanung

Rekursive Optimierung produkt- und fertigungsbezogener Freiheitsgrade am Beispiel der hybrid-additiven Fertigung

Band 247

Dr.-Ing. Patrick Moll

Ressourceneffiziente Herstellung von Langfaser-Preforms im Faserblasverfahren

Band 248

Dr.-Ing. Eric Thore Segebade

Erhöhung der Verschleißbeständigkeit von Bauteilen aus Ti-6Al-4V mittels simulationsgestützter Zerspanung und mechanischer Mikrotexturierung

Band 249

Dr.-Ing. Shun Yang

Regionalized implementation strategy of smart automation within assembly systems in China

Band 250

Dr.-Ing. Constantin Carl Hofmann

Vorausschauende und reaktive Mehrzieloptimierung für die Produktionssteuerung einer Matrixproduktion

Band 251

Dr.-Ing. Paul Ruhland

Prozesskette zur Herstellung von hybriden Faser-Metall-Preforms

Modellbildung und Optimierung des Binderauftrags und der Drapierung für stabförmige Bauteile

Band 252

Dr.-Ing. Leonard Schild

Erzeugung und Verwendung von Anwendungswissen in der industriellen Computertomographie

Band 253

Dr.-Ing. Benedikt Klee

Analyse von Phaseninformationen in Videodaten zur Identifikation von Schwingungen in Werkzeugmaschinen

Band 254

Dr.-Ing. Bruno Vargas

Wälzschalen mit kleinen Achskreuzwinkeln

Prozessgrenzen und Umsetzbarkeit

Band 255

Dr.-Ing. Lucas Bretz

Function-oriented in-line quality assurance of hybrid sheet molding compound